Development of novel imaging biomarkers using positron emission tomography for characterization of malignant phenotype and response evaluation

A thesis presented by

Dr Sree Amarnath Rao Challapalli

MBBS, MD, MRCP (UK), FRCR

Department of Surgery and Cancer

Commonwealth Building, Hammersmith Hospital

Imperial College of Science, Technology and Medicine

To

Imperial College, London

For the degree of

Doctor of Philosophy (PhD)

2013

Declaration

I declare that this thesis is my own and original work except where duly acknowledged.

Dr Sree Amarnath Rao Challapalli

Dedication

To

My daughter, Chinmayi who made it all worthwhile

Abstract

Positron emission tomography (PET) enables noninvasive tumour imaging, as changes in metabolic activity secondary to therapy can be measured before changes in tumour size are evident on standard anatomic imaging. Two imaging approaches representing proliferation dependent and independent technologies are evolving as potential methods for assessing growth signalling and, thus, treatment response: [^{18}F]3'-deoxy-3'-fluorothymidine (FLT) and [^{11}C]choline. The validity of the former in patients with pancreatic cancer is unproven and likewise, the role of the latter in response to androgen deprivation/radiotherapy in prostate cancer (PCa) remains unexplored. Using a variety of approaches, the aim of this thesis was to provide an understanding of the role of these tracers in lesion detection and response assessment in patients by PET/computed tomography (PET/CT).

Given the high physiological hepatic localisation of FLT, a recently reported kinetic spatial filtering (KSF) algorithm was evaluated as a way to de-noise abdominal FLT-PET data from patients with advanced pancreatic cancer. Application of KSF led to improved lesion detection. FLT uptake ($SUV_{60,max}$) significantly increased in mid-treatment (gemcitabine based) progressors ($p=0.04$). In this limited number of patients, reduction in FLT uptake did not predict overall survival.

The role of [^{11}C]choline PET/CT in lesion detection and response in prostate cancer (PCa) was also investigated using semi-quantitative and quantitative methods. As a prelude to the quantitative imaging studies, it was established that irreversible tracer uptake characterised tumour (breast cancer) [^{11}C]choline kinetics. Similar irreversible uptake characterised PCa. An important finding was that tumour [^{11}C]choline uptake (in 29 PCa patients) correlated with choline kinase (CHK)

expression but not proliferation, as assessed by Ki67 labelling index. Immunohistochemistry of the above patients' prostate cores with CHKα antibody demonstrated a spectrum of CHKα expression, ranging from expression in prostatic-intraepithelial-neoplasia to low to high expression in malignant cores. These findings were further corroborated in a larger cohort of 75 malignant cores derived from non-imaging studies. Having established [^{11}C]choline as a proliferation independent marker of growth, its role in assessing treatment response was investigated. [^{11}C]choline PET was sensitive to metabolic changes within prostate tumours following androgen deprivation and radical radiotherapy.

While promising data were obtained with [^{11}C]choline PET, the radiotracer is subject to metabolic degradation complicating data analysis. To this end, a novel metabolically stable analogue of choline ([^{18}F]fluoromethyl-[1,2-$^{2}H_4$]-choline ([^{18}F]D4FCH)) was transitioned into volunteers and patients to study its pharmacokinetics and preliminary diagnostic potential. This tracer embodies deuterium isotope substitution as a means to discourage systemic metabolism. The radiotracer had favourable dosimetry (effective-dose: 0.025mSv/MBq) and safety. Preliminary results in non-small cell lung cancer showed that the tracer is taken up in tumours. Further studies are warranted to characterise this new tracer in different tumour types.

As a prelude to imaging cancer cell death in tumours, a caspase-3 specific radiotracer, [^{18}F](S)-1-((1-(2-fluoroethyl)-1H-[1,2,3]-triazol-4-yl)methyl)-5-(2(2,4-difluorophenoxymethyl)-pyrrolidine-1-sulfonyl) isatin ([^{18}F]ICMT-11) was also transitioned into volunteers. The radiotracer had favourable dosimetry (effective-dose: 0.025mSv/MBq) and safety.

In summary, FLT-PET/CT combined with KSF and [^{11}C]choline PET/CT were shown to be promising methods for imaging early treatment response in patients.

Further work will be required to evaluate the clinical relevance of these data in terms of overall patient outcome. Furthermore, a new choline-based radiotracer and a caspase-3 specific radiotracer have been transitioned into humans.

Table of Contents

Table of figures

Tables

List of Abbreviations

[18F]D4-FCH	[^{18}F]fluoromethyl-[1,2-$^{2}H_4$]-choline
[18F]ICMT-11	[^{18}F](S)-1-((1-(2-fluoroethyl)-1H-[1, 2, 3]-triazol-4-yl)methyl)-5-(2(2,4-difluorophenoxymethyl)-pyrrolidine-1-sulfonyl) isatin
ADT	Androgen deprivation therapy
AE	Adverse events
AICw	weighted Akaike Information Criterion
AJCC	American Joint Cancer Committee
ANOVA	Analysis of Variance
APD	Avalanche Photo Diode
ATM	Mutated in Ataxia Telangiectasia
AUC	Area Under Curve
BGO	Bismuth Germanate Oxide
BM	Bone marrow
BrdU	Bromodeoxyuridine
BRT	Brachytherapy
BSA	Bovine Serum Albumin
BW	Body weight
cdk	Cyclin Dependent Kinase
CDP-Choline	Cytidine di-phosphate Choline
CECT	Contrast Enhanced CT
CHK	Check point Kinase
CHKα	Choline Kinase alpha
CHT	High affinity choline transporters
CI	Common Iliac
CK	Cytokeratin
CMR	Complete Metabolic Response
CR	Complete Response
CT	Computed Tomography
CTC	Common Toxicity Criteria
CTL	Choline transporter-like proteins
CZT	Cadmium-Zinc-Telluride
DAPI	Diamidino-2-phenylindole
DCE-MRI	Dynamic Contrast Enhanced MRI
DMAE	Dimethylaminoethanol
DWI-MRI	Diffusion Weighted Imaging MRI
ECG	Electrocardiogram
ECOG	Eastern Cooperative Oncology Group
ED	Effective Dose
EDE	Effective Dose Equivalent
eLPL	extended laparoscopic Pelvic Lymphadenectomy
EMT	Epithelial to mesenchymal transition
EORTC	European Organisation for Research and Treatment of Cancer
FBP	Filter Back Projection
FCH	[^{18}F]Fluorocholine
FCS	Foetal Calf Serum
FDG	[^{18}F]Fluoro-deoxyglucose

FDOPA	[^{18}F]Fluorodihydroxyphenylalanine
FFPE	Formalin Fixed Paraffin Embedded
FLT	[^{18}F]3'-deoxy-3'fluorothymidine
FMP	FLT Mono-Phosphate
FN	False Negative
FNH	Focal nodular hyperplasia
FOV	Field of View
FP	False Positive
FRT	Fractional Retention of Tracer
FWHM	Full width Half Maximum
G1	First preparatory phase
G2	Second preparatory phase
GBq	Giga Becquerel
GF	Growth Factor
GLUT	Glucose uptake transporter proteins
GM	Gluteus Maximus
GS	Gleason score
H&E	Haematoxylin & Eosin
Hb	Haemoglobin
HCC	Hepatocellular carcinoma
hcG	Human chorionic Gonadotropin
hENT1	human Equilibrative Nucleoside Transporter
HGG	High grade glioma
HiVox	High intensity voxel
HK	Hexokinase
HPLC	High Performance Liquid Chromatography
ICHNT	Imperial College Healthcare NHS Trust
ICRP	International Commission on Radiation Protection
IF	Input Function
IF	Immuno Fluorescence
IHC	Immunohistochemistry
IMP	Investigative Medicinal Product
IRF	Impulse Response Function
kBq	Kilo Becquerel
keV	Kilo electron volt
KSF	Kinetic Spatial Filtering
LD	Longest Diameter
LHRH	Luteinising Hormone Releasing Hormone
LN	Lymph nodes
LOR	Line of Response
LoVox	Low intensity voxel
LSAB	Labelled Streptavidin Biotin
LSO	Lutetium ortho silicate
MAPK	Mitogen Activated Protein Kinase
MBq	Mega Becquerel
MHRA	Medicines and Healthcare products Regulatory Agency
MIRDOSE	Medical Internal Radiation Dose
MPF	Mitosis Promoting Factor
MRI	Magnetic Resonance Imaging
MRS	Magnetic Resonance Spectroscopy

NAD	Neoadjuvant Androgen Deprivation
NEC	Noise equivalent counting
NHNFT	Newcastle Hospitals NHS Foundation Trust
NSCLC	Non-Small Cell Lung Cancer
OCT	Organic Cationic Transporter
OI	Obturator Internus
OLINDA/EXM	Organ Level Internal Dose Assessment and Exponential Modelling
OS	Overall Survival
OSEM	Ordered Subset Expectation Maximisation
PARP	Poly ADP ribose polymerase
PC	Phosphatidyl Choline
PCa	Prostate Cancer
PCho	Phospho Choline
PCNA	Proliferating Cell Nuclear Antigen
PD	Progressive Disease
PD	Pharmacodynamics
PERCIST	PET Response Criteria in Solid Tumours
PET	Positron Emission Tomography
PFS	Progression Free Survival
PIN	Prostatic Intraepithelial Neoplasia
PIP3	Phosphatidylinositol (3, 4, 5) tri phosphate
PK	Pharmacokinetics
PLK	Polo like Kinase
PMD	Progressive Metabolic Disease
PMR	Partial Metabolic Response
PMT	Photo Multiplier Tube
PR	Partial Response
PSA	Prostate specific antigen
PSAPD	Position sensitive avalanche photodiode
PTEN	Phosphatase and tensin homolog
PVDF	Polyvinylidene difluoride
qRT-PCR	quantitative Reverse Transcriptase Polymerase Chain Reaction
RB	Retinoblastoma
REC	Research Ethics Committee
RECIST	Response Evaluation Criteria in Solid Tumours
ROC	Receiver Operating Characteristic
ROI	Regions of Interest
RSS	Residual Sum Squares
RT	Radiotherapy
RT	Residence Time
RT-CAD	Radiotherapy-Concurrent Androgen Deprivation
S phase	Synthesis phase
SD	Stable Disease
SD	Standard Deviation
SMD	Stable Metabolic Disease
SNR	Signal to Noise Ratio
SUV	Standardised Uptake Value
TAC	Time Activity Curves
TBS	TRIS buffered saline
TBST	TRIS buffered saline-Tween

TGF-β	Transforming Growth Factor-Beta
TK 1	Thymidine Kinase 1
TMR	Tumour to muscle ratio
TN	True Negative
TNM	Tumour, Node, Metastasis
TOF	Time of Flight
TP	True Positive
TRUS	Trans rectal Ultrasound
USPIO	Ultra small particles of Iron oxide
VOI	Volume of Interest
WBC	White blood cells
WHO	World Health Organisation
WPRT	Whole Pelvic Radiotherapy

Acknowledgements

It would not have been possible to complete this PhD thesis without the support, encouragement and timely help of numerous people including my well wishers, colleagues and various institutions. At the end of my thesis, it is a pleasant task to express my thanks to all those who contributed in many ways to the success of the studies and made it an enriching experience for me.

Firstly, I would like to express my heartfelt thanks to my principal supervisor, Prof. Eric Aboagye who was instrumental and the driving force for my PhD. He was a constant source of support and inspiration, not to mention his advice and unsurpassed knowledge of molecular imaging. I immensely value his advice, constructive criticism and his extensive discussions around my work. His constant quest for perfection enabled me to hone my writing skills.

I would like to thank Dr. Stephen Mangar for supporting me in my studies including providing ideas for the clinical aspects of my PET studies as well as his constant source of encouragement and in recruiting patients for my studies as well as reviewing papers for publication. Dr. Tara Barwick deserves my sincere expression of thanks for reviewing the image data and for willingly devoting so much time in giving guidance to me and for the critical appraisal of my work.

I am particularly indebted to Dr Kaiyumars Contractor, who has shared my initial research journey and taught me the practical aspects of modelling and been an excellent colleague to work with. I am also thankful to him for letting me re-analyse part of the data which he used for his PhD studies which led to a greater understanding of my work.

The work described in this thesis was carried out primarily in the Comprehensive Cancer Imaging Centre, at Imperial College, Hammersmith Hospital Campus, London. I would like to express my gratitude to all the chemists and radiographers of Hammersmith-Imanet, in particular Mr Andy Blyth, Ms Andreanna Williams and Ms Hope McDevitt for their help with scanning and ensuring patient comfort. I extend my thanks to Prof. Adil Al-Nahhas, Dr. Michael O'Doherty and the PET teams at Charing Cross Hospital, St Thomas' Hospital, Newcastle Hospitals NHS Foundation Trust and Imanova Centre for Imaging Sciences. Without their efforts, it would have been difficult to complete these studies. I take this opportunity to sincerely acknowledge Cancer Research UK (CRUK) for funding my fellowship which buttressed me to perform my work comfortably and the Medical Research Council (MRC) for funding the PET scans.

I would also like to extend my thanks to Ms Kasia Kozlowski for her professional help in recruiting patients and healthy volunteers for PET studies and for her editorial assistance. I am grateful to Dr. Steve Hazell, Dr. Mihir Gudi, Dr. David Pinato, Sebastian Trousil, Mr. David Peston and staff of Imperial Tissue Bank for their help with the immunohistochemistry as well as validating the results. My colleagues and friends, Dr. Rohini Sharma, Dr. Laura Kenny, Dr. Giampaolo Tomasi and Dr. Shairoz Merchant deserve special thanks for their support, encouragement, humour and timely advice.

A warm thanks goes to the clinicians, the team of cancer network research nurses and staff of the Imperial Clinical Research Facility who helped in recruitment and were instrumental in ensuring all my studies were successfully completed. I would also like to acknowledge and thank Dr. Alexandra Taylor and Dr. Stephen Mangar, who encouraged me to pursue my research interests and were the source of inspiration for me in my early days and who taught me many things.

I would like to gratefully acknowledge the support of my wife Rasmi, for her personal support and great patience at all times. My parents and sisters have given me their sincere encouragement, unequivocal support and inspiration throughout my research work, as always, for which my mere expression of thanks likewise does not suffice.

Lastly, but importantly, I would like to thank all the patients and their carers for selflessly agreeing to take part in this research, even though it was of no direct benefit to them. For this I am forever in their debt. Besides this, several people have knowingly and unknowingly helped me in the successful completion of this project.

Amar

Chapter 1: Introduction

Cancer cells exhibit diverse phenotypic abnormalities, such as loss of differentiation, increased motility/ invasiveness, decreased drug sensitivity and dysregulation of cell cycle control. The growth of tumours, characteristic of cancerous process is related to the balance between growth (sustained proliferation) and cell death properties. A cell's ability to replicate in an orderly and controlled fashion is an essential component of life. The molecular machinery controlling the cell division is performed with great fidelity and is highly organised. Aberrations of normal cell cycle control lead to molecular alterations that are characteristic of cancer cells.

Cell Cycle

In any proliferating mammalian cell, the process of replication can be broken down into 4 distinct phases (**Figure 1**).

Cells have evolved checkpoints to regulate the complex and irreversible process of cell division. These are biochemically defined points in the cell cycle which can be activated to prevent transition across certain phases (Alberts 2008). Loss of these checkpoints is implicated in malignant transformation.

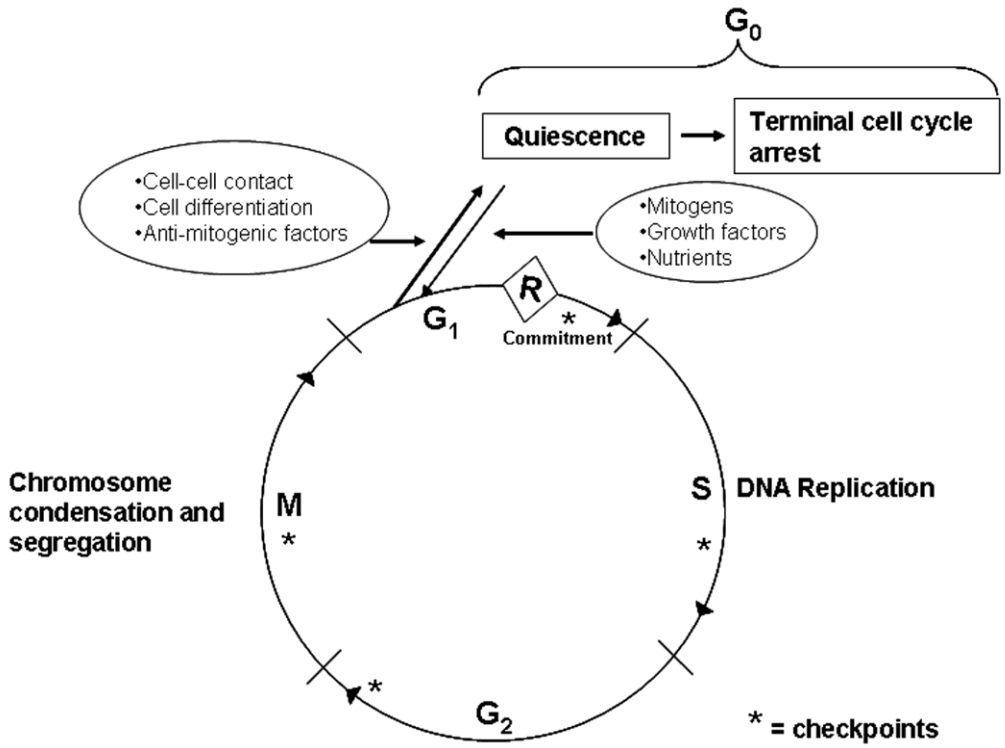

Figure 1: Schematic representation of phases of cell cycle.

Growth factors drive a quiescent cell from G_0 into cell cycle. Once the cell cycle passes beyond the restriction point (R), mitogens are not required for progression. DNA replication occurs in S phase and the chromosomes are condensed in mitotic (M) phase. Cell cycle check points are denoted by *. **G_0 phase**: a quiescent state, **G_1 phase:** first phase of the cell cycle where the cell undergoes biochemical changes in preparation for entry into S phase, **S phase:** synthesis phase where new DNA is synthesisesynthesised. A complete copy of the cells genetic material is generated, **G_2 phase:** second preparatory phase called Gap 2 (G_2), **M phase:** Mitotic phase, in which replicated DNA is condensed into compact chromosomes that are precisely segregated and distributed into daughter cells. Following M phase, a proliferative cell directly enters G_1 phase in preparation for further replication.

Regulation of cell cycle

Regulation of the cell cycle involves control of the key regulatory proteins by post-translational modifications in a cell cycle dependent manner orchestrated by cyclins and cyclin-dependent kinases (cdk), which are central to all phases of the cell cycle and shown in **Figure 2** (Sherr and Roberts 2004; Malumbres and Barbacid 2005).

There is an elegant system of several regulators which control the transition between the different phases of the cell cycle (Schafer 1998; Alberts 2008). The activated cyclin/cdk complex phosphorylates a variety of substrates to facilitate both the G_1 to S phase and G_2 to M phase transitions. The M phase entry and exit is regulated by mitosis promoting factor (MPF) which is characterised by a complex of cyclin B and cdk1.

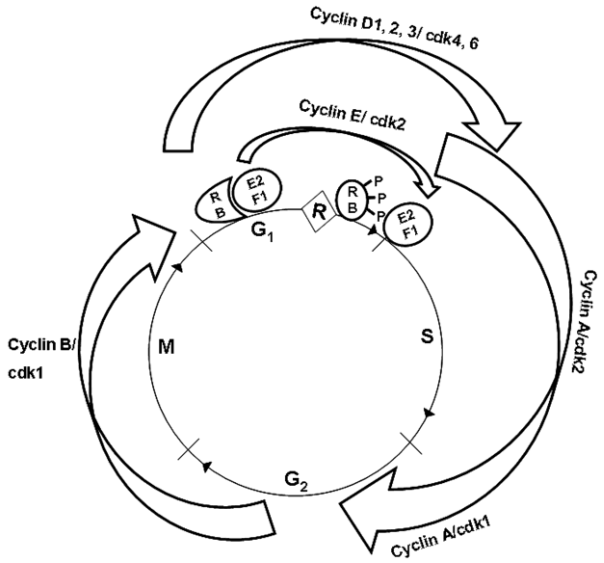

Figure 2: **Schematic representation of changes in cyclins and cdk through cell cycle.**
Growth factors stimulate synthesis of cyclin D in G_1 phase. Cyclin E is synthesised later in G_1 phase. Cyclin A is synthesised late in G_1, throughout S and into early G_2 phase. Cyclin B is synthesised in late G_2 and M phase. The loss of cyclin B/ cdk1 at end of M phase is required for re-entry into next G_1 phase.

Cell cycle checkpoints

The events of cell cycle are highly ordered and sequential such that the initiation of any event in the cell cycle is dependent on completion of earlier events. DNA damage by intrinsic or extrinsic processes inhibits cell cycle progression by invoking the check points: before entry into S phase, with in S phase or before entry into mitosis (Bertoli, Skotheim et al. 2013; Foley and Kapoor 2013). This limits the propagation of genetic mutations to daughter cells by allowing for DNA repair (**Figure 3**).

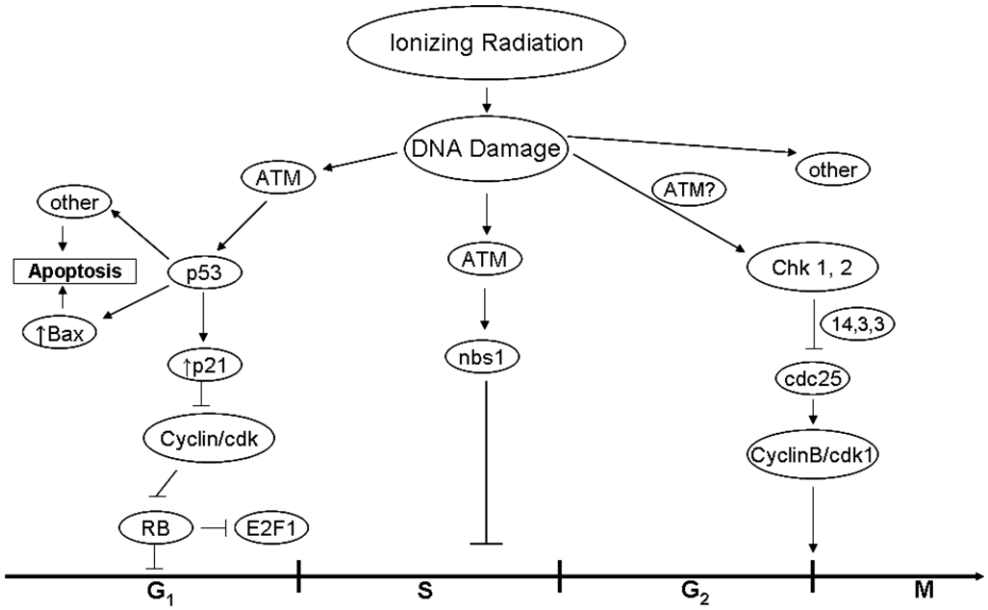

Figure 3: Schema of cell cycle check points.

Ionising radiation causes DNA damage in the form of strand breaks and activates several signal transduction pathways. For cells in G_1, DNA damage leads to increase in the p53 protein through ATM. This induces apoptosis or an increase in p21 and causes cell cycle arrest. For cells in S phase, DNA damage arrests further DNA synthesis in an ATM and nbs-1 dependent manner (Lim, Kim et al. 2000). For cells in G_2 and M phase, DNA damage activates check point kinases (CHK 1 & 2) which phosphorylate cdc25. This prevents activation of cyclin B/ cdk1 (Mitosis promoting factor: MPF) which is critical for entry into mitosis. Another checkpoint involves the spindle apparatus, which prevents metaphase to anaphase transition (Foley and Kapoor 2013).

Hallmarks of Cancer

Mammalian cells possess molecular machinery that regulates their proliferation, differentiation, and death. Malignant transformation is a multistep process involving genetic alterations, disruption of regulatory circuits and dynamic changes in the genome. It has been suggested that malignant growth is governed by six essential alterations in cell physiology: self-sufficiency in growth signals, insensitivity to growth-inhibitory (antigrowth) signals, evasion of programmed cell death (apoptosis), limitless replicative potential, sustained angiogenesis, and tissue invasion and metastasis (Hanahan and Weinberg 2000).

Recent advances in understanding tumour biology led to the notion that progressive evolution of normal cells to a neoplastic state involves not only acquiring a succession of these hallmark capabilities, but also requires the contributions of the recruited normal cells (which form tumour-associated stroma, constituting the ‘‘tumour microenvironment’’) to tumourigenesis (Hanahan and Weinberg 2011).

It has been suggested that sustained proliferative signalling could also be attributed to:

- Somatic mutations activating downstream signalling such as Raf to mitogen-activated protein (MAP)-kinase pathway in melanoma (Davies and Samuels 2010), and mutations in phosphoinositide 3-kinase (PI3-kinase) isoforms in an array of tumour types, hyper-activate the PI3-kinase signalling pathway (Yuan and Cantley 2008; Jiang and Liu 2009).
- Telomere maintenance and delayed activation of telomerase (Hansel, Meeker et al. 2006; Kawai, Hiroi et al. 2007).

The six hallmarks are all linked to cell proliferation of cancerous cells, thus making cell proliferation an important capability leading to immortalisation and generation of macroscopic tumours.

The above framework of hallmarks assumes a homogeneous population of cancer cells and considers the hallmarks as distinct entities, with a one-to-one relation between oncogenic events (the inducers), the signalling pathways (transmission), and the hallmarks (the effects). However, one oncogenic event, or one signalling cascade, could induce several hallmarks accounting for the dynamic and spatial heterogeneity of tumours (Floor, Dumont et al. 2012). This heterogeneity provides a framework to interpret pathological, diagnostic, and therapeutic observations of tumours and supports the need for noninvasive serial studies on the whole tumour mass and the use of simultaneous, multi target therapies for treating cancer.

Need for imaging

Cell Proliferation

As discussed in the previous section, the basic tenet of all the deranged cell regulatory processes is an increase in cell proliferation. The rates of tumour cell division have been demonstrated to be of prognostic value with the slow growing tumours having a markedly different prognosis than the aggressive ones. Hence the quantification of cell proliferation would facilitate decisions to be accurately made in choosing the right therapeutic options to treat cancer.

Cells in the M phase show morphological features called “mitotic figures” which can be counted and the mitotic index has been the most commonly used quantitative measure to assess proliferative activity (O'Leary and Steffes 1996). However, the

number of mitotic figures may not correlate well with proliferation and are subject to sampling artifacts (Lehr, Rochat et al. 2013). The other methods explored to improve measurement of proliferation include estimation of growth fraction of tumour cells. Growth fraction quantification using immunohistochemistry techniques (estimate nuclear antigens such as Ki67, proliferating cell nuclear antigen (PCNA) and geminin) have demonstrated good applicability (Lopes, Hannisdal et al. 1998; Colozza, Azambuja et al. 2005; Yerushalmi, Woods et al. 2010). Other measures include flow cytometry (Barnard 2012), and two dimensional or three dimensional assessment of the S-phase fraction (Montironi, Diamanti et al. 1992; Tekola, Baak et al. 1996).

The "gold standard" for assessing proliferation is using bromodeoxyuridine (BrdU) and tritiated thymidine assays (Cavanagh, Walker et al. 2011). However this has limited clinical utility due to the need for fresh material, invasiveness and involvement of radioactivity. Therefore, at tissue level, mitotic counting and the Ki67 labelling index (Ki67) provide the most feasible and accurate means of quantifying proliferation.

Apoptosis

Apoptosis is an essential process for eliminating unwanted cells during embryonic development, growth, differentiation and maintenance of tissue homeostasis. Deregulation of apoptosis signalling pathways is, therefore, associated with various pathologies (Reed 2002), and the capacity to evade apoptosis has been defined as one of the hallmarks of cancer (Hanahan and Weinberg 2011). Most of the current anti-cancer therapeutics and radiotherapy act by a variety of mechanisms but, by shifting the proliferation: apoptosis ratio, may share the common outcome of apoptosis (Kaufmann and Earnshaw 2000; Storey 2008).

The classical assessment of apoptosis was based on morphological criteria (Wyllie, Kerr et al. 1972) and biochemical criteria (Kroemer, Galluzzi et al. 2009). Other methods, which utilise tumour biopsies, have been developed. These include the TUNEL assay where the double strand breaks generated secondary to DNA fragmentation, are marked by labelled bromodeoxyuridine, and catalysed by terminal deoxynucleotidyl transferase (Loo 2011; Wlodkowic, Telford et al. 2011). The other method includes morphological assessment by H&E staining alongside immunohistochemistry (IHC) to assess caspase substrates such as cytokeratin 18 (CK18) or Poly ADP-ribose polymerase (PARP) (Tong, Chen et al. 2010). However, these methods applied to biopsies fail to provide detailed spatial relationship data on a pharmacodynamic response, as only a small part of the tumour can be evaluated, leading to lack of appreciation of intra-tumoural heterogeneity. Moreover, quantification of IHC is somewhat subjective and only observes a snapshot of cell death at a given point in time.

Hence, there is a need for development of imaging techniques that could enable monitoring of these biological processes. Imaging biomarkers differ from conventional tumour biopsy derived biomarkers as they allow noninvasive serial studies on the whole tumour mass.

Current standards for response evaluation

The clinical evaluation of cancer therapeutics involves assessment of the change in tumour burden (anatomical measurements). Tumour shrinkage (objective response) and time to disease progression are both important, as these have been linked to an improvement in overall survival or other time to event measures in randomised phase III studies (Buyse, Thirion et al. 2000). These also determine the

efficacy of the drug under consideration. In order to have standardised and widely accepted criteria for measurement of response to allow comparisons to be made across studies, the Response Evaluation Criteria in Solid Tumours (RECIST) criteria were formulated (Therasse, Arbuck et al. 2000). These criteria have been widely adopted for trials where the primary endpoints are objective response or disease progression. Since the introduction of RECIST in 2000, the increasing utilisation of imaging technologies such as MRI, FDG PET and targeted cytostatic therapies, have prompted an update in the guidelines (RECIST v1.1) (Eisenhauer, Therasse et al. 2009).

According to RECIST v1.1 guidelines, tumour responses to cancer treatment are graded as follows:

1) Complete Response (CR): disappearance of all target lesions. Any pathological lymph nodes (whether target or non-target) must have reduction in short axis to <10 mm.

2) Partial Response (PR): at least a 30% decrease in the sum of diameters of target lesions, taking as reference the baseline summed diameters.

3) Progressive Disease (PD): at least a 20% increase in the sum of diameters of target lesions, taking as reference the smallest sum on study (this includes the baseline sum if that is the smallest on study). In addition to the relative increase of 20%, the sum must also demonstrate an absolute increase of at least 5 mm. Appearance of new lesions not present previously is also considered progression.

4) Stable Disease (SD): neither enough shrinkage to qualify for PR nor sufficient increase to qualify for PD, taking as reference the smallest sum of diameters.

However, since measuring response by RECIST relies on the change in tumour size with therapy, this method has certain limitations. Firstly, uni-dimensional measurements may be apparent only after 3-4 cycles of chemotherapy. In non-responders, this means subjecting them to cumulative toxicity of 3-4 cycles of treatment with little benefit. Moreover, the change in the tumour diameter may not be uniform. Secondly, changes in measurements of smaller lesions are not reliable (Revel, Bissery et al. 2004). Thirdly, tumours may be responding to cytostatic treatment which may not necessarily cause a decrease in tumour size or volume even though they may be affecting tumour proliferation. Due to these limitations in quantifying objective response to treatment, the advent of functional imaging has changed the way in which response to cancer therapy can be measured.

Positron Emission Tomography

Positron emission tomography (PET) is an imaging method which uses short lived radioisotopes to visualise their distribution, to study molecular interactions and quantify regional biochemistry or metabolism in living tissues. A typical PET study comprises of (i) radiotracer production (ii) synthesis of radiopharmaceuticals from the tracers (iii) patient administration of radiopharmaceutical (iv) measuring the radioactivity distribution in the region of interest and (v) interpretation of activity distribution as a physiologic function parameter.

A positron is a positively charged electron. The positrons used in PET arise from disintegration of unstable atomic nuclei having an excess positive charge. The

radio nuclides are produced in a cyclotron. **Table 1** gives the reactions used to produce the principal radio nuclides used in PET.

Table 1: Principal radio nuclides used in PET and the nuclear reaction notations and physical characteristics of the isotopes

Positron emitting product	Stable element	Nuclear reaction	Half life of product (min)	Stable nucleus after positron emission	Average Positron energy (keV)	Positron range In soft tissue (mm)
^{11}C	Nitrogen (^{14}N)	$^{14}N(p, \alpha)^{11}C$	20.4	^{11}B	386	1.23
^{18}F	Oxygen (^{18}O)	$^{18}O(p, n)^{18}F$	109.8	^{18}O	250	0.61
^{15}O	Nitrogen (^{14}N)	$^{15}N(p, n)^{15}O$	2.03	^{15}N	735	2.97
^{13}N	Carbon (^{12}C)	$^{13}C(p, n)^{13}N$	10	^{13}C	491	1.73

The nuclear reaction notation $^{14}N(p, \alpha)^{11}C$ implies that a proton (p) is bombarded into a target ^{14}N nucleus, ejecting an alpha particle (α), resulting in a ^{11}C nucleus. n= neutron.

The success of these positron emitters as *in vivo* radiotracers is due to the fact that (i) they are radioisotopes of physiological elements like carbon, oxygen and fluorine and (ii) they have short half lives (time taken for activity to decay to half the original activity, $t_{1/2}$) requiring the need for an on-site cyclotron. The radiotracer produced is normally incorporated into a specific compound, target agent or drug which is to be imaged and is injected intravenously into the body. The radiotracer is taken up preferentially by certain tissues in the body depending on the region or metabolic pathway to be imaged.

The isotopes (^{11}C, ^{18}F) emit positrons which travel a short distance in tissues before colliding with an electron in the tissues causing annihilation energy in the form of two 511 keV photons at 180 degrees to each other **(Figure 4)**.

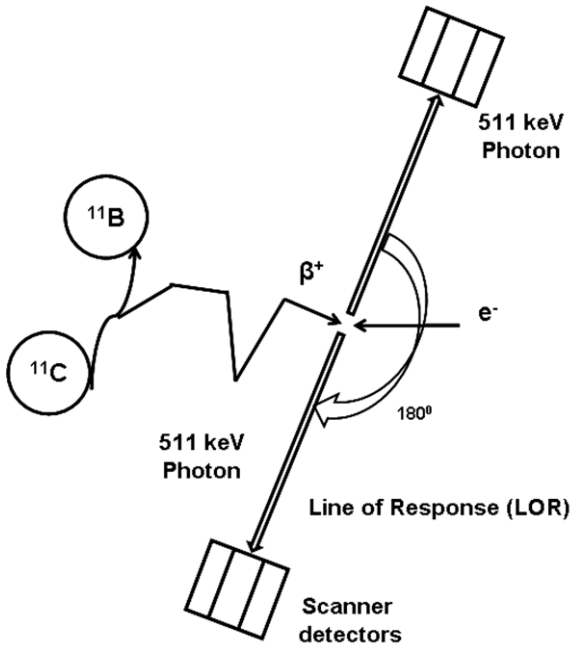

Figure 4: Coincidence detection along the Line of Response (LOR).

The emitted positron interacts with an electron in the tissue leading to annihilation photons at 180^0. These photons are detected by the ring detectors containing bismuth germinate oxide (BGO) crystals which convert photons into an electric signal.

As these photons are emitted in opposite directions, a “true” count or a “coincidence event” is one which consists of paired photons from a single atom somewhere along the line that joins the two detectors (LOR). In addition to the true coincidence, there could be “random” events which occur when photons from two or more atoms strike two oppositely arranged detectors at the same time or "multiple" coincidences when more than 2 photons arrive in coincidence.

Image reconstruction

The coincident events detected are stored over preselected time frames in sinogram data matrices which are a stack of slices of the acquired projection views from 0^0 to 360^0. There is a greater interest to store data in a list mode, where each

event is stored separately to disk. This allows correction for patient motion and improves temporal resolution. The slices from the projection views are processed into transaxial slices by the process of reconstruction. This is done by (a) Filtered Back Projection (FBP) (Webb 1990; Abella, Vaquero et al. 2009) or (b) Iterative reconstruction (Hudson and Larkin 1994; Hutton 2011).

Resolution of the scanner

The resolution of a scanner is the smallest distance (in millimetres) that side by side objects can be differentiated as separate in an image with infinite counts. This depends on (a) the distance travelled by the positron before annihilation (between 0.5 – 2 mm) (b) variation in angle between the annihilated photons and (c) the size of the detectors (typically 1-3 mm). These factors taken together limit the resolution to about 4-7 mm. Recent advances in novel detectors with 3D positioning capability (**Figure 5**) such as cadmium-zinc-telluride (CZT) and position-sensitive avalanche photodiodes (PSAPDs) have a great potential for achieving spatial resolution better than 1 mm (Peng and Levin 2010).

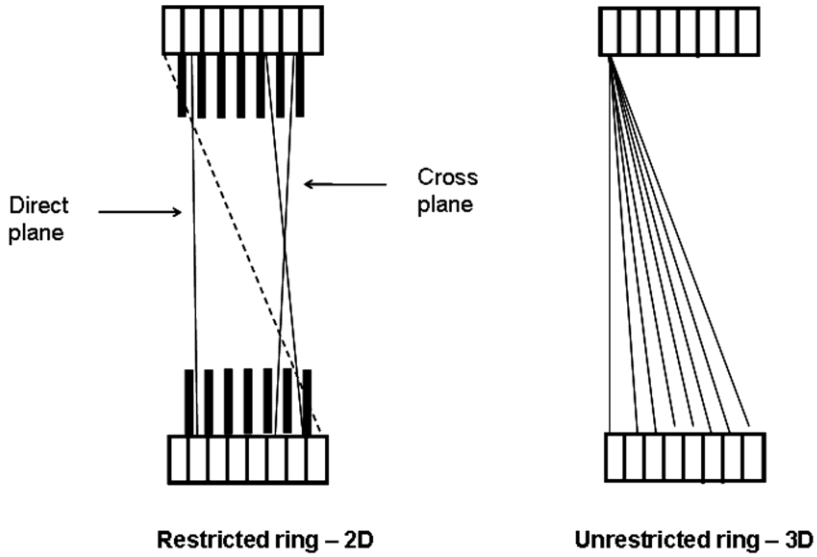

Figure 5: **Coincidence combinations for 2D and 3D modes.**
Axial cross section of a multiple ring scanner showing, the septae absorbing the photons scattered between the planes (dotted line), in the 2D mode. The 3D mode records the events between the planes increasing the number of events recorded for the same amount of radioactivity in the patient. This will enable reduction in scanning time.

Recent Advances in PET

Advances in PET detector technology

Lutetium oxyorthosilicate (LSO) and its derivates paved the way for fast coincidence timing thereby reducing random events and improving image quality. There is also an increasing impetus for replacing the photo multiplier tubes (PMTs) by novel semiconductor-based light detectors, such as avalanche photodiodes (APDs). The advantages are their compactness and their insensitivity to magnetic fields and therefore ideal as PET light detectors in combined PET-MRI scanners (Judenhofer, Wehrl et al. 2008). These novel, high-sensitivity, and high-resolution PET detectors along with an improved computer power, and advanced electronics could potentially aid in the reduction of scanning time and the injected radioactivity dose.

Time-of-Flight PET

Conventional PET uses a coincidence timing window of 3–15 nanoseconds, to determine if two events occur close enough in time to be a valid coincidence event. Therefore, it is unable to determine which voxel along the line is the source of the annihilation photons, giving the same probability of emission to all the voxels along the LOR. TOF technology provides a precise estimate of the arrival time of a photon in the scintillator to within a few hundred picoseconds and uses this estimate to better locate the annihilation position of the emitted positron with much higher precision than is achieved in conventional PET. This has the potential to improve image quality in PET scans, especially those of obese patients, due to a gain in the signal-to-noise ratio (SNR) (Conti 2009), and improved contrast resolution ultimately resulting in more efficient imaging and possibly shortened imaging times that are better tolerated by patients (Karp, Surti et al. 2008). This other clinical benefit is increased confidence of lesion detectability and accuracy of quantification (Basu, Kwee et al. 2011).

PET/MRI

The merging of PET and MRI allows the combination of functional information provided by PET with the high soft-tissue contrast offered by MRI. Scanners that combine PET and MRI imaging have recently been assembled for use in humans, and may have diagnostic performance superior to that of PET/CT for particular clinical and research applications. The major strengths of MRI compared to CT, include: superior soft-tissue contrast, multiplanar image acquisition, functional imaging capability through specialised techniques such as diffusion-weighted (DW) imaging, MR spectroscopy, and lack of ionising radiation from MRI (Torigian, Zaidi et al. 2013). The other

advantages of MRI include guiding PET image reconstruction, partial volume correction, and motion compensation. These features enable more accurate disease quantification and improve anatomic localisation of sites of radiotracer uptake in various clinical disorders. However, the clinical applications of PET/MRI are currently not clearly defined as the PET/MRI technology is not clinically mature yet. The challenges include lack of PMT's compatible with magnetic field, MRI data not readily usable for PET attenuation correction, and interference of surface coils with gamma rays from PET (von Schulthess, Kuhn et al. 2013).

Quantification of PET data

Semi-quantitative Analysis

PET images can be acquired in a static or dynamic mode. Static mode refers to the image acquired in a specific time period usually after sufficient clearance of the radiotracer from circulation. This is the commonest method in clinical PET imaging used for diagnosis and relies on the difference in tracer uptake between the region of interest and surrounding tissues. Visual assessment of such images is often employed for staging and diagnosis in oncology but is non-quantitative. For static imaging, a semi-quantitative index of uptake like the Standardised Uptake Value (SUV) normalised by body weight, which is unit less, is useful for response assessment (Young, Baum et al. 1999; Tomasi and Aboagye 2013).

$$SUV(t) = \frac{Ae^{\lambda t}}{A_{inj}} xBW \qquad \textbf{Equation 1}$$

where, A is the activity (kBq/mL) at time t, λ -the decay constant for [^{18}F] (6.311×10^{-3}) and for [^{11}C] is (3.379×10^{-2}), A_{inj} is the injected dose of tracer (kBq) and BW is body weight in grams.

Quantitative Analysis

Although, in clinical practice [^{18}F]FDG data are usually assessed visually and/ or using SUV, there is a need for quantitative analysis in oncology to characterise the pharmacokinetic properties, especially for the newer radiotracers (such as [^{18}F]3'-deoxy-3'fluorothymidine, [^{11}C]choline) being introduced. Quantitative assessment is superior to visual assessment as it is more objective and less user dependent. It can be fully automated and it allows an easier comparison between centres. The changes in quantitative indices with treatment may help in the interim evaluation of therapeutic efficacy and to predict early response assessment (Tomasi and Aboagye 2013).

Quantitative analysis requires dynamic scanning and invasive arterial blood sampling to measure the radiotracer concentration time activity curve in plasma (TAC). The parent plasma input function (IF: parent fraction of radiotracer) and total plasma IF (total radiotracer in plasma (parent plus metabolite)) are used together with a modelling approach appropriate for the radiotracer in order to estimate physiological parameters (the ''rate constants''), such as delivery, clearance, irreversible uptake rate, and rate of binding.

The most common approach is to assign the possible distribution of the radiotracer to a number of discrete compartments, within which it could be free or trapped. This is called compartmental modelling and is the most accurate method to analyse PET data. There are other more data-led approaches such as Graphical and Spectral analyses, which have been explored as an alternative to compartmental modelling (Tomasi, Turkheimer et al. 2012).

As arterial sampling requires considerable technical expertise, is invasive for the patient and inappropriate for routine clinical practice, alternative strategies are being considered which could be applied routinely in the clinical setting. If the heart is in the

scanner field of view the radiotracer concentration time activity curve in blood can be estimated directly from the PET image (image derived IF) (Cheebsumon, Velasquez et al. 2011). The validity of this approach however, depends on several factors, one of which is the confounding signal in the left ventricle due to the myocardial uptake. Alternative methods, such as population derived IF (Contractor, Kenny et al. 2012) and reference-region approach (Zheng, Wen et al. 2012), are also being extensively studied.

In oncology there are other specific issues which require further consideration. The influence of partial volume correction (PVC), motion correction, and the penetration of radiometabolites into tissue and contribution to the signal measured with PET need to be taken into account. Deconvolution algorithms (Soret, Bacharach et al. 2007) and respiratory gating (Rahmim 2007) have been evaluated for PVC and motion correction, respectively. To account for the contribution of radiometabolites, especially for tracers that are rapidly metabolised, compartmental modeling and spectral analysis based on a double-input-function approach in which the parent radiotracer and the radiometabolite plasma TACs are both required as input functions has been proposed (Tomasi, Kimberley et al. 2012; Tomasi and Aboagye 2013).

The standard modelling approaches are described in brief, below.

Compartmental analysis

This enables the application of the model to arterial/ venous blood and tissue data to calculate equilibrium blood- tissue exchange rate constants and binding kinetics of radiotracer into tissues like tumours (Gunn, Gunn et al. 2001; Gunn, Gunn et al. 2002). This helps in quantitatively measuring the behaviour of radiotracer in tumours, reflecting tumour biology as well as possible changes in uptake with treatment. In compartmental modelling, knowledge of the compartments into which the radiotracer is

expected to be present spatially is defined *a priori*. These compartments include blood or tissue compartments including tumour **(Figure 6)**. Kinetic parameters of interest which can be derived include:

K1 - rate constant of clearance from plasma to tissue (mL/g/min)

k2 - rate constant of clearance from tissue to plasma (min^{-1})

k3 - rate constant of phosphorylation of radiotracer in tumours (min^{-1})

k4 – rate constant of dephosphorylation of radiotracer in tumours (min^{-1})

Compartmental modelling is based on the following assumptions:

1. The radiotracer mixes instantly within the compartments.

2. Concentration of the radiotracer is very small so as not to interfere with the system under study.

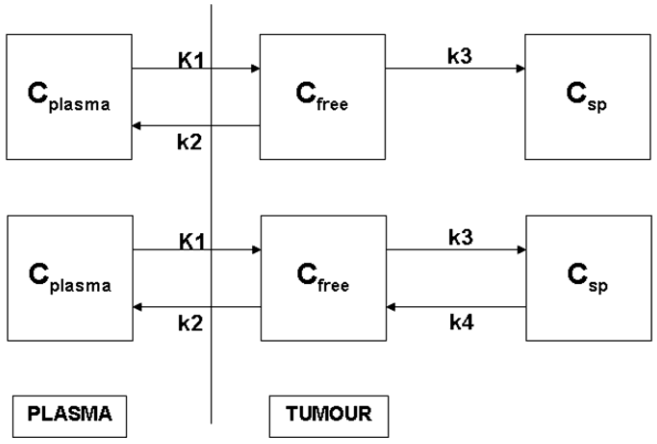

Figure 6: Schematic representation of the Compartmental model.
The radiotracer enters the tissue and can be in the free or the trapped (C_{sp}) state. The rate constants (K1, k2) represent clearance between plasma and tissue. The top panel represents a 3k model where in there is irreversible trapping of the tracer (k3). The bottom panel represents a 4k model where there is dephosphorylation (k4).

Compartmental analysis is performed by modelling dynamic PET tissue uptake data with the blood arterial IF. If dephosphorylation is assumed to be negligible (i.e.; k4 is negligible) during the PET scanning period, then a 3-constant (K1, k2 and k3) approach (3k) may be used. If dephosphorylation is expected with a radiotracer, then a 4-constant (4k) approach (all 4 kinetic rate constants) may give better fits with this modelling technique. The fit of the model is decided by the goodness of fit estimated by one of a number of methods including the akaike information criteria (AICw) and the residual sum of squares (RSS).

Modified Patlak's method

The original Patlak technique (Patlak, Blasberg et al. 1983) allows estimation of blood-to-tissue transfer constants from multiple time uptake data. This method is valid if there are no reversible metabolites. If the parent tracer is metabolised, then a correction is needed (Mankoff, Shields et al. 1996) to exclude the contribution of metabolites (which is betaine in the case of choline and FLT-glucuronide in the case of FLT) in the tissue-blood interface (modified Patlak method). This modification of Patlak's original method has been developed for irreversible tracers to allow estimation of Ki (rate constant for net irreversible uptake of radiotracer into tumour) in the presence of reversible metabolites (Kenny, Vigushin et al. 2005). The modified Patlak method for [^{11}C]choline uptake in tumours assumes that tumours don't convert choline to betaine, but rather that almost all the betaine is from circulation (from liver and kidneys). Therefore, it is hypothesised that the Ki for [^{11}C]choline thus derived reflects true net phosphorylation of [^{11}C]choline in tumours. The Modified Patlak formula is:

$$\frac{A}{C_{Tot}} = K_x \frac{\int C_x \delta\tau}{C_{Tot}} + V \qquad \textbf{(Equation 2)}$$

where V is defined as (Mankoff, Shields et al. 1996; Kenny, Vigushin et al. 2005);

$$V = V_{ox}\frac{C_x}{C_{Tot}} + \sum V_{om}\frac{C_m}{C_{Tot}} + V_b \qquad \textbf{(Equation 3)}$$

A= total tissue radioactivity (kBq/mL)

$K_x = K_i$ for [^{11}C]choline (ml plasma/s/ml tissue)

C_{Tot}= total blood radioactivity (kBq/ml),

C_x= radioactivity of parent compound determined by HPLC (kBq/ml)

C_m = radioactivity of metabolite (kBq/mL)

T= time interval from time (s) of injection

V_{ox}= steady state space of exchangeable region occupied by parent

V_{om}= steady state space of exchangeable region occupied by the metabolite

V_b= blood volume.

Using this modified form of Graphical analysis, the rate constant of net uptake of radiotracer Ki can be calculated by fitting the metabolite corrected parent plasma IF to tissue activity data. If a discernible linear phase fit is observed, it signifies irreversible uptake; the higher the slope, the higher the Ki in tumours for the concerned radiotracer. The goodness of fit is expressed as the value of standard deviation (SD) of the fit.

Spectral analysis

Use of compartmental analysis is useful if the fate of the radiotracer in tissue and blood is known correctly. This requires prior knowledge of the biological properties of the radiotracer. Compartmental models however could be biased, especially in heterogeneous tissues such as tumours (Meikle, Matthews et al. 1998). This may also be the case when *a priori* knowledge is unavailable such as with experimental radiotracers. Therefore a generalised modelling approach called Spectral Analysis was

proposed (Cunningham and Jones 1993). With spectral analysis, linear kinetics are modelled without any prior assumptions of the compartmentalisation of the tracer. This method produces a simple spectrum of the kinetic components which relate the tissue's response to the blood activity curve. From this summary of the kinetic components, the tissue's unit impulse response (IRF) can be derived. The convolution of the arterial input function with the derived unit impulse response function gives the curve of best fit to the observed tissue data (Cunningham and Jones 1993). The IRF also helps in deriving fractional retention of radiotracer (FRT) at 60 min relative to 1 minute. Therefore, this method takes into account the time dependent contribution of radioactivity from plasma. The tissue activity at time “t” using spectral analysis can be expressed as:

$$A(t) = IRF(t) \otimes C_x(t) \qquad \textbf{(Equation 4)}$$

Kinetic parameters, IRF and FRT, are derived from this as described below, where;

$$IRF(t) = \sum_{i=1}^{n} \alpha_i \exp^{-\beta_i t} \qquad \textbf{(Equation 5)}$$

$$FRT = \frac{IRF_{60\,\min}}{IRF_{1\,\min}} \qquad \textbf{(Equation 6)}$$

n=number of identifiable kinetic components.

β=constant such that $\lambda < \beta_i < 1$ (λ=decay constant)

α=intensity of the kinetic component at β_i

PET in Oncology

Evaluation of response to anti-cancer therapy, currently, relies on routine imaging methods like x-rays, ultrasound scanning and computed tomography (CT). These methods give information about changes in anatomy and dimension of the tumour, which may take weeks or months to occur. The use of PET has resulted in accurate imaging of subtle changes in tumour biology and the detection of early response to anti-cancer therapy (Dose Schwarz, Bader et al. 2005). Increasing use of PET would help in noninvasive evaluation of early response to efficacious treatment agents and stop research into those with no response.

The use of PET has generated interest in tumour imaging as biologic activity of the tumour and early response to therapy could be measured. This may be evident before any clinical or radiological response is evident by change in tumour size. PET imaging uses compounds labelled with a radioisotope, which is taken up by a particular metabolic pathway of the human cells. Since tumours have increased activity of certain pathways, it results in their taking up greater amounts of radioactive tracer as compared to adjacent normal functioning tissue. Similarly any change in activity of a pathway due to therapy or treatment would result in change in uptake of the tracer on PET (Juweid and Cheson 2006). Thus, PET is a useful tool in oncology to image certain metabolic pathways and response to therapy.

[^{18}F]Fluoro-deoxyglucose ([^{18}F]FDG)

Energy production in normal viable cells is predominantly the result of oxidative phosphorylation, as opposed to glycolysis. However, tumours use glycolysis as a means of energy production irrespective of oxygen levels (Warburg O 1924), resulting

in much faster energy production and utilisation (Warburg effect). The high rate of glycolysis in tumours is associated with increased glucose uptake into cells secondary to up regulation of membrane bound glucose-uptake-transporter proteins (GLUT1 and GLUT3). The glucose transporters primarily transport glucose into cells by an active-transport mechanism and are up regulated in a wide variety of cancers (Ohba, Fujii et al. ; Chung, Lee et al. 1999; Laudanski, Koda et al. 2004; Nguyen, Lee et al. 2007; Ciampi, Vivaldi et al. 2008; Fonteyne, Casneuf et al. 2009). In addition, cancer cells also demonstrate up regulation of hexokinase (HK) enzymes HK1 and HK2 causing increased conversion of glucose to glucose-6-phosphate and ultimately to lactate (Arora, Parry et al. 1992). This up regulation of GLUT and HK accounts for the high levels of [^{18}F]FDG uptake in tumours (Mamede, Higashi et al. 2005).

Initially developed as an anti-glycolytic agent, but later discontinued due to its adverse side-effect profile, deoxyglucose was used to measure local brain utilisation of glucose using [^{14}C]deoxyglucose (Sokoloff, Reivich et al. 1977). It was shown that fluoro-deoxyglucose (FDG) follows the same metabolic pathway of glucose, being transported into cells by GLUT1 and GLUT3 and phosphorylated to FDG-6-phosphate. However, unlike glucose-6-phosphate, [^{18}F]FDG-6-phosphate is not a substrate for further glycolytic metabolism due to substrate specificity of glucose phosphate isomerase, and is thus retained in the cells (Kelloff, Hoffman et al. 2005). This forms the basis for imaging glucose metabolism of tumours with FDG. FDG is a stable molecule and does not interfere with metabolic processes, making it an ideal PET radiotracer. Radiolabelling FDG with [^{18}F] (medium half life of 109.7 min) enables transport to other centres for clinical use.

Application of [^{18}F]FDG-PET in oncology

[^{18}F]FDG-PET is widely used in assessing various tumour types and has shown usefulness in staging, diagnosis and response assessment. In a large pooled review of over 18,000 patient studies, it has been shown that [^{18}F]FDG-PET has a sensitivity of 84% and a specificity of 88% for tumour detection (Gambhir, Czernin et al. 2001). The intrinsic variability or the reproducibility of [^{18}F]FDG uptake (without treatment) ranges from 10 to 20% in different tumour phenotypes (Minn, Zasadny et al. 1995; Weber, Ziegler et al. 1999). Some of the various tumour types that have been imaged with [^{18}F]FDG PET are described in **Table 2**.

Table 2: Role of [^{18}F]FDG PET in different tumour sites

Tumour site	Role of [^{18}F]FDG
Central Nervous system	
(Chen 2007; Herholz, Coope et al. 2007)	• For guiding biopsy and grading • Determination of recurrence and anaplastic transformation
Head and Neck	
(Menda and Graham 2005; Facey, Bradbury et al. 2007; Isles, McConkey et al. 2008)	• Local staging (Sn:82-87%, Sp:94-100%) • Detection of distant metastases • Assessment of treatment response • Detection of recurrence (Sn:94%, Sp:80%)
Breast	
(Isasi, Moadel et al. 2005; Fletcher, Djulbegovic et al. 2008; Shie, Cardarelli et al. 2008; De Giorgi, Mego et al. 2010)	• For detection of recurrence and metastases • Limited value in lobular cancers, small tumours and low grade tumours • Useful for differentiating scar from recurrence in breast cancer
Lung	
(Fischer, Mortensen et al. 2001; Hellwig, Ukena et al. 2001; van Tinteren, Hoekstra et al. 2002; Mac Manus and Hicks 2003; Vansteenkiste and Stroobants 2004; Fischer and Mortensen 2006; Vansteenkiste and Dooms 2007; Fletcher, Kymes et al. 2008)	• Distinguishing benign from malignant lung nodules (Sn: 97%, Sp: 78%). • Accurate detection of both nodal and distant metastatic disease • Useful in staging, diagnosis and assessing recurrence - accuracy of 95% compared to CT. • Reduce futile thoracotomies compared to conventional work up • Predictive of patient survival

GI tract	
Oesophageal (van Westreenen, Westerterp et al. 2004)	• Staging-detection of distant metastases
Pancreatic cancer (Pakzad, Groves et al. 2006)	• For initial diagnosis
GIST (Esteves, Schuster et al. 2006)	• Role in restaging- of prognostic value
Colorectal cancer (Huebner, Park et al. 2000; Esteves, Schuster et al. 2006; Wiering, Krabbe et al. 2007)	• Primary utility is for detecting metastasis after definitive therapy. • Detecting hepatic metastasis (Sn: 97, Sp: 76%). • Preoperative tool for potentially resectable liver metastases
Genito-urinary	
(Jadvar and Conti 2004; Bouchelouche and Oehr 2008)	• Staging of Seminoma • Detection of recurrence and residual mass evaluation
Lymphoma	
(Isasi, Lu et al. 2005; Zijlstra, Lindauer-van der Werf et al. 2006)	• Initial staging (pooled Sn: 91%) • Early response evaluation
Sarcoma	
(Bourguet 2003; Bastiaannet, Groen et al. 2004)	• Guiding biopsy and detection of local recurrences • Differentiating low grade and high grade tumours
Melanoma	
(Friedman and Wahl 2004)	• Initial staging

Based on pooling together reproducibility data, a consensus for quantifying PET response by The European Organisation for Research and Treatment of Cancer (EORTC) PET study group was reached (Young, Baum et al. 1999) . The tumour responses were graded as follows:

1) Complete metabolic response (CMR): Complete resolution of FDG uptake.
2) Partial metabolic response (PMR): A decrease (across all lesions) of minimum of 15% in tumour SUV after one cycle or >25% after more than 1 cycle of chemotherapy.

3) Stable metabolic disease (SMD): An increase of < 25% or a decrease of < 15% in SUV, and no visible increase in extent of FDG tumour uptake (20% in longest dimension).

4) Progressive metabolic disease (PMD): An increase in FDG tumour SUV of > 25% within tumour region defined on baseline scan; visible increase in extent of FDG tumour uptake (20% in longest dimension) or appearance of new FDG uptake in metastatic lesions.

More recently PET Response Criteria in Solid Tumours (PERCIST) guidelines have been formulated (Wahl, Jacene et al. 2009). These are based on the premise that cancer response as assessed by PET is a continuous and time dependent variable. The tumour responses were graded as follows:

1) CMR: Visual disappearance of all metabolically active tumours.
2) PMR: More than a 30% and a 0.8-unit decline in SUL_{peak} between the most intense lesion before treatment and the most intense lesion after treatment, although not necessarily the same lesion.
3) SMD: Not CMR, PMR, or PMD.
4) PMD: More than a 30% and 0.8-unit increase in SUL_{peak} or new lesions, if confirmed. A greater than 75% increase in total lesion glycolysis is also proposed as another metric of progression.

The differences between EORTC and PERCIST criteria are discussed in **Table 3**.

Table 3: Comparison between EORTC and PERCIST criteria

EORTC criteria	PERCIST criteria
SUV normalisation • To body surface area (calculated with Dubois formula).	**SUV normalisation** • To lean body mass (SUL: with no particular algorithm stated).
Target lesion • The most [^{18}F]FDG avid lesion on baseline scans, and followed on each subsequent scan.	**Target lesion** • The single most metabolically active lesion with highest SUL_{mean}, identified, with a 1.2 cm diameter spherical region of interest (ROI) drawn in the hottest part of that lesion. SUL_{mean} of this ROI is SUL_{peak}. • Baseline SUL_{peak} had to exceed 1.5*liver SUL_{mean}+2*SD of liver SUL_{mean} or 2*aorta SUL_{mean}+2*SD of aorta SUL_{mean} for the tumour to qualify as a target lesion. • On subsequent scans, SUL_{peak} could be located in a different lesion from the one measured at baseline, as long as the lesion had been present since baseline.
Number of lesions • Not specified	**Number of lesions** • Five tumours (up to 2 per organ) with the most intense [^{18}F]FDG uptake.
Imaging variable • Not specified whether to use SUV_{max} or SUV_{mean} for response calculation.	**Imaging variable** • Recommended to use SUL_{mean} (as it has better test–retest variability (8%–10%) and is statistically less susceptible to variance.
Cutoff value • 25% for PMR and PMD is based on a literature review	**Cutoff value** • 30% for PMR and PMD is based on the correlation found between a decrease in SUV of > 30%–35% and good outcome.
Background level of [^{18}F]FDG uptake • No definitions are stated of a background level of [^{18}F]FDG uptake that a viable tumour should exceed in order to qualify as a target lesion.	**Background level of [^{18}F]FDG uptake** • Because of less test–retest variance, a liver background area is recommended, and clear definitions of target lesion [^{18}F]FDG uptake in proportion to background uptake are given.
• The size of the ROI, number of target lesions to be considered are outlined more as guidelines with options rather than clear definitions, therefore more susceptible to inter-observer differences than PERCIST.	• Clear definitions of target lesions and therefore less subjective

However, [^{18}F]FDG has the following limitations: (1) False positive uptake in some benign processes, such as infectious and inflammatory lesions (van Waarde and Elsinga 2008); (2) low sensitivity in well-differentiated low-grade tumours that have relatively low glucose metabolism such as carcinoid tumours, bronchoalveolar cell carcinoma, and renal cell carcinoma (Higashi, Ueda et al. 1998; Schoder and Larson 2004; Fleming, Gilbert et al. 2010); (3) low sensitivity in hypo cellular cancers such as desmoplastic or mucinous tumours (Higashi, Saga et al. 2003); (4) increased [^{18}F]FDG accumulation in some normal body areas such as lymphoid tissue and brown fat (Wechalekar, Sharma et al. 2005); and (5) Lack of clinical utility due to increased urinary excretion and lower expression of GLUT in prostate cancer (Schoder and Larson 2004). Thus, newer radiotracers to image tumours accurately are being developed to address these shortcomings, as well as explore other metabolic pathways of tumours which can be imaged using PET.

[^{18}F]3'-deoxy-3'fluorothymidine ([^{18}F]FLT)

Proliferation Imaging

Self-sufficiency in growth signals, insensitivity to growth-inhibitory (antigrowth) signals and limitless replicative potential, all lead to increased cellular proliferation; a hallmark of cancer (Hanahan and Weinberg 2000; Hanahan and Weinberg 2011). Of the 4 nucleosides, thymidine is exclusively used in DNA synthesis, making it an attractive substrate to image cell proliferation. Various methods of measuring the rate of tumour growth have been proposed as early as 1960. The first methods to measure proliferation involved incorporation of radiolabelled [^{3}H-methyl]thymidine or [^{14}C-methyl]thymidine by either injecting these radiochemicals directly into tumours before

biopsy or applying to fresh tumour samples and then assayed by thin-section autoradiography. Quantification was done by counting the fraction of tumour cells containing the radioactivity (the thymidine labelling index).

Thymidine transport and metabolism

Thymidine, after entering the cells by multiple different transporters passively or actively (Perumal, Pillai et al. 2006; Plotnik, Emerick et al. 2010), is phosphorylated by thymidine kinase 1 (TK1) into a more charged molecule and cannot freely exit the cells. Tumour uptake of [^{3}H]thymidine was first demonstrated in mice and dogs by Shields et al (Shields, Larson et al. 1984). Its use in nuclear imaging, when labelled with [^{11}C], has been limited by the short half-life of the tracer and its rapid catabolism in the body (Shields, Mankoff et al. 1996). This limitation has led to development of a newer thymidine analogue, 3'-deoxy-3'fluorothymidine (Grierson and Shields 2000).

[^{18}F]3'-deoxy-3'fluorothymidine (FLT)

The replacement of the hydroxyl group at the 3' position of deoxyribose converts thymidine to FLT. FLT has been developed as a tracer for imaging proliferation. FLT is transported into the cell by Na^{+}-dependent active nucleoside transporters and to a lesser extent by passive diffusion (Reske and Deisenhofer 2006; Plotnik, Emerick et al. 2010). FLT is a selective substrate for TK1 and a very poor substrate for TK2 (Munch-Petersen, Cloos et al. 1991). TK1 phosphorylates FLT to FLT-monophosphate (FMP) which, being a highly charged molecule, is trapped intracellularly. Slow dephosphorylation of FMP probably occurs via a putative 5-nucleotidase enzyme (Grierson, Schwartz et al. 2004; Wells, West et al. 2004). Unlike thymidine, FLT is not incorporated into DNA and remains trapped in the cytoplasm. FLT

incorporation into the DNA fraction is negligible (0.2%) (Toyohara, Waki et al. 2002). TK1 activity is virtually absent in quiescent cells but is up regulated in the S-phase of the cell cycle in proliferating cells. Therefore, up regulated TK1 activity is representative of the S-phase fraction (Toyohara, Waki et al. 2002) and FLT uptake as a measurement of TK1 activity, acts as an indirect marker of cell proliferation. Animal studies (Barthel, Cleij et al. 2003; Leyton, Latigo et al. 2005) have validated [^{18}F]FLT as a marker of proliferation and formed the basis of clinical studies using [^{18}F]FLT as PET ligand (**Table 4**). A meta-analysis of the studies on [^{18}F]FLT uptake and tumours expressing Ki-67 showed a persistent correlation between them (Chalkidou, Landau et al. 2012).

Application of [^{18}F]FLT in imaging tumours

Imaging of tumour proliferation with [^{18}F]FLT can be applied to predict the response to treatment based on imaging values obtained during the course of treatment. The rationale being, treatment-induced changes in tumour physiology will predict tumour cell viability earlier than anatomic imaging. To date, early clinical trials using [^{18}F]FLT PET, supported by pre-clinical data, have shown encouraging results in validating [^{18}F]FLT to be a biomarker of tumour proliferation and for predicting response to cancer therapy (Bading and Shields 2008; Tehrani and Shields 2013) (**Table 4**). In general [^{18}F]FLT uptake has frequently been reported to be lower than [^{18}F]FDG uptake in these tumours. No toxicities have been reported in the literature in relation to the use of [^{18}F]FLT for PET imaging (Spence, Muzi et al. 2008).

However, abdominal imaging with [^{18}F]FLT is challenging due to glucuronidation of the radiotracer resulting in the physiological uptake in the liver (Shields 2003); in the kidneys and bladder, where it is excreted; and in the marrow, where proliferation

occurs. A scanning protocol and an associated mathematical kinetic spatial filtering (KSF) algorithm that permits imaging of abdominal tumours, including liver metastases have been developed (Gray, Contractor et al. 2010). No data were found in the literature with respect to [^{18}F]FLT-PET as a marker of early tumour response in pancreatic cancer, and this marker therefore needs to be qualified in order to define its potential role in clinical practice and in assessing the efficacy of new, targeted therapies. Hence [^{18}F]FLT was chosen as a PET radiotracer in this thesis to further explore the feasibility of the kinetic filter to enable visualisation of the pancreatic primary and liver metastases and to evaluate detection of early tumour response (Chapter 2).

Table 4: Selected studies evaluating the role of [^{18}F]FLT

Preclinical	
(Barthel, Cleij et al. 2003)	52.2% and 72.9% reduction of [^{18}F]FLT at 24 and 48 hours respectively after administration of 5-Fluorouracil to mice bearing radiation induced fibrosarcomas.
(Barthel, Perumal et al. 2005)	*In vivo* [^{18}F]FLT kinetics in mouse lymphoma tumours are dependant on thymidine kinase (TK1) protein expression.
(Sugiyama, Sakahara et al. 2004; Waldherr, Mellinghoff et al. 2005)	Tumour bearing mice imaged with [^{18}F]FLT and [^{18}F]FDG showed that [^{18}F]FLT levels in tumours declined by 30% at 6 hours whereas [^{18}F]FDG uptake decreased at 3 days following treatment. [^{18}F]FLT uptake in these studies also reflected decrease in tumour proliferation.
(Leyton, Latigo et al. 2005)	Mean tumour [± Standard deviation (± SD)] [^{18}F]FLT uptake decreased by 24% (± 8%) and 49% (± 8%) at 1 and 2 days, respectively after administration of cisplatin in mice bearing radiation induced fibrosarcomas.
(Leyton, Alao et al. 2006)	[^{18}F]FLT PET evaluated for monitoring the biological activity of the histone deacetylase inhibitor, LAQ824 showed that drug induced changes in tumour [^{18}F]FLT uptake were due to reductions in TK1 transcription and translation.
(Perumal, Pillai et al. 2006)	Thymidylate synthase inhibition measured by [^{18}F]FLT PET, as early as 1 to 2 hours after treatment with 5-FU involves redistribution of nucleoside transporters to the plasma membrane.
(Perumal, Stronach et al. 2012)	Therapeutic inhibition of AKT activation in acquired platinum-resistant ovarian cancer can be imaged noninvasively by [^{18}F]FDG and [^{18}F]FLT PET.
These studies underpinned clinical studies using [^{18}F]FLT as a radiotracer in PET.	
Central Nervous System	
(Miyake, Shinomiya et al. 2012)	A comparative study of [^{18}F]FDG, [^{18}F]FLT, and [^{11}C]methionine PET showed that both [^{18}F]FLT and [^{11}C]methionine are able to differentiate patients with grade II–IV gliomas. The mean [^{18}F]FLT SUVs were 0.36 and 2.38, respectively, and [^{11}C]methionine SUVs

	were 3.04 and 5.12, respectively. [^{18}F]FLT retention correlated with Ki-67 index.
(Schwarzenberg, Czernin et al. 2012)	In 30 patients with gliomas [^{18}F]FLT, particularly at 6 wk post bevacizumab combination therapy, was the best predictor of overall survival (responders; 12.5 m vs. nonresponders; 3.8 m (P <0.001)) and more accurate than MR imaging alone.
(Harris, Cloughesy et al. 2012)	[^{18}F]FLT uptake was associated with longer progression-free survival in recurrent malignant gliomas after bevacizumab treatment.
Head & Neck Cancer	
(Linecker, Kermer et al. 2008)	In 19 untreated patients of primary head and neck cancers, who had both [^{18}F]FLT and [^{18}F]FDG PET, the mean SUVmax of [^{18}F]FLT was lower than that of [^{18}F]FDG SUV (5.81 ± 2.28 vs. 8.91 ± 3.58). There was no correlation between the number of Ki-67–positive cells and [^{18}F]FLT uptake.
(Troost, Bussink et al. 2010)	In 10 patients undergoing radiation treatment for oropharyngeal tumours, [^{18}F]FLT uptake decreased rapidly (as early as 1 wk) after the start of therapy and before CT volumetric changes. There was even further reduction before the fourth week of treatment.
(Hoshikawa, Kishino et al. 2012)	In 23 patients with metastatic lymph nodes who had [^{18}F]FLT PET and [^{18}F]FDG PET, the [^{18}F]FLT SUV was lower than that of [^{18}F]FDG SUV (4.8 ± 2.9 vs. 6.9 ± 4.9, respectively (P <0.001)).
(Kishino, Hoshikawa et al. 2012)	[^{18}F]FLT PET during radiation treatment and early follow-up may help with prediction of outcome. 28 patients with head and neck squamous cell carcinomas undergoing chemo radiation, had [^{18}F]FLT and [^{18}F]FDG PET before therapy, 4 wk after the start of therapy, and then 5 wk after completing radiation therapy. Both FLT & FDG had high negative predictive value (97% & 100%, respectively).
Breast Cancer	
(Smyczek-Gargya, Fersis et al. 2004)	In a study of newly diagnosed breast cancer patients, [^{18}F]FLT was able to detect 13 of 14 primary lesions and 7 of 8 patients with positive axillary nodes.

(Kenny, Coombes et al. 2007)	Changes in [^{18}F]FLT uptake were detectable as early as 1 wk after initiation of chemotherapy with 5-fluorouracil, epirubicin, and cyclophosphamide. The average decrease in SUV in responding lesions was 41.3%, in contrast to an increase of 3.1% in nonresponders. This study also tested the reproducibility of [^{18}F]FLT; i.e. the intrinsic variability between two scans before treatment. An [^{18}F]FLT-PET metabolic response is defined as a decrease in average semi-quantitative [^{18}F]FLT uptake SUV of > 18% from baseline.
(Contractor, Kenny et al. 2011)	Early changes in [^{18}F]FLT PET uptake after initiation of neoadjuvant docetaxel chemotherapy in 20 breast cancer patients, predicted midtherapy lesion response with 85% sensitivity and 80% specificity.
Lung Cancer	• Most studied malignancy using [^{18}F]FLT PET. • Uptake of [^{18}F]FLT in lung cancers is significantly lower than that of [^{18}F]FDG, with lower sensitivity, higher specificity, and higher positive predictive value
(Buck, Halter et al. 2003)	Twenty-six patients with lung cancer were imaged with [^{18}F]FDG and [^{18}F]FLT. [^{18}F]FLT uptake was only a third of that of [^{18}F]FDG with a lower sensitivity of detection (85% for FLT compared with 100% for FDG). However, this study demonstrated that [^{18}F]FLT uptake correlated better with proliferation in lung tumours as measured by Ki-67.
(Yamamoto, Nishiyama et al. 2007; Yamamoto, Nishiyama et al. 2008)	Eighteen patients with newly diagnosed NSCLC were imaged with [^{18}F]FLT PET and [^{18}F]FDG PET. The sensitivity was detected to be 72% and 89%, respectively. Four of the 5 false negative [^{18}F]FLT PET findings occurred in bronchoalveolar carcinoma. This could be attributed to the slower growth and differences in the kinetics and dynamics of [^{18}F]FLT in these tumours.
Sohn (Sohn, Yang et al. 2008)	This study showed the ability of [^{18}F]FLT in predicting response to an EGFR inhibitor gefitinib in lung cancer patients, as early as 7 days after initiation of therapy.
(Brockenbrough, Souquet et al. 2011)	Twenty-five suspected lung cancer patients underwent [^{18}F]FLT PET before surgical resection. The SUV_{max} was compared to Ki-67 and TK1 expression determined by immunohistochemical staining and TK1 enzymatic activity. The SUV_{max} correlated with the overall ($r = 0.57$, $P = 0.006$) and maximal ($r = 0.69$, $P < 0.001$) immunohistochemical

	expressions of Ki-67 and TK1 but not with TK1 enzymatic activity (r = 0.34, P = 0.146).
(Zander, Scheffler et al. 2011)	In this study, 34 patients were imaged with [^{18}F]FDG and [^{18}F]FLT uptake after 1 and 6 wk of erlotinib treatment. The changes in uptake were compared with response measured by CT after 6 wk of treatment. Early [^{18}F]FLT response predicted longer PFS but not overall survival and could not predict non-progression after 6 wk of therapy.
(Yang, Zhang et al. 2012)	SUV_{max} significantly correlated with the Ki-67 in 68 patients with NSCLC
(Kahraman, Holstein et al. 2012)	Thirty patients with stage IV NSCLC were imaged with [^{18}F]FLT and [^{18}F]FDG PET, before, 1 wk, and 6 wk after the start of erlotinib treatment. Patients with lower early and late residual [^{18}F]FDG and [^{18}F]FLT uptake had a significantly prolonged progression-free survival (PFS). A cut-off value of 30% decrease in [^{18}F]FLT uptake was used to define metabolic response.
Gastro-intestinal Cancers	
(van Westreenen, Cobben et al. 2005)	In this study on 10 patients with biopsy-proven **oesophageal and gastro-oesophageal cancer**, the SUV_{mean} of [^{18}F]FDG was higher than that of [^{18}F]FLT and neither correlated with Ki-67 expression.
(Herrmann, Ott et al. 2007)	Forty-five **gastric cancer** patients had both [^{18}F]FLT and [^{18}F]FDG PET. All tumours were visible with [^{18}F]FLT PET but 14 tumours were not detectable with [^{18}F]FDG because of high normal gastric uptake. The SUV_{mean} of [^{18}F]FDG was higher than that of [^{18}F]FLT. Interestingly, signet ring cell tumours had similar uptake of both tracers.
(Herrmann, Eckel et al. 2008)	In 31 patients with **pancreatic lesions**, receiver-operating-characteristic analysis using a [^{18}F]FLT SUV_{mean} cut off of 1.8 had a sensitivity of 81% and specificity of 100% to differentiate cancer from benign pancreatic lesions. On visual interpretation, 15 of 21 malignant tumours had higher uptake (sensitivity-71.4%). All 10 benign pancreatic lesions were negative on [^{18}F]FLT PET.

(Quon, Chang et al. 2008)	Visual discrimination between benign and malignant **pancreatic tumours** has proven difficult in this study with 5 patients.
(Kameyama, Yamamoto et al. 2009)	In 21 patients with advanced **gastric cancer,** the sensitivities of [^{18}F]FLT PET and [^{18}F]FDG PET were 95.2% and 95.0%, respectively. The SUV_{mean} of [^{18}F]FDG was higher than that of [^{18}F]FLT and neither correlated with Ki-67 expression.
(Eckel, Herrmann et al. 2009)	[^{18}F]FLT PET imaging in untreated patients with **hepatocellular carcinoma** (16 patients) showed sensitivity for tumour detection of 69%, correlating with Ki-67 score.
(Yamamoto, Kameyama et al. 2009)	In evaluation of **colon cancer** patients, all primary tumours were detected. [^{18}F]FLT uptake was found to be lower than [^{18}F]FDG uptake, with a SUV_{mean} of 5.4 and 12.4, respectively (P=0.003). There was no correlation between [^{18}F]FLT uptake and Ki-67.
(Yue, Chen et al. 2010)	In imaging proliferation and response to radiation and chemotherapy in **oesophageal squamous tumours,** it was shown that [^{18}F]FLT uptake rapidly decreased after the start of radiotherapy, as early as after 2 Gy of radiation.
(Ott, Herrmann et al. 2011)	In 45 patients with **gastric cancer**, early response (2 wk after initiation) to neo-adjuvant chemotherapy was evaluated with [^{18}F]FLT PET and [^{18}F]FDG PET. [^{18}F]FLT was found to have significant prognostic impact and a good correlation with histological proliferation (Ki-67). However, neither [^{18}F]FLT nor [^{18}F]FDG uptake predicted clinical or pathologic response.
(Kameyama, Yamamoto et al. 2011)	Demonstrated a significant correlation between [^{18}F]FLT SUV and thymidine kinase 1 (TK1) messenger RNA expression, in 21 patients with GI cancer. However, no significant correlation was found between SUV and messenger RNA expression of equilibrating nucleoside transporter 1 (ENT1).
(Herrmann, Erkan et al. 2012)	**Pancreatic cancer** has significantly lower uptake of [^{18}F]FLT than of [^{18}F]FDG, leading to lower sensitivity (70% vs. 91%, respectively) and higher specificity (75% vs. 50%) in differentiating malignant from benign tumours, in a study with 41 patients (33 with pancreatic malignancy and 8 with benign disease). The average SUV_{max} in all malignant

	tumours was 3.0 (range, 1.1–6.5) for [^{18}F]FLT and 7.9 (range, 3.3–17.8) for [^{18}F]FDG.
(Dehdashti, Grigsby et al. 2013)	In **rectal cancer** patients receiving neo-adjuvant chemo-radiotherapy, [^{18}F]FLT uptake and the percentage decrease during therapy predicted the disease-free survival, but did not predict the pathologic response to treatment.
Hematologic Malignancies	
(Herrmann, Wieder et al. 2007)	In patients with high-grade NHL, treatment with CHOP/R-CHOP (rituximab, cyclophosphamide, hydroxydaunomycin, vincristine, and prednisone) resulted in a 77% decrease in [^{18}F]FLT retention as early as a week after therapy initiation.
(Vanderhoek, Juckett et al. 2011)	A pilot study on 7 patients imaged with [^{18}F]FLT PET immediately after completion of induction chemotherapy was able to accurately predict remission (5 patients) or relapse (2 patients) at 1 month.
(Herrmann, Buck et al. 2011)	In a study of 66 patients with mantel cell lymphoma, the relative uptake of [^{18}F]FLT before the start of therapy was predictive of the ultimate response to treatment, with those achieving complete response having a lower mean SUV of 7.1, compared with 9.5 in the other patients The authors also noted a rapid decline in [^{18}F]FLT retention after 1 wk of therapy.
(Wang, Zhu et al. 2012)	In this study of 38 non-Hodgkin lymphoma (NHL) patients, staging with [^{18}F]FLT PET/CT had a higher sensitivity and specificity than CT alone.

[^{11}C]methylcholine

Choline transport and metabolism

Choline is one of the components of phosphatidylcholine (PC), an essential part of phospholipids in the cell membrane (Zeisel 1981) and is required for structural stability and cell proliferation. It is also essential for the synthesis of neurotransmitters like acetylcholine (by reaction of choline with acetyl-CoA), and production of potent lipid mediators such as platelet-activating factor. Choline kinase (CHK) is the first enzyme in the Kennedy pathway (Gibellini and Smith 2010), and is responsible for the de novo synthesis of PC. CHK phosphorylates choline to phosphocholine (PCho), the rate limiting step in the Kennedy pathway. PCho is further phosphorylated to cytidine diphosphate-choline (CDP-choline) by the enzyme cytidyltransferase and then to other intermediates before being incorporated into cell membrane phospholipids as PC.

Besides choline metabolism, altered choline transport has also been proposed to play an important role in multiple clinical manifestations in various cancers, including prostate, breast, lung and ovarian cancer (Iorio, Ricci et al. ; Ackerstaff, Pflug et al. 2001; Villa, Caporizzo et al. 2005; Wang, Li et al. 2007). As cells have a limited capacity to synthesise choline, the major source of choline is principally from the extra cellular choline pool through uptake by the choline transport system (Zeisel 2000; Michel, Yuan et al. 2006). Three protein mediated, saturable uptake systems for transport have been documented (van Rossum and Boyd 1998):

1. Facilitated diffusion – driven by a choline concentration gradient.
2. High affinity active transport – this is Na^+ and energy dependent and plays a role in acetylcholine synthesis in neuronal tissues.

3. Low affinity active transport – this process is more widely distributed and plays a role in choline uptake for the purpose of phospholipid synthesis.

Depending on the affinity for choline, the proteins playing a role in transport have been categorised into 3 groups (Michel, Yuan et al. 2006):

1. Organic cation transporters (OCTs and OCTNs) – both with low affinity for choline, have been widely detected in human tissues and they may be involved in transport of choline for phospholipid synthesis.
2. Choline transporter-like proteins (CTLs) – intermediate affinity for choline. They are responsible for Na^+ independent choline transport and production of membrane phospahtidyl choline in some non-neuronal tissues.
3. High affinity choline transporters (CHTs) – involved in acetylcholine synthesis. These have been detected in human brain and spinal cord.

In addition to phosphorylation, free choline also participates in 2 other enzyme catalyzed pathways in mammalian tissues: oxidation and acetylation, of which the predominant pathway is oxidation. Choline is oxidised to betaine aldehyde, which is then converted into betaine by the enzyme system of choline oxidase (choline dehydrogenase and betaine aldehyde dehydrogenase) (Ueland 2011). Liver and kidney are the major sites for choline oxidation. Betaine synthesis from choline is controlled by the choline transport into the mitochondria (O'Donoghue, Sweeney et al. 2009).

Hence, the expression pattern and characteristics of choline transporters choline phosphorylation and choline oxidation are of central importance to understand the process of choline metabolism that underlies cell signalling & growth and membrane integrity in various diseases.

Choline and Malignancy

Malignant tumours show high proliferation and increased cell membrane components that will lead to an increased uptake of choline. The progression of normal cells to malignant phenotype is associated with altered membrane choline phospholipid metabolism (Aboagye and Bhujwalla 1999). Generation of PCho from CHK activity has been described as an essential event in growth factor induced mitogenesis in fibroblasts (Jimenez, del Peso et al. 1995) and has been found to cooperate with several mitogens (Chung, Crilly et al. 1997). CHK has been extensively linked to cell proliferation and human carcinogenesis (Ramirez de Molina, Penalva et al. 2002; Ramirez de Molina, Rodriguez-Gonzalez et al. 2002; Yoshimoto, Waki et al. 2004). CHK consists of 2 sub-types α and β (Gallego-Ortega, Ramirez de Molina et al. 2009).

CHKα is thought to regulate cell proliferation and transformation by regulating the G_1 to S phase transition of the cell cycle and apoptotic signalling (Ramirez de Molina, Gallego-Ortega et al. 2008). A strong correlation between CHK activity and cancer onset has been proposed based on the fact that CHK dysregulation is a frequent event occurring in a variety of human tumours such as breast, lung, colorectal and prostate tumours (Ramirez de Molina, Rodriguez-Gonzalez et al. 2002; Ramirez de Molina, Banez-Coronel et al. 2004). CHKα has also been described as a new relevant prognostic factor in lung cancer (Glunde and Bhujwalla 2007; Ramirez de Molina, Sarmentero-Estrada et al. 2007).

All this evidence points to the central role of CHKα in the progression of certain tumour types, hence detecting increased CHKα expression in cancer patients could enable identification of a cohort in whom CHK inhibitors may prove beneficial.

Application of [^{11}C]choline in imaging tumours

Malignant transformation is postulated to be associated with changes in pathways of choline transport, utilisation and increased CHKα expression that will lead to an increased uptake of choline (Ackerstaff, Pflug et al. 2001; Glunde, Bhujwalla et al. 2011). Radiolabelling of choline with [^{11}C] enables this molecule to be used as a PET tracer. During phosphorylation, the carbon label [^{11}C] is trapped intracellularly (Hara, Kosaka et al. 1998), thus enabling imaging of this metabolic pathway. Hara and colleagues have also shown that [^{11}C]choline had good uptake in brain tumours with almost negligible activity in the blood after 5 minutes. This work inspired others to use [^{11}C]choline as a PET radiotracer to image other tumours including renal (Schoder and Larson 2004), oesophageal (Kobori, Kirihara et al. 1999; Jager, Que et al. 2001; Tamura, Yoshikawa et al. 2002; Tian, Zhang et al. 2004; Ramirez de Molina, Sarmentero-Estrada et al. 2007) and NSCLC (Ramirez de Molina, Sarmentero-Estrada et al. 2007).

[^{11}C]choline is particularly useful in prostate cancer as there is negligible urinary bladder excretion, a problem with [^{18}F]FDG due to rapid excretion of FDG in urine, causing an accumulation of activity in the bladder, making visualisation of the prostate difficult. The utility of [^{11}C]choline in visualising and staging prostate cancer has been published (Hara, Kosaka et al. 1998; Reske, Blumstein et al. 2006). The published studies show varied and conflicting results in the sensitivity of detection of the primary prostate tumours and the nodal metastases (Farsad, Schiavina et al. 2005; Kwee, Coel et al. 2005; Yamaguchi, Lee et al. 2005; Reske, Blumstein et al. 2006).

Preliminary studies of [^{11}C]choline PET in pelvic nodal staging in prostate cancer patients have shown early promise (Kotzerke, Prang et al. 2000; de Jong,

Pruim et al. 2003; Schiavina, Scattoni et al. 2008). However, no study to date has established a direct relationship between CHKα expression and [^{11}C]choline uptake in prostate tumours. Hence, [^{11}C]choline PET/CT was evaluated as a non invasive method for detecting pelvic lymph node status in patients with high risk localised prostate cancer. The relationship between [^{11}C]choline uptake (SUV), choline kinase expression (immunohistochemistry scores) and Ki67 in prostate tumours and involved nodes were compared.

Furthermore, there has been no prior study documenting the use of [^{11}C]choline PET/CT to predict early response to a combination of androgen deprivation and radiotherapy. Hence, [^{11}C]choline has been chosen to establish [^{11}C]choline PET/CT as a biomarker for assessing early response of neo-adjuvant androgen deprivation and radiotherapy in patients receiving radical treatment for prostate cancer. These studies are described in detail in subsequent chapters.

Choline Kinase Immunohistochemistry

Malignant transformation causes the prostate epithelial cells to lose their differentiation. In addition, there is an increased turnover of cells, with proliferation of tumour cells and apoptosis. This increased cell turnover results in an increase of choline-containing molecules within the prostate gland (Daly, Lyon et al. 1987; Ackerstaff, Pflug et al. 2001). *In vitro* data and Magnetic Resonance Spectroscopy (MRS) of the prostate have demonstrated that it is possible to distinguish between healthy prostate tissue, with high concentration of citrate and low concentration of free choline containing molecules, and malignant prostate tissue with decreased concentration of citrate and increased concentration of free choline-containing molecules (Garcia-Segura, Sanchez-Chapado et al. 1999; Ackerstaff, Pflug et al. 2001).

Immunohistochemistry (IHC) is an investigative tool which provides supplemental information to the routine morphological assessment of tissues. Its use in studying cellular markers that define specific phenotypes has provided important diagnostic, prognostic, and predictive information about the disease status and tumour biology. IHC against CHKα has been used with encouraging results in human breast and lung cancer tissue samples (Gallego-Ortega, Ramirez De Molina et al. 2006). However, there is a paucity of data with regards to the patterns of expression of CHKα in human prostate cancer tissue samples.

The correlation between the expression of CHKα and [^{11}C]choline uptake parameters will help evaluate if [^{11}C]choline PET can be used as a surrogate for CHKα expression. Hence a new CHKα antibody staining protocol has been optimised to assess patterns of CHKα expression in human prostate tissue samples. The rationale and findings are discussed in detail in chapter 3.

Modelling of [^{11}C]choline PET data

After [^{11}C]choline injection, the specific PET signal is due to its phosphorylated product, [^{11}C]phosphocholine. This PET signal is confounded by the contribution from the parent tracer [^{11}C]choline (transport), and the oxidative by-product [^{11}C]betaine (**Figure 7**). The [^{11}C]choline is oxidised to [^{11}C]betaine by choline oxidase mainly in the kidney and the liver. The metabolites are detected in the plasma soon after the injection of the radiotracer (Roivainen, Forsback et al. 2000). This makes the discrimination of the relative contributions of the parent radiotracer and the metabolites difficult. It has been shown preclinically in tumours in mice, that there could be oxidation of choline to betaine even in the tumour tissues contributing to the radiotracer uptake (Leyton, Smith et al. 2009). However, there is inadequate data on the proportion of betaine oxidised in the liver , kidney

and that oxidised in tumours. Moreover, the metabolism is faster in rodents than in humans (Roivainen, Forsback et al. 2000). The two possible mechanisms contributing to betaine levels in the blood could therefore be: (1) rapid elimination through oxidation in liver and kidney; (2) efflux from the tumour cells. Therefore, assessment of [^{11}C]choline phosphorylation and choline oxidation by kinetic modelling of PET data may help in our understanding of the role of choline metabolism in tumours and improve the specificity of the choline signal. The full arterial blood data available from the [^{11}C]choline PET breast data have been explored and the information has been used to predict the performance of a limited sampling venous data set in prostate cancer patients. The results have been described in detail in chapter 3.

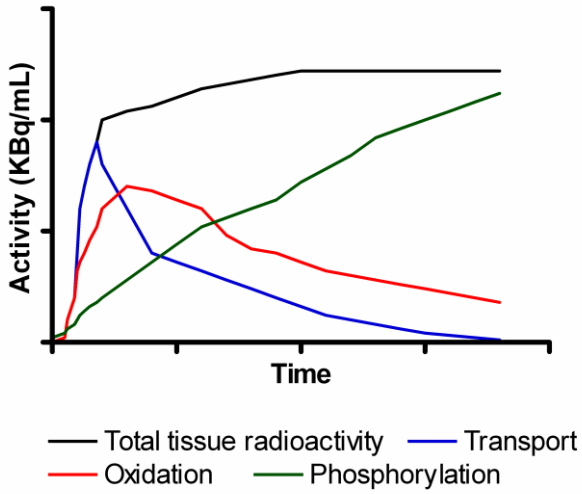

Figure 7: Putative fate of [^{11}C]choline after injection into blood stream.
Choline is transported into tissues by choline transporters or passive diffusion. It is then phosphorylated into phosphocholine by CHK via the Kennedy pathway. Choline is oxidised to betaine in the liver and kidney.

New Tracers: [^{18}F]fluoromethyl-[1,2-$^{2}H_4$]choline ([^{18}F]D4FCH)

[^{18}F]Fluorocholine

[^{18}F]Fluorocholine ([^{18}F]FCH) was developed to overcome the short physical half-life of carbon-11 (20.4 min). The longer half-life (109.8 min) of [^{18}F] was deemed potentially advantageous in permitting late imaging of tumours when sufficient clearance of parent tracer in systemic circulation had occurred. Since the use of [^{18}F]FCH was first reported by DeGrado and co-workers (DeGrado, Coleman et al. 2001), [^{18}F]FCH has been extensively used in patients and has been proven safe for human administration **(Table 5)**. None of the studies have reported any adverse effects with the use of this radiopharmaceutical. Furthermore the radiopharmaceutical has been approved for diagnostic use in Europe. The main approved indications are for the detection of bone metastases of prostate cancer, the localisation of lesions of well-differentiated hepatocellular carcinoma, and the characterisation and/or staging of hepatocellular carcinoma, when [^{18}F]FDG PET is inconclusive and/or when surgery is scheduled (http://www.rcr.ac.uk/docs/radiology/pdf/BFCR%2812%293_PETCT.pdf).

Table 5: Summary of selected [^{18}F]FCH PET studies in humans.

Author	Sample size	Conclusions
Prostate		
(Schmid, John et al. 2005)	9	Nine patients evaluated with FCH PET for staging prostate cancer. FCH could not differentiate between Benign Prostate Hypertrophy (BPH) and Carcinoma Prostate (PCa).
(Kwee, Coel et al. 2005)	17	Increased uptake of FCH was demonstrated in biopsy positive regions than in biopsy negative areas in 17 patients.
(Kwee, Wei et al. 2006)	15	Delayed imaging up to 1 hour is needed to differentiate between BPH and PCa.
(Hacker, Jeschke et al. 2006)	10	In node negative patients, FCH PET detected nodes in 1 patient and 2 cases were false positive.
(McCarthy, Siew et al. 2010)	26	In hormone refractory prostate cancer (HRPC), FCH findings were concordant with bone scan and CT in detecting metastases.
(Husarik, Miralbell et al. 2008)	111	Delayed imaging increased pick up rate of bone metastases, but time of scan had no influence on Local Recurrence (LR)/nodal metastases.
(Langsteger, Heinisch et al. 2006)	49	6/49 high risk patients were upstaged with FCH PET.
(Cimitan, Bortolus et al. 2006)	52	Cannot detect LR/Metastases if the PSA<4ng/ml
(Pelosi, Arena et al. 2008)	56	FCH PET sensitivity increases with increasing PSA.
(Beauregard, Williams et al. 2010)	16	Compared FDG and FCH PET. Both were more sensitive than MRI/CT in providing clinical information (88% vs. 56%)
(Beheshti, Imamovic et al. 2010)	130	In pre op staging of Intermediate Risk (IR)/High Risk (HR) patients, FCH PET changed treatment in 15% of all patients and in 20% of HR patients. It also excluded bone metastases.
(Poulsen, Bouchelouche et al. 2010)	25	FCH PET is a tool for nodal staging, but larger studies are needed.
Central Nervous System		
(Lam, Ng et al. 2010)	2	High Grade Glioma (HGG) showed increased choline uptake
(Hara 2002)		Showed an increased tumour to normal tissue uptake ratio with FCH and hence better image quality.
(DeGrado, Coleman et	1	FCH is feasible for brain tumour imaging

al. 2001)		
(Kwee, Coel et al. 2004)	2	Increased uptake in areas of HGG correlates with increased areas of choline metabolites on Magnetic resonance spectroscopy (MRS).
(Kwee, Ko et al. 2007)	30	Used FCH PET in differential diagnosis of solitary brain lesions. FCH can differentiate between Gliomas, metastases, benign lesions. FCH can differentiate between Radiotherapy changes and tumour recurrence.
(Roselli, Pisciotta et al. 2010)	1	FCH PET aids in the selection of therapeutic options.
Hepatocellular carcinoma (HCC)		
(Talbot, Gutman et al. 2006)	12	FCH can localise Hepatocellular carcinoma (HCC) in the liver.
(Talbot, Fartoux et al. 2010)	81	FCH is more sensitive than FDG at detecting HCC. It is useful for the detection and surveillance of HCC.
(van den Esschert, Bieze et al. 2010)	21	FCH can differentiate between focal nodular hyperplasia (FNH) and adenoma.
Lung		
(Balogova, Huchet et al. 2010)	15	FCH & FDG PET have similar detection rates in lung nodules suggestive of bronchoalveolar carcinoma.

Deuterium Substituted Fluorocholine ([^{18}F]D4-FCH)

Impetus for compound development

[^{11}C]choline (and its fluoro-analogue ([^{18}F]FCH)) is oxidised to [^{11}C]betaine by choline oxidase mainly in kidney and liver tissues, with metabolites detectable in plasma soon after injection of the radiotracer (Roivainen, Forsback et al. 2000). This makes discrimination of the relative contributions of parent radiotracer and catabolites difficult when a late imaging protocol is used.

A more metabolically stable FCH analogue, [^{18}F]fluoromethyl-[1,2-$^{2}H_4$]choline ([^{18}F]D4-FCH), based on the deuterium isotope effect (Gadda 2003) has been developed. The simple substitution of Deuterium (^{2}D) for Hydrogen (^{1}H) improves the stability of the compound and reduces degradation of the parent tracer. This could increase the net availability of the parent tracer for phosphorylation and trapping within cells leading to an improved signal-to-background contrast, thus improving the sensitivity of the PET imaging of tumours. [^{18}F]D4-FCH has been validated for imaging tumours pre-clinically and was found to be a very promising, metabolically stable radiotracer for imaging choline metabolism in tumours (Leyton, Smith et al. 2009). Therefore this tracer has been translated into humans in the form of a micro-dosing, first-in-human study in healthy volunteers. The safety, biodistribution and radiation dosimetry of [^{18}F]D4-FCH were evaluated.

New Tracers: [^{18}F]ICMT-11

Apoptosis is an essential process for eliminating unwanted cells during embryonic development, growth, differentiation, and maintenance of tissue

homeostasis. Apoptosis is regulated by both intrinsic (via mitochondria) and extrinsic (activation of death receptors) signalling networks that control a family of enzymes known as caspases (cysteine aspartate specific proteases) (Nicholson and Thornberry 1997; Degterev, Boyce et al. 2003). Based on various biochemical events that characterise apoptosis, a number of positron emitting radiotracers have been developed to noninvasively detect this process, both in preclinical studies and in humans (Nguyen, Challapalli et al. 2012).

[^{18}F](S)-1-((1-(2-fluoroethyl)-1H-[1,2,3]-triazol-4-yl)methyl)-5-(2(2,4-difluorophenoxymethyl)-pyrrolidine-1-sulfonyl) isatin ([^{18}F]ICMT-11) was designed as a small molecule radiotracer with potential advantages such as facile radiolabelling, improved biodistribution and clearance profiles. It has been characterised as a novel reagent designed to noninvasively image caspase-3 activation and, hence, drug-induced apoptosis. The promising mechanistic and biological profile of [^{18}F]ICMT-11 supports its transition into clinical development (Nguyen, Challapalli et al. 2012). Therefore this tracer has also been translated into humans in the form of a micro-dosing, first-in-human study in healthy volunteers. The safety, biodistribution and radiation dosimetry of [^{18}F]ICMT-11 were evaluated.

Thesis Overview

This thesis expounds the imaging of growth and death of cancer cells in tumours. It aimed to investigate tumour growth signalling using [^{18}F]FLT to assess proliferation and the choline analogue ([^{11}C]choline) to measure phospholipid metabolism, and to develop them as imaging biomarkers for response assessment in lesions where they are likely to be used.

This chapter describes the cell cycle, its regulation and hallmarks of cancer: in particular sustained proliferation and evading apoptosis. The mechanisms of action of common anti-cancer treatment strategies causing alteration in the balance between cell proliferation and cell death have been alluded to highlighting the need for imaging. The traditional methods of quantification of cell proliferation and cell death and their limitations, along with the limitations of standard anatomic measurements have been discussed. The roles of PET, recent advances in PET technology and the newer PET radiotracers have also been described in this chapter.

The thesis initially explored the modulation of FLT kinetics employing the kinetic spatial filter (KSF) in pancreatic tumours as well as quantifying the changes in kinetics with gemcitabine based chemotherapy. The molecular and physiological basis of [^{11}C]choline as a PET radiotracer in prostate tumours was studied next, to establish the correlation of [^{11}C]choline uptake in prostate tumours with quantitative estimation of CHKα expression on immunohistochemistry. The further application of [^{11}C]choline as an imaging biomarker in detecting changes in choline metabolism following androgen deprivation and radical radiotherapy to the prostate was studied.

To overcome the metabolic instability of [^{11}C]choline, a novel choline analogue that has improved systemic stability ([^{18}F]D4-FCH) was evaluated in humans. In order to translate [^{18}F]D4-FCH into clinical imaging, its uptake and kinetics were studied in patients with newly diagnosed non-small cell lung cancer (NSCLC). As a prelude to imaging cancer cell death in tumours, a caspase-3 specific radiotracer has also been transitioned into humans. **Table 6** gives a brief overview of the studies in this thesis.

Table 6: Overview of the studies in this thesis

Study	Chapter No	Author
• Imaging cell proliferation with [^{18}F]Fluorothymidine in advanced pancreatic cancer: Effect of gemcitabine based therapy	2	A. Challapalli
• Non invasive detection of pelvic lymph nodal metastases from prostate cancer using [^{11}C]choline PET/CT and relationship with choline kinase expression	3	A Challapalli (image data of patients from Dr Contractor's thesis analysed and reported; Western Blotting & PCR was by S. Trousil; Choline breast data of Dr Contractor completely re-analysed).
• Exploring the potential of [^{11}C]choline PET/CT as a novel imaging biomarker for predicting early treatment response in prostate cancer.	4	A. Challapalli
• Deuterium substituted [^{18}F]fluoromethyl-[1,2-$^{2}H_4$]choline PET/CT: Biodistribution, radiation dosimetry and imaging in Non-Small Cell Lung Carcinoma.	5	A. Challapalli
○ [^{18}F]D4-FCH: Biodistribution and radiation dosimetry in healthy volunteers.		
○ [^{18}F]D4-FCH PET/CT in Non-Small Cell Lung Carcinoma: Proof of concept study.		
Additional work		
• [^{18}F]ICMT-11, a Caspase-3 specific PET tracer for Apoptosis: Biodistribution and Radiation dosimetry.	6	A. Challapalli

Hypotheses Tested

The hypotheses tested include:

1. Use of Kinetic Spatial Filtering (KSF) would improve localisation of tumours in the pancreas and liver metastases (Chapter 2).
2. Use of functional imaging with PET would predict early response to treatment and the potential for alternative management strategies (Chapter 2, 4).
3. Untreated malignant lesions will have enhanced radiolabelled choline accumulation due to their high expression and activity of CHKα (Chapter 3, 5).
4. Altered choline transport and choline oxidation could confound the specificity of [^{11}C]choline uptake in tumours (Chapter 3).
5. The novel PET tracers ([^{18}F]D4-FCH and [^{18}F]ICMT-11) would have a favourable dosimetry profile and safe for use in humans (Chapter 5, 6).

Aims of Thesis

- To validate and explore FLT kinetics using FLT PET/CT combined with kinetic spatial filtering (FLT PET/CT$_{KSF}$) in pancreatic tumours and in response to therapy (Chapter 2).

- To evaluate the accuracy and biological basis for [^{11}C]choline PET/CT in the nodal staging of high risk localised prostate cancer, to understand the molecular and physiological basis of [^{11}C]choline tracer kinetics in prostate tumours, and to establish the correlation of [^{11}C]choline uptake in prostate tumours with quantitative estimation of CHKα expression on immunohistochemistry (Chapter 3).

- To explore the potential of [^{11}C]choline PET/CT as an early response biomarker to neo-adjuvant androgen-deprivation (NAD) and radical radiotherapy combined with concurrent androgen-deprivation (RT-CAD) in patients with prostate cancer (Chapter 4).

- To transition a novel metabolically stable analogue of choline ([^{18}F]fluoromethyl-[1,2-$^{2}H_4$]-choline ([^{18}F]D4FCH)) into humans and to study its pharmacokinetics in patients with NSCLC (Chapter 5).

- To evaluate the biodistribution, internal dosimetry and the safety profile of [^{18}F]ICMT-11 in healthy volunteers (Chapter 6).

CHAPTER 2: Imaging cell proliferation with [^{18}F]fluorothymidine in advanced pancreatic cancer: Effect of gemcitabine based therapy

Rationale

Pancreatic cancer is the fourth leading cause of cancer mortality world-wide (Siegel, Naishadham et al. 2012). It is a genetically heterogeneous disease with alterations in several core signalling pathways and processes including K-ras, JNK, Wnt/Notch, hedgehog and integrin signalling, as well as control of G_1/S transition control and apoptosis (Jones, Zhang et al. 2008). A combination of aggressive tumour biology and a propensity to present with inoperable disease, makes advanced pancreatic cancer incurable with median survival of less than 1 year, despite systemic therapy (Cartwright, Richards et al. 2008). Symptom control and quality of life are extremely important in these patients. Randomised trials have demonstrated a potential benefit both in terms of survival and symptom control in patients who receive gemcitabine based chemotherapy (Sultana, Smith et al. 2007). However the use of combination chemotherapy is not without significant toxicity and many patients will experience significant morbidity due to febrile neutropenia, anemia, thrombocytopenia, nausea, and vomiting (Ciliberto, Botta et al. 2013). Therefore there is a need for early assessment of tumour response in order to minimise patient exposure to potentially toxic treatment regimens, especially in those patients who are unlikely to respond.

Objective response to chemotherapy is routinely assessed by change in tumour size on CT imaging based on RECIST 1.1 criteria (Eisenhauer, Therasse et al. 2009). However, reliable estimation of therapeutic effect is challenging as changes in tumour dimensions may take months to become apparent limiting evaluation of therapeutic effect early during treatment, and these techniques may not provide information

regarding the viability of the residual tumour mass. The emergence of PET technology has generated interest in imaging the biologic activity of the tumour and early response to therapy. Qualification of PET as an early response biomarker would also enable its subsequent use as noninvasive marker of novel drug efficacy or a pharmacodynamic marker in the management of pancreatic cancer. Notably, there are no accepted predictive or response biomarkers for pancreatic cancer although several, including hENT1, miR-21, and circulating tumour cells are being evaluated (Costello, Greenhalf et al. 2012).

[^{18}F]Fluorodeoxyglucose (FDG), a glucose analogue, is the most widely used oncological PET tracer for staging and response assessment (Juweid and Cheson 2006; Zhu, Lee et al. 2011). In a tabulated summary of the FDG PET literature, the weighted sensitivity and specificity of FDG PET for detection of the primary pancreatic tumours was 94% and 90 %, respectively (Gambhir, Czernin et al. 2001). Several small studies have assessed the utility of FDG PET to predict survival in pancreatic cancer patients (Maisey, Webb et al. 2000; Choi, Heilbrun et al. 2010) and the early effects of radiotherapy (Higashi, Sakahara et al. 1999) and/ or chemotherapy (Rose, Delbeke et al. 1999; Bang, Chung et al. 2006; Kuwatani, Kawakami et al. 2009; Choi, Heilbrun et al. 2010). A study of 10 pancreatic cancer patients showed that FDG PET aided in assessing the effectiveness, 2 weeks after completion of treatment with concurrent arterial chemo infusion and 5 weeks of external radiation (Yoshioka, Sato et al. 2004). Small studies in patients with locally advanced pancreatic adenocarcinoma have evaluated FDG PET post neoadjuvant chemoradiotherapy (CRT) to predict which patients would achieve complete surgical resection and have found % change in tumour SUV_{max} to be of some utility but not consistently reliable (Rose, Delbeke et al. 1999; Choi, Heilbrun et al. 2010).

The sensitivity and specificity of predicting response to CRT (4 weeks after completion of treatment) was 30% and 60%, respectively in 15 patients using clinical benefit as the standard (Bang, Chung et al. 2006). However, the use of FDG-PET is limited by false positive uptake in the presence of active, chronic or autoimmune pancreatitis, which can mimic pancreatic cancer (Buck, Schirrmeister et al. 2001) and low sensitivity in relatively hypo cellular cancers such as desmoplastic or mucinous tumours (Higashi, Saga et al. 2003). Furthermore, there was no association between FDG uptake and proliferative activity in pancreatic cancer, even though the proliferative activity was tenfold higher in malignant pancreatic tumours than in benign tumours (Buck, Schirrmeister et al. 2001).

Pancreatic adenocarcinomas show a relatively high average Ki-67 labelling index, of 37% (Klein, Hruban et al. 2002), and several drug combinations in use for this disease target DNA replication (Costello, Greenhalf et al. 2012). Hence there may be a potential for alternative tracers such as [^{18}F]3'-deoxy-3'-fluorothymidine (FLT), a surrogate marker of DNA synthesis, which are less susceptible to inflammatory changes (van Waarde, Cobben et al. 2004), as imaging biomarkers for prognosticating pancreatic cancer and response evaluation (Barwick, Bencherif et al. 2009). An initial FLT PET/CT pilot study by Quon and co-workers in 5 patients showed that a standard 2-dimensional static imaging protocol, 40 min post FLT injection was unsuitable for detection of pancreatic tumours (Quon, Chang et al. 2008). They concluded that FLT PET/CT was not suitable for primary detection of pancreatic adenocarcinoma and may serve as a poor baseline scan for subsequent follow-up imaging when monitoring therapy (Quon, Chang et al. 2008). More recently, FLT PET was shown to detect malignant tumours of the pancreas in a study of 31 patients (Herrmann, Eckel et al. 2008). FLT PET was evaluated for the detection and characterisation of pancreatic

tumours in 41 patients and was found to be more specific than FDG (75% vs. 50%, respectively). A SUV_{max} cut off of 2 was proposed for the discrimination of benign and malignant lesions in their series (Herrmann, Erkan et al. 2012).

There are no data in the literature with respect to FLT PET/CT as a marker of early tumour response in pancreatic cancer. Furthermore assessment of liver metastases may be hampered by high background activity due to glucuronidation of FLT and hence, physiological accumulation in the liver (Shields, Grierson et al. 2002), making abdominal imaging challenging. Recently, the Aboagye group devised a new temporal intensity information-based voxel-clustering approach – kinetic spatial filter (KSF) - for removing the normal liver FLT uptake and to enable visualisation of specific uptake (i.e. uptake due to phosphorylation) in liver metastases (Gray, Contractor et al. 2010; Contractor, Challapalli et al. 2012). Briefly, the KSF compares, on a voxel by voxel basis, the time activity curves (TACs) of the image with the TAC of predefined tissue classes. The set of predefined tissue classes were determined by generating the average TACs for each of the major tissue types, including the cardiac blood pool, lungs, liver, tumour, normal breast and vertebra. Since the time profile of an individual voxel is too noisy to allow the accurate determination of the tissue type it represents, the mean time profile obtained from a voxel and its six nearest neighbours was considered. An additional background curve was also defined, to fit voxels located within the field of view, but outside the body of the patient. These TACs were normalised to the injected dose, and then the mean and standard deviation activity were calculated for every tissue type. Each voxel in turn was compared against the seven predefined classes. Only the voxels classified by the filter as being “tumour-like” will be saved in the post-filter image, thereby removing areas of physiological uptake that do not relate to FLT retention.

Therefore, this prospective nonrandomised exploratory clinical trial was conducted

- To generate data for assessing the efficiency of the FLT PET/CT_{KSF} in pancreatic cancer.
- To assess whether FLT PET/CT and FLT PET/CT_{KSF} could be used to predict the clinical responsiveness of gemcitabine based chemotherapy in patients with pancreatic cancer.

This study was used to test the hypotheses that the use of KSF would improve localisation of tumours in the pancreas and liver metastases and that the use of functional imaging with PET would predict early response to treatment and the potential for alternative management strategies.

Materials & Methods

Patients

Patients with histologically confirmed locally advanced or metastatic carcinoma of the pancreas, suitable for gemcitabine based chemotherapy, ECOG performance status ≤2 and with at least one (primary or metastatic) lesion ≥20 mm as assessed by CT imaging were included. Patients who progressed after previous radical surgery or from previous treatment, and were due to start gemcitabine based chemotherapy were also eligible. Patients who received chemotherapy or radiotherapy 8 weeks prior to the baseline FLT PET/CT were excluded.

Thus the main inclusion and exclusion criteria for this study were:

Inclusion criteria:

1) Diagnosis of histologically/ cytologically proven carcinoma of the pancreas.
2) Locally Advanced or metastatic disease.
3) Patient planned for treatment with gemcitabine based chemotherapy.
4) At least one measurable lesion $\geq$ 2 cm, suitable for imaging
5) ECOG PS $\leq$ 2
6) Aged 18 years and above
7) Written informed consent.

Exclusion criteria:

1) Patients who received chemotherapy/ radiotherapy within 8 weeks of study enrolment
2) Psychological, familial, sociological or geographical condition potentially hampering compliance with the study protocol
3) Pregnant or lactating women
4) Presence of any underlying medical conditions which in the investigators opinion would make the patients unsuitable for treatment
5) Baseline hematologic and liver/renal function not acceptable for chemotherapy
6) Patient not expected to be able to tolerate the scanning sessions

Fifteen patients were recruited from Imperial College Healthcare NHS Trust (ICHNT) and 5 patients from Newcastle-Upon-Tyne Hospitals NHS Foundation Trust (NHNFT). All patients received gemcitabine as a single agent or in combination with other agents.

Ethical approval for the study was granted by the West London REC 1 Committee. All patients gave fully informed consent to participate in the study, which was done according to the Declaration of Helsinki guidelines. The administration of radioactivity for the PET scans was approved by the Administration of Radioactive Substances Advisory Committee, United Kingdom.

Imaging protocol

FLT was manufactured according to standard protocol (Cleij 2001). All patients were scanned on a Siemens Biograph PET/CT scanner (15 on a 64-slice with True V at ICHNT, 5 on a 40-slice with True V at NHNFT: axial field-of-view (FOV), 21.6 cm; transaxial, 60.5 cm)). Baseline FLT PET/CT was performed within a week prior to start of chemotherapy. Post-treatment PET/CT was performed three weeks after the start of first cycle of chemotherapy. There was a minimum of 72 hrs gap between the last dose of gemcitabine and the FLT PET/CT (median of 5 days). All the baseline and post-treatment scans were performed on the same scanner. In all cases the primary tumour and any liver metastases, were imaged in a single bed position (covering the liver and the pancreas). Patient positioning was followed by a diagnostic quality CT scan (300 mA, 120kVp, 1.35 pitch, 0.8 sec/rotation) that was used for both attenuation correction and co-registration with PET images, to allow good anatomical visualisation and localisation of FLT activity. FLT was injected as a bolus intravenously and a dynamic emission scan in the 3D mode, lasting 66 minutes was undertaken (Contractor, Kenny et al. 2011).

All patients had a staging contrast-enhanced CT (CECT) 3 weeks before (baseline) and 3 months after the start of treatment.

Image analysis

Raw PET data were corrected for scatter, attenuation and reconstructed with an iterative algorithm consisting of 8 iterations and 21 subsets. The data were binned into time frames as follows: 1 * 30 (background), 6* 10, 4* 20, 4* 30, 5* 120, 4* 180 and 4* 600 seconds. The KSF was applied to the dynamic PET data. Decay corrected images (unfiltered and filtered) were then viewed using Analyze® software (Analyze Version 11; Biomedical Imaging Resource, USA). Volumes of interest (VOI) were defined on the summed images manually around the tumours, employing the patient's diagnostic contrast-enhanced CT (CECT) scan and the filtered images. The VOI encompassed the whole tumour for the SUV and voxel analysis. The FLT radioactivity concentration within the VOIs was then normalised for injected radioactivity and body weight to obtain the average and maximum SUV at 60 minutes ($SUV_{60,ave}$, and $SUV_{60,max}$) on the baseline and post-treatment FLT PET/CT (unfiltered) studies. The percentage change in SUV was then calculated for each patient.

Selection of target lesions

Target lesions in the pancreas and the liver were defined as lesions with the longest diameters (LD) as defined by RECIST 1.1 (Eisenhauer, Therasse et al. 2009) on CT. The lesions on the FLT PET/CT corresponding to those on the CT, showing an increased uptake and visualised on both the unfiltered and the filtered images were considered as target lesions. In patients with multiple lesions, the parameters of the most metabolically active lesion on the FLT PET/CT was considered for further analysis, as per the PERCIST guidelines (Wahl, Jacene et al. 2009). Data analyses with the sum of the parameters (SUV) of all the lesions, in patients with multiple lesions

are described in **Appendix 2**. The LD of the target lesions was measured using electronic callipers on the PACS work station. Lesions smaller than 20 mm were documented but not chosen as targets to enable the visualisation of the lesions on the FLT PET/CT_{KSF}: the tissue classes defined in the KSF considered the individual voxel and 6 of its neighbouring voxels (Gray, Contractor et al. 2010). The same target lesions were used for analyses on both the PET/CT and CECT, before and after treatment.

Voxel analysis

Voxel quantification analysis was performed on filtered data by determining the number of voxels in each tumour volume and then binning the number of occurrences of each voxel intensity value. The maximum voxel intensity was limited to 30 (single unit intervals) as none of the tumours had a voxel intensity value greater than 25. Each voxel-intensity was then normalised by injected dose and body weight and decay corrected to obtain the SUV for the voxel. Two variables representing both low and high intensity voxels (LoVox: SUV ≥ 1) or only high intensity voxels (HiVox: SUV ≥ 2 for pancreatic tumours and SUV ≥ 3 for liver metastases (Contractor, Challapalli et al. 2012)) were computed. The arbitrary SUV cut-off values are typically characteristic of low and high FLT uptake in different malignant lesions (Francis, Freeman et al. 2003; Buck, Hetzel et al. 2005; Kenny, Vigushin et al. 2005; Quon, Chang et al. 2008).

Response assessment

According to the RECIST 1.1 criteria (Eisenhauer, Therasse et al. 2009), the sum of the LD's of the target lesions was computed on the CECT scans before and after treatment. Patients with either partial response or stable disease were classed as non-progressors (NP) and those with progressive disease were classed as progressors

(P). The changes in the FLT imaging variables ($SUV_{60,ave}$, $SUV_{60,max}$, and HiVox) were then categorised into R and NR, retrospectively using the receiver operating characteristic (ROC) curve analysis and prospectively using 20% reduction in SUV as a threshold for response (Kenny, Coombes et al. 2007; de Langen, Klabbers et al. 2009).

The progression-free survival (PFS) was calculated as the time from start of treatment to unequivocal progression as documented clinically or on CT, and the overall survival (OS) was calculated as the time from the diagnosis to death.

Statistical considerations

Preliminary data have shown that patients with changes in FLT uptake of >20% in individual patients can be classified as radiotracer responsive (Kenny, Coombes et al. 2007). Variability in the measured change within individuals in FLT has been estimated at ~0.15 (Kenny, Coombes et al. 2007; de Langen, Klabbers et al. 2009). Expected response to therapy is 20% of patients receiving chemotherapy. This will dilute the expected "group" effect to 0.124 and inflate the variability to 0.17. Power calculation (paired t-test) suggests that a number n=20 of patients will give to the design a minimum power of .80 to detect a group difference in FLT at a 0.05 error rate. The addition of n=4 patients to compensate for dropout and/or 4 patients to compensate for technical problems with imaging brings the total number of patients to n=28.

Quantitative measurements of the FLT imaging variables are reported using descriptive statistical measures. ROC curves were used to identify the optimal cut-off value of the imaging variables to differentiate R and NR. Statistical comparisons

between pre and post-treatment, unfiltered and filtered, variables were done using Wilcoxon signed rank test. Analysis of PFS and OS was performed by using Kaplan-Meier estimates and the log-rank test. A two-sided p value <0.05 was considered statistically significant. All analyses were done using Graph Pad (Prism software®-version-4). The ROC analysis was performed using MedCalc statistical software (version 11.6.1, Mariakerke, Belgium).

Results

Patients

The study recruited 25 patients out of whom 20 patients had completed both the baseline and post-treatment FLT PET/CT. Fifteen patients were recruited from Imperial College Healthcare NHS Trust (ICHNT) and 5 patients from Newcastle-Upon-Tyne Hospitals NHS Foundation Trust (NHNFT). All patients received gemcitabine as a single agent or in combination with other agents. Ten patients had locally advanced disease and 10 had metastatic disease (**Table 7**). All patients tolerated the FLT PET/CT scans without any complications. The mean (±SD) age of patients was 69 (±8) years and all patients had gemcitabine based chemotherapy. The mean (±SD) injected activity of FLT was 211 (±10.4) MBq with a radiochemical purity of >95%.

Table 7: Patient characteristics

Pt No	Age (yrs)	Sex	Stage	Target Lesion	LD (mm)	Non-Target Lesion	LD (mm)	Chemotherapy	PFS (m)	OS (m)
1	62	M	LA	Primary	58			Gemcitabine, Caecitabine	2.97	4.33
2	67	F	M	LM	71	Primary	34	Gemcitabine, Cisplatin	6.10	9.43
3	78	M	M	LM2	40	Primary	58	Gemcitabine, Cisplatin	2.63	7.80
						LM1	57			
4	73	M	M	LM2	22	LM1	18*	Gemcitabine, Cisplatin	8.57	12.80
5	73	M	LA	Primary	36			Gemcitabine, Caecitabine	7.60	32.43
6	60	F	M	Primary	30	LM	17*	Gemcitabine, Cisplatin	5.60	11.10
7	77	F	M	Primary	40	LM	9*	Gemcitabine	11.77	17.53
8	61	M	LA	Primary	58			Gemcitabine	3.97	8.73
9	70	M	M	LM2	42	Primary	49	Gemcitabine	0.47	1.43
						LM1	20			
10	68	F	LA	Primary	34			Gemcitabine	11.83	12.90
11	64	M	LA	Primary	51			Gemcitabine, Dasatinib/Placebo	8.63	11.50
12	77	M	M	Remnant †	24			Gemcitabine, Vandatinib/Placebo	7.37	7.37
13	69	M	LA	Primary	26			Gemcitabine, Vandatinib/Placebo	8.03	8.03
14	78	F	M	LM	20	Primary	58	Gemcitabine	1.20	1.87
15	69	M	LA	Primary	24			Gemcitabine, Cisplatin	1.77	4.27
16	65	F	M	LM	20	Primary	56	Gemcitabine	1.80	3.73
17	62	F	LA	Primary	29			Gemcitabine	2.63	13.07
18	61	M	LA	Primary	38			Gemcitabine	4.83	8.43
19	86	F	M‡	Primary	32			Gemcitabine	9.47	9.47
20	56	M	LA	Primary	48			Gemcitabine	10	10
Mean	**69**								**5**	**10**

PFS-progression free survival, OS-Overall survival, m-months, LM-liver metastases, LA-locally advanced, M-metastatic

* Liver metastases not seen on Kinetic Spatial Filter, †Recurrence in pancreatic remnant, ‡ Liver metastasis (10mm) seen on CT not visualised on unfiltered FLT PET/CT.

Imaging characteristics of FLT uptake at baseline

On visual analysis of the unfiltered images the pancreatic tumours were visible above the background in 15 out of 20 (75%) patients. The mean unfiltered $SUV_{60,max}$ (±SD) for the primary tumours and normal pancreas were 4.23 (±1.52), and 2.14 (±1.26), respectively. The 11 liver metastases, seen in 8 patients, were typically photopenic relative to normal liver background on the unfiltered images (**Figure 8**). The mean unfiltered $SUV_{60,max}$ (±SD) for the liver metastases and the surrounding normal liver background was 8.41 (±2.21) and 7.99 (±1.83), respectively. Physiological activity was seen in the liver, kidneys and the vertebrae.

KSF qualitatively improved image visualisation of the tumours (**Figure 8**). All the pancreatic tumours were visualised on the filtered FLT PET/CT images. However, only 8 liver metastases (out of 11) were visible on the filtered images. The 3 liver metastases not visualised by the KSF, were less than 20 mm and had higher tissue activity than the average for the liver metastases (**Table 7, Figure 9**). Small liver lesions typically had a homogeneous appearance, whereas liver lesions >3 cm were characterised by perilesional tracer uptake with no measurable FLT trapping in the necrotic centre of the liver metastases. As seen previously (Contractor, Challapalli et al. 2012), and unrelated to proliferation, liver capsule resembling a thin margin, retained signal following application of KSF. Since KSF is associated with removal of delivery components within the data (Gray, Contractor et al. 2010), there was a mean (±SD) signal reduction in untreated primary tumours of 18.3% (±24.6) and 27.5% (±1.6) in liver metastases relative to the unfiltered images and the background signal in the liver and pancreas were reduced to ~0. Thus, KSF provides a measure of FLT retention within the tumour tissue. The time course of injected activity, decay corrected and

normalised to injected activity (tissue activity (mL^{-1})) for the tumours and normal tissue compared well with the tissue activity curves of the tissue classes defined by Gray and co-workers (**Figure 9**)**.**

A voxel-by-voxel representation of data was also computed to appreciate the heterogeneity of the tumours **(Figure 10a-d)**. KSF-derived voxel-based data were available for all the pancreatic tumours and the 8 liver metastases (**Table 8**). The variable representing both low and high intensity voxels (LoVox) was unremarkable with respect to changes between R and NR and therefore was not further explored. Hence, only high intensity voxels (HiVox) derived from KSF were explored **(Figure 11a-d)**.

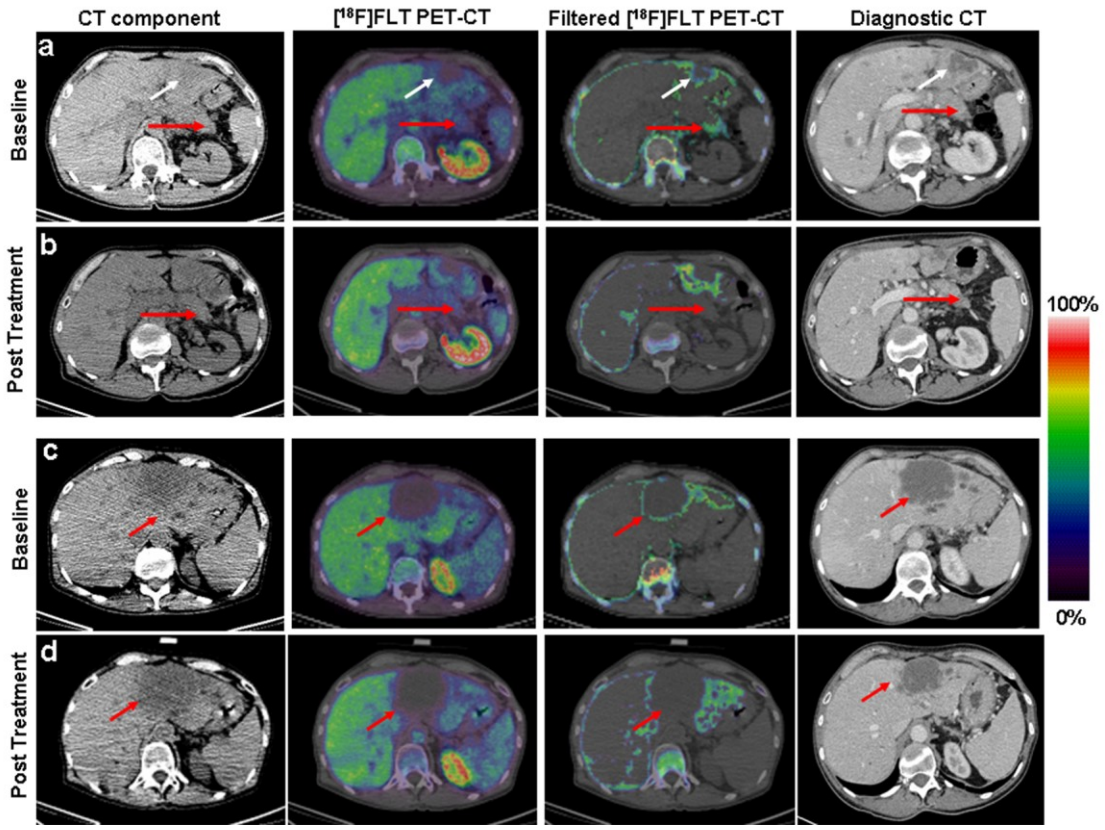

Figure 8: [^{18}F]FLT uptake in tumours and normal tissues and changes with treatment.

The primary tumour (red arrow) is not visible above background and the liver metastasis (white arrow), is photopenic on the unfiltered PET-CT **(a)**. The filtered image shows better tumour visualisation in the tail of the pancreas (red arrow) and the liver metastasis a rim of uptake with no uptake in the necrotic centre **(c)**. There is physiological uptake in liver, kidney and vertebra. After treatment there is a marked reduction of activity in the primary tumour (red arrow), most obvious in the filtered images **(a, b)**, The liver metastases also show a reduction in the [^{18}F]FLT uptake with treatment (red arrow; **c, d**). The diagnostic CT (done after 4 cycles of chemotherapy) shows a slight reduction in the lesion size. Overall this patient (Pt No. 2 in Table 7) had a partial response to treatment.

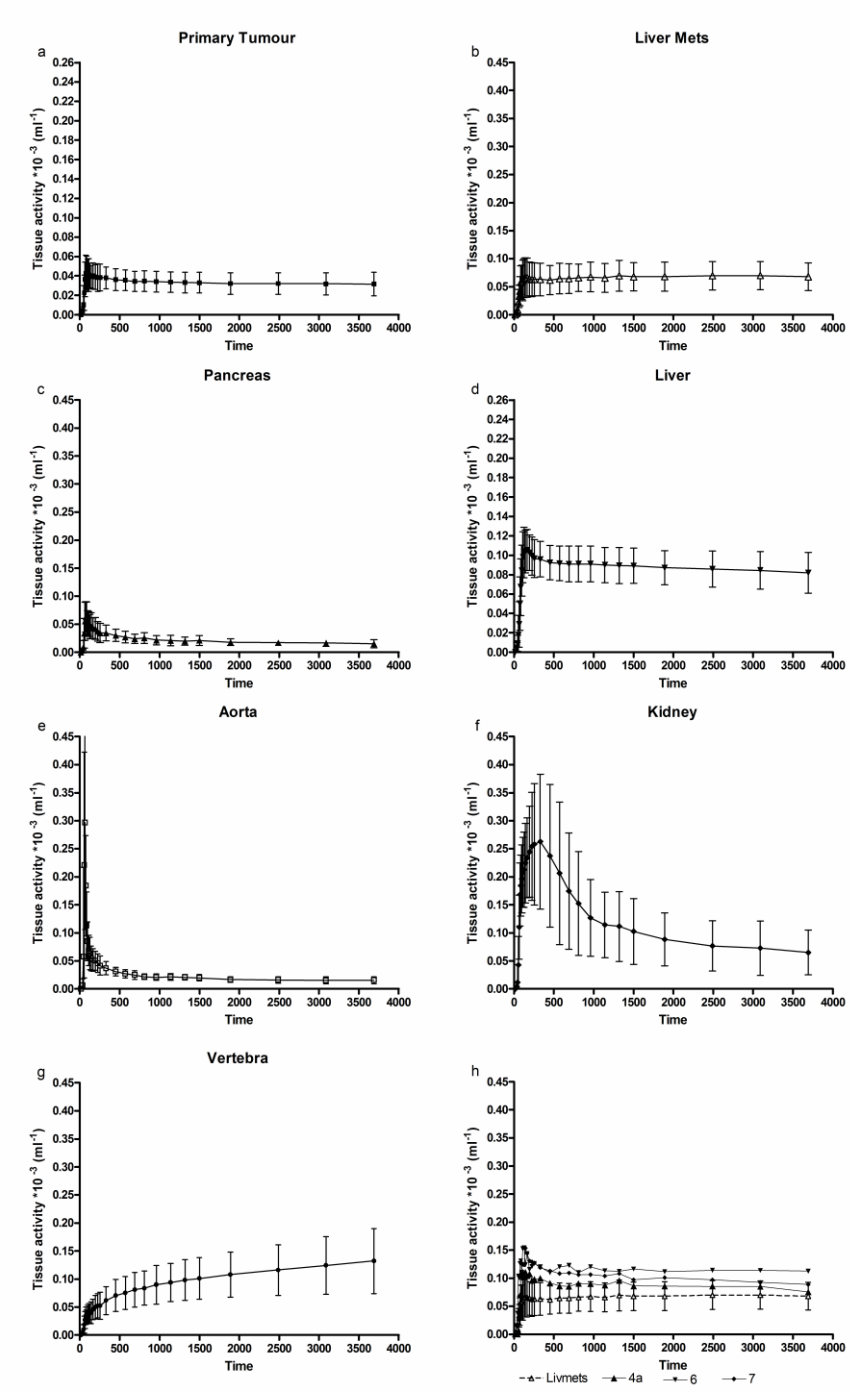

Figure 9: Decay corrected time activity curves, normalised by injected activity (tissue activity) for selected tissue types including **(a)** tumour, **(b)** liver metastases, **(c)** pancreas, **(d)** liver, **(e)** aorta, **(f)** kidney, **(g)** vertebra and **(h)** liver metastases not visualised on KSF. Data are average tissue activity values and error bars represent one SD.

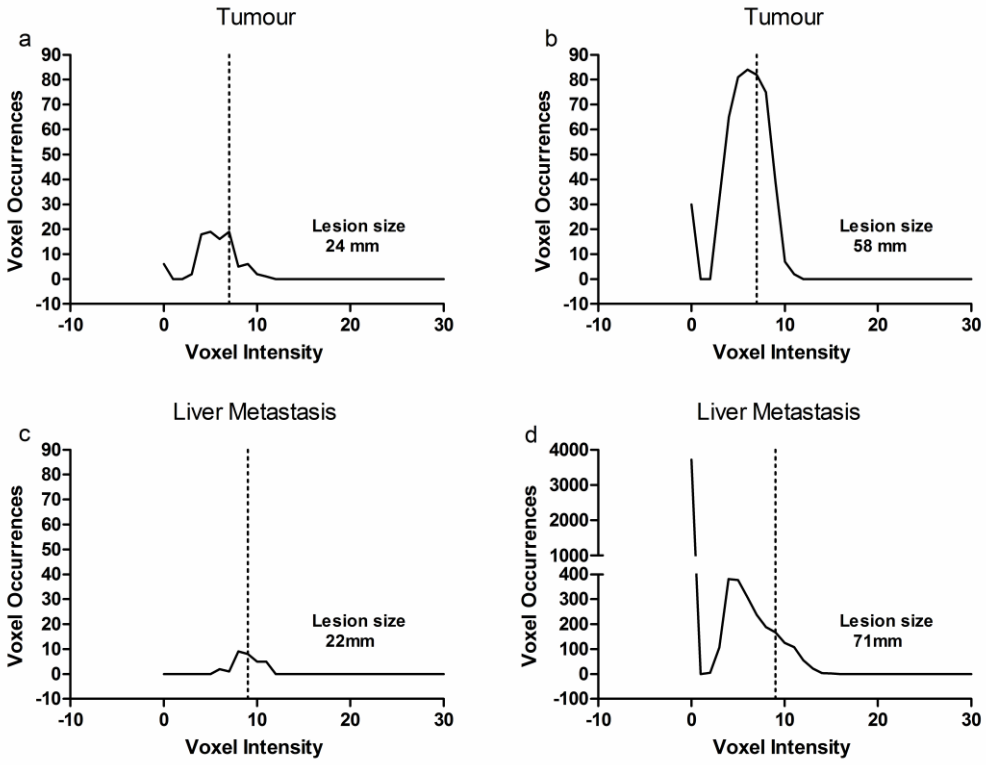

Figure 10: **Voxel representations depicting tumour heterogeneity**

in pancreatic tumours **(a-b)** and liver metastases **(c-d)** in a tumour of size<30 mm (homogeneous tumour on filtered images), and in a tumour of size>55 mm (heterogeneous tumour on filtered images). The dotted line on the X-axis corresponds to SUV of 2 (a-b) and to SUV of 3 (c-d). Note different scales of Y-axis.

Table 8: **Baseline characteristics of lesions: Unfiltered SUV and percentage occurrences of KSF derived voxels with high intensities.**

Pt No	Lesion(s)	Overall RECIST response*	$SUV_{60,ave}$	$SUV_{60,max}$	HiVox
1	Primary	PD	2.19	5.01	85.7
2	Primary	PR	1.61	3.08	33.7
	LM		2.13	5.58	23.2
3	Primary	PD	2.17	5.51	71.7
3a	LM1		3.43	10.08	78
3b	LM2		5.22	10.96	99.5
4a	LM1	PR	5.48	9.40	†
4b	LM2		4.38	7.05	100
5	Primary	SD	2.56	8.50	83.5
6	Primary	SD	2.79	4.68	83.9
	LM		6.55	7.39	†
7	Primary	SD	1.86	3.37	40.4
	LM		4.20	4.47	†
8	Primary	SD	2.23	4.78	43.9
9	Primary	PD	2.93	5.62	71.3
9a	LM1		7.34	10.02	100
9b	LM2		4.80	10.28	69
10	Primary	SD	0.92	2.17	6.7
11	Primary	SD	2.13	4.85	48.2
12	Remnant	SD	1.53	2.98	13.9
13	Primary	SD	0.94	2.84	16.7
14	Primary	PD	2.22	5.25	48
	LM		4.48	7.43	79.1
15	Primary	PD	1.85	3.42	37.5
16	Primary	SD	1.96	3.74	36.6
	LM		5.65	5.90	100
17	Primary	PD	1.43	2.85	51.2
18	Primary	PD	1.65	2.88	50.6
19	Primary	SD	2.49	5.54	0.65
20	Primary	SD	1.79	3.26	30.8

* RECIST response based on mid treatment CT scan.

†Tumours not visible on filtered images. Data were excluded from further analysis.

PR-partial response, SD-stable disease, PD-progressive disease, $SUV_{60,ave}$- SUV average, $SUV_{60,max}$ -SUV maximum, HiVox - high intensity voxels (corresponding to SUV≥2 for primary pancreatic tumours and SUV≥3 for the liver metastases).

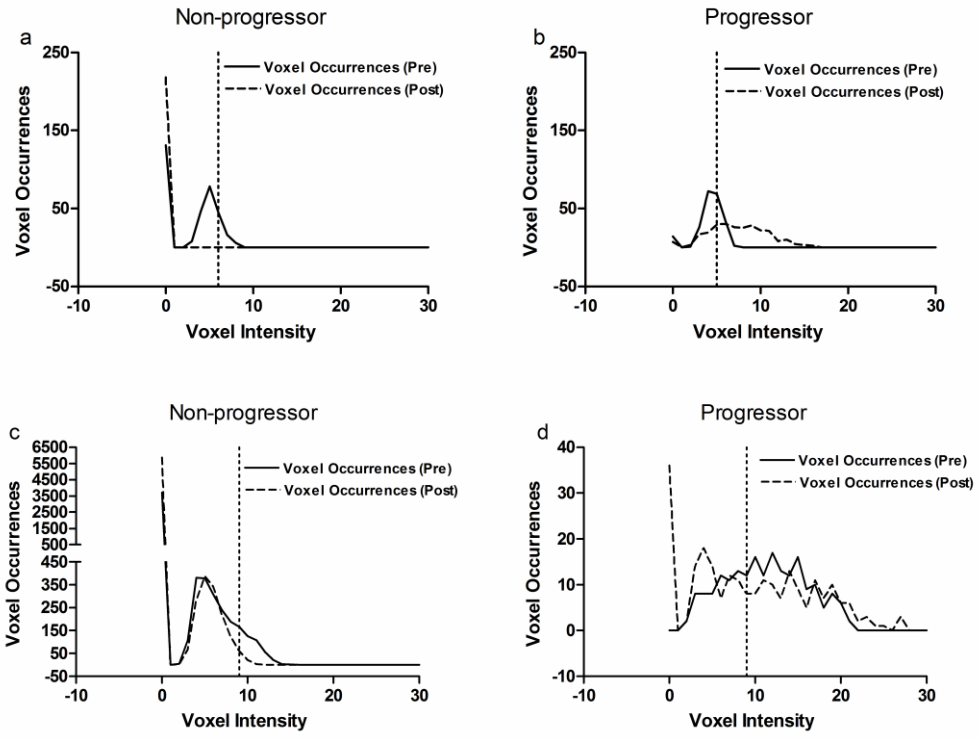

Figure 11: **Changes in voxel intensities with therapy**

in the pancreatic tumour **(a, b)** and in the liver metastases **(c, d)** with treatment in a non-progressor and progressor, respectively. The dotted line on the X-axis corresponds to SUV of 2 **(a, b)** and to SUV of 3 **(c, d)**. Note different scales of Y-axis.

Effect of Treatment on FLT PET variables

Since this is, to the best of our knowledge, the first study of early response assessment with FLT PET/CT in pancreatic cancers, the characteristics of the different imaging variables that could be used to describe proliferation in this tumour type were evaluated. All proportional comparisons were performed only in the lesions visible after kinetic filtering (i.e. all target lesions (>2cm) and a subset of non-target lesions). A reduction in proliferation detected by FLT PET/CT was seen in several tumours at three weeks post-treatment (**Figure 8**). The waterfall plots of the most metabolically active tumours and the ROC curves are shown in **Figure (12 a-d)**. For $SUV_{60,ave}$ and $SUV_{60,max}$ nearly half of the tumours showed some degree of reduction in proliferation. Most of tumours also showed some degree of reduction in proliferation when the measure was HiVox (**Figure 13**). Interestingly, majority of the RECIST lesion P showed an increase in $SUV_{60,max}$; 6 out of the 7 progressors had a 12-132% increase in the $SUV_{60,max}$. The one progressed patient, who had a decrease in the $SUV_{60,max}$, was classed as a P by virtue of developing new liver metastases. The RECIST lesion response showed a good correlation with the FLT lesion response (Spearman's r=0.43, p=0.04). The mean percentage reduction after treatment was 2%, -3%, and 19% for $SUV_{60,ave}$, $SUV_{60,max}$, and HiVox, respectively. Using a prospective cut-off of 20% reduction in $SUV_{60,max}$ (Kenny, Coombes et al. 2007; de Langen, Klabbers et al. 2009) as response, the sensitivity and specificity of FLT PET/CT in predicting a progressor was 38.5% and 85.7%. However, using a retrospective cut-off of 12% reduction in $SUV_{60,max}$ based on the ROC curves, the sensitivity improved to 46.2% retaining the same specificity (85.7%; AUC-0.88, p=0.0001). These results suggest that $SUV_{60,max}$ is the variable of choice at discrimination between non-progressors and progressors.

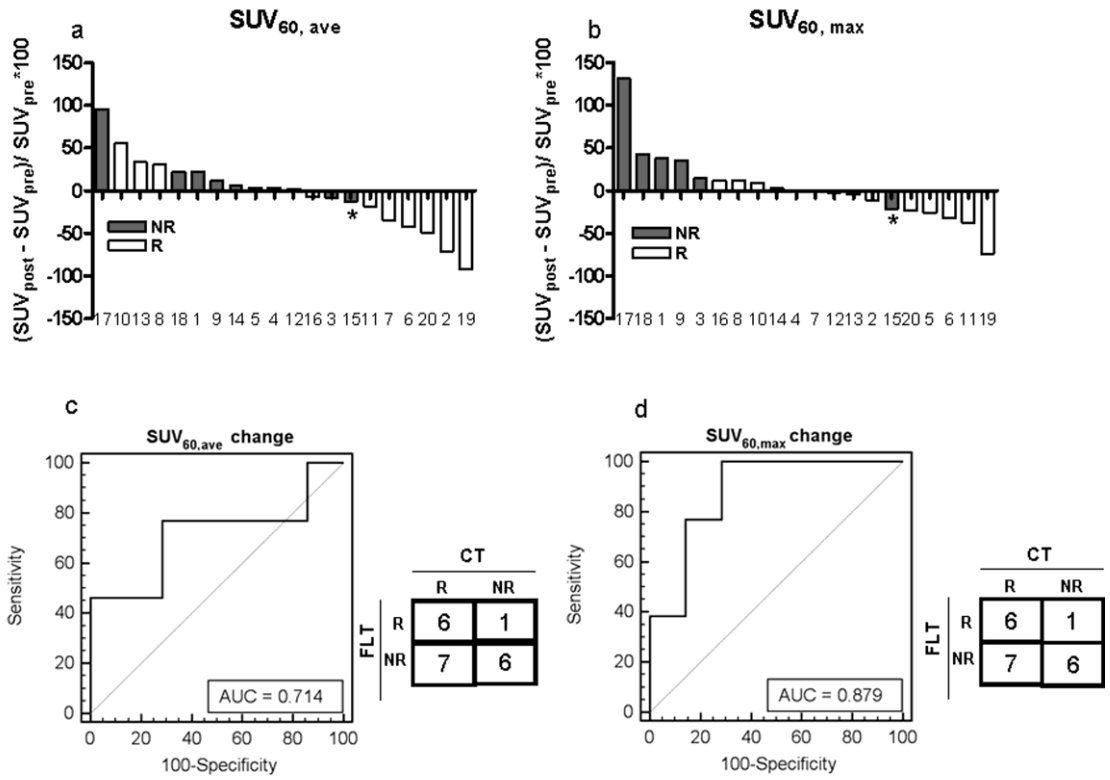

Figure 12: **Waterfall plots and Receiver Operating Characteristic curves of the most metabolically active lesions.**

Waterfall plots for the measures of **(a)** $SUV_{60,ave}$, **(b)** $SUV_{60,max}$. The RECIST lesion non-responders are shaded in grey. Majority of the RECIST lesion progressors showed an increase in FLT uptake when the measure was $SUV_{60,ave}$, $SUV_{60,max}$; 6 out of the 7 progressors had the biggest increase in $SUV_{60,\ max}$. The * refers to the patient who was a progressor by virtue of developing new liver metastases. Receiver Operating Characteristic curves for changes in **(c)** $SUV_{60,ave}$, **(d)** $SUV_{60,max}$.

Group analyses of the imaging data were also performed. The difference between baseline and post-treatment FLT uptake showed a statistically significant increase of $SUV_{60,max}$ in the progressors **(Figure 14 a-c)**.

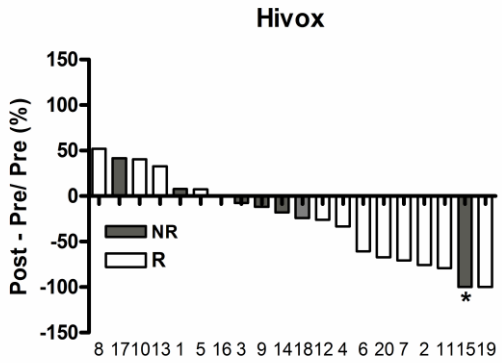

Figure 13: Waterfall plot of changes in HiVox for the most metabolically active lesions.
The * refers to the patient who was a progressor by virtue of developing new liver metastases.

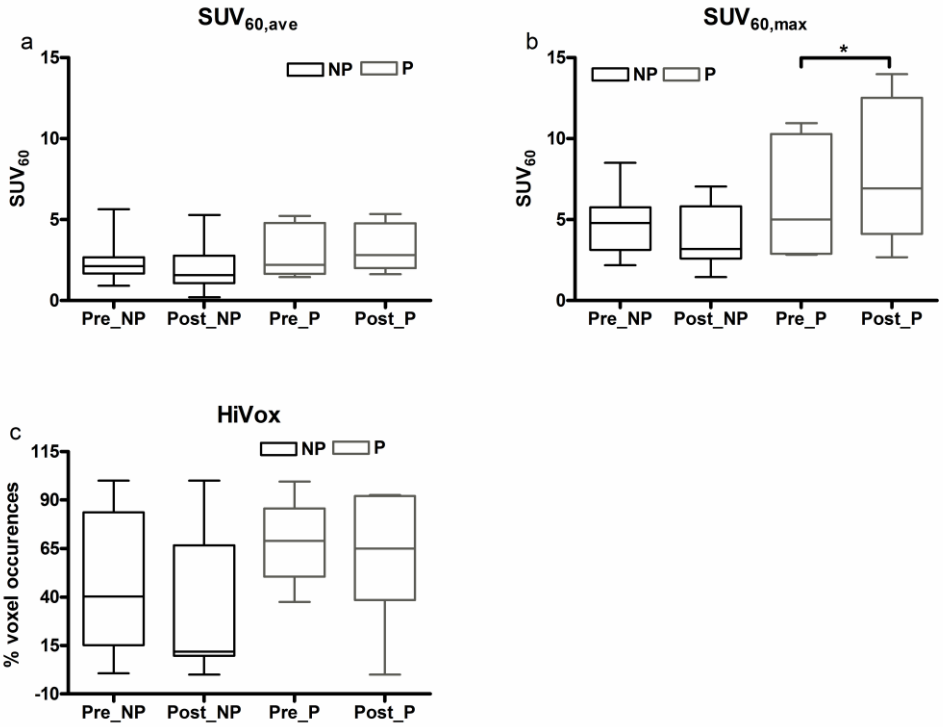

Figure 14: **Group analysis of the imaging data**
showing the difference between baseline and post-treatment FLT uptake in the most metabolically active lesions in non-progressors and progressors: box and whiskers plots for the measures of **(a)** $SUV_{60,ave}$, **(b)** $SUV_{60,max}$, and **(c)** HiVox.

Prediction of Survival

Of the 20 patients only 6 patients were alive after mean follow up of 10 months (range: 1.4 to 32.4 months). Based on the cut-off of 12% reduction in $SUV_{60,max}$ derived from the ROC curves, the median PFS of FLT non-progressors and progressors was 7.6 and 3.9 months (p=0.5, CI=0.24-2.01; Log rank test), respectively and the median OS was 11.5 and 8.7 months (p=0.15, CI=0.15-1.33; Log rank test), respectively in the non-progressors and progressors. When the CT RECIST criteria were used for response assessment, the median PFS of non-progressors and progressors were 8.6 and 2.6 months (p<0.0001, CI=0.006-0.16; Log rank test), respectively and the median OS was 11.5 and 7.8 months (p=0.03, CI=0.06-0.88; Log rank test), respectively in the non-progressors and progressors (**Figure 15**).

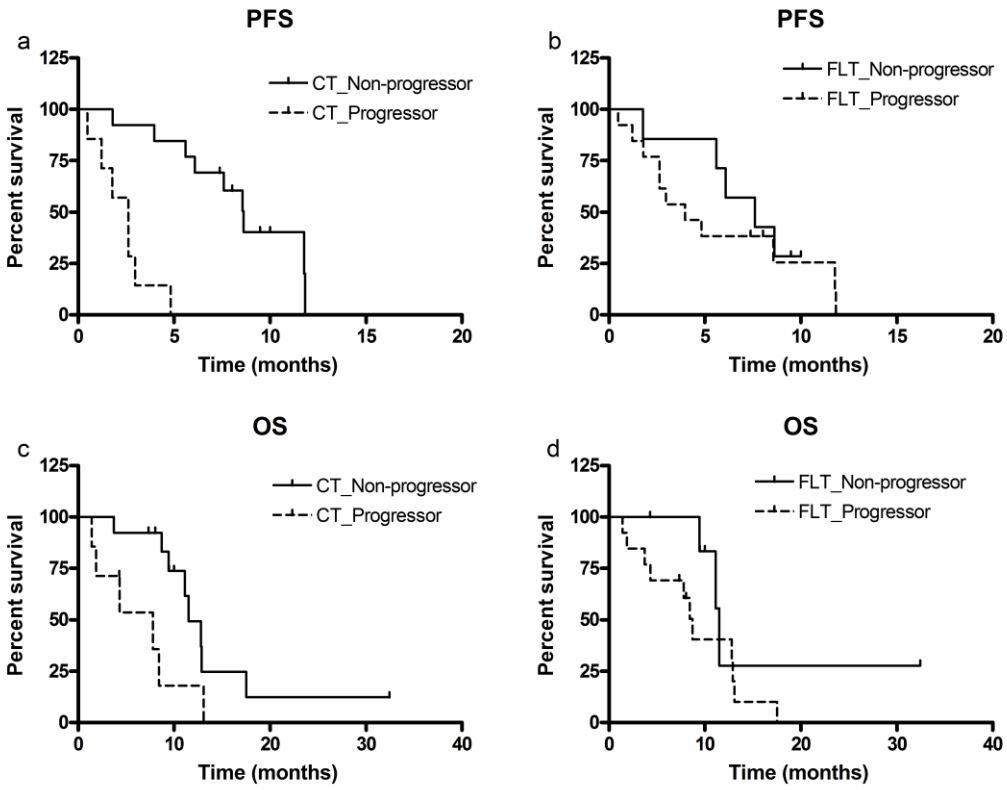

Figure 15: **Kaplan-Meier Survival curves**
for progression free survival (PFS; **a, b**) and overall survival (OS; **c, d**). The response classification was based on RECIST response (CT) and a cut-off of 12% reduction in $SUV_{60,\ max}$ for FLT.

Discussion

FLT PET/CT is increasingly being explored as an early biomarker of response to therapy (Weber 2010; Tehrani and Shields 2013). In this exploratory study it was demonstrated that FLT PET may be useful in the setting of advanced pancreatic cancer. In particular a qualitative visual distinction between tumours, normal pancreas and normal liver was seen in FLT PET/CT_{KSF} images. $SUV_{60,max}$ (unfiltered) was able to

differentiate between non-progressors and progressors. There was a significant increase in the $SUV_{60,max}$ in progressors (**Figure 10**), suggesting that rise in $SUV_{60,max}$ is a poor prognostic indicator, i.e. patients who have an early increase in $SUV_{60,max}$ are less likely to respond to the treatment. However, overall changes in FLT uptake were not predictive of PFS or OS.

The KSF has previously been validated (Gray, Contractor et al. 2010) and its utility in imaging proliferation in liver metastases been evaluated (Contractor, Challapalli et al. 2012). As seen in these 2 studies, the KSF was able to completely remove the signal from the normal liver and pancreas (fast and reversible kinetics), thus exposing the underlying tumours (slow and irreversible kinetics). Similarly, the larger liver metastases showed a central core of almost no FLT uptake surrounded by a rim of varying uptake at the periphery, as seen previously (Gray, Contractor et al. 2010; Contractor, Challapalli et al. 2012). This suggests that the rim of proliferation phenotype of the liver metastases is independent of the site of origin of the primary tumours. These findings were also consistent with that from Semelka et al, who using gadolinium enhanced magnetic resonance imaging, showed that there was perilesional contrast enhancement. They concluded that this could be due to hepatic parenchymal changes secondary to vascular proliferation (Semelka, Hussain et al. 2000). This reflects the fact that rapidly growing tumours may undergo central hypoxia and necrosis at the core with proliferating cells at the rim due to better blood supply (Harris 2002).

All the primary pancreatic tumours were visible on the FLT PET_{KSF}, but only 8 out of the 11 liver metastases were visualised, thus detecting 73% of the liver metastases. This detection rate is similar to that seen in our earlier study (Contractor, Challapalli et al. 2012). Interestingly, the 3 liver lesions that were completely “filtered

out" by the KSF were less than 20 mm. Their kinetic profiles were found to be remarkably different from those employed in the KSF validation (**Figure 19**) (Gray, Contractor et al. 2010). The inability of the KSF to retain signal in lesions <20 mm could also be due to the consideration of the mean time profile obtained from a voxel and its six nearest neighbours to allow the accurate determination of the tissue type it represented (Gray, Contractor et al. 2010).

Other than tumour detection, the very heterogeneous nature of these tumours supports the use of quantitative voxel analysis (**Figure 10**). However, most of the non-responders (5 out of 7) showed a reduction in proliferation when the measure was HiVox. Furthermore, HiVox could not differentiate non-progressors and progressors. This could be due to the lower uptake of FLT in the primary pancreatic tumours (mean $SUV_{60,max}$ of 4.23), similar to that previously reported; mean $SUV_{60,max}$ of 3.0 (Herrmann, Erkan et al. 2012), and that the early voxel changes do not necessarily translate into durable suppression of proliferation. Longer post-treatment imaging interval may improve the predictive value of durable responses.

FLT PET/CT and FLT PET/CT_{KSF} variables detected the sensitivity of chemotherapy, demonstrated as a decrease in imaging variables at 3 weeks post-treatment. FLT PET/CT correctly predicted mid-therapy clinical progression with sensitivity and specificity of 46.2% and 85.7% when the measure was $SUV_{60,ave}$ or $SUV_{60,max}$. Sensitivity and specificity could be calculated prospectively with 20% used as the cut-off for response, for changes in SUV (Kenny, Coombes et al. 2007; Shields, Lawhorn-Crews et al. 2008; de Langen, Klabbers et al. 2009). The sensitivity & specificity of 46.2% & 85.7% are superior to those seen by FDG PET; 30% and 60%, respectively from a study by Bang and co-workers (Bang, Chung et al. 2006). However,

clinical response was used as a comparator and >50% reduction in FDG uptake was considered as partial response. Unlike SUV, reproducibility of HiVox has not been assessed. Therefore, the individual sensitivity and specificity of HiVox were not assessed prospectively. For HiVox, specificity was reasonable at 85.7% when the cut-off was arbitrarily set at 50%. Retrospective ROC curves, however, favoured $SUV_{60,max}$ as the imaging variable of choice (AUC-0.88, p=0.0001).

In patients with pancreatic cancer, levels of human equilibrative nucleoside transporter 1 (hENT1) have been linked with survival (Farrell, Elsaleh et al. 2009). hENT's mediate the transport of both Gemcitabine and FLT, therefore performing FLT PET/CT after gemcitabine therapy may indicate response to therapy and it could be hypothesised that baseline FLT uptake would predict gemcitabine uptake (Paproski, Young et al. 2010). Gemcitabine is known to cause an increase in FLT uptake at 24 hrs after treatment, decreasing to baseline by 72 hrs (Dittmann, Dohmen et al. 2002). To obviate the early increase of FLT uptake it was ensured that the post-treatment FLT PET/CT was performed with a minimum of 72 hrs after a dose of gemcitabine. Therefore, the changes in FLT uptake seen represent a true effect of suppression of proliferation rather than change in uptake due to the pharmacodynamic effect of gemcitabine.

Early changes in FLT uptake have been shown to predict long term outcome in breast, lung and brain tumours, but not in rectal cancer, lymphoma and germ cell tumours (Weber 2010). Likewise, there was no significant difference observed in the median PFS or OS between FLT non-progressors and progressors, in this study. This suggests that inhibition of proliferation may be necessary but not sufficient for a favourable response with certain types of treatment.

A small sample size and the lack of Ki-67 indices are limitations of our study. However, pancreatic adenocarcinomas have been shown to have an average Ki-67 labelling index of 37% (Klein, Hruban et al. 2002). This supports the use of FLT PET/CT in our cohort of patients. Another limitation of this study is the consideration of just the most metabolically active lesion for the evaluation of treatment response.

In summary, this study has shown that FLT PET/CT could potentially be a promising imaging biomarker to assess response to gemcitabine based therapy in advanced pancreatic cancer. $SUV_{60,max}$ appeared to be the variable of choice to differentiate between non-progressors and progressors and is a strong negative predictor. This enables subsequent use of FLT PET/CT as a vehicle to evaluate efficacy of newer therapeutic agents and targeted therapy in the management of pancreatic cancer. However, changes in FLT uptake were not predictive of PFS or overall survival. Further studies, in a larger cohort of patients are needed to establish the value of FLT PET/CT in predicting long term outcome.

CHAPTER 3: Non invasive detection of pelvic lymph nodal metastases from prostate cancer using [^{11}C]choline PET/CT and relationship with choline kinase expression

3.1.1: Rationale

The evaluation of lymph nodes (LNs) has important therapeutic and prognostic significance in patients diagnosed with prostate cancer (PCa). Whilst a curative approach can be adopted for those with organ confined node-negative disease with modalities such as surgery, external beam radiotherapy or brachytherapy, those with node-positive disease ultimately relapse with metastatic disease (relapse rate 30-50% at 5 years, 90% at 10 years) (Danella, deKernion et al. 1993; Leibel, Fuks et al. 1994). As such, the presence of LN involvement reduces the 5 year disease free survival from 85% to approximately 50% with a shift in the focus of treatment to long-term androgen deprivation with the addition of pelvic radiotherapy to reduce loco-regional recurrence (Robnett, Whittington et al. 2002; Kumar, Shelley et al. 2006). Pelvic LN dissection is currently the gold standard for evaluating the presence of nodal involvement (Stone and Stock 1999; Allaf, Partin et al. 2006). This procedure can either be open or laparoscopic and is usually limited to the external iliac and obturator nodes, though a more extended procedure to include the internal iliac nodes is usually advocated for those with a higher risk of nodal disease (Wyler, Sulser et al. 2006). Either way, both these methods are invasive, associated with morbidity (Parkin, Keeley et al. 2002) and importantly may not be able to sample all potential LN areas.

It is thus important to have a sensitive and reliable noninvasive means of detecting nodal involvement. The criteria for nodal characterisation using cross-

sectional imaging such as CT or Magnetic Resonance Imaging (MRI) relies primarily on morphological assessment based on size and shape, with a nodal short axis diameter of 1cm generally accepted as an upper limit of normal. A threshold of 1cm in the short axis diameter for oval nodes and 0.8cm for round nodes has been recommended as criteria for diagnosis of prostate cancer nodal metastases (Jager, Barentsz et al. 1996). A recent meta-analysis on the diagnostic accuracy of cross-sectional imaging in the staging of pelvic LNs in prostate cancer reported a high pooled specificity for MRI of 0.82 with a low and heterogeneous pooled sensitivity of 0.39 (Hovels, Heesakkers et al. 2008). The lack of sensitivity belies the fact that nodal involvement is not always correlated with enlargement and enlarged nodes may also be due to a benign aetiology. Neither MRI nor lymphangiography has demonstrated higher sensitivity than CT scanning in the detection of nodal metastases (Rorvik, Halvorsen et al. 1998; Hovels, Heesakkers et al. 2008). The use of an MR contrast agent containing ultra-small particles of iron oxide (ferumoxtran10-Sinerem, USPIO) has been shown to yield sensitivity and specificity above 90% in the detection of prostate cancer LN metastases (Harisinghani, Barentsz et al. 2003). However, this is not widely available and its intravenous infusion is not without side effects (Bernd, De Kerviler et al. 2009). Further studies using diffusion weighted MRI have demonstrated that the method, while undoubtedly having improved intra-prostatic tumour detection and localisation, it is less satisfactory for assessing pelvic nodal disease (Roy, Bierry et al. 2010).

PET offers functional information regarding tissue activity, thereby having the potential to provide superior staging information as well as the ability to monitor the response to treatment. The clinical experience with [^{18}F]FDG PET in prostate cancer is limited due to variable uptake of [^{18}F]FDG in prostate cancer and the rapid excretion of

FDG in urine, causing an accumulation of activity in the bladder (Effert, Bares et al. 1996; Hoh, Seltzer et al. 1998; Hain 2005).

[^{11}C]choline is a radiopharmaceutical for PET imaging and its utility in visualising and staging prostate cancer has been published (Hara, Kosaka et al. 1998; Reske, Blumstein et al. 2006). The tumour PET signal from [^{11}C]choline, comprises of free [^{11}C]choline and [^{11}C]phosphocholine, as well as the oxidation product, [^{11}C]betaine (Leyton, Smith et al. 2009). The PET signal (tumour [^{11}C]choline uptake) therefore, largely reflects transport and phosphorylation of [^{11}C]choline, and to a lesser extent (given that liver and kidneys produce most of the circulating [^{11}C]betaine), [^{11}C]choline oxidation. Unlike [^{18}F]FDG it has low renal elimination, and therefore visualisation of the prostate and surrounding nodes may be enhanced by the low accumulation of tracer within the bladder (Hain 2005). Preliminary studies of [^{11}C]choline-PET in pelvic nodal staging in prostate cancer patients have shown early promise (Kotzerke, Prang et al. 2000; de Jong, Pruim et al. 2003; Schiavina, Scattoni et al. 2008). However, no study to date has established a direct relationship between CHKα expression and [^{11}C]choline uptake in prostate tumours. Also the accurate documentation of the pelvic nodal status would facilitate image guidance and allow safe radiotherapy dose escalation, minimising the dose to small bowel in the radiotherapy field.

To summarise, the main aims of the study were:

- To compare the use of [^{11}C]choline PET/CT with MRI in determining pelvic nodal status in patients with high risk localised prostate cancer undergoing surgical staging with pelvic lymphadenectomy (reference standard).
- To document the early kinetics of [^{11}C]choline from dynamic imaging up to 60 minutes post radiotracer injection.

- To evaluate the association between [^{11}C]choline uptake (SUV) and immunohistochemistry scores for CHKα expression, Ki67 in prostate tumours and involved nodes.

This study was used to test the hypothesis that untreated malignant lesions will have enhanced radiolabelled choline accumulation due to their high CHKα expression.

3.1.2: Materials and Methods

3.1.2.1: Patients

Patients with histologically confirmed prostate cancer staged as either high risk localised (either PSA >20ng/mL or Gleason score 8-10 or TNM stage ≥ T2) / locally advanced (nodal disease on staging MRI of the pelvis), were eligible for the study. Patients with visceral or bone metastases were ineligible. Thus the main inclusion and exclusion criteria for this study were:

Inclusion criteria:

1) Histologically confirmed adenocarcinoma of the prostate.
2) High risk prostate cancer- either PSA >20ng/mL, or Gleason score 8-10 or AJCC Stage T2c or higher, who on cross sectional MRI imaging of the pelvis, demonstrated nodal disease.
3) More than 30% risk of nodal disease based on the Roach formula.
4) WHO performance status 0 or 2.
5) Normal blood counts; Haemoglobin >10g/dl, WBC >4000/mm^3, platelets >100,000/mm^3.
6) Normal liver and renal function.

7) Written informed consent and fit for surgery.

Exclusion criteria:

1) Patients with visceral or bone metastases.
2) Prior radical prostatectomy or previous open lower abdominal or pelvic surgery which may contra-indicate laparoscopic pelvic nodal dissection.
3) On any concurrent investigational agent.
4) Life expectancy less than 5 years.
5) Previous malignancy within the last five years other than basal cell carcinoma.

Ethical approval for the study was granted by the Hospital Research Ethics Committee. All patients gave written informed consent to participate in the study, which was carried out according to the Declaration of Helsinki guidelines. The administration of radioactivity for the PET scans was approved by the Administration of Radioactive Substances Advisory Committee, United Kingdom.

3.1.2.2: Imaging protocol

[^{11}C]choline was synthesised at Hammersmith Imanet® according to the method described by Pascali et al (Pascali 2000). To minimise post-biopsy effects, all imaging studies were performed at least 6 weeks after the transrectal biopsy. Subjects were asked to fast for 6 hours prior to the procedure (as bowel choline uptake interferes with interpretation of [^{11}C]choline images). All patients were scanned on a PET/CT (GE-Discovery RX®) scanner after being positioned such that the field of view (FOV) included the whole pelvis and the lower abdomen. This was followed by a diagnostic

quality CT scan (settings were; 300 mA, 120kVp, 0.8 sec/rotation i.e. 65 mAs, 8 x 2.5mm slices and pitch 1.35) which was used for attenuation correction and co-registration with the PET images. [^{11}C]choline was administered by a bolus intravenous injection over 10 to 30 seconds. PET scanning (3-dimensional acquisition) was commenced over 2 bed positions (3 minutes per bed position) starting from the distal margin of the pelvic floor, covering the pelvis and lower abdomen (axial FOV per bed position, 15.7 cm; transaxial, 70 cm) for 65 minutes. Raw PET data were corrected for scatter and attenuation, and reconstructed with an iterative OSEM (ordered subset expectation maximum) algorithm comprising 8 iterations and 21 subsets. Decay corrected images were then viewed using Analyze® software (Analyze Version 7; Biomedical Imaging Resource, Rochester, MN, USA). From summed images, regions of interest (ROIs) were drawn manually around visible tumours in the prostate, and any visible pelvic nodes. The [^{11}C]choline radioactivity concentration within the ROIs was then determined and normalised for injected radioactivity and body weight to obtain SUV. The average and maximum SUV at 60 minutes ($SUV_{60,ave}$, and $SUV_{60,max}$) were determined. Due to the rapid systemic metabolism of [^{11}C]choline (Kenny, Contractor et al. 2010), SUV has also been determined at an earlier time point ($SUV_{15,ave}$, and $SUV_{15,max}$).

3.1.2.3: MRI acquisition

All patients underwent standard non-contrast staging MRI of the pelvis from aortic bifurcation to pubic symphysis comprising of T1-weighted axial images; axial, sagittal and coronal T2-weighted images and small FOV axial T2-weighted images through the prostate. The imaging was performed on a 1.5 Tesla Philips scanner in 5 patients and a 1.5 Tesla Siemens-Magnetom scanner in 21 patients.

3.1.2.4: Extended Laparoscopic extra-peritoneal Pelvic Lymphadenectomy (eLPL)

This was performed in a standard pre-defined protocol by the Urologists within an average of 22 days (2-49 days) of the [^{11}C]choline PET/CT. Nodal status was discussed with the surgeon before lymphadenectomy using information from both MRI and the [^{11}C]choline PET/CT images. The eLPL included nodes along the external and internal iliac vessels to the ureter proximally, obturator nerve medially and the genitofemoral nerve laterally. All nodes removed were carefully labelled for size and anatomical location. Nodes were fixed, paraffin embedded, stained with haematoxylin and eosin and reported as negative or positive for metastasis by a histopathologist with a specialist interest in urologic malignancy. The samples were also subjected to additional immunohistochemistry with Ki67 and CHKα (*vide infra*).

3.1.2.5: Image interpretation

The images of the [^{11}C]choline PET/CT were interpreted prospectively in order to outline the ROIs, perform SUV analysis and discuss outcome with surgeons pre-operatively. Furthermore, all the imaging data (MRI, [^{11}C]choline PET and [^{11}C]choline PET/CT were pooled and evaluated by a dual accredited nuclear medicine radiologist, blinded to the results of the histopathology, on separate occasions to avoid reporting bias. Any discrepancy between the two observers was resolved by a consensus reading. The criteria for nodal involvement on the PET only images were any focal uptake outside the normal physiological distribution of tracer in locations which corresponded to LN chains. For the PET/CT images, nodes with increased tracer uptake above background were considered positive for metastatic spread, even when they were <10mm in short-axis diameter. The site and size of nodes with increased

uptake were noted. In addition the level of diagnostic confidence for the PET and fused PET/CT scans was indicated on a five-point scale:

i) Definitely normal

ii) Probably normal (more likely to be physiological)

iii) Indeterminate (equally likely to be pathological or physiological)

iv) Probably abnormal (more likely to be pathological)

v) Definitely abnormal.

For subsequent analysis definitely normal, probably normal and indeterminate were considered benign and probably abnormal and definitely abnormal were considered malignant.

For MRI analysis the short-axis and long-axis diameters of the identifiable LNs were measured using electronic callipers on the scanner console. The criteria used for the node diagnosis on MRI were size ratio criteria - nodes less than 8 mm short axis were considered benign, nodes more than 10 mm short axis were considered metastatic, and for nodes with a short axis between 8 and 10 mm, if the ratio of the short to long axis was more than 0.8 (i.e., a round node), the node was considered positive (Jager, Barentsz et al. 1996; Harisinghani, Barentsz et al. 2003). The following 5 point scale was used for ROC curve analysis of MRI:

i) Nodes <4mm or not seen

ii) Nodes = 4 – 5.9 mm

iii) Nodes = 6 – 7.9 mm

iv) Nodes ≥ 8mm but <10mm

v) Nodes ≥ 10mm

3.1.2.6: Blood sampling and [^{11}C]choline metabolite analysis

The concentration of [^{11}C]choline in venous blood was measured from discrete blood samples taken at 2.5, 5, 10, 30 and 60 minutes after [^{11}C]choline injection. The relative contributions of [^{11}C]choline parent fraction and its metabolite, [^{11}C]betaine, were determined using reverse-phase high-performance liquid chromatography as previously described (Contractor, Kenny et al. 2009).

3.1.2.7: Modelling of PET data

Within the PET imaging time window (65 min), tumour [^{11}C]choline uptake is a function of perfusion, and transport of the radiotracer from the extracellular space into cells, where it is either phosphorylated into phosphocholine or oxidised to betaine. Notably, incorporation of phosphocholine to membrane phosphatidylcholine is negligible within this time window (Yoshimoto, Waki et al. 2004; Bansal, Shuyan et al. 2008; Kuang, Salem et al. 2010). Chromatographic analysis also indicates that further betaine metabolism or conversion of choline to acetylcholine is negligible (Leyton, Smith et al. 2009). Hence radiotracer uptake broadly represents transport and phosphorylation on the one hand, and transport and oxidation on the other.

The full arterial blood data available from the [^{11}C]choline PET breast data have been explored and the information has been used to predict the performance of a limited sampling venous data set in prostate cancer patients.

3.1.2.7.1: Kinetic modelling of [^{11}C]choline PET breast data

The aim was to evaluate the specificity of [^{11}C]choline uptake and understand the role of choline metabolism in tumours through kinetic modelling of PET data. This evaluation was used to test the hypothesis that altered choline transport and choline oxidation could confound the specificity of [^{11}C]choline uptake in tumours.

The raw image data of 18 patients (8 primary and 10 metastatic cases) who had [^{11}C]choline PET scans, from previous published data of Dr Contractor (Contractor, Kenny et al. 2011) were completely re-analysed for this thesis with his prior permission. The primary and metastatic lesions were manually outlined using the Analyze™ software (Analyze Version 7; Biomedical Imaging Resource, Rochester, MN, USA). The average [^{11}C]choline SUV normalised to body weight at 60 minutes: $SUV_{60,ave}$, in the VOIs was calculated from the tissue radioactivity concentrations. The kinetic rate constants were determined by 2-tissue irreversible (3k) and 2-tissue reversible (4k) compartment modelling and the best model fit assessed. The [^{11}C]choline kinetic variable, Ki representing the net irreversible uptake of the radiotracer at steady state, was derived by Graphical analysis using in-house software. In addition, Spectral analysis of tumours was done to derive the IRF_{60} as well as FRT. The exponential range of base ($\log_{10}\beta$) used during analysis was from 0 to -3.24, with the minimum value -3.24 being the $\log_{10}$ of the decay constant λ for [^{11}C]choline. IRF_1 (the relationship between parent plasma radioactivity and tissue radioactivity at 1 minute) was used instead of the intercept of the IRF curve due to high noise variance of IRF at zero time (IRF_0) shown previously in a study (Cunningham and Jones 1993). Comparisons were done on a lesion by lesion basis for tumours. Descriptive statistics

were used to report SUV, Ki and FRT. Comparison of PET variables between primary and metastatic tumours was done using the Mann-Whitney test.

Results

Primary and metastatic tumours (total of 29 lesions from 18 patients) were well visualised with the steady state of tissue [^{11}C]choline concentration achieved in approximately 20 minutes post injection of [^{11}C]choline and showed a good retention up to 60 minutes post injection (**Figure 16**). The mean (± SD) $SUV_{60,ave}$ in primary, locally recurrent and metastatic lesions was 2.64 (± 0.9), 5.47 (± 1.41) and 3.43 (± 1.27) respectively.

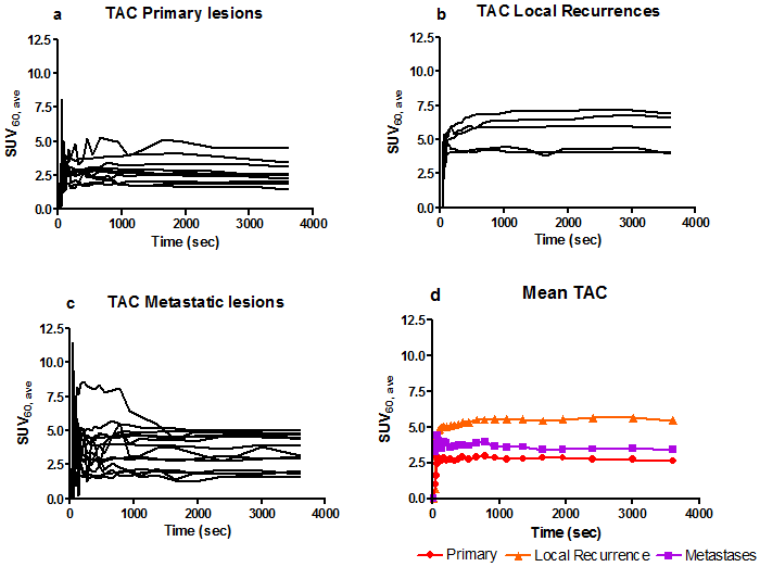

Figure 16: **Decay corrected time activity curves of [^{11}C]choline** in **(a)** Primary (n=10), **(b)** Locally recurrent (n=5), **(c)** Metastatic lesions (n=14) and the **(d)** mean TACs. The SUV is higher for the locally recurrent tumours and lowest for the primary tumours.

The 3k and 4k model were equivalent in terms of comparison of weighted akaike information criterion (AICw) and residual sum squares (RSS) for individual primary, nodal and bone metastases ($p>0.05$, Mann-Whitney test). However, in the 5

locally recurrent lesions the kinetics was better explained by the 4k model, suggesting that there could be dephosphorylation of the phosphocholine. The different rate constants derived by the 4k model in the primary, locally recurrent and metastatic lesions are shown in **Figure 17**. The average rate constants were K1 = 0.003553 mL/g/min, k2 = 0.011862 min^{-1}, k3 = 0.004799 min^{-1} and k4 = 0.0002078 min^{-1}. The k2 was high with a low k4. This high k2 could suggest that there is betaine efflux from the tumour cells (i.e. k2= very low, but k2'= high) hypothesizing that betaine is produced in the tumour tissues even in humans.

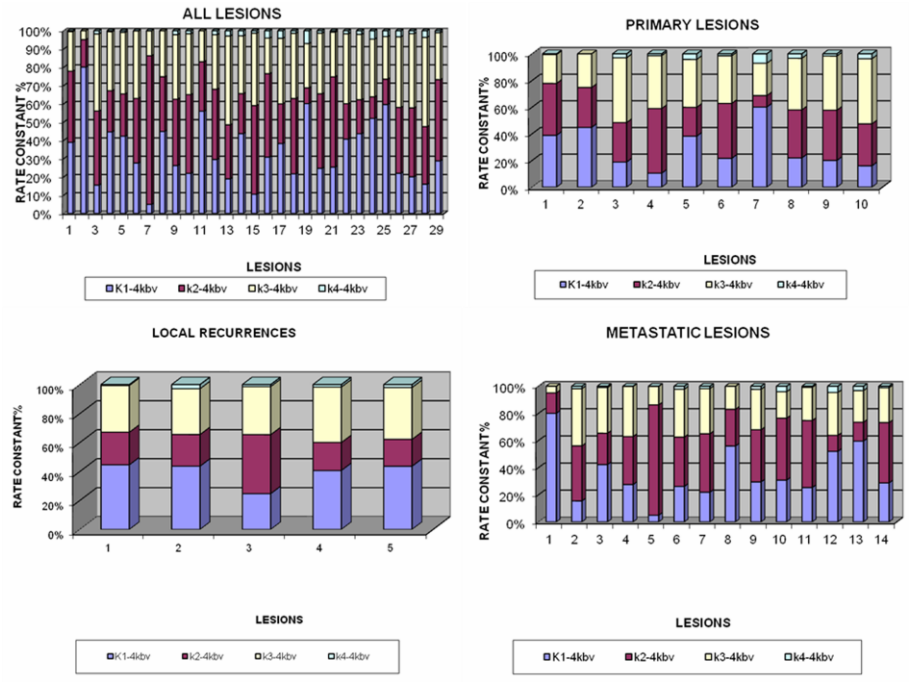

Figure 17: The proportion of K1, k2, k3, k4 in the primary, locally recurrent and metastatic lesions calculated from the 4k model.

There appears to be a negligible k4 but a higher k2.

The model fits obtained by the modified Patlak method were acceptable with low SD of the goodness of fit (**Figure 18**). The median $Ki_{mod\text{-}pat}$ in primary tumours (8.17

x 10^{-4} mL plasma/mL tissue/sec) was significantly lower (p=0.004) than the median $Ki_{mod\text{-}pat}$ in the locally recurrent tumours (20.93 x 10^{-4} mL plasma/mL tissue/sec), but not significantly lower (p=0.46) than the metastatic lesions (10.44 x 10^{-4} mL plasma/mL tissue/sec). The high median $Ki_{mod\text{-}pat}$ in the locally recurrent lesions is indicative of an irreversible kinetic component, suggesting that the appearance of the recurrences is driven by CHK activity.

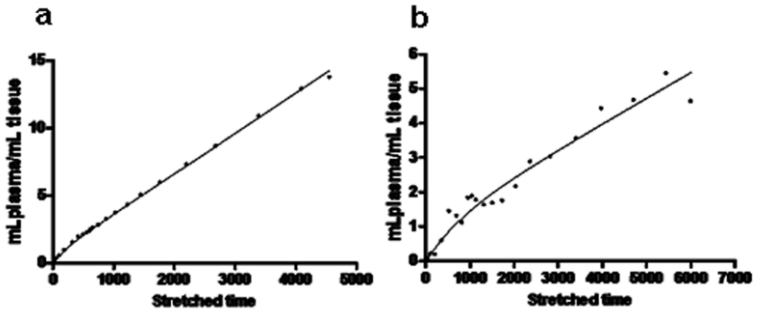

Figure 18: Modified Patlak plots of tumour [^{11}C]choline activity modelled with the metabolite corrected parent plasma IF.
(a) Good fit using the modified Patlak model, **(b)** noisy fit seen in a metastatic axillary node from breast cancer.

Spectral plots showed fast and slow kinetics including kinetic components corresponding to irreversible uptake in tumours (at -3.24; λ) and reversible components (~0) blood volume (**Figure 19**). Tumour tissue fits were good with low RSS. The median FRT for primary, locally recurrent and metastatic tumours was 0.48, 0.63 and 0.57 respectively. The FRT in primary tumours was not statistically different (p=0.06) from FRT of locally recurrent lesions or metastatic tumours (p=0.84) (**Figure 20**). However IRF_{60} was significantly higher in locally recurrent tumours compared to primary tumours (p=0.003). This suggests that there could be more metabolism of

choline to betaine in the metastatic lesions (low IRF_{60}) and that the growth of metastases could be driven by pathways other than by choline kinase.

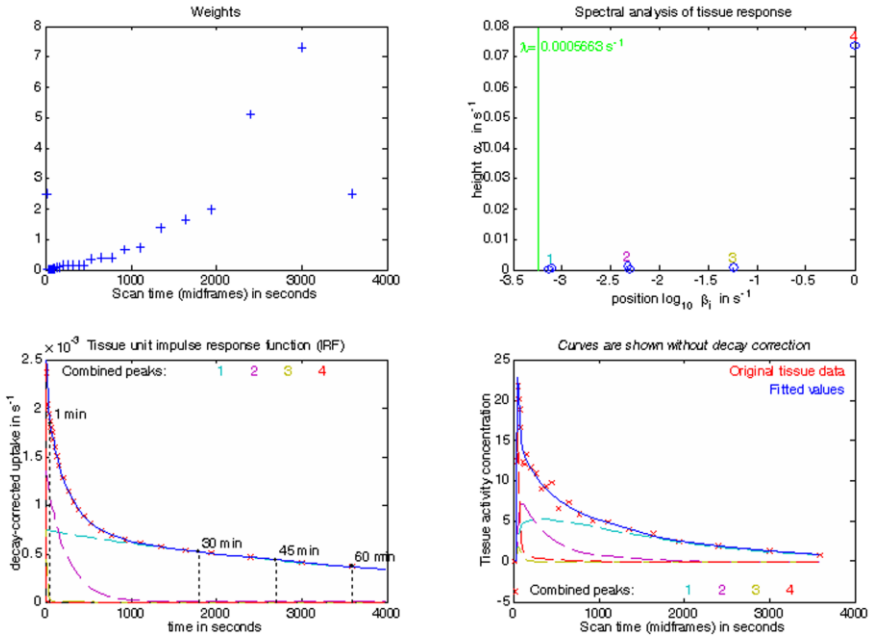

Figure 19: **Spectral analysis of [^{11}C]choline in tumours showing IRF and spectra of modelled responses of a representative patient.**

Slower spectra signify irreversible kinetics (closest to λ) whereas fast kinetics signifies reversible kinetics signifying blood volume flow around tumour.

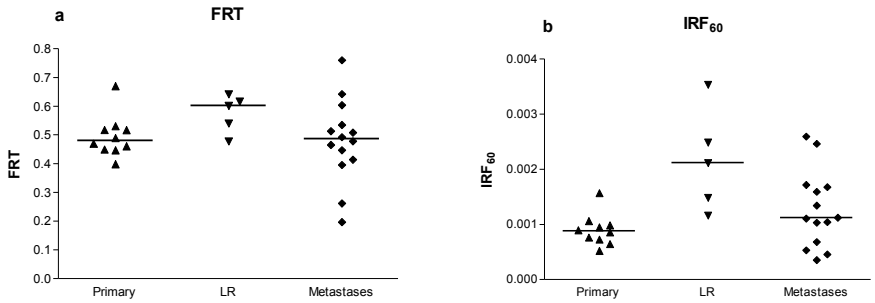

Figure 20: FRT and IRF.

Differences between a) FRT and b) IRF_{60} of primary, locally recurrent (LR) and metastatic lesions from Spectral analysis.

3.1.2.7.2: Kinetic modelling of [^{11}C]choline PET prostate data

A population-based total plasma input function $C^{TOTAL}_{POP}(t)$ was derived from the [^{11}C]choline breast cancer data set discussed in the previous section (Contractor, Kenny et al. 2011), by averaging the measured arterial plasma concentration time course after normalisation by injected dose and body weight. An approximated input function for each subject was then derived by fitting the ratios between measured venous plasma samples and corresponding values of $C^{TOTAL}_{POP}(t)$ to a quadratic function g(t) as per equation 7.

$$C^{TOTAL}_{INDVID}(t) = C^{TOTAL}_{POP}(t) \times g(t) \qquad \textbf{Equation 7}$$

The parent fraction measured in the venous samples was then fitted to a sigmoid function (Gunn, Yap et al. 2000) as per equation 8.

$$pf(t) = 1 - \frac{X_1 + X_2 t_i}{\left(X_3 / t_i\right)^{X_4} + 1} \qquad \textbf{Equation 8}$$

The individual plasma concentrations of the parent [^{11}C]choline (C^{PARENT}_{INDVID}) and the metabolite [^{11}C]betaine (C^{METAB}_{INDVID}) were, respectively, obtained as

$$C^{TOTAL}_{INDVID}(t) \times pf(t) \quad \text{and} \quad C^{TOTAL}_{INDVID}(t) \times [1 - pf(t)] \qquad \textbf{Equation 9}$$

The modified Patlak plot (Mankoff, Shields et al. 1996), which takes account of plasma metabolites of [^{11}C]choline, as well as labeled metabolites within the exchangeable space in tumour, was used to derive Ki ($Ki_{mod\text{-}pat}$); a measure of the net irreversible retention at steady state within a VOI. The method implicitly assumes that the majority of labelled betaine in tumours derives from systemic circulation (Roivainen, Forsback et al. 2000; Witney, Alam et al. 2012).

3.1.2.8: Immunohistochemistry

The CHKα staining was initially performed using the immunofluorescence (IF) method. However, there was difficulty in differentiating and interpreting the glandular architecture on these slides. Therefore a conventional IHC method was pursued and developed. The labelled streptavidin-biotin (LSAB) method was used (**Figure 21**). This involved the use of a biotinylated secondary antibody that links primary antibodies to a streptavidin-peroxidase conjugate (Chilosi, Lestani et al. 1994). As part of the protocol development, the CHKα primary antibody was optimised on human bronchus samples to determine the appropriate antigen retrieval method (heat induced retrieval in a citrate for 20 min) and the antibody dilution (1 in 75). The secondary antibody and peroxidase conjugation used were kit based.

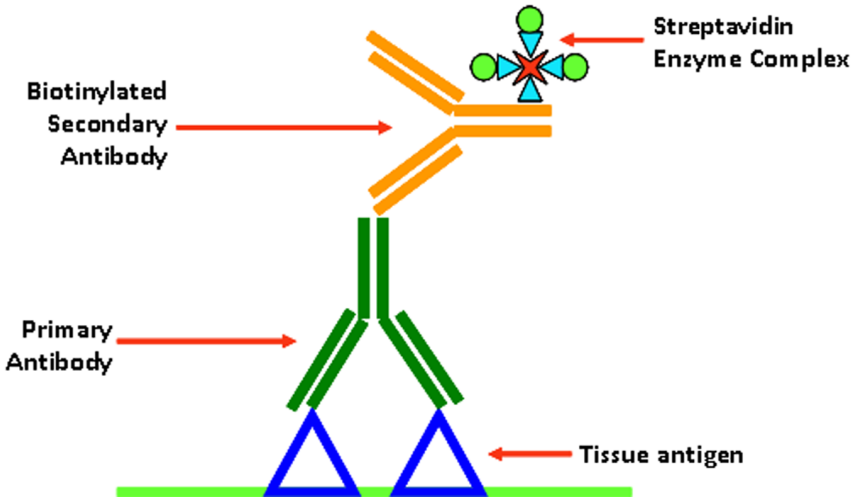

Figure 21: Labelled Streptavidin Biotin (LSAB) method.
This uses a biotinylated secondary antibody that links primary antibodies to a streptavidin-peroxidase conjugate.

3.1.2.8.1: Material analysed

Twenty prostate tumour cores, 7 metastatic pelvic node sections from the 26 patients, and 9 prostate tumour cores from 10 patients in the study discussed in chapter 4 were analysed (total 29 tumour cores and 7 nodal sections). All the tumour paraffin fixed sections were initially deparaffinised in xylene and then serially dehydrated using decreasing grades of ethanol (100 – 70%).

3.1.2.8.2: CHKα Immunofluorescence

The sections were subjected to heat-induced antigen retrieval pre-treatment with sodium citrate buffer, pH 6.0, in a water bath at 100^0 Celsius for 20min. The sections were left to cool for approximately 10 min at room temperature and washed in running water. Endogenous peroxidase was neutralised with 3% hydrogen peroxide for 10 minutes. The sections were washed twice in TRIS buffered saline (TBS) for 5 min each. Non-specific binding was blocked by incubating with a blocking buffer (1% bovine serum albumin (BSA) and 10% foetal calf serum (FCS)) for 1h. Incubation with primary antibody took place at 4^0C overnight in a humidified chamber with a mouse CHKα primary antibody (1:50 dilution; Abcam, Cambridge, UK, catalogue no ab38290). Human bronchus was used as positive control. The sections were then washed with TBS and incubated at room temperature with secondary antibody (1:400 dilution, Alexa Fluor® 594 goat anti-mouse antibody (Invitrogen, catalogue no A11005, Paisley, UK), for 1 hour and counter-stained with DAPI (ProLong® Gold Antifade, Paisley, UK) to stain the nuclei. Then cover slips were mounted using a mounting solution and sections visualised using red, blue and green filters. Areas of immunoreactivity were red and the

nuclei, blue. If there was nuclear staining with CHKα it stained pink. Negative control was obtained by omitting the primary antibody, replacing it with TBS+BSA.

3.1.2.8.3: CHKα Immunohistochemistry

After antigen retrieval and quenching endogenous peroxidase activity as described above, the sections were washed twice in TRIS buffered saline-Tween (TBST) for 5 min each. Non-specific binding was blocked by incubating with a blocking buffer (5% BSA and 5% goat serum) for 1h. Incubation with primary antibody took place at 4^0C overnight in a humidified chamber with a polyclonal rabbit anti-human CHKα primary antibody (1 in 75 dilutions: catalogue No HPA024153, Sigma-Aldrich™, Dorset, UK). Human bronchus was used as positive control. The sections were then washed with TBST, and for subsequent reaction, a labelled streptavidin biotin (LSAB) kit (Novocastra™, Newcastle Upon Tyne, UK) was used. Biotinylated secondary antibody (anti-mouse and anti-rabbit) was added to the slides and incubated at room temperature for 60 minutes in a humidified chamber. The slides were again washed and incubated with streptavidin peroxidase for an additional 30 minutes. The peroxidase activity was developed with the substrate, 3, 3'-diaminobenzidine (DAB) chromogen for 5 minutes. Tissues were counterstained with haematoxylin for one minute and dehydrated with absolute ethanol and xylene. Then cover slips were mounted using a mounting solution and sections examined by light microscopy. Areas of immunoreactivity were brown and nuclei, blue (haematoxylin). Negative control was obtained by omitting the primary antibody and replacing with TBST+BSA (**Figure 22**). Tumour slides were then independently scored. The intensities were scored as: 1+, mild intensity; 2+, moderate intensity; 3+, high intensity, including nuclear staining as compared to the positive control.

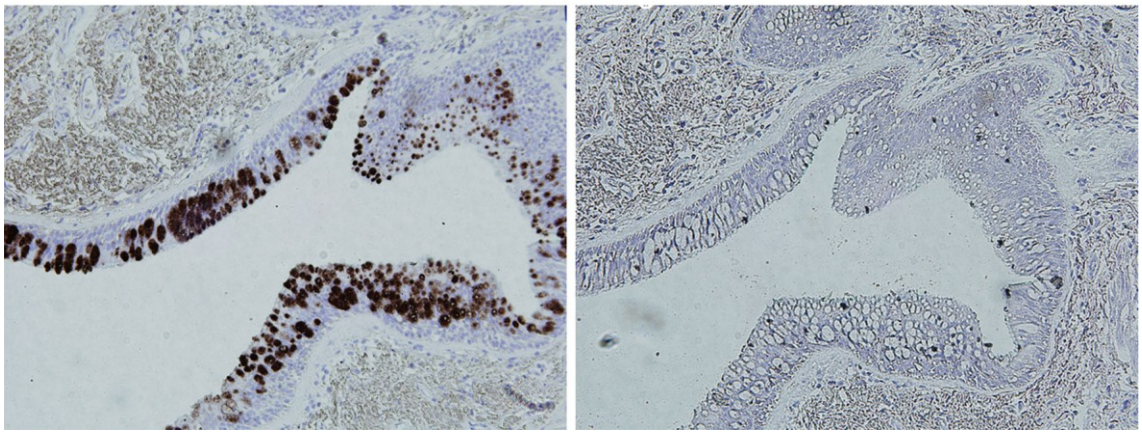

Figure 22: **CHKα immunostaining in the human bronchial tissue.**
It was used as a positive control. Note brown staining in the positive control and lack of staining in the negative control. Magnifications of 200X.

3.1.2.8.4: Ki67 labelling index

After antigen retrieval, quenching endogenous peroxidase activity and blocking non specific binding as described above, sections were incubated with the primary antibody (1 in 200 dilutions: mouse Anti-Ki-67 antibody, Ki-67-MM1, Dako, Denmark) for 1 hour at room temperature. Human tonsil tissue was used as a positive control. The sections were then washed with TBST, and for subsequent reaction, a labelled streptavidin biotin (LSAB) kit (Novocastra^{TM}, Newcastle Upon Tyne, UK) was used according to the manufacturer's instructions. Finally, the slides were stained with weak haematoxylin before viewing. Areas of immunoreactivity with brown nuclear staining were positive for Ki67. The numbers of total tumour cells and positive Ki67 cells were then manually counted in four randomly selected tumour fields of view. The Ki67 labelling index (expressed as a percentage) was calculated as the ratio of Ki67 positive tumour cells to total tumour cells.

3.1.2.8.5: Haematoxylin and Eosin (H&E) staining

After deparaffinisation, the adjacent sections to those used for CHKα IHC were stained in haematoxylin for 10 minutes and washed in running water. They were then dipped in 1% acid alcohol, washed in running water and dipped in Scott's tap water substitute for 30 sec. The sections were then stained with 1% Eosin for 5 minutes and washed in water. After dehydration with industrial methylated spirit and xylene, cover slips were mounted using a mounting solution and sections examined by light microscopy. The nuclei are stained blue and eosin counter-stains the cytoplasm and different types of connective tissue fibres with differing shades of pink.

Photomicrographs were obtained using BX51 Olympus microscope (Olympus Optical, Tokyo, Japan) at 200x and 400x magnifications.

3.1.2.9: Statistical considerations

The sample size for the study took into consideration two cohorts of patients with prostate cancer. The first cohort involved cases of locally advanced prostate cancer with no visible nodes on MRI/CT but with greater than 30% chance of pelvic nodal disease based on Roach's formula (Roach 1993) . The second cohort consisted of those patients with nodal disease (> 1cm) present on MRI (assuming a 70% sensitivity of MRI in detecting nodal disease (Harisinghani, Barentsz et al. 2003)). The prevalence of overt nodal disease present on staging CT/MRI in clinical practice is much less than that of high risk localised prostate cancer. In the local hospital clinical practice it was evident that approximately three times more high risk disease cases were seen on average compared to those with overt node positive disease. Therefore, if for example 21 patients from the high risk group were recruited, there would be a 1 in

3 chance of finding positive lymph nodes on nodal dissection, i.e.; 7 patients. Correspondingly, if 7 patients with node positive disease on their staging MRI/CT were recruited, this would be sensitive in ~75% of cases, i.e.; 5 patients (assuming the maximum sensitivity of MRI to be ~75%). Thus 28 patients (21 pts + 7 pts) would give a reasonable chance of finding at least 12 node positive patients at the time of nodal dissection.

The mean, standard deviation (SD), medians, range, and frequencies were used as descriptive statistics. The sensitivity, specificity and number of correctly recognised cases with MRI, [^{11}C]choline PET and [^{11}C]choline PET/CT in nodal detection were calculated for per patient and per node analysis. The comparison of each imaging method was performed using the McNemar test implemented in its uncorrected exact form, based on the binomial distribution (Hawass 1997). Receiver operating characteristic (ROC) analysis and the area under the curve (AUC) was determined by recalculating sensitivity and specificity for MRI, PET and PET/CT along the five-point grading scale for a per patient and a per nodal analysis using MedCalc statistical software (version 11.6.1, Mariakerke, Belgium). $SUV_{60,ave}$ and $SUV_{60,max}$ were compared with CHKα and Ki67 scores using Spearman's correlation test and a p value of ≤ 0.05 was considered significant.

3.1.3: Results

3.1.3.1: Patients

Twenty eight patients underwent [^{11}C]choline PET/CT after fulfilling the inclusion criteria. Two patients could not undergo surgery after [^{11}C]choline PET/CT as one

became unwell and the other changed his mind about undergoing surgery. Thus 26 patients underwent [^{11}C]choline PET/CT followed by eLPL/ sampling (one had LN sampling rather than dissection due to fibrotic and calcified lymph nodes). All patients subsequently had neo-adjuvant androgen deprivation followed by radical radiotherapy to the prostate and the pelvis. The median (mean; range) age of subjects was 67 years (67.7; 51 to 83 years), Gleason score of primary prostate biopsies was 7 (7.6; 6-9) and the pre-treatment PSA levels were 26.25 (44.25; 8.1 – 209).

The interval between the [^{11}C]choline PET/CT and eLPL was an average of 22 days (2-49 days). From the 26 patients, a total of 406 pelvic LNs sampled were available for pathology, with a median of 16 (range 3-36) nodes harvested per patient. 27 (6.7%) involved pelvic nodes at eLPL were detected in 9 patients (**Table 9**). Of the involved nodes 17 out of the 27 LN were less than 10 mm in size. The average nodal size of the histologically positive nodes was 9.8 mm with an average tumour focus of 5.7mm. The [^{11}C]choline PET/CT was well tolerated with no immediate or delayed complications observed.

3.1.3.2: [^{11}C]Choline uptake within the malignant prostate and pelvic nodes

In addition to visualisation of nodal uptake, primary prostate tumours in all 26 patients were well visualised with good tumour-to-background ratios (**Figure 23 and 24**). The median (mean ± SD; range) $SUV_{60,ave}$ and $SUV_{60,max}$ were 4.85 (4.92 ± 1.75; 2.19-9.28) and 9.97 (11.05 ± 3.72; 4.73-20.54) respectively (median $SUV_{15,ave}$ and $SUV_{15,max}$ were 4.82 and 8.80 respectively; **Figure 25**). Dynamic time versus radioactivity curves (TAC's) for [^{11}C]choline in primary prostate tumours and the nodal metastases demonstrated a good retention of activity after plateauing (achieving a

steady state) at ~15 min until 60 min with SUV_{ave} (**Figure 26, 27**). However, with SUV_{max} there is a suggestion of increasing activity at 60 min which may be due to the contribution of [^{11}C]betaine.

There was a good linear fit of the modified Patlak plots suggesting net retention of [^{11}C]choline. The median (range) $Ki_{mod\text{-}pat}$ variables in the primary tumours, TP pelvic nodes and detected inguinal nodes were 0.095 mL/min/cm^3 (0.03-0.23), 0.05 mL/min/cm^3 (0.021-0.18) and 0.021 mL/min/cm^3 (0.006-0.08), respectively. A significant association was seen between the $Ki_{mod\text{-}pat}$ and tumour [^{11}C]choline uptake when the imaging variable was $SUV_{60,ave}$ (Spearman's r=0.9, p<0.0001) $SUV_{60,max}$ (r=0.8, p<0.0001). This association was seen even at earlier time points ($SUV_{15,ave,}$ $SUV_{15,max}$).

Table 9: **Characteristics of patients with histologically positive nodes (9/26) and false positive nodes on PET/CT**

Pt No	Age	GS	iPSA	cT	pN	No of + LN	Site of + LN	MRI	Size (mm)		PET		PET/CT	Size (mm)	
1	73	7	8.54	T3a	N1	1	1-R Obt	R Obt	11	TP	1-R Obt	TP	R Obt	11	TP
10	82	8	13.5	T3	N1	5	3-R Obt, 1-R II, 1-R GF	2-R EI	21,8	TP	3-R EI	TP	3-R EI	20,11,7	TP
13	56	7	50	T1c	N1	1	1-L Obt			FN		FN			FN
15	65	9	209	T2b	N1	7	4-L EI, 3-R II	R II	19	TP	1-L EI, 3-R II	TP	1-L EI, 3-R II	9,18,11,5	TP
17	76	7	169	T4	N1	1	1-R Obt	L Obt	9	FP	R Obt	TP	R Obt	9	TP
20	76	7	21	T2b	N1	1	1-R Obt			FN	R Obt	TP	R Obt	4	TP
24	61	9	45	T3	N1	8	1-R II, 2-R Obt, 3-L EI, 2-L Obt			FN	1-R Obt	TP	1-R Obt, 2-R II	6,6,4	TP
25	76	9	24.5	T2b	N1	2	2-R EI			FN		FN			FN
27	51	7	44.8	T3b	N1	1	1-L II	L II	10	TP		FN	L II	10	TP
Mean	**68.44**	**7.8**	**65.04**						**13.8**					**9.4**	
Median	**73**	**7**	**44.8**						**11**					**9**	
	False Positives														
1	73	7	8.54	T3a	N1			L Obt	6	TN	L Obt	TN	L Obt	6	FP
								R EI	7	TN	R EI	FP	R EI	7	FP
11	70	7	8.1	T2	N0			R EI	7	TN	R EI	FP	R EI	12	FP
								L EI	10	FP	L EI	FP	L EI	10	FP
21	64	6	12	T3a	N1			R EI	26	FP	R EI	FP	R EI	26	FP
26	69	7	8.2	T2a	N1			L Obt	10	FP	L Obt	FP	L Obt	10	FP

GS-Gleason score; iPSA- initial prostate specific antigen; cT-clinical tumour stage; pN-pathological nodal stage; LN-lymph node; R-right; L-left; Obt-obturator; EI-external iliac; II-internal iliac; GF-genitofemoral; TP-true positive; FN-false negative; FP-false positive; + - positive.

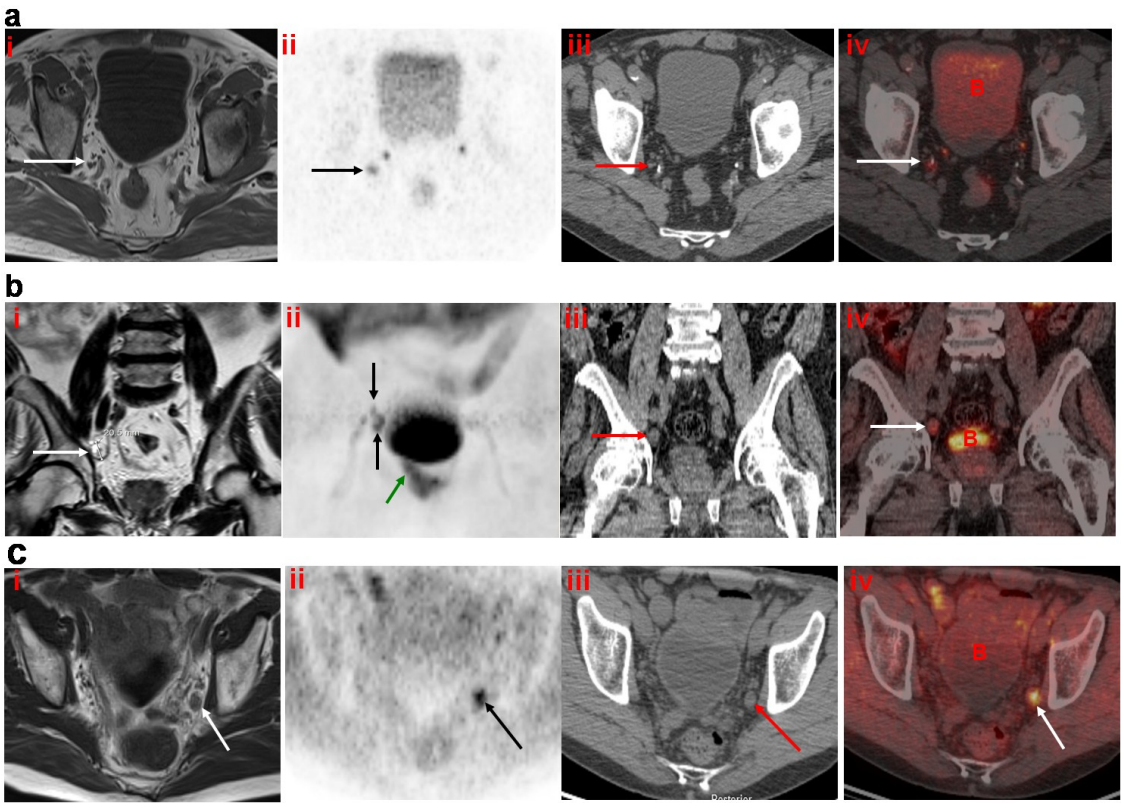

Figure 23: **T1 weighted MRI (i), Axial [^{11}C]choline PET (ii), CT (iii), and fused PET/CT (iv) showing uptake in pelvic nodes.**

(a) Focal uptake seen in a 4mm right obturator node (arrowed) clearly separate to the ureter on the PET only **(ii)**. In retrospect visible on MRI **(i)** but not called as well below size criteria, (**b)** Coronal T2 weighted MRI **(i)**, [^{11}C]choline PET Maximum Intensity Projection (MIP) **(ii)**, CT **(iii)**, and PET/CT fused (**iv)** shows focal uptake in cluster of right external iliac nodes (arrowed). Note uptake in prostate extending to seminal vesicle (green arrow on coronal MIP), (**c)** T1 weighted MRI **(i)** axial [^{11}C]choline PET **(ii)**, CT **(iii)**, and PET/CT fused **(iv)** shows focal uptake in 10 mm left obturator node (arrowed) which was false positive.

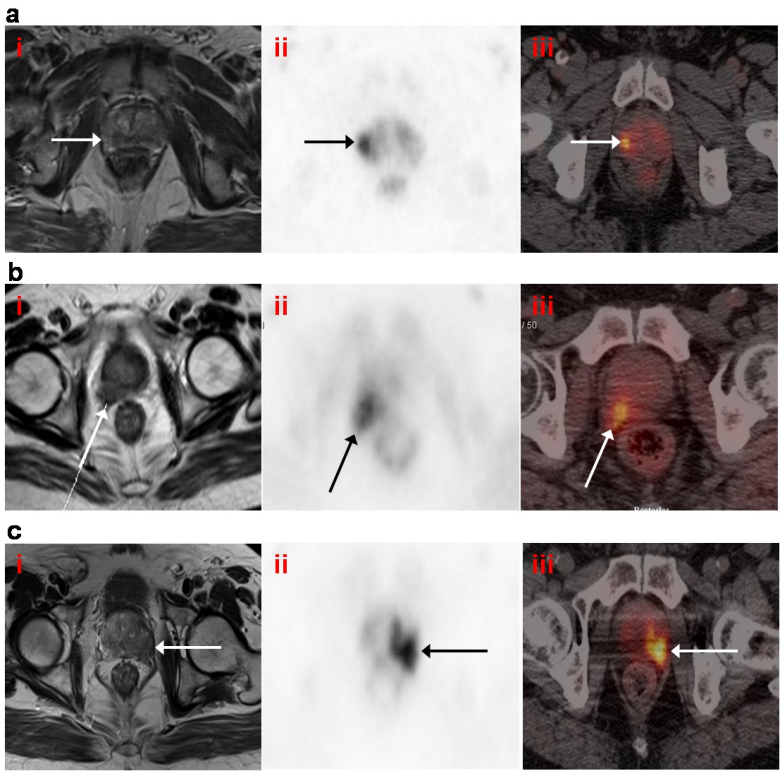

Figure 24: **T2 weighted MRI (i), Axial [^{11}C]choline PET (ii) and fused PET/CT (iii) showing uptake in the prostate and Seminal vesicles.**

(a) Focal uptake in the prostate (arrowed), (**b)** right seminal vesicle involvement (arrowed), (**c)** capsular breech (T3a disease) on the left (arrowed).

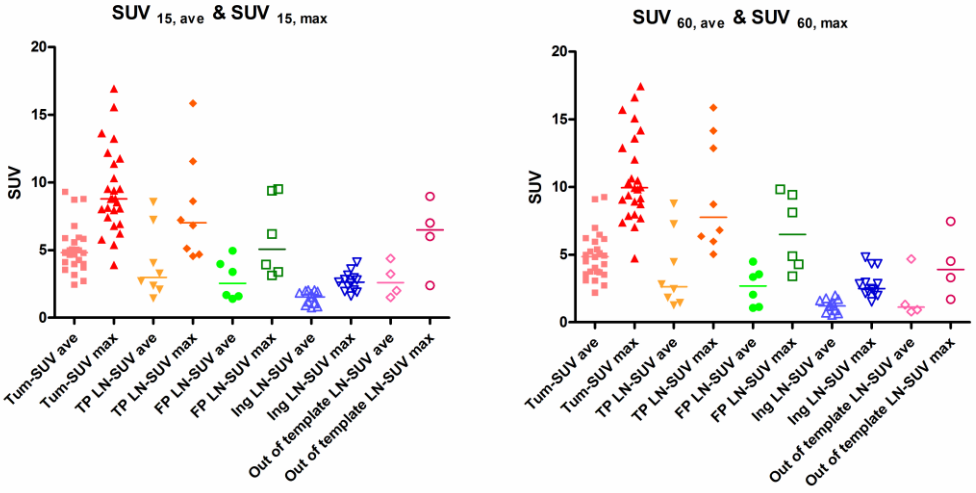

Figure 25: **SUV_{ave} and SUV_{max} at early and late time points for primary prostate tumours and nodes.**

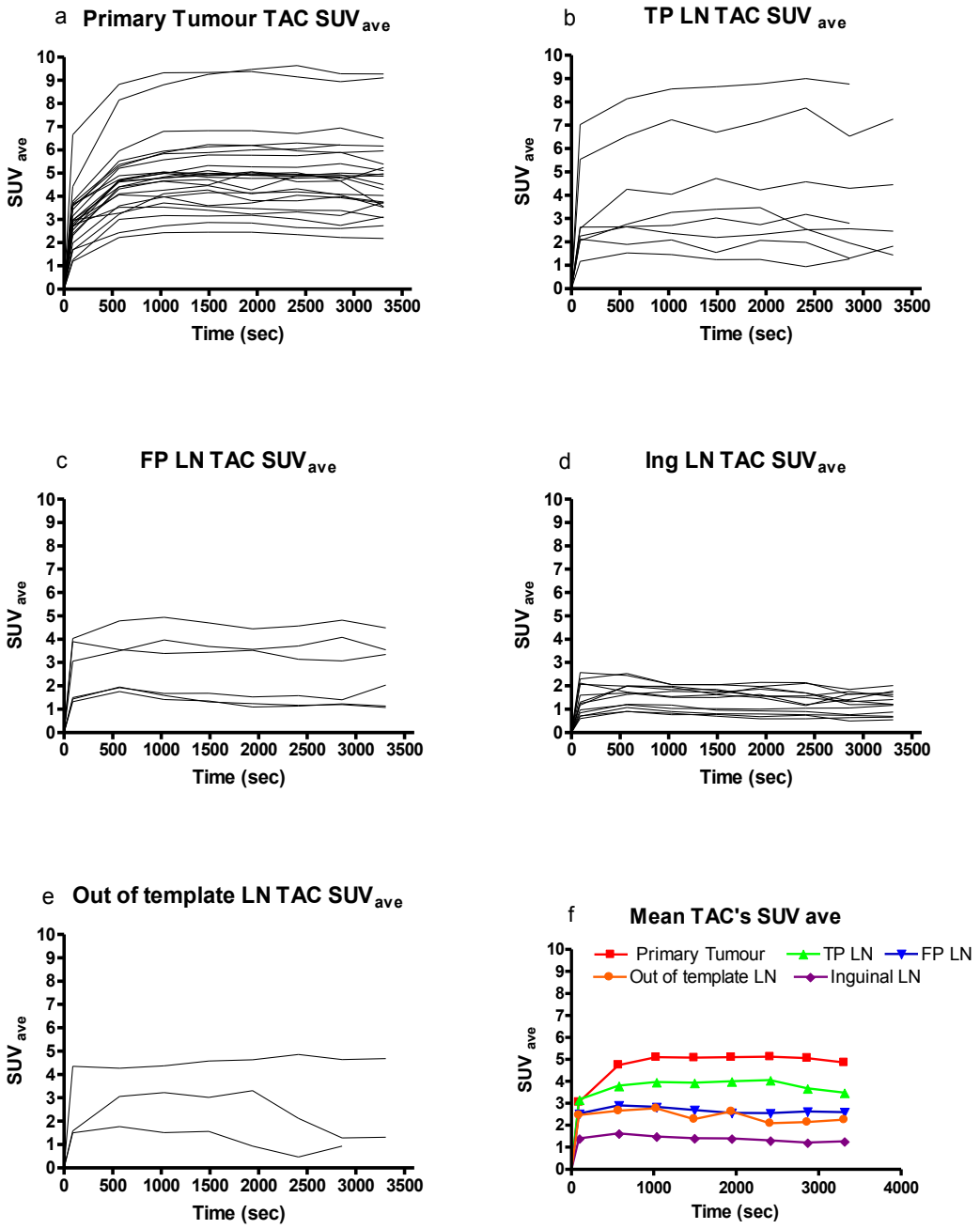

Figure 26: **[^{11}C]Choline SUV_{ave} TAC curves.**

Profiles in **(a)** primary prostate tumours, **(b)** true positive nodes, **(c)** false positive nodes, **(d)** inguinal nodes, **(e)** out of template (common iliac & para aortic) nodes and, **(f)** the mean TACs demonstrating a good retention of activity after plateauing after ~15 min.

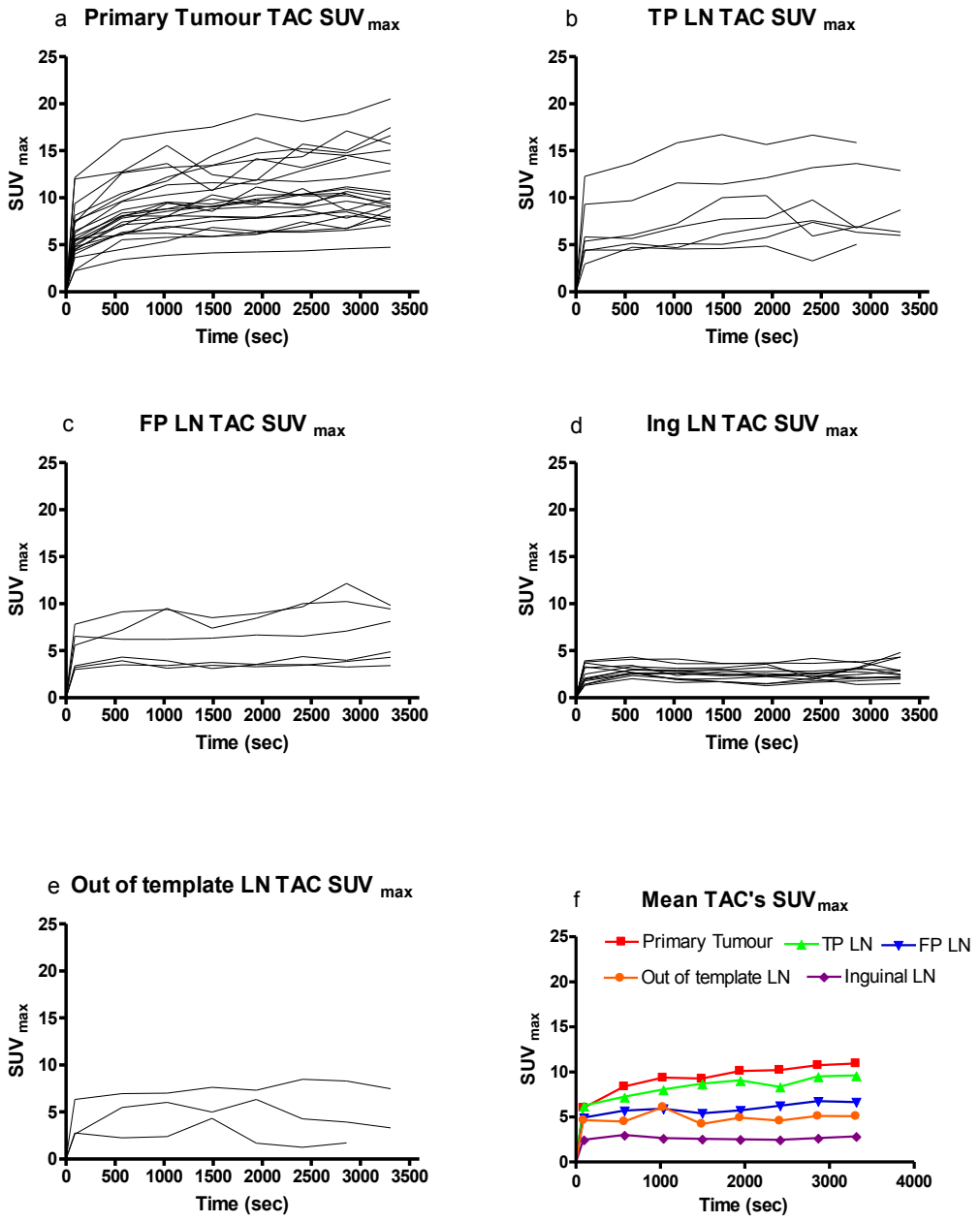

Figure 27: **[^{11}C]Choline SUV_{max} TAC curves.**

Profiles in **(a)** primary prostate tumours, **(b)** true positive nodes, **(c)** false positive nodes, **(d)** inguinal nodes, **(e)** out of template (common iliac & para-aortic) nodes and, **(f)** the mean TACs demonstrating a good retention of activity after plateauing after ~15 min. There is a hint of increasing activity at 60 min which may be due to contribution of [^{11}C]betaine.

3.1.3.3: Diagnostic performance of MRI, [^{11}C]choline PET and [^{11}C]choline PET/CT in detection of nodal disease

On a per patient basis, the sensitivity and specificity were 50 % and 72.2%; 66.7% and 76.4 % and 77.8% and 82.4% respectively for MRI, [^{11}C]choline PET and [^{11}C]choline PET/CT. On a per nodal basis the sensitivity and specificity were 18.5 % and 98.7%; 40.7% and 98.4 %; and 51.9% and 98.4% respectively for MRI, [^{11}C]choline PET and [^{11}C]choline PET/CT (**Table 10**). No statistical difference between any two modalities was detected in the patient analysis, mainly owing to the relatively low number of subjects. In the per nodal analysis the sensitivity was significantly improved with the use of [^{11}C]choline PET/CT (p=0.007) and [^{11}C]choline PET (p=0.07) compared to MRI imaging, without a decrease in the specificity (p= 1, 1 and 0.48 for [^{11}C]choline PET versus MRI, [^{11}C]choline PET/CT versus MRI and [^{11}C]choline PET/CT versus [^{11}C]choline PET comparisons, respectively).

ROC analysis (**Figure 28**) showed the overall diagnostic performance improved in the following order MRI < [^{11}C]choline PET < [^{11}C]choline PET/CT. **Table 11** shows the detection rate of MRI, [^{11}C]choline PET and [^{11}C]choline PET/CT for nodal metastases according to the diameter of the infiltrated LNs. A higher LN detection rate, including the detection of sub centimetre nodes, was seen with [^{11}C]choline PET/CT than MRI. The mean diameter of the positive LNs on histopathology was 9.8mm and that of the true positive LNs was 13.8 and 9.4 mm, respectively, on MRI and [^{11}C]choline PET/CT (using CT component for size definition).

Table 10: **Sensitivity & Specificity Analysis**

Imaging modality	Histology Positive		Histology Negative		Sensitivity (%) (CI)	Specificity (%) (CI)	PPV (%) (CI)	NPV (%) (CI)	+ LR (CI)	-LR (CI)
	TP	FN	FP	TN						
per Patient Basis										
MRI	4	4	5	13	50 (15.7 -84.3)	72.2 (46.5 - 90.3)	44.4 (13.7 - 78.8)	76.5 (50.1 -93.2)	1.8 (0.9 -3.8)	0.7 (0.3-1.9)
[11C]choline PET	6	3	4	13	66.7 (29.9 - 92.5)	76.4 (50.1 -93.2)	60 (26.2 - 87.8)	81.2 (54.4 - 96)	2.8 (1.7 - 4.8)	0.4 (0.1 - 1.5)
[11C]choline PET/CT	7	2	3	14	77.7 (40.0- 97.2)	82.4 (56.6- 96.2)	70 (34.8- 93.3)	87.5 (61.7- 98.4)	4.4 (2.9-6.7)	0.3 (0.05-1.3)
per Nodal basis										
MRI	5	22	5	374	18.5 (6.3-38.1)	98.7 (96.9 - 99.6)	50 (17.3 - 82.7)	94.4 (91.7 - 96.5)	14 (6.4 - 31.0)	0.8 (0.3 - 2.0)
[11C]choline PET	11	16	6	373	40.7 (22.4-61.2)	98.4 (96.6 - 99.4)	64.7 (38.3 - 85.8)	95.9 (93.4 - 97.6)	25.7 (16.3 - 40.6)	0.6 (0.3 - 1.4)
[11C]choline PET/CT	14	13	6	373	51.9 (31.9-71.3)	98.4 (96.6 - 99.4)	70 (45.7 - 88.1)	96.6 (94.3 - 98.2)	32.8 (22.8 - 47.1)	0.5 (0.2 - 1.2)

TP-true positive; FN-false negative; FP-false positive; TN-true negative; CI-confidence intervals; PPV-positive predictive value; NPV-negative predictive value; LR-likelihood ratio; + positive; - negative.

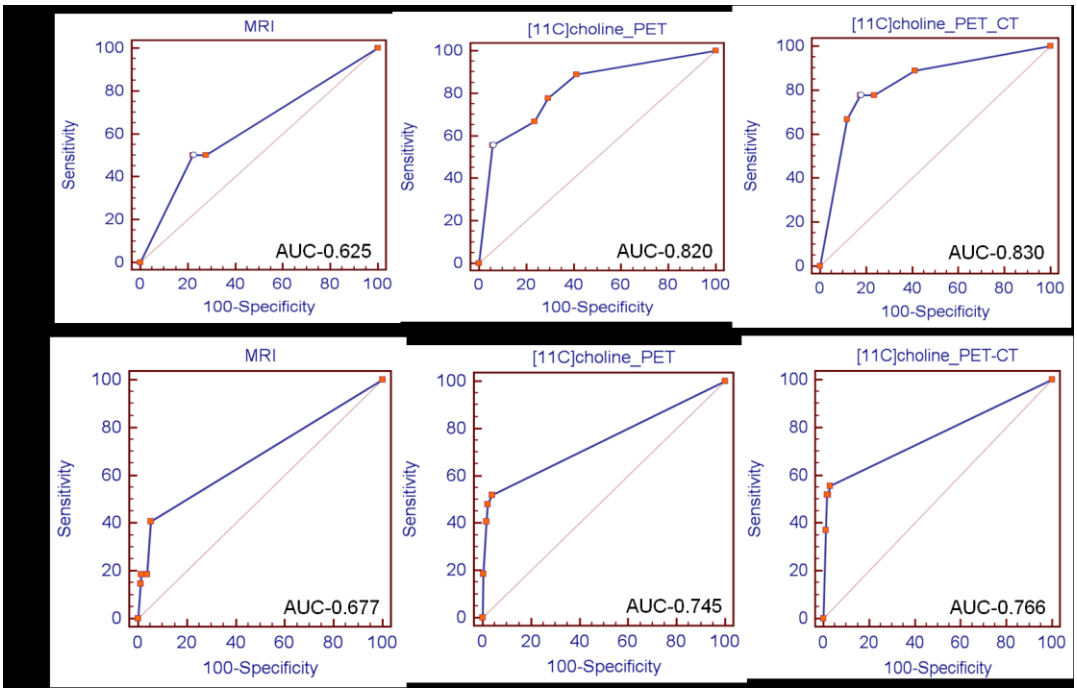

Figure 28: **ROC curve analysis.**

The area under the curve was 0.625, 0.820 and 0.830 respectively for MRI, [^{11}C]choline PET and [^{11}C]choline PET/CT on a per patient basis and 0.677, 0.745 and 0.766 respectively on per nodal analysis. The overall diagnostic performance improved in the following order MRI < [^{11}C]choline PET < [^{11}C]choline PET/CT.

Table 11: **Detection rate of the 3 imaging modalities by the size of the node**

Size of infiltrated nodes (mm)	No of Lymph nodes (LN)	MRI + (%)	[^{11}C]choline PET + (%)	[^{11}C]choline PET/CT+ (%)
0.1 – 1.9	1	0 (0)	0 (0)	0 (0)
2 – 4.9	4	0 (0)	0 (0)	1 (25)
5 – 9.9	12	0 (0)	4 (33)	4 (33)
≥ 10	10	5 (50)	7 (70)	9 (90)

+ - Positive

3.1.3.4: Sites of nodal involvement

The majority of the nodes were detected within the standard surgical template. However, four of 26 patients (15.4%) had focal increased uptake above the region of eLPL (Common Iliac (CI) region and lower para-aortic region – median $SUV_{60,ave}$ and $SUV_{60,max}$ of 1.12 and 3.91; median $SUV_{15,ave}$ and $SUV_{15,max}$ of 2.61 and 6.51 respectively) as detected on imaging and therefore were not sampled. 8 out of 26 (31%) patients had nodes detected below the surgical template, out of which 3 patients had discrete unilateral uptake in the inguinal LNs (median $SUV_{60,ave,}$ $SUV_{60,max}$ and $Ki_{mod\text{-}pat}$ of 1.21, 2.50 and 0.0002; median $SUV_{15,ave}$ and $SUV_{15,max}$ of 1.54 and 2.63 respectively); significantly lower as compared with true positive pelvic nodes (p-values of 0.002, 0.0002, 0.004, 0.0002 and 0.04, respectively, for $SUV_{15\ ave}$, $SUV_{15\ max}$, $SUV_{60,ave,}$ $SUV_{60,max}$ and $Ki_{mod\text{-}pat}$ in the two-sided t-test) which was interpreted as probably reactive uptake and therefore were considered non-metastatic (**Figure 29**). One patient had a 5mm tumour focus in a genitofemoral node, which was outside the FOV.

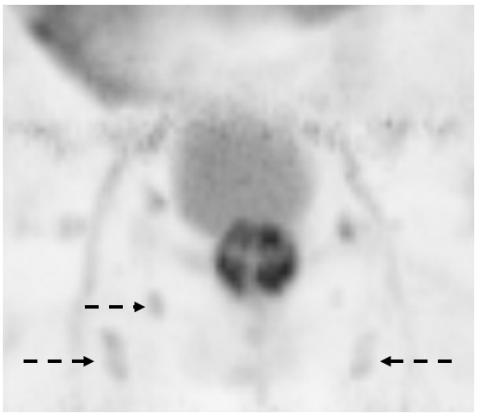

Figure 29: **Coronal MIP showing focal uptake in bilateral inguinal nodes (hashed arrows).**

3.1.3.5: Nodal Analysis on MRI

In 4 of 9 patients, MRI was positive for 5 malignant (true-positive (TP)) nodes with a median maximum diameter of 11 mm (range: 9 –21 mm; mean: 13.8 mm).

In 22 malignant nodes using size criteria, MRI was false negative (FN). 18/ 22 (82%) nodes were sub-centimetre and were reported as normal. Four nodes > 10 mm were missed. This was due to a cluster of 3 nodes reported as one (**Figure 24**), lateral extension of tumour obscuring the obturator node and 2 nodes measuring 12 and 15 mm on histology, which measured 4 and 5 mm on MRI , highlighting the pitfall of gross nodal measurements which may include surrounding perinodal fat and soft tissue.

In 4 patients, MRI was false-positive (FP) (a total of 5 nodes). This was due to a probable sampling error in 2 patients (**Figure 23**), reactive external iliac (EI) nodes in 1 patient and a positive round reactive obturator node which was negative on PET/CT.

3.1.3.6: Nodal Analysis on [^{11}C]choline PET

In 6 of the 9 patients, [^{11}C]choline PET alone was TP for 11/ 27 malignant LNs. In the 16 FN malignant nodes, 13 were due to micro-metastases, 2 were mistaken for focal ureteric activity which was resolved with PET/CT and one node was in the saturation band (i.e. where there was an overlap when the 2 bed positions were fused). This saturation band, obscuring some parts of the imaged area is not a general feature of PET/CT but probably related to specific equipment settings or reconstruction.

In 4/ 17 patients [^{11}C]choline PET was FP (total of 6 nodes). There are varying reasons for this: one FP node was due to focal uptake in a calcified vessel mistaken for a node which was resolved with PET/CT; 2 nodes were reactive EI nodes; one node

was situated in the saturation band and for the remaining nodes in 2 patients, there was a probable sampling error given that 15 and 28 nodes were removed in total from those patients respectively. The median $SUV_{15,ave}$: $SUV_{60,ave}$ and $SUV_{15,max}$: $SUV_{60,max}$ of the false positive LNs were 2.54: 2.70 and 5.07: 6.51, respectively. SUVs of the TP LNs tended to be higher (median $SUV_{15,ave:}$ $SUV_{60,ave}$ – 2.99: 2.64 and $SUV_{15,max}$: $SUV_{60,max}$ – 7.04: 7.77 respectively) than SUVs of the FP LNs although statistical significance was never reached (p-values of 0.48, 0.28, 0.56 and 0.22 for $SUV_{15,ave}$, $SUV_{15,max}$, $SUV_{60,ave}$ and $SUV_{60,max}$ in the two-sided t-test).

3.1.3.7: Nodal Analysis on [^{11}C]choline PET/CT

In 7/ 9 patients, [^{11}C]choline PET/CT was TP for 14 malignant LNs (**Figure 23**). The median maximum diameter of the malignant LNs detected was 9 mm (range: 4 – 20 mm; mean: 9.4 mm).

In 13 malignant nodes, [^{11}C]choline PET/CT was FN as explained in the preceding paragraph. In 3 patients, [^{11}C]choline PET/CT was FP in 6 nodes. In one patient, a further FP node close to the saturation band was called on PET/CT but not PET only. The other 5 nodes in two patients were FP on both PET only and combined PET/CT as explained above.

3.1.3.8: CHKα, Ki67expression and association with [^{11}C]choline uptake

3.1.3.8.1: CHKα Immunofluorescence (IF)

Using IF, there was a good demonstration of cytoplasmic CHK expression (**Figure 30**). However, it was not possible to differentiate the glandular differentiation

and architecture in the sections. Hence staining by IF was stopped in favour of conventional IHC.

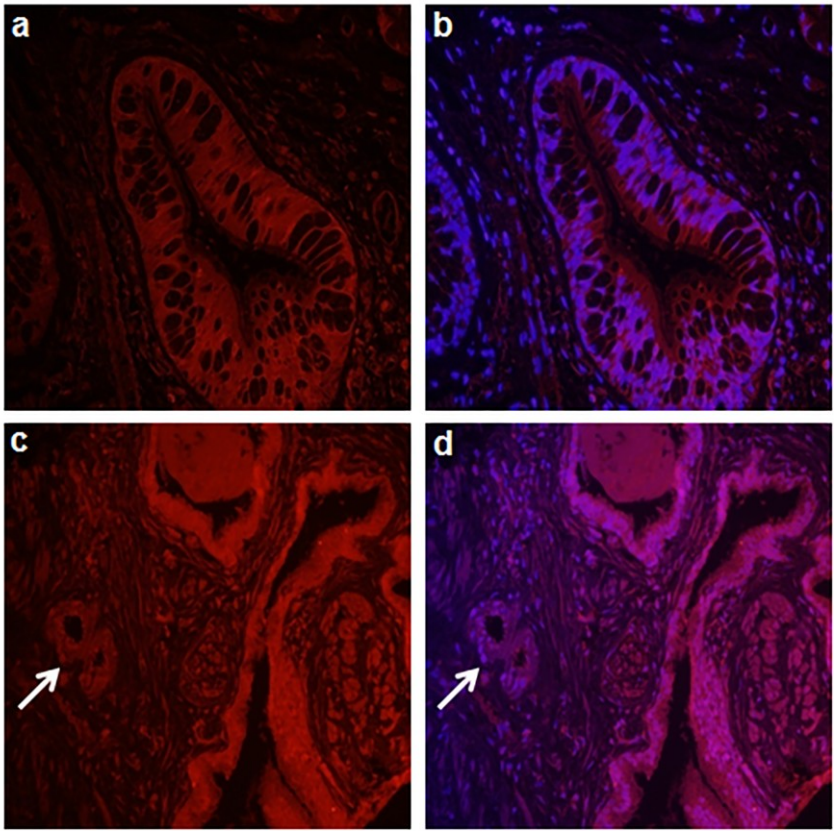

Figure 30: CHKα Immunofluorescence.
Cytoplasmic CHK expression is seen as red and the nuclei stain blue. The images to the left show cytoplasmic expression and the merged images to the right show nuclear staining (DAPI; appear pink) and cytoplasmic expression. Bronchus used as positive control **(a, b)**, cytoplasmic and nuclear staining (white arrow) in the malignant prostate core **(c, d)**.

3.1.3.8.2: CHKα IHC

There was CHKα staining in all the malignant prostate cores that varied in intensity from 1-3 (predominantly cytoplasmic and some nuclear staining) compared to the positive control. The different intensities of CHKα staining along with adjacent H&E

stained sections are shown in **Figure 31**. Various patterns of staining were observed in various sections (**Figure 32**). There was a varying intensity of staining seen in Gleason 3, 4 and 5 glands. In one section an increased nuclear staining for CHKα with increasing Gleason scores was also observed, especially between Gleason 3 and 5 visually differentiating the two grades. In one section, some benign glandular areas adjacent to the malignant glands were also stained. There was no relationship between cytoplasmic intensity and nuclear staining of CHKα. In one section an area of prostatic intra-epithelial neoplasia (PIN) showed nuclear staining. When the pelvic node sections were stained, benign nodes showed no CHKα staining (**Figure 33**) whereas malignant nodes showed cytoplasmic and nuclear staining in the metastatic deposit. In 3 patients, the cores from one of the lobes of the prostate gland were benign and the cores from the other lobe were malignant. The benign cores of these patients also demonstrated an increased CHKα expression (**Figure 34**). Ki67 staining revealed (**Figure 35**) that most primary and nodal prostate tumours had a low proliferation index (median 3%, range 1 to 17%).

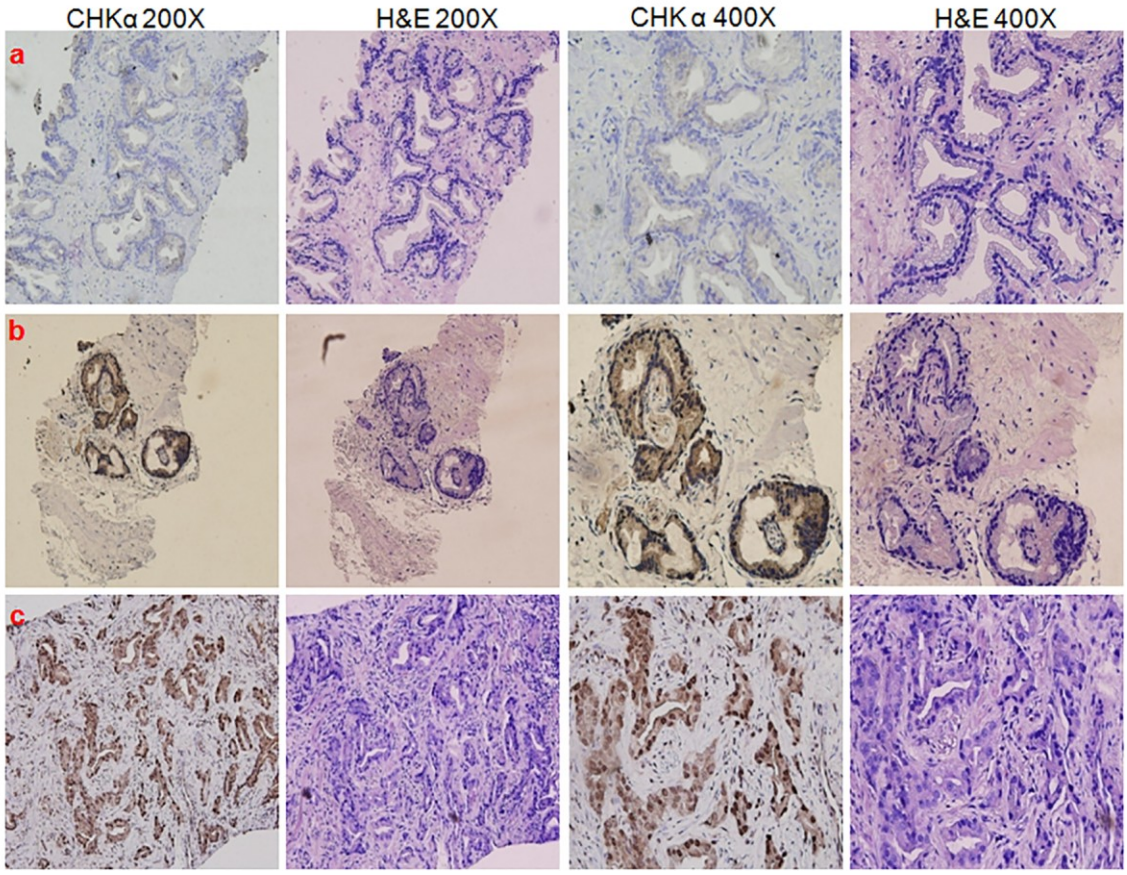

Figure 31: CHK staining and the matched H&E sections in malignant prostate cores.
The panels show different staining intensities at low (200X) and high (400X) magnifications. Panel **(a)** shows mild (grade 1) staining, panel **(b)** shows moderate (grade 2) staining, panel **(c)** shows strong cytoplasmic and nuclear staining (grade 3).

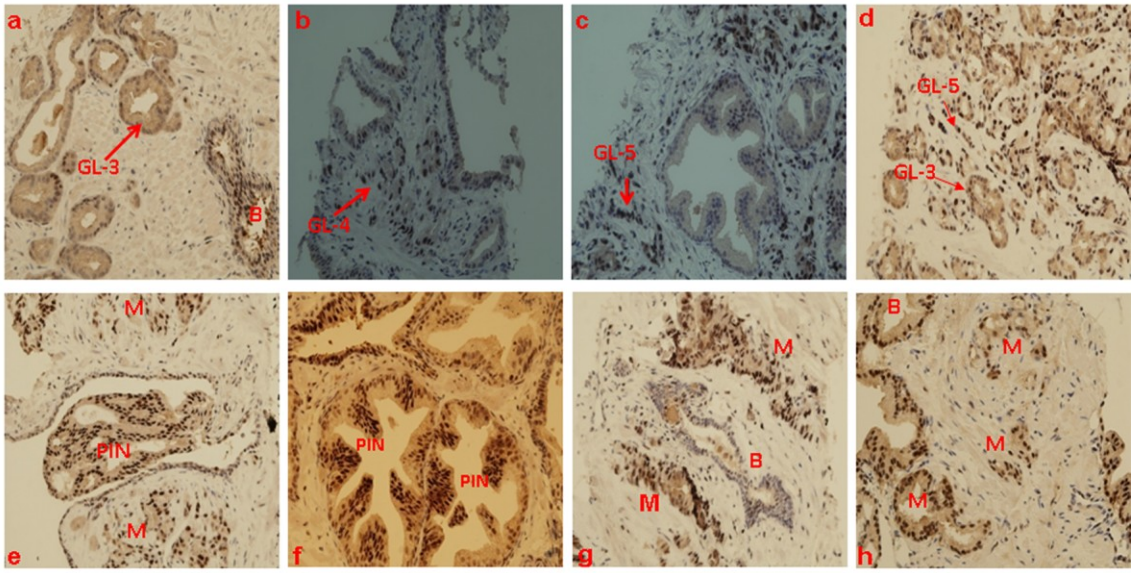

Figure 32: Patterns of CHK staining in malignant cores.

(a) Cytoplasmic staining in Gleason 3 glands, **(b)** nuclear staining in Gleason 4 glands, and **(c)** in Gleason 5 glands, **(d)** increasing intensity of staining with increasing Gleason score (3 and 5), **(e, f)** nuclear staining in areas of PIN, **(g)** cytoplasmic and nuclear staining in malignant glands but not in benign gland and **(h)** cytoplasmic and nuclear staining in both malignant and benign glands. B – Benign, M – malignant, PIN – prostatic intra-epithelial neoplasia, GL – Gleason.

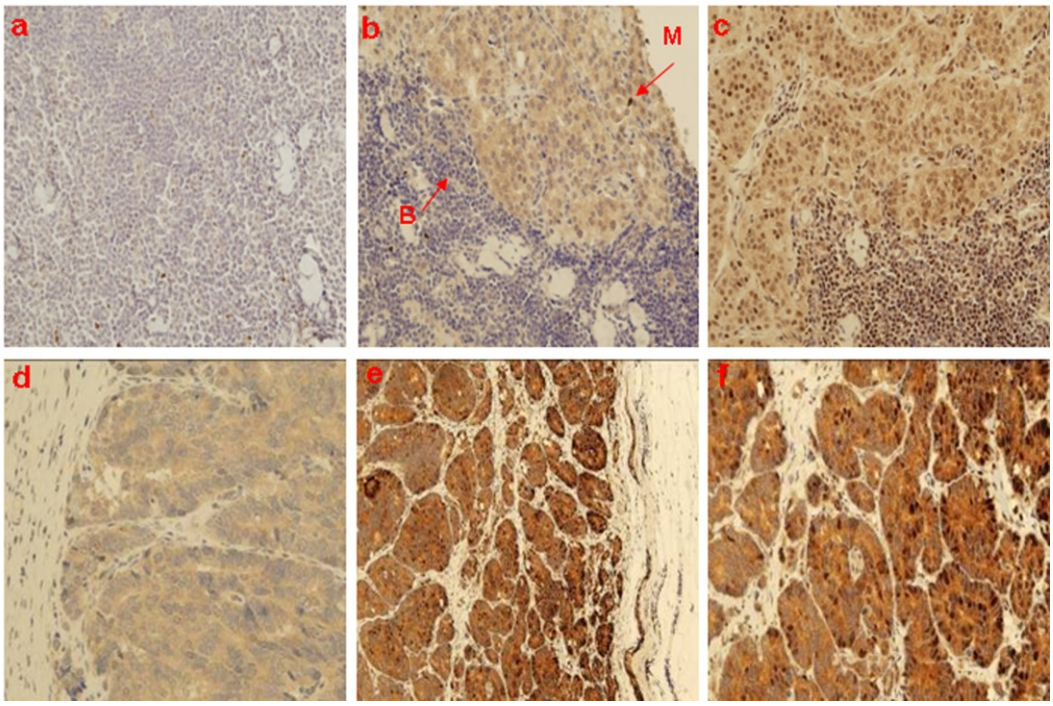

Figure 33: CHK expression in nodal tissue.

(a) No staining seen in benign nodes, **(b, c)** brown cytoplasmic staining in a metastatic deposit, **(d)** mild cytoplasmic staining, **(e, f)** strong cytoplasmic and nuclear staining in the metastatic deposit.

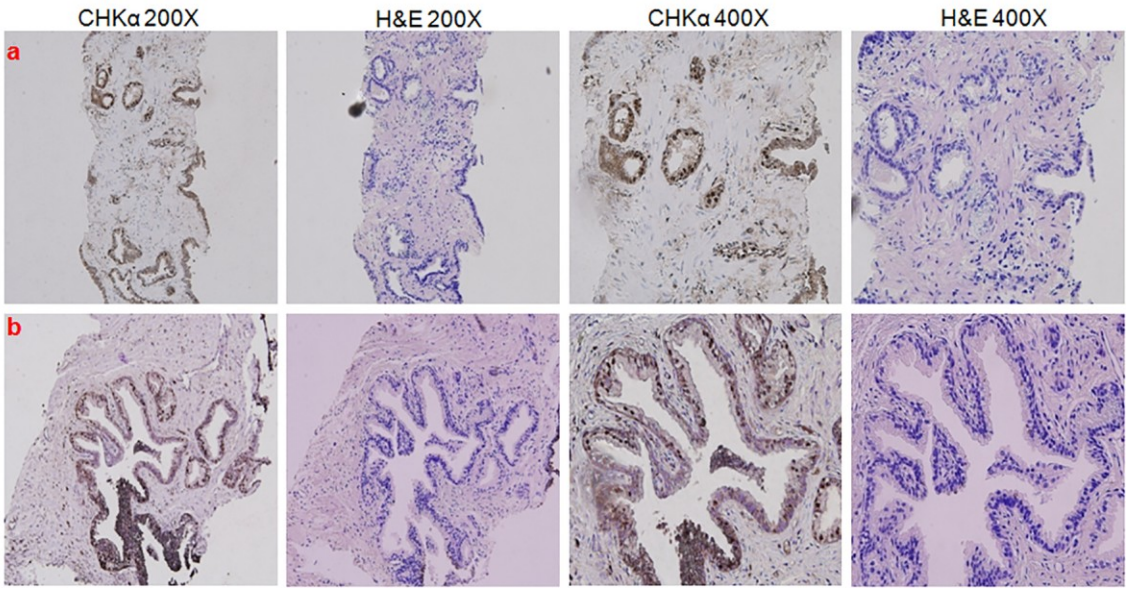

Figure 34: CHK staining and the matched H&E sections in the benign cores of a malignant prostate gland.

Mild staining is seen in the benign glands at low (200X) and high (400X) magnifications **(a, b)**. The benign architecture is made out in the corresponding H&E sections; note the frilly pattern of the gland in **(b)**.

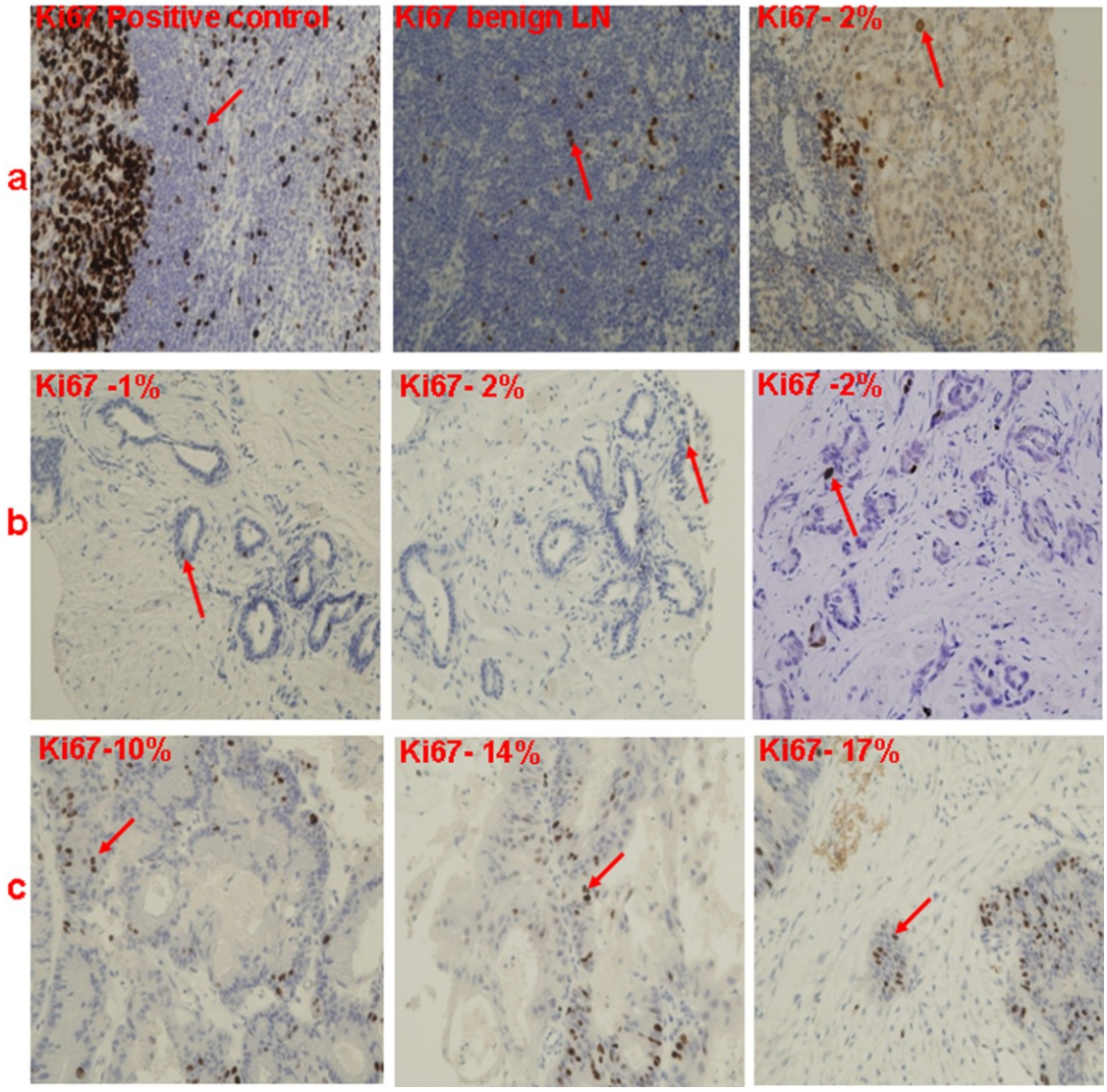

Figure 35: Ki67 staining of prostate tumour cores and nodal tissue.

The panel **(a)** shows a positive control, benign node and a node with metastatic deposit. Panel **(b)** shows prostate cores with lowest Ki-67 index and panel **(c)** showing cores with highest index.

3.1.3.8.3: Correlation with [^{11}C]choline PET/CT parameters

The [^{11}C]choline uptake variables ($SUV_{60,ave}$ or $SUV_{60,max}$) of the patients who had samples available for IHC, along with CHKα intensity scoring and Ki-67 indices are given in **Table 12**. There was a positive correlation between $SUV_{60,ave}$, and $SUV_{60,max}$ (**Figure 36**) with cytoplasmic CHKα intensity in prostate tumours (r=0.7, p<0.0001, and r=0.6, p=0.0001 respectively). This positive correlation was seen even at early time points ($SUV_{15,ave}$, $SUV_{15,max}$: r= 0.5, p=0.0009 and r=0.5, p=0.003 respectively). There was a moderate correlation of $SUV_{60,max}$ with the initial PSA levels (r=0.6, p=0.0003), but not with $SUV_{60,ave.}$ However, there was no association between [^{11}C]choline uptake and Ki67 scores (**Figure 36**). The association between IHC scores for CHKα and Ki67 with Gleason's scores or PSA were also assessed **(Table 13)**. Only Gleason scores and Ki67 indices showed a positive correlation (r=0.5, p=0.004).

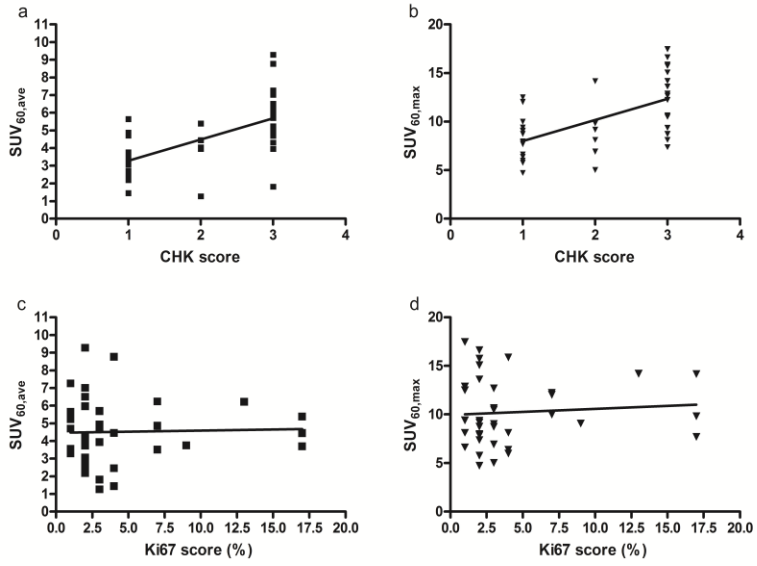

Figure 36: Correlation of [^{11}C]choline uptake with IHC scores for CHKα and Ki67.
The best Spearman's correlation was with, (**a**) $SUV_{60,ave}$ with CHKα followed by, (**b)** $SUV_{60,\ max}$ and CHKα. There was no correlation between [^{11}C]choline uptake and Ki67 (**c and d**).

Table 12: [^{11}C]choline PET/CT parameters and the IHC scores for CHKα and Ki67 indices in malignant pelvic nodes and primary prostate tumours.

Pt No*	Tissue	SUV 15,ave	SUV 15,max	SUV 60,ave	SUV 60,max	CHKα score	Ki67 score	Gleason score	PSA
1	node	7.24	11.57	7.26	12.88	3	1	7	8.5
2	tumour	5.88	11.79	5.96	15.08	3	2	6	21
4	tumour	5.03	15.56	5.24	17.46	3	1	7	84
5	tumour	4.84	9.52	4.94	10.64	3	3	9	27.5
6	tumour	4.27	8.81	3.52	9.99	1	7	9	79.4
7	tumour	3.54	6.95	3.74	8.74	1	2	6	16.4
8	tumour	5.57	8.55	5.39	9.83	2	17	9	29.6
10	tumour	4.79	8.81	4.86	12.03	1	7	8	13.5
	node	4.05	8.61	4.45	14.16	2	17		
11	tumour	4.99	7.44	4.3	7.38	3	2	7	8.1
12	tumour	8.80	13.24	9.28	16.62	3	2	7	51
14	tumour	3.98	6.24	3.7	7.7	1	17	9	15
15	tumour	5.83	11.37	6.22	14.19	3	13	9	209
	node	2.71	4.68	8.77	15.87	3	4		
17	tumour	8.75	13.65	7.01	13.6	3	2	7	169
	node	2.37	5.11	2.46	5.99	1	4		
20	tumour	4.11	9.41	3.75	9.08	1	9	7	21
	node	3.27	7.24	1.44	6.37	1	4		
22	tumour	3.97	6.80	4.03	9.18	2	2	7	22.7
23	tumour	6.81	12.21	6.5	15.72	3	2	8	59.5
24	tumour	4.67	8.04	4.84	10.49	3	3	9	45
24	node	1.45	4.56	1.27	5.03	2	3		
25	tumour	4.65	9.52	3.55	9.39	1	1	9	24.5
26	tumour	2.44	3.89	2.19	4.73	1	2	7	8.2
27	tumour	2.72	5.38	2.73	7.98	1	2	7	44.8
	node	2.09	6.84	1.82	8.72	3	3		
28	tumour	3.71	8.09	3.08	7.87	1	2	7	25
2	tumour	3.79	6.85	3.95	6.92	2	3	7	5.4
3	tumour	4.51	8.10	4.46	8.12	2	4	7	20
4	tumour	4.98	9.34	5.64	12.49	1	1	6	9.2
5	tumour	2.62	5.79	2.33	5.78	1	2	6	11
6	tumour	5.11	10.23	4.70	8.13	3	1	7	13
7	tumour	5.25	11.48	4.71	9.03	1	3	6	17.1
8	tumour	6.61	12.74	6.24	12.23	3	7	7	16.5
9	tumour	3.79	7.16	3.30	6.62	1	1	6	10.1
10	tumour	4.38	10.81	3.95	9.35	3	2	7	30

* Correspond to Pt Nos. in chapter 3 and 4.
Tumour – indicates malignant cores from prostate biopsy
Node – indicates metastatic pelvic nodes from eLPL

Table 13: Correlation of [^{11}C]choline PET/CT SUVs with IHC and biomarkers in prostate tumours.

	$SUV_{15,ave}$		$SUV_{15,max}$		$SUV_{60,ave}$		$SUV_{60,max}$	
	r	**p**	**r**	**p**	**r**	**p**	**r**	**p**
CHKα score	0.5	0.0009	0.5	0.003	0.7	<0.0001	0.6	0.0001
Ki 67 score	-0.1	0.42	-0.2	0.27	-0.03	0.86	-0.03	0.98
GS	0.2	0.41	0.04	0.82	0.13	0.5	0.3	0.18
PSA levels	0.3	0.07	0.5	0.01	0.3	0.07	0.6	0.0003

GS= Gleason score, r= Spearman's correlation coefficient, p= significance value.

3.1.4: Discussion

This study supports the feasibility of using [^{11}C]choline PET/CT in determining pelvic LN status in patients with high-risk prostate cancer. It is specific and shows early promise in yielding a greater diagnostic accuracy than either MRI or PET only scanning. This is especially evident in detecting sub-centimetre disease, although the sensitivity is not sufficient to exclude lymphadenectomy, as metastases <6 mm in particular may be missed. However, it has the potential to highlight nodal uptake outside the surgical template for LN dissection, especially in the CI and para-aortic area as demonstrated in this study, which can have significant consequences in terms of patient management.

The somewhat disappointing performance of [^{18}F]FDG PET in the setting of prostate cancer has prompted interest in newer PET tracers such as [^{18}F] and [^{11}C]choline for the detection of primary tumour within the prostate and the staging of pelvic nodal disease. For the detection of the primary tumour, some authors have reported 100% sensitivity (Kwee, Coel et al. 2005; Yamaguchi, Lee et al. 2005; Reske, Blumstein et al. 2006) while others report lower detection rates ranging from 19 – 58% depending on whether results were reported on a per patient or per lesion basis (Farsad, Schiavina et al. 2005; Martorana, Schiavina et al. 2006; Scher, Seitz et al.

2007; Giovacchini, Picchio et al. 2008). For staging of pelvic nodal disease, the reported sensitivity and specificity ranged from 50 – 80% and 90 to 96%, respectively in the two studies that employed PET alone, based on a per patient analysis (Kotzerke, Prang et al. 2000; de Jong, Pruim et al. 2003). The published studies assessing LN stage using PET/CT showed varied and conflicting results with the sensitivity and specificity ranging from 10-100% and 82-100% (Hacker, Jeschke et al. 2006; Husarik, Miralbell et al. 2008; Schiavina, Scattoni et al. 2008; Beheshti, Imamovic et al. 2010; Poulsen, Bouchelouche et al. 2010; Budiharto, Joniau et al. 2011; Poulsen, Bouchelouche et al. 2012). The variation in sensitivity may be in part due to patient selection. **Table 14** summarises the published studies.

Table 14: **Review of literature for nodal staging**

Author	Tracer (Administered Activity MBq)	No. of patients	Prevalence of LN metastases	Sn (%)	Sp (%)
Sensitivity & Specificity – Per-patient analysis					
De Jong et al (de Jong, Pruim et al. 2003)	[^{11}C]choline PET (400)	67	22.4% (15/67)	80	96
Kotzerke et al (Kotzerke, Prang et al. 2000)	[^{11}C]choline PET (mean 1000: range of 370-1250)	12	16.6% (2/12)	50	90
Schiavina et al (Schiavina, Scattoni et al. 2008)	[^{11}C]choline PET/CT (370)	57	26% (15/57)	60	98
Husarik et al (Husarik, Miralbell et al. 2008)	[^{18}F]choline PET/CT (200)	25	12% (3/25)	33	100
Hacker et al (Hacker, Jeschke et al. 2006)	[^{18}F]FCH PET/CT (4.07 MBq/ kg)*	20	50% (10/20)	10	80
Behesti et al (Beheshti, Imamovic et al. 2010)	[^{18}F]FCH PET/CT (4.07 MBq/ kg)*	130 (111 LND)	31% (40/130)	45	96
Budiharto et al (Budiharto, Joniau et al. 2011)	[^{11}C]choline PET/CT (700-1000)	36	47% (17/36)	18	95
Poulsen et al (Poulsen, Bouchelouche et al. 2010)	[^{18}F]FCH PET/CT	25	12% (3/25)	100	95
Poulsen et al (Poulsen, Bouchelouche et al. 2012)	[^{18}F]FCH PET/CT	210	20% (41/210)	73	88
This study	[^{11}C]choline PET/CT (700)	26	34.6% (9/26)	77.7	82.4
Sensitivity & Specificity – Per-nodal analysis					
Author	Tracer (Administered Activity MBq)	No. of nodes	Prevalence of LN metastases	Sn (%)	Sp (%)
Schiavina et al (Schiavina, Scattoni et al. 2008)	[^{11}C]choline PET/CT (370)	892	4.6% (41/892)	41.4	99.8
Husarik et al (Husarik, Miralbell et al. 2008)	[^{18}F]choline PET/CT (200)	115	4.3% (5/115)	20	100
Budiharto et al (Budiharto, Joniau et al. 2011)	[^{11}C]choline PET/CT (700-1000)	733	5.2% (38/733)	9.4	99.7
Poulsen et al	[^{18}F]FCH PET/CT	1093	7% (73/1093)	56	94

(Poulsen, Bouchelouche et al. 2012)					
This study	[^{11}C]choline PET/CT (700)	406	6.7% (27/406)	52	98.4

* Average weight of individual-70 kg - Administered activity of 285 MBq, Sn-sensitivity, Sp-specificity

In this study the value of MRI, [^{11}C]choline PET and [^{11}C]choline PET/CT imaging in the preoperative staging of high-risk prostate cancer patients has been assessed. An overall sensitivity and specificity of [^{11}C]choline PET/CT on a per patient basis, of 77.7% and 82.4% respectively in the detection of nodal metastases was seen. These results were superior to both MRI (50% and 72.2%), and [^{11}C]choline PET (66.6% and 76.4%), though were not significantly different probably due to relatively low patient numbers. For MRI, the sensitivity & specificity achieved in our study are in keeping with previously reported data (Hricak, Dooms et al. 1987; Harisinghani, Barentsz et al. 2003). Dynamic contrast MRI may help with tumour localisation within the prostate but there are no specific reports on the additional benefit in nodal staging. More importantly on a per nodal basis (27/406), the sensitivity was significantly higher for [^{11}C]choline PET/CT (51.9%) compared with MRI (18.5%) ($p=0.007$) with a greater confidence for identifying sub-centimetre involved LNs, which occurred in 30% of the cases. However, in this study apart from one 4mm node, no other low volume metastases of less than 5mm in diameter were detectable, probably reflecting the limited spatial resolution of the current generation of scanners.

In one of the first published series, De Jong et al, obtained promising results with [^{11}C]choline PET in the preoperative nodal staging of 67 patients, with a sensitivity of 80% in a per patient-based analysis. Metastatic LNs ranging from 0.5 – 3 cm in size with a mean SUV of 4.7 (2.9 – 9.1) were demonstrated. FP activity in 2 patients was attributed to inflammatory change and focal bowel activity. However, in their study, about 50% of the node positive patients had a PSA of >50ng/mL (range: 3-500), compared to our mean PSA value of 44.25 ng/mL (range: 8.1-209), which may have contributed to a selection bias and may under-represent the cohort of high risk localised prostate cancer patients for which radiotherapy to the pelvis would be indicated (de Jong, Pruim et al. 2003). Conversely Hacker et al (Hacker,

Jeschke et al. 2006) reported a very low sensitivity of 10% in a study of 20 patients assessed with F-18 fluorocholine. The mean diameter of metastatic lymph nodes in their study was 3.8mm which is well below the resolution of PET.

In studies utilising [^{11}C]choline PET/CT, Schiavina et al, (Schiavina, Scattoni et al. 2008) evaluated 57 intermediate or high-risk prostate cancer patients prior to surgical treatment. They reported a sensitivity of 60% and a specificity of 98% for the detection of nodal metastases. Husarik et al, (Husarik, Miralbell et al. 2008) evaluated 111 patients with prostate cancer in a [^{18}F]choline PET/CT study, 43 of whom had staging for assessment of primary disease. The PET/CT findings were correlated to the histopathological findings of 115 sampled LNs in 25 patients, with sensitivity & specificity on a per patient basis of 33% and 100% respectively.

Beheshti et al (Beheshti, Imamovic et al. 2010) evaluated 130 patients with intermediate or high-risk prostate cancer with [^{18}F]fluorocholine (FCH) PET/CT prior to extended pelvic node dissection with sensitivity and specificity in the detection of malignant nodes of 45% and 96%, respectively. Furthermore they reported a change in management in 15% of cases. The authors also noted discrete FCH uptake in inguinal lymph nodes which was interpreted as probable reactive uptake and therefore excluded from data analysis. This was similarly observed in our study cohort (8 out of 26 patients), although the visible inguinal nodes had significantly lower SUVs than both the metastatic LNs and the malignant prostate. As nodal dissection does not routinely remove inguinal nodes as part of standard practice, it may be difficult to ascertain if these were involved. The underlying assumption is that inguinal nodes were all within physiological limits of <10 mm in dimension based on the fact that prostate tumours normally do not spread to inguinal nodes (Clements 2010).

Budiharto et al. assessed 36 patients with [^{11}C]choline PET/CT and diffusion weighted MRI (DW-MRI) prior to radical prostatectomy (RP) and pelvic lymphadenectomy (LND). Seventeen patients (47%) were pathologically node positive, with a total of 38 metastatic nodes identified. On a patient-based analysis, the sensitivity and specificity were 18.8% and 95% for PET/CT and 42.9% and 81.8% for MRI, respectively. The poor performance of the [^{11}C]choline PET/CT was attributed to the majority of the positive nodes (53.1%) containing micro metastases (Budiharto, Joniau et al. 2011). Poulsen et al. prospectively evaluated, 25 newly diagnosed high-risk PCa patients undergoing RP and LND with [^{18}F]FCH PET/CT. Of these 25 patients, three patients had LN metastases on histology and four patients had PET positive nodes. On a patient basis, the sensitivity and specificity of [^{18}F]FCH PET/CT were 100% and 95%, respectively (Poulsen, Bouchelouche et al. 2010). In a more recent study, Poulsen et al. evaluated, 210 newly diagnosed intermediate and high-risk PCa patients undergoing LND with [^{18}F]FCH PET/CT. Forty-one patients (20%) were pathologically node positive, with a total of 73 metastatic nodes identified. On a patient-based analysis, the sensitivity and specificity were 73% and 88%, while on a nodal analysis they were 56% and 94%. In addition the PET detected bone metastases in 18 patients. They concluded that [^{18}F]FCH PET/CT is not ideal for primary LN staging in patients with prostate cancer due to low sensitivity (Poulsen, Bouchelouche et al. 2012). However, the main limitation of this study was the lack of extended lymphadenectomy. More recently, in a meta-analysis of 10 selected studies, with 441 patients in total, the pooled sensitivity and specificity reported were 49.2% and 95% respectively. The authors concluded that the low sensitivity was due to limited patient numbers and inhomogeneous group of patients, and further studies in larger homogeneous patient population are warranted (Evangelista, Guttilla et al. 2013).

Four other studies have reported on a per nodal analysis (**Table 14**). Husarik et al in their study including 25 patients staged with [^{18}F]fluorocholine reported a low sensitivity of 20% (1out of 5 involved nodes) and a specificity of 100%. All the FN nodes had tumour foci of < 5 mm. The mean SUV_{max} of the detected LNs was 5.04 (range 4.9–5.2). Notably only obturator nodes were removed rather than a more extensive lymphadenectomy and the authors did not comment on FCH positive nodes outside the obturator region. Similarly, Budiharto et al reported a sensitivity and specificity to be 9.4% and 99.7% (Budiharto, Joniau et al. 2011). Schiavina et al, in the study mentioned earlier, reported a sensitivity of 41.4% and a specificity of 99.8% on a per-nodal analysis. The mean diameter (in mm) of the metastatic deposit of true positive nodes was significantly higher than that of false negative nodes (9.2 vs. 4.2; p = 0.001).

The per nodal results of sensitivity & specificity with [^{11}C]choline in this study were similar at 51.9% & 98.4%. A limitation of this study was the technical difficulties encountered with the interpretation of findings on the PET scans in the region of the saturation band (where there was an overlap when the 2 bed positions were fused) which accounted for some of the FP results on the PET alone. In the two patients in whom MRI and PET/CT were FP for a 26mm and 10mm node, there is the potential, despite careful use of surgical templates, that these nodes were not sampled. The median $SUV_{60,\ max}$ of FP LNs was 6.51, compared to 7.77 for the TP nodes.

This study is one of the first to evaluate the time dependent uptake of [^{11}C]choline in prostate tumours up to 60 minutes. Dynamic TACs for [^{11}C]choline in primary prostate tumours and the nodal metastases demonstrated a good sustained retention of activity after plateauing at ~15 min until 60 min with SUV_{ave}. However, with $SUV_{max,}$ there is a hint of increasing activity at 60 min which may be due to the

contribution of [^{11}C]betaine. The results from the modelling of the [^{11}C]choline breast data using arterial IF suggest that irreversible kinetics account for [^{11}C]choline uptake in breast tumours. A discernable linear phase up to 60 minutes was seen in the modified Patlak model fits in most tumours signifying an irreversible net uptake component. Spectral analysis of tumour data was also suggestive of irreversible uptake both from the IRF and the presence of kinetic components at $\log_{10}\beta$ approximating λ. The use of a validated population-based total plasma IF from the breast data, predicted that irreversible kinetics also account for [^{11}C]choline uptake in prostate cancer, thus further validating the limited venous sampling approach (Contractor, Kenny et al. 2012).

It was shown for the first time in prostate tumour samples that tumour radiolabelled choline uptake ($SUV_{60,ave,}$ $SUV_{60,max,}$ and $Ki_{mod\text{-}pat}$) is closely related to CHKα expression in prostate cancer. Both semi-quantitative parameters of choline uptake in tumours correlated well with CHKα scores (best with $SUV_{60,ave}$ $r=0.7$, $p<0.0001$, Spearman's test). It was observed that areas of PIN in the malignant cores also showed staining which may represent the range of CHKα expression in pre-malignant and malignant tissues. In certain tissue sections, nuclear staining was observed, particularly in areas of PIN and in certain high Gleason grade tumours and although this phenomenon is not fully understood, a possible reason is that, phosphorylated CHKα may translocate to the nucleus. This hypothesis needs further evaluation.

This study also showed that proliferation in prostate tumours was low, as reflected by the low Ki67 index in most tumours (median 3%; range: 1-17%), contrary to the high CHKα expression. This may account for the lack of correlation between [^{11}C]choline SUV and Ki67 scores in tumours. A possible explanation for this is that CHKα expression is not directly linked to proliferation and may be an

independent marker of the prostate tumour phenotype. This is contrary to the evidence in other cell/ tumour types linking CHKα or choline metabolites and proliferation (Katz-Brull, Seger et al. 2002; Ramirez de Molina, Banez-Coronel et al. 2004; Al-Saeedi, Welch et al. 2005). The lack of correlation between [^{11}C]choline uptake and proliferation marker has been previously demonstrated (Sutinen, Nurmi et al. 2004; Breeuwsma, Pruim et al. 2005; Reske, Blumstein et al. 2006). Of note, one study using mean tumour to benign prostate background ratio has reported an association between choline uptake and Ki67 scores in prostate tumours (Piert, Park et al. 2009). Piert et al showed that tumour to benign prostate background ratio was significantly high in tumours with a Ki67 score of > 5% ($p<0.01$). They also reported a good correlation between Ki67 score and Gleason score, similar to that seen in this cohort of patients ($r=0.5$, $p=0.004$).

The main drawback to [^{11}C]choline is the relatively short half life (20.9 minutes) and thus the compound needs to be used close to where it is manufactured. Newer more stable and specific choline compounds are in development ((Leyton, Smith et al. 2009): Chapter 5).

In summary, this detailed study establishes the feasibility of [^{11}C]choline PET/CT as a noninvasive means of staging pelvic LNs in prostate cancer, being highly specific (98.4%) and more sensitive than PET alone or MRI. The high specificity is potentially helpful clinically in terms of selecting out those patients with high risk prostate cancer who may not need pelvic radiotherapy. Although it cannot currently replace MRI as a staging tool, its ability to detect sub-centimetre nodes and a differential SUV value between involved and physiological LNs, allows for a functional imaging methodology for assessing the radiation response to involved nodes. The relationship between CHKα expression and [^{11}C]choline uptake, together with the avid intra-tumoural uptake of choline demonstrated in this study,

suggests that [^{11}C]choline PET/CT could potentially be used as a noninvasive surrogate for CHK expression.

3.2: Patterns of CHKα and Ki67 expression in additional prostate tissues.

3.2.1: Rationale

Based on the interesting observations seen in the cores of prostate tissue stained in the previous section, further cores of prostate tissue from 75 patients diagnosed with prostate cancer (malignant) and 25 patients with no prostate cancer (normal) were subsequently analysed. The aim was to reproduce and validate the patterns of CHKα expression seen in the patient cohorts discussed in the previous section, in a larger number of normal and malignant prostate cores. Ethical approval was obtained from the hospital tissue bank.

3.2.2: Materials and Methods

The CHKα, Ki67 IHC and H&E staining to check primary antibody specificity were performed as discussed in the previous section. Paraffin embedded prostatectomy specimen blocks of 5 patients were also analysed for CHKα protein and gene expression in normal and malignant prostate tissue using western blotting and polymerase chain reaction (PCR), respectively.

3.2.2.1: Western Blot analysis of CHKα protein

Protein and mRNA of formalin fixed paraffin embedded (FFPE) prostate tissues were extracted using Qproteome FFPE Tissue Kit (Qiagen, Cat. Nr: 37623)

and RNeasy FFPE Kit (Cat. Nr: 73504). After protein extraction the tissue lysates were analysed using Western Blot analysis. Twenty to thirty micrograms of tissue lysates were heated to 70°C for 10 minutes with LDS sample buffer and reducing agent (Invitrogen). Proteins were separated on Biorad 4-15% Mini-Protean TX-gels at 200V for 15 minutes. Following electrophoresis, proteins were transferred to a PVDF membrane using a semi-dry transfer system, Transblot Turbo Transfer system (Biorad) and then blocked with blocking buffer (1% milk in Tris-Buffered Saline and Tween 20 TBST) for 1h. The membranes were then probed with the CHKα primary antibody (Sigma-Aldrich, Cat. Nr: HPA024153) and β-actin loading control (Abcam, Cat. Nr: ab6276). Overnight antibody incubation in blocking buffer, was followed by 3x 10 min washes in fresh blocking buffer. The PVDF membrane was then incubated with peroxidase labelled relevant secondary antibodies (mouse and rabbit antibodies; Santa Cruz, Cat. Nr: sc-2004 and sc-2005). The Western blot reactions were detected by chemiluminescence-based photoblot system (ECL –. GE Healthcare, Chalfont St Giles, Bucks, UK).

3.2.2.1: Quantitative Reverse transcriptase polymerase chain reaction (qRT-PCR)

The extracted RNA was reverse transcribed to cDNA using QuantiTect reverse transcription kit (Qiagen, Cat. Nr: 205311). Gene expression was quantified on a 7900HT Fast Real-Time PCR system (Applied Biosystems) using TaqMan® Fast Advanced Master Mix (Applied Biosystems, Cat. Nr: 4444963) and TaqMan® gene expression assays (Applied Biosystems) detecting CHKα (Assay ID: Hs00957875_m1), CHKβ (Assay ID: Hs01925200_s1) and GAPDH (Assay ID: Hs02758991_g1). Relative expression was calculated by comparative (C_T) method (Schmittgen and Livak 2008).

3.2.3: Results

3.2.3.1: CHKα expression in normal prostate gland

There was no CHKα expression demonstrable in a majority of the normal prostate cores (**Figure 38**). However, there was mild CHKα expression in 28% (7/25) of the normal prostate cores. This suggests that increased CHKα expression may not be specific to malignant prostate tissue.

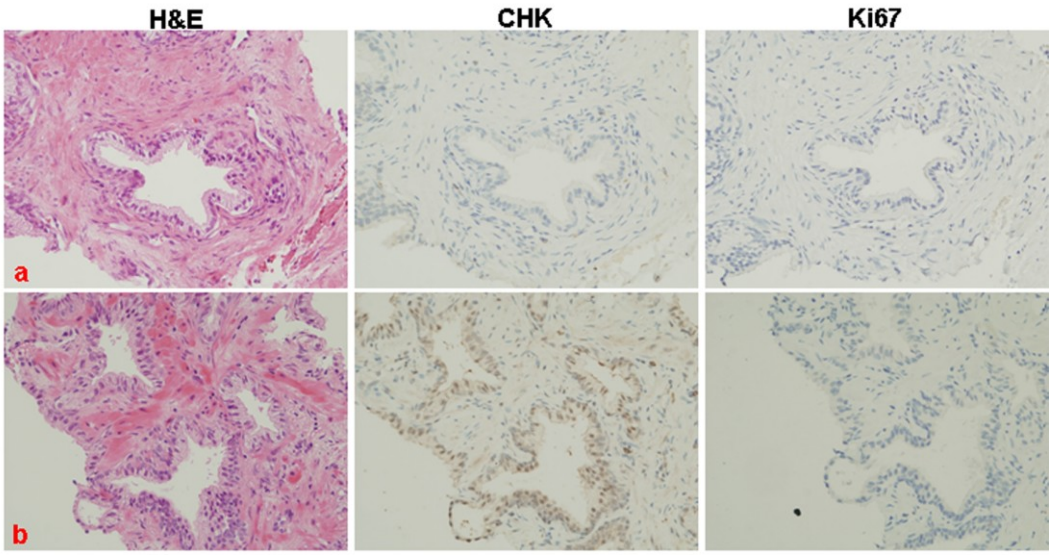

Figure 37: CHKα and Ki67 IHC on cores from a normal prostate gland and corresponding H&E stained sections.
The sections show lack of CHKα and Ki67 expression in a majority of the cores **(a)** and mild CHKα expression (28% of the cores) but no Ki67 expression in any of the cores **(b)**.

3.2.3.2: CHKα and Ki67 IHC in malignant prostate cores

There was CHKα expression in all the malignant prostate cores (n=75) that varied in intensity from 1-3 (predominantly cytoplasmic and some nuclear staining) similar to that seen in the cores from patients discussed in the previous section. Areas of PIN consistently showed nuclear staining. However, visually there

appeared to be no increased CHKα expression with increasing Gleason scores. As seen before Ki67 staining revealed that most of the primary prostate tumours had a low proliferation index (median 2%, range 1 to 7%). In 28 patients the cores from one of the lobes of the prostate gland were benign and the cores from the other lobe were malignant. The benign cores in 7 of these patients showed that there was increased CHKα expression as seen before, which is similar to the pattern seen in the cores from the normal prostate gland.

There was a good correlation between the intensity of the CHKα staining and PSA but not with the degree of differentiation (Gleason score) in the malignant cores (**Table 15**). There was no association between Ki67 labelling index and Gleason scores or PSA.

Table 15: Correlation of CHK and Ki67 scores with PSA and Gleason score in malignant prostate cores.

	PSA		GS	
	r	**p**	**r**	**p**
CHKα score	0.3	0.04	0.3	0.05
Ki 67 score	-0.1	0.52	-0.1	0.70

GS= Gleason score, r= Spearman's correlation coefficient, p= significance value.

3.2.3.3: CHKα protein and gene expression in normal and malignant prostate tissue

Immunoblotting of the tissues from 2 patients showed good resolution of the CHKα protein in the malignant prostate. Amplification of CHKα mRNA by quantitative reverse transcriptase polymerase chain reaction (qRT-PCR) showed CHKα gene expression in both normal and malignant prostate tissues (**Figure 38**).

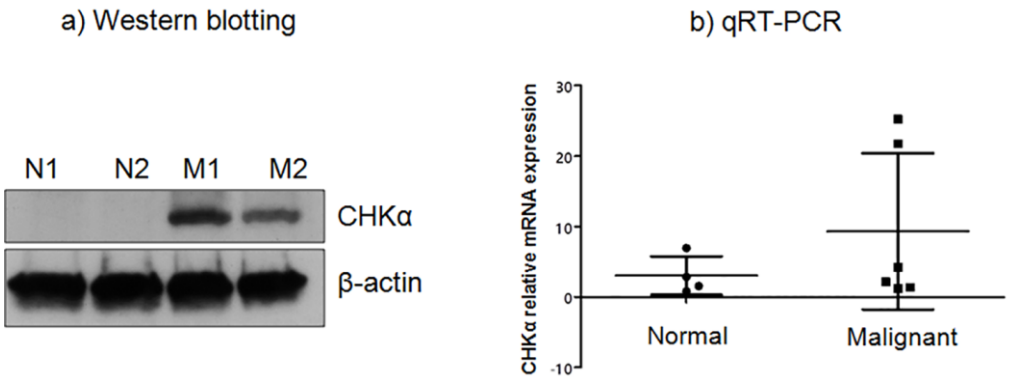

Figure 38: **Expression of CHKα protein and genes in the normal (N) and malignant (M) prostate tissue.**

(a) Western blot analysis of CHKα protein showed good resolution of bands in the malignant prostate tissue. β-actin was probed as protein loading control. **(b)** Quantitative expression of CHKα genes (mRNA) showed no significant differential expression in the normal and malignant prostate tissues. qRT-PCR - Quantitative reverse transcriptase polymerase chain reaction.

3.2.4: Discussion

The results obtained with the CHKα IHC are very interesting. There was increased expression of CHK (mild staining intensity) in up to 28% of the normal prostate cores and the benign cores in a malignant prostate. CHKα staining in areas of PIN, different intensities of positive staining and the low Ki67 labelling index in the malignant prostate cores were consistently seen. The CHKα primary antibody used in this study was able to identify cytoplasmic and nuclear CHK expression. The minor degree of CHKα expression (28%) in the normal prostate cores is supported by the CHKα gene expression in the normal prostate tissue seen on qRT-PCR. This could form the basis for the differential [^{11}C]choline uptake seen in the normal and tumour prostate (as shown in chapter 4). The predominant nuclear staining seen in areas of PIN, could be due to the morphological and cytological features of PIN such as nuclear enlargement, prominent nucleoli and hyperchromasia (Merrimen,

Evans et al. 2013). Furthermore, the localisation of choline in areas of PIN has also been shown with MRS and dynamic contrast-MRI (Sciarra, Panebianco et al. 2010).

The two isoforms of CHK: CHKα and CHKβ are significantly different in their role in tumourigenesis (Gallego-Ortega, Ramirez de Molina et al. 2009). Therefore, in order to confirm the specificity of the polyclonal antibody against CHKα used in this study, *in vitro* studies in cell lines (including siRNA knockdown and western blotting with both CHKα and CHKβ antibodies separately) were performed by another member of the Aboagye group. CHKα and CHKβ proteins have very different molecular weights and therefore were well resolved by western blot.

As seen earlier, the prostate cores had low proliferation indices (median Ki67 of 2%; range: 1-7%). However, the Ki67 indices did not correlate with the Gleason score ($r=-0.1$, $p=0.70$, Spearman's test). This lack of correlation could be due to the inhomogeneous group of patients selected randomly.

In summary, a spectrum of cytoplasmic CHK expression was seen in the pre-malignant and malignant lesions. This could be exploited to develop new drug targets.

CHAPTER 4: Exploring the potential of [^{11}C]choline PET/CT as a novel imaging biomarker for predicting early treatment response in prostate cancer.

Rationale

[^{11}C]Choline PET/CT has been shown to be an effective noninvasive method for detecting nodal disease (Contractor, Challapalli et al. 2011), metastatic disease (Krause, Souvatzoglou et al. 2011), and relapsed disease (Picchio and Castellucci 2012) in prostate cancer (PCa). However, there is limited data on [^{11}C]choline PET/CT in assessing response to a combination of androgen-deprivation and radiotherapy.

Radiotherapy (RT), along with androgen deprivation is a curative option for patients with localised or locally-advanced PCa (Peeters, Heemsbergen et al. 2006; Heidenreich, Bellmunt et al. 2011). Response to treatment is routinely assessed by prostate-specific antigen (PSA) levels. Standard magnetic resonance imaging (MRI) has limited value in assessing residual viable disease post-radiotherapy due to loss of zonal anatomy and diffuse low signal (Westphalen, McKenna et al. 2008). This limitation could potentially be overcome with dynamic contrast enhancement (DCE-MRI), diffusion weighted imaging (DWI-MRI), magnetic resonance spectroscopy (MRS) and PET, which can provide biological information about tissue perfusion, cellularity and metabolism.

Functional MRI techniques using DWI and choline metabolism have been evaluated for monitoring therapy response with varying results (Barrett, Gill et al. 2012; Valentini, Gui et al. 2012). The variable sensitivity of [^{11}C]choline PET/CT in identifying intra-prostatic lesions (Souvatzoglou, Weirich et al. 2011; Van den Bergh, Koole et al. 2012) and its high cost mandates a prospective feasibility study.

Therefore, this study was designed with the aim

- To evaluate the potential of [^{11}C]choline PET/CT as an early response biomarker to neo-adjuvant androgen-deprivation (NAD) and radical radiotherapy combined with concurrent androgen-deprivation (RT-CAD).

This study was used to test the hypothesis that use of functional imaging with PET would predict early response to treatment and the potential for alternative management strategies.

Materials and Methods

Patients

Consecutive patients with newly diagnosed, histologically confirmed localised (node-negative based on MRI size criteria) PCa fit for radical radiotherapy were enrolled. Thus the main inclusion and exclusion criteria for this study were:

Inclusion Criteria:

1) Histologically confirmed adenocarcinoma of the prostate.
2) Patients with localised prostate cancer with disease visible on the staging MRI scan.
3) Patients suitable for radical radiotherapy (conformally planned and treated with a dose of 74Gy/37fractions/7.5 weeks).
4) WHO performance status ≤ 2
5) Age 18 years and above.
6) Written informed consent.

Exclusion Criteria:

1) Node positive patients on staging investigations.

2) Any serious co-existing medical illness which will contradict radical radiotherapy.

3) Patients on any concurrent investigational agent.

4) Life expectancy <5 years.

5) Psychological, familial, sociological or geographical condition potentially hampering compliance with the study protocol and follow-up schedule.

6) Previous androgen deprivation.

7) Gold seed fiducial markers within the prostate.

Each patient underwent sequential [^{11}C]choline PET/CT scans at the following time points: prior to initiation of therapy (baseline), after at least 6-8 weeks of NAD (post-NAD) and finally at 4 months post radical RT-CAD (post-RT-CAD scan). Ethical approval for the study was granted by the North-London Ethics Committee. All patients gave written informed consent to participate in the study, according to the Declaration of Helsinki guidelines. The administration of radioactivity for the PET scans was approved by the Administration of Radioactive Substances Advisory Committee, United Kingdom.

Treatment: NAD and RT-CAD

In all patients, androgen deprivation was achieved using depot injections of luteinizing-hormone releasing hormone (LHRH) agonists in conjunction with initial anti-androgens. Patients received NAD for at least 6-8 weeks prior to the post-NAD scan and concurrently (CAD) with radical radiotherapy. Radiotherapy was planned and delivered as per standard departmental protocol. The aim was to deliver a minimum dose of 74 Gy to the prostate prescribed according to the International Commission on Radiation Units guidelines, respecting rectal dose constraints.

Imaging protocol

[^{11}C]choline was synthesised according to the method described by Pascali et al (Claudio Pascali 2000). Subjects fasted for 6 hours prior to procedure. All patients were scanned initially on a GE-Discovery-RX® PET/CT scanner. Due to unit closure, two patients could not have their post-NAD scans. The post RT-CAD scans in all ten patients were performed on a GE-Discovery-VCT PET/CT scanner. The images for both scanners were calibrated in Bq/mL which is the important parameter in calculating SUV. Phantom studies were performed to ensure protocol reproducibility on each machine, using near identical reconstruction parameters (**Table 16**). The patients were positioned such that the field of view (FOV) included the prostate with the lower border at the bottom of the ischial tuberosities. This was followed by a diagnostic quality CT scan (settings: 300 mA, 120kVp, 0.8 sec/rotation, 40mm beam collimation (total beam width), pitch 1.375 and slice thickness 3.75mm) which was used for attenuation correction and co-registration with the PET images. [^{11}C]choline was administered through a bolus intravenous injection over 10-30 seconds. The median (range) radioactivity administered per scan was 691 (479-745) MBq (specific activity of 5.7 GBq/μmol: radiochemical purity >97%). Dynamic PET scanning (3-dimensional acquisition) was commenced over a single bed position, covering the pelvis (axial FOV 15.7 cm; transaxial, 70 cm), for 65 minutes. Raw PET data were corrected for scatter and attenuation and reconstructed using iterative ordered subset expectation maximisation (OSEM) algorithm (**Table 16**).

All patients, except one in whom MRI was contraindicated, underwent standard MRI of the pelvis with phase array pelvic coil, from aortic bifurcation to pubic symphysis consisting of T1-weighted axial images; axial, sagittal and coronal T2 weighted sequences and small field of view (FOV) axial T2 weighted sequences

through the prostate. Diffusion weighted imaging was also available in 7 patients. The imaging was performed on a 1.5 Tesla scanner (Philips) in 2 patients and a 1.5 Tesla scanner (Siemens: Magnetom) in 7 patients.

Table 16: **Reconstruction parameters used in the 2 scanners involved in this study.**

Reconstruction Parameters	GE Discovery RX PET/CT scanner	GE Discovery VCT PET/CT scanner
Image reconstruction	OSEM, 8 iterations 21 subsets*	OSEM, 8 iterations 20 subsets*
Reconstruction zoom diameter	33.5 cm	33.5 cm
Reconstructed voxel size	2.6 mm, 2.6 mm and 3.3 mm in X, Y and Z co-ordinates, respectively	2.6 mm, 2.6 mm and 3.3 mm in X, Y and Z co-ordinates, respectively
Scanner Resolution (distance from FOV centre)	FWHM (mm)	FWHM (mm)
Axial (1cm)	5.3	5.8
Axial (10cm)	6.0	6.3
Transaxial (1cm)	4.8	4.9
Transaxial (10cm)	5.6	5.6

OSEM-Ordered subsets expectation maximisation, FOV-field of view, FWHM-Full width half maximum

* Data were binned into time frames as follows: 1 * 30 (background), 6* 10, 4* 20, 4* 30, 5* 120, 4* 180 and 4* 600 seconds.

Even though the two scanners do not have identical sensitivity, noise-equivalent counting (NEC) characteristics and spatial resolution, due to the similarity of the detectors, these differences would be relatively small and would not have a significant impact on SUV calculation.

Image analysis

The [^{11}C]choline PET/CT summed data (10–65 minutes) were reviewed slice-by-slice alongside the staging MRI studies by two experienced observers (AC, TB) in consensus, to manually outline the volumes of interest (VOIs; ROIs over several slices) for quantitative analysis. In addition the T2 weighted axial MRI was fused to the PET using MRI PET fusion software (**Figure 39**) to assist with ROI positioning, particularly for 'normal' prostate (Hermes diagnostics, Sweden). The following were outlined: most active tumour focus, normal (non-cancerous) prostate gland, obturator internus muscle (in high dose region of radiotherapy field), gluteus

maximus muscle (in low dose region of radiotherapy field), bone marrow (acetabulum; in radiotherapy field) and visible pelvic nodes (with uptake above background). The prostate volume in cm^3 was determined using a planimetric approach on the CT component of the PET/CT images. Data analysed with the whole prostate outlined and the results are given in **Appendix 3**.

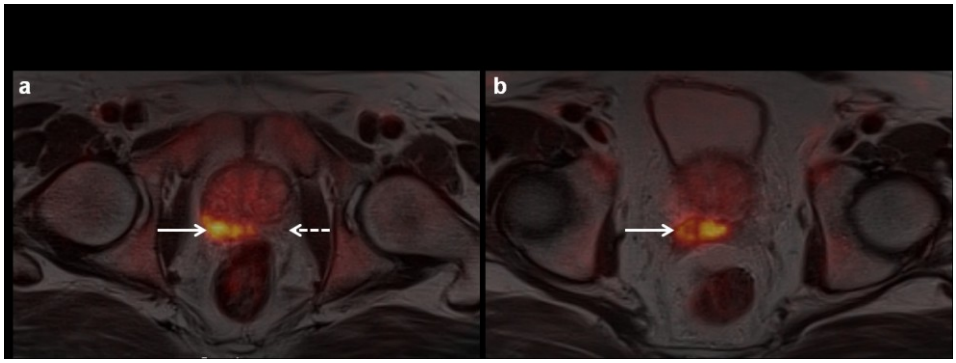

Figure 39: Axial [^{11}C]choline PET (Baseline) fused with T2 weighted axial MRI.
(**a**) Fused image at level of prostate showing active tumour focus (white arrow) in the right peripheral zone (PZ) and normal prostate (white dotted arrow) in the left PZ. (**b**) Fused image at level of seminal vesicles. The images correspond to patient no.1 as listed in Table 17.

The criteria for outlining the VOIs in each patient were as follows: The region with the most intense choline uptake corresponding to an area of disease on MRI (low T2 signal intensity with associated restricted diffusion) was outlined as tumour (Yamaguchi, Lee et al. 2005). The criteria for outlining 'normal' prostate was a region in the peripheral zone with no focal choline activity, absence of MRI criteria for disease and sextant free of disease on TRUS biopsy. In the one patient in whom MRI was contraindicated, tumour was outlined based on focal choline uptake in a sextant positive for disease on TRUS and normal prostate was not outlined (bilateral cores were positive on TRUS).

For the follow up measurements, the VOIs for tumour and normal prostate were positioned in the same sextant of the prostate for each patient by visually

referring to the baseline PET/ CT and MRI images, according to the distance from the level of the femoral head and pubic symphysis on the MR and CT images (Yamaguchi, Lee et al. 2005). All diameters of the manual ROIs were greater than 3 times the full-width-half-maximum (FWHM) of the camera (Boellaard 2009).

Analyses of the dynamic PET data were performed using Analyze® software (Analyze Version 7; Biomedical Imaging Resource, Rochester, USA). The [^{11}C]choline radioactivity concentration within the VOIs was determined and normalised to injected radioactivity and body weight to obtain the average and maximum SUV at 60 minutes ($SUV_{60,ave}$ and $SUV_{60,max}$). In order to account for inflammation post-radiotherapy, $TMR_{60,max}$ (ratio of tumour to gluteus maximus muscle $SUV_{60,max}$) was also estimated. SUV_{max} of tumour was also estimated at 15 and 30 min ($SUV_{15,max}$ and $SUV_{30,max}$). Baseline parameters were estimated in all ten patients. The percentage change in [^{11}C]choline uptake variables with treatment was calculated in eight patients who completed all scans as follows: changes with NAD as $((SUV_{baseline} - SUV_{post\text{-}NAD})/ SUV_{baseline})*100$ and changes with combined NAD and RT-CAD as $((SUV_{baseline} - SUV_{post\text{-}RT\text{-}CAD})/ SUV_{baseline})*100$.

Modelling of PET data

The venous blood proportions of [^{11}C]choline and its metabolite, [^{11}C]betaine were determined as previously described (Contractor, Kenny et al. 2009). A validated population-based total plasma input-function approach (Contractor, Kenny et al. 2012), and the modified-Patlak plot (Mankoff, Shields et al. 1996), were used (as described in detail in Chapter 3) to derive Ki ($Ki_{mod\text{-}pat}$) - a measure of net irreversible retention at steady-state within a VOI. The method implicitly assumes that the majority of labelled betaine in tumours is derived from systemic circulation (Roivainen, Forsback et al. 2000; Witney, Alam et al. 2012).

Statistical considerations

Preliminary studies have shown that patients with changes in [^{11}C]choline uptake >40% in individual patients can be classified as radiotracer responsive; i.e., statistically greater than noise (Kenny, Contractor et al. 2010). Variability in the measured change in choline within individuals has been estimated at ~0.15. Expected response to therapy is 60% of patients receiving radiotherapy. Power calculation (paired t-test) suggests that a number, n=7, of patients will give to the design a minimum power of .90 to detect a group difference in choline at a .05 error rate. The addition of n=2 patients to compensate for dropout and 2-3 patients to compensate for technical problems with imaging brings the total number of patients to n=12.

The median (range) was used as the primary descriptive statistics measure. Repeated-measures Analysis of Variance (ANOVA) and Tukey's multiple comparisons test was used to assess the significance of the change in [^{11}C]choline uptake between treatments (for the eight patients who completed all three scans). The association between baseline $SUV_{60,ave}$ or $SUV_{60,max}$ and initial PSA (n=10 patients), as well as similar associations between changes in uptake variables and changes in PSA levels, were assessed by Pearson's correlation test. The significance of differential uptake in tumour and the normal prostate was assessed by unpaired t test. A p value of ≤ 0.05 was considered significant. Statistical analyses were performed using Graph-Pad™ Prism software (version 4.0, San Diego California USA).

Results

Patient Characteristics

In total, 10 patients were recruited for the study, all of whom had [^{11}C]choline scans at baseline, post-NAD, and post-RT-CAD, except two patients who could not complete their post-NAD scans. Patients were scanned (post-NAD) after a median NAD duration of 77 days (range: 46 – 107 days). Post-RT-CAD scans were performed after a median of 113 days (range: 99 – 128 days) following completion of RT-CAD. The patient characteristics are shown in **Table 17**.

Table 17: **Patient characteristics**

Pt No	Stage (MRI)	Tumour on TRUS Biopsy	GS (positive cores/total cores) R, L	Overall GS	iPSA (ng/mL)	RT dose (Gy/#)	WPRT	Pelvic nodes*	Inguinal nodes*	Nadir PSA (ng/mL)	Recent PSA (ng/mL) §
1	T3bN0M0	Bilateral	4+3(3/5), 4+4(5/5)	8	28.5	74/37	Y	-	-	0.06	0.79
2	T2cN0M0	Bilateral	3+4(4/5), 3+3(1/5)	7	5.4	74/37	N	-	-	0.15	0.15
3	T3aN0M0	Bilateral	3+3(5/5), 3+4(5/5)	7	20	74/37	Y	R, L EI	R, L ing	<0.01	<0.01
4	T1cN0M0	Bilateral	3+3(1/5), 3+3(4/4)	6	9.2	74/37	N	-	R, L ing	0.02	0.40
5	T2aN0M0	Unilateral	0(2/2), 3+3(6/9)	6	11	74/37	N	R, L EI	R ing	0.11	0.27
6	T3aN0M0	Bilateral	3+4(4/6), 3+4(3/6)	7	13	46/23 + BRT	N	-	R, L ing	0.11	0.11
7	T2bN0M0	Unilateral†	0(6/6), 3+3(1/3)	6	17.1	74/37	Y	R, L EI	R, L ing	0.16	0.16
8	no MRI‡	Bilateral	4+3(6/6), 4+3(6/6)	7	16.5	72/32	Y	L, II	-	0.1	0.1
9	T3aN0M0	Unilateral	3+3(2/7),0(7/7)	6	10.1	74/37	N	-	-	0.01	0.01
10	T3aN0M0	Bilateral	4+3(1/3), 4+3(3/3)	7	30	74/37	N	R, L EI	R, L ing	<0.05	<0.05
	Median			**6.5**	**14.75**						

TRUS – Trans-rectal ultrasound guided biopsy, GS – Gleason score, iPSA – initial Prostate specific antigen, RT – Radiotherapy, WPRT- whole pelvic radiotherapy, BRT-Brachytherapy, Y- yes, N – no, R – right, L – left, EI – external iliac, II – internal iliac, * nodes picked up on PET/CT, † Unilateral disease on biopsy, but bilateral on MRI, ‡ MRI contra-indicated due to presence of pacemaker, § PSA at 26 months since completion of radiotherapy.

[^{11}C]Choline uptake in tumour, normal prostate, detected nodes and normal tissue

The primary prostate tumours were visible in all the patients (**Figure 40a**). The baseline median (range) $SUV_{60,ave}$ and $SUV_{60,max}$ in the tumours was 4.58 (2.33-7.08) and 8.58 (5.78-14.96), respectively. The median $SUV_{60,ave}$ and $SUV_{60,max}$ (2.76 and 5.87) of the normal prostate gland were significantly lower than those of the tumours (unpaired-t test; p= 0.004 and 0.007, respectively). There was physiological activity in the rectum, small bowel and bone marrow. In addition, there was tracer uptake above background activity in iliac nodes in five patients and in inguinal nodes in six patients (**Table 17**). In four of the patients, these were bilateral distal external iliac nodes and in one patient, a left internal iliac node (**Figure 41**). All of these nodes were less than a centimetre in size, and hence reported as node negative on the staging investigations based on size criteria. The median (range) $SUV_{60,ave}$ and $SUV_{60,max}$ in the detected iliac nodes was 2.33 (1.31-3.18) and 4.65 (3.06-9.34), respectively. The median $SUV_{60,ave}$ and $SUV_{60,max}$ (1.57 and 3.49) of the inguinal nodes were significantly lower than those of the tumour ($p<0.0001$: unpaired t-test) and was considered as probably reactive uptake and, therefore, non-metastatic. Similar findings were seen in the patient cohort discussed in Chapter 3.

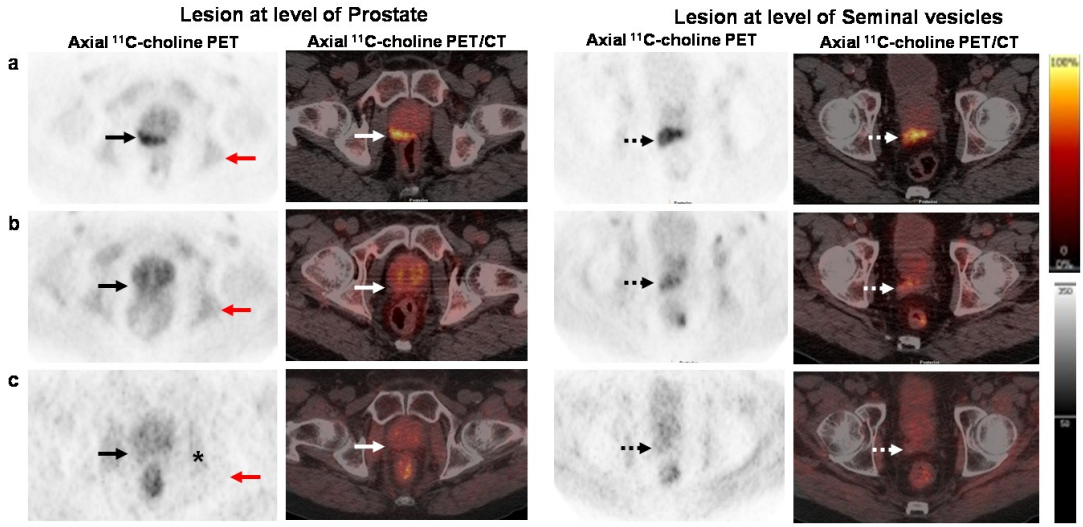

Figure 40: Axial [^{11}C]choline PET and fused PET/CT at level of the prostate and seminal vesicles (SV).

(a) Baseline scan with focal activity in the right peripheral zone (black & white arrows) and right SV (black & white dotted arrows). **(b)** Post-NAD scan (8-10 weeks after initiating neo-adjuvant androgen deprivation) with a marked reduction in [^{11}C]choline uptake in the peripheral zone and SV. **(c)** Post-RT-CAD scan (four months after completion of radiotherapy combined with concurrent androgen deprivation) with a further reduction in prostate activity, increased obturator internus muscular activity (asterisk) and reduced bone marrow activity (red arrows). The images correspond to patient no.1 as listed in **Table 17**.

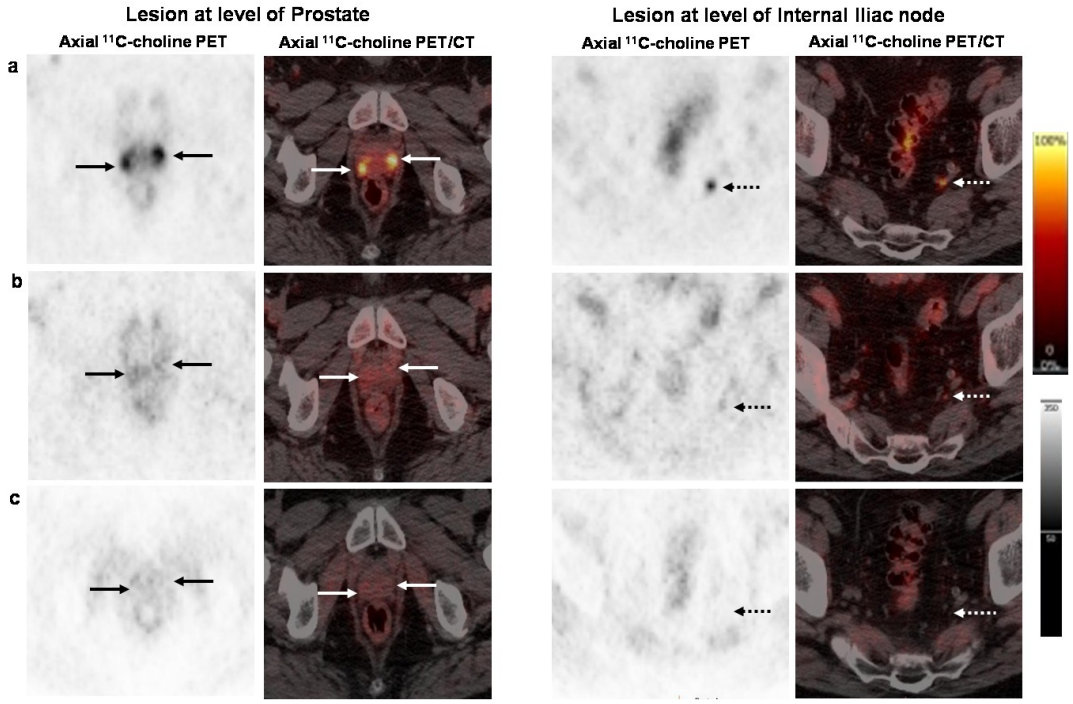

Figure 41: **Axial [^{11}C]choline PET and fused PET/CT at the level of prostate and left internal iliac node.**

(**a**) Baseline scan shows bilateral focal intense activity in the peripheral zone (arrows) and a 5mm left internal iliac node (dotted arrows). (**b**) Post-NAD (8-10 weeks after initiating neo-adjuvant androgen deprivation) scan shows a marked reduction, but focal low uptake in bilateral prostate (arrows) and focal low uptake in left internal iliac node (dotted arrows). Post-RT-CAD (4 months after completion of radiotherapy combined with concurrent androgen deprivation) scan shows very low uptake in the prostate but no uptake in the node **(c)**. The images correspond to patient no.8 as listed in **Table 17**.

The median time-activity curves (TACs) of the tumour, normal prostate and the iliac nodes are shown in **Figure 42**. In the primary prostate tumours, TACs expressed as $SUV_{60,ave}$ plateaued at ~ 15 min and demonstrated retention of activity until 60 min. There was an initial rise in the tumour radioactivity, when TACs were expressed as $SUV_{60,max}$, probably due to heterogeneous tumour delivery. In contrast to the primary tumour, there was lower radioactivity (over time) in the normal prostate and the detected iliac nodes.

There was a good linear fit of the modified Patlak plots suggesting net retention of [^{11}C]choline. The median (range) $Ki_{mod\text{-}pat}$ variables in the tumours, normal prostate and detected iliac nodes were 0.055 mL/min/cm^3 (0.019-0.113), 0.039 mL/min/cm^3 (0.015-0.069) and 0.032 mL/min/cm^3 (0.010-0.052), respectively. A significant association was seen between baseline tumour [^{11}C]choline uptake and initial PSA when the imaging variable was $SUV_{60,max}$ (Pearson's r=0.7, p=0.04) but not $SUV_{60,ave}$ (r=0.6, p=0.11) or $Ki_{mod\text{-}pat}$ (r=0.2, p=0.16).

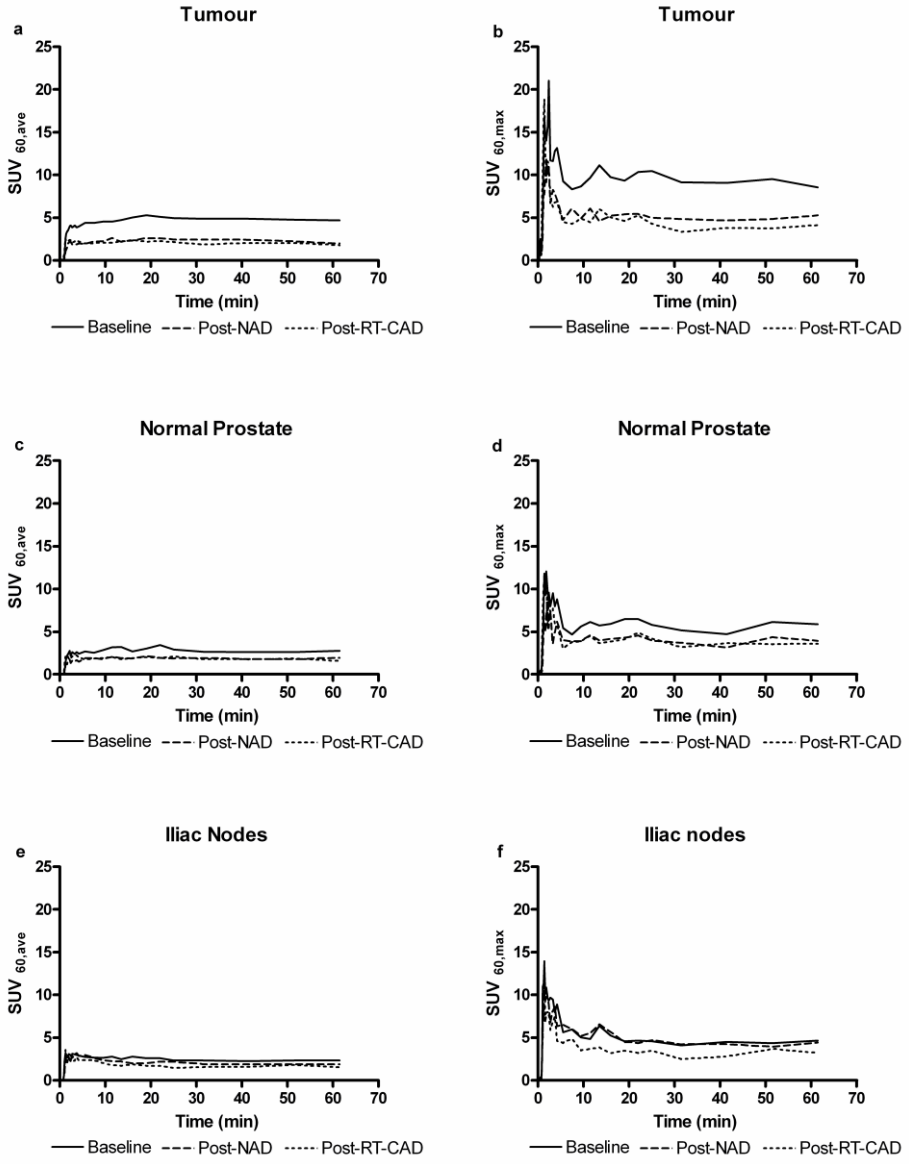

Figure 42: **Time activity curves (TACs) in tumour, normal prostate and detected iliac nodes.**

Median TACs expressed as $SUV_{60,ave}$ and $SUV_{60,max}$ at baseline, following treatment with neo-adjuvant androgen deprivation (Post-NAD), and radiotherapy combined with concurrent androgen deprivation (Post-RT-CAD) in the prostate tumour (**a, b**), normal prostate (**c, d**) and in the iliac nodes (**e, f**).

Effect of NAD and RT-CAD on tissue [^{11}C]choline uptake

The effect of therapy on [^{11}C]choline uptake in primary prostate tumours and normal tissues was compared. NAD and RT-CAD decreased tumour radiotracer uptake variables in all eight patients who completed both post-NAD and post-RT-CAD scans (**Figure 43; Table 18**). Repeated measures ANOVA demonstrated significant reductions for the following imaging variables: $SUV_{60,ave}$, $SUV_{60,max}$, $TMR_{60,max}$ and $Ki_{mod\text{-}pat}$ ($p<0.001$). There was a large reduction in radiotracer uptake in the interval between baseline and post-NAD scan. Within this period, NAD decreased tumour imaging variables by 26-60% for the following imaging variables: $SUV_{60,ave}$, $SUV_{60,max}$, TMR_{ave}, TMR_{max}, and $Ki_{mod\text{-}pat}$. The impact of NAD on iliac nodes (**Figure 41, Table 18**) and inguinal nodes (**Table 19**) was less remarkable. There was a reduction in [^{11}C]choline uptake seen within primary prostate tumours after RT-CAD treatment, though the magnitude of reduction was much less (12-27%; $p>0.05$) compared to that seen with NAD, except for TMR_{max} where a significant reduction (40%; $p<0.05$) was seen (**Table 20**). [^{11}C]Choline uptake was lower with the combined NAD and RT-CAD, by 52-62 % for the following imaging variables compared to baseline values: $SUV_{60,ave}$, $SUV_{60,max}$, $TMR_{60,max}$, and $Ki_{mod\text{-}pat}$ (**Table 18**). The magnitude of reduction in uptake was similar even at early time points ($SUV_{15,max}$ and $SUV_{30,max;}$ $p<0.001$, Repeated measures ANOVA; **Table 21**). The reduction in tumour [^{11}C]choline uptake variables was also seen when the patients who did not have a post-NAD scan were included in the analysis (**Table 22**). Again, the effects of treatment were less remarkable for iliac lymph nodes. Notably, the reduction in imaging variable, $Ki_{mod\text{-}pat}$ was more strongly associated with reduction in $SUV_{60,ave}$ ($r=0.7$, $p=0.04$) and $SUV_{60,max}$ ($r=0.6$, $p=0.05$) when all data (NAD and RT-CAD) were combined.

The therapy also caused a reduction in the [^{11}C]choline uptake in the normal prostate gland ($SUV_{60,ave}$: 43%; range: 13.8 – 72.2% and $SUV_{60,max}$: 39%; range: -13.7–70%: **Figure 42**). However, this was significantly lower than that observed in the primary tumours when the imaging variable was $SUV_{60,ave}$, $SUV_{60,max}$ and $Ki_{mod\text{-}pat}$ (unpaired t test; p=0.006, 0.02 and 0.04, respectively) with NAD and (unpaired t test; p=0.01, 0.02 and 0.03 respectively) with combined NAD and RT-CAD.

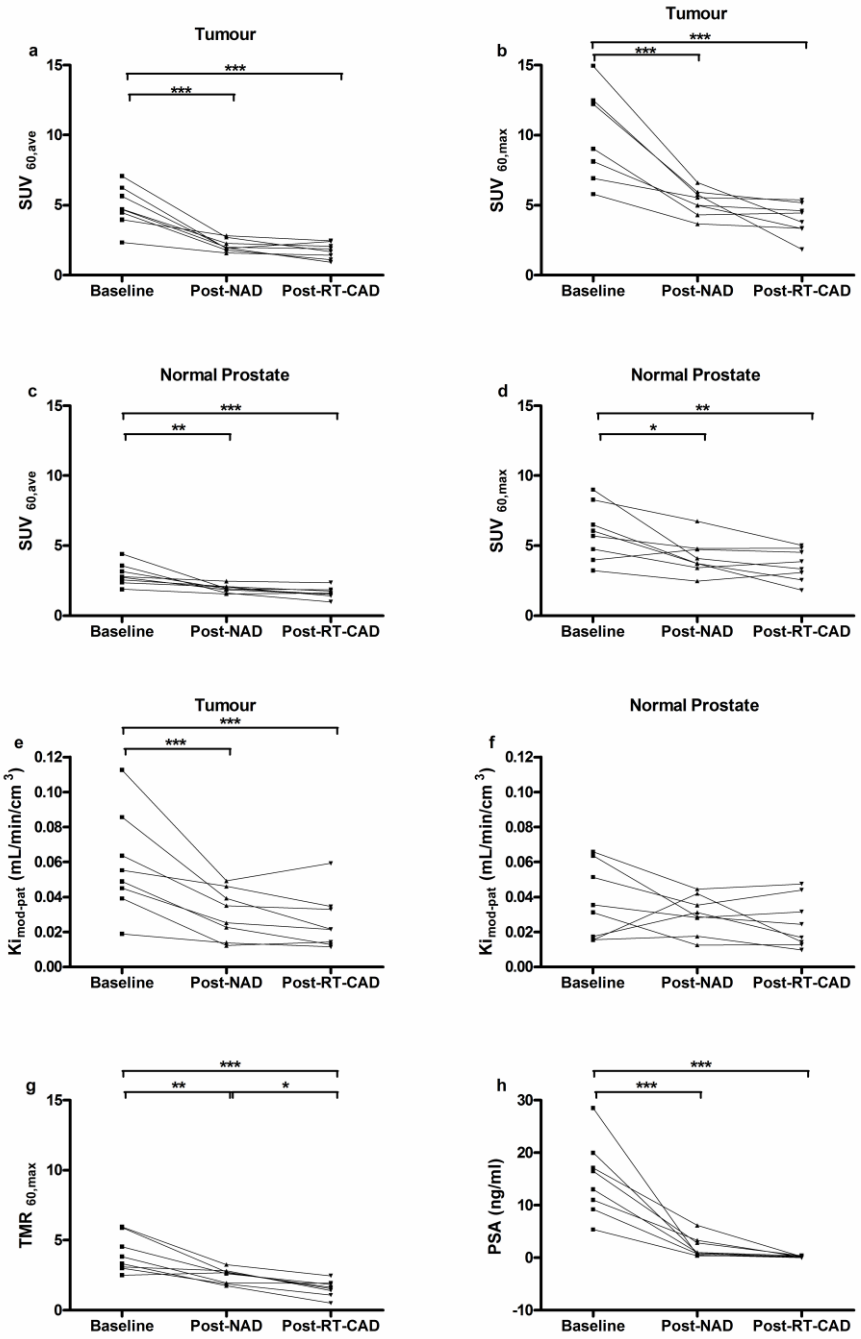

Figure 43: **Semi-quantitative and quantitative measures of choline uptake in prostate tumour, normal prostate and PSA levels.**

Trends in $SUV_{60,ave}$ and $SUV_{60,max}$ of tumour (**a**, **b**), normal prostate (**c, d**), Ki of tumour (**e**) and normal prostate (**f**), maximum tumour-muscle ratio TMR_{max}, (**g**) and PSA (**h**) at baseline, following neo-adjuvant androgen deprivation (Post-NAD) and radiotherapy combined with concurrent androgen deprivation (Post-RT-CAD) in eight patients who completed all three scans. *, **, *** denotes significant changes $p< 0.05$, $p<0.01$ and $p<0.001$ respectively.

Table 18: **Median [^{11}C]choline uptake variables in tumour, normal prostate and iliac nodes.**

Variables at baseline and reduction with neo-adjuvant androgen-deprivation (NAD) and radiotherapy combined with concurrent androgen-deprivation (RT-CAD) in 8 patients.

		SUV $_{60,ave}$	**SUV $_{60,max}$**	**Ki$_{mod-pat}$** (mL/min/cm^3)	**TMR $_{60,max}$**
Tumour	**Baseline**	4.71	8.58	0.052	3.58
		(2.33-7.08)	(5.78-14.96)	(0.019-0.113)	(2.50-5.96)
	Post-NAD	1.97	5.27	0.030	2.66
		(1.58-2.82)	(3.66-6.61)	(0.012-0.049)	(1.75-3.25)
	Post RT-CAD	1.79 (0.92-2.45)	4.13 (1.83-5.38)	0.022 (0.011-0.059)	1.59 (0.5-2.45)
	% Reduction NAD	58***	39***	42**	26***
	% Reduction NAD+RT-CAD	62***	52***	59*	57***
Normal Prostate	**Baseline**	2.76	5.87	0.033	
		(1.88-4.41)	(3.23-9.01)	(0.015-0.066)	
	Post-NAD	1.94	3.92	0.029	
		(1.56-2.47)	(2.48-6.75)	(0.012-0.044)	
	Post RT-CAD	1.57 (0.99-2.36)	3.60 (1.82-5.03)	0.021 (0.009-0.047)	
	% Reduction NAD	30**	33*	12	
	% Reduction NAD+RT-CAD	43***	39**	36	
Iliac nodes	**Baseline**	2.59	4.96	0.032	
		(1.31-3.18)	(3.06-9.34)	(0.010-0.052)	
	Post-NAD	1.89	4.43	0.032	
		(1.43-2.74)	(3.45-7.68)	(0.010-0.052)	
	Post RT-CAD	1.93 (0.42-3.10)	3.80 (0.87-7.73)	0.022 (0.005-0.041)	
	% Reduction NAD	27	11	0	
	% Reduction NAD+RT-CAD	25	23*	31*	

TMR-Tumour-to-muscle ratio, *, **, *** denotes significant changes ($p< 0.05$, $p<0.01$, $p<0.001$, respectively; Repeated measures ANOVA, Tukey's multiple comparison), Values in brackets represent the range.

Table 19: **Median [^{11}C]choline uptake variables in inguinal nodes at baseline and reduction with neo-adjuvant androgen-deprivation (NAD) in 8 patients.**

		$SUV_{60, ave}$	$SUV_{60, max}$
Inguinal nodes	**Baseline**	1.61 (1.15-2.69)	4.24 (2.38-8.57)
	Post-NAD	1.43 (0.78-2.22)	3.57 (1.85-7.29)
	% Reduction NAD	11	16

% Reduction with NAD not statistically significant
Values in brackets represent the range.

Table 20: **Median [^{11}C]choline uptake variables in tumour, normal prostate and iliac nodes.**
Reduction with radiotherapy combined with concurrent androgen-deprivation (RT-CAD) in 8 patients.

		$SUV_{60,ave}$	$SUV_{60,max}$	$Ki_{mod-pat}$ (mL/min/cm^3)	$TMR_{60,max}$
Tumour	**Post-NAD**	1.97 (1.58-2.82)	5.27 (3.66-6.61)	0.030 (0.012-0.049)	2.66 (1.75-3.25)
	Post RT-CAD	1.79 (0.92-2.45)	4.13 (1.83-5.38)	0.022 (0.011-0.059)	1.59 (0.5-2.45)
	% Reduction RT-CAD	12	22	27	40*
Normal Prostate	**Post-NAD**	1.94 (1.56-2.47)	3.92 (2.48-6.75)	0.029 (0.012-0.044)	
	Post RT-CAD	1.57 (0.99-2.36)	3.60 (1.82-5.03)	0.021 (0.009-0.047)	
	% Reduction RT-CAD	19	8	28	
Iliac nodes	**Post-NAD**	1.89 (1.43-2.74)	4.43 (3.45-7.68)	0.032 (0.010-0.052)	
	Post RT-CAD	1.93 (0.42-3.10)	3.80 (0.87-7.73)	0.022 (0.005-0.041)	
	% Reduction RT-CAD	-2	14	30*	

TMR-Tumour-to-muscle ratio, * denotes significant changes ($p < 0.05$; Repeated measures ANOVA, Tukey's multiple comparison), Values in brackets represent the range.

Table 21: **SUV_{max} of tumour at early and late imaging time points**
Median [^{11}C]choline uptake variables in tumour at baseline and reduction with neo-adjuvant androgen-deprivation (NAD) and radiotherapy combined with concurrent androgen-deprivation (RT-CAD) in 8 patients.

		$SUV_{15,max}$	$SUV_{30,max}$	$SUV_{60,max}$
Tumour	**Baseline**	9.78 (5.79-12.74)	9.15 (4.35-11.77)	8.58 (5.78-14.96)
	Post-NAD	5.22 (3.28-801)	4.84 (2.80-5.49)	5.27 (3.66-6.61)
	Post RT-CAD	5.05 (3.20-6.66)	3.32 (2.20-4.38)	4.13 (1.83-5.38)
	% Reduction NAD	47***	47***	39***
	% Reduction NAD+RT-CAD	48***	64***	52***

*** denotes significant changes ($p<0.001$; Repeated measures ANOVA, Tukey's multiple comparison), Values in brackets represent the range.

Table 22: **Median [^{11}C]choline uptake variables in tumour, normal prostate, iliac nodes, normal tissue and PSA at baseline and changes with combined neo-adjuvant androgen-deprivation (NAD) and radiotherapy combined with concurrent androgen-deprivation and RT-CAD in 10 patients.**

		$SUV_{60,ave}$	$SUV_{60,max}$	$Ki_{mod-pat}$ (mL/min/cm^3)			$SUV_{60,ave}$	$SUV_{60,max}$	$Ki_{mod-pat}$ (mL/min/cm^3)			
Tumour	**Base line**	4.58	8.58	0.055	**OI**	**Base line**	1.12	3.30	0.016	**PSA**	**Base line**	14.75
		(2.33-7.08)	(5.78-14.96)	(0.019-0.113)			(0.64-2.06)	(1.65-4.36)	(0.006-0.030)	**(ng/mL)**		(5.4-30)
	Post Tx	1.79	4.04	0.027		**Post Tx**	1.96	4.63	0.031		**Post Tx**	0.12
		(0.92-2.45)	(1.83-5.38)	(0.011-0.059)			(1.15-2.33)	(1.82-7.20)	(0.015-0.044)			(0.03-0.4)
	% Reduction	61***	53***	51***		**% Reduction**	-76**	-40**	-89***		**% Reduction**	99***
Iliac nodes	**Base line**	2.33	4.65	0.032	**GM**	**Base line**	0.76	2.43	0.013	**Prostate Volume**	**Base line**	33.73
		(1.31-3.18)	(3.06-9.34)	(0.010-0.052)			(0.50-1.10)	(1.79-3.75)	(0.004-0.018)	**(cm^3)**		(17.29-73.87)
	Post Tx	1.52	3.22	0.022		**Post Tx**	0.97	2.78	0.014		**Post Tx**	27.3
		(0.42-3.10)	(0.87-7.73)	(0.005-0.041)			(0.69-1.14)	(2.11-3.66)	(0.007-0.027)			(14.58-56.03)
	% Reduction	35*	31*	30*		**% Reduction**	-27**	-14**	-8*		**% Reduction**	19*
$TMR_{60,max}$	**Base line**		3.53		**BM**	**Base line**	1.22	4.25	0.021			
			(2.50-5.96)				(0.98-2.16)	(2.47-6.71)	(0.007-0.034)			
	Post Tx		1.48			**Post Tx**	0.39	1.65	0.006			
			(0.50-2.45)				(0.26-0.90)	(0.76-3.19)	(0.002-0.021)			
	% Reduction		58***			**% Reduction**	68***	61***	71***			
Normal Prostate	**Base line**	2.76	5.87	0.039								
		(1.88-4.41)	(3.23-9.01)	(0.015-0.069)								
	Post Tx	1.57	3.6	0.024								
		(0.99-2.36)	(1.82-5.35)	(0.009-0.047)								
	% Reduction	43**	39**	39*								

-ve sign indicates an increase. Tx- treatment (NAD+ RT-CAD), TMR-Tumour-to-muscle ratio, OI-obturator internus, GM-gluteus maximus, BM-bone marrow, PSA-Prostate specific antigen. Values in brackets represent the range. *, **, *** denotes significant changes ($p< 0.05$, $p<0.01$, $p<0.001$, respectively; Paired t-test).

In contrast to changes in uptake seen in primary prostate tumours and to a lesser extent in iliac lymph nodes, NAD did not affect [^{11}C]choline imaging variables within muscle (obturator internus and gluteus maximus muscles) or bone marrow (**Figure 44, Table 23**). RT-CAD in comparison significantly increased tracer uptake in muscle within the high-dose region of the radiotherapy field (obturator internus) by 47-123% depending on imaging variable. Visually, there was an increase in uptake in the obturator internus muscle (**Figure 40c**). Expectedly there was a less remarkable increase in uptake after RT-CAD, in muscle within the low-dose region of the radiotherapy field (gluteus maximus) by 2-26%. While NAD alone had no effect on bone marrow tracer uptake, RT-CAD significantly decreased tracer uptake in the bone marrow by 60-70%.

Effect of NAD and RT-CAD on PSA levels

The combination of NAD and RT-CAD decreased PSA levels in all eight patients who completed both post-NAD and post-RT-CAD scans (**Table 23**). Repeated measures ANOVA demonstrated significant reductions in PSA levels after combined therapy (99%; $p < 0.0001$) with a large reduction (94%) after NAD (**Figure 43**). There was no measurable change in prostate volume within the study period.

There was a good association between reductions in tumour tracer uptake and corresponding reductions in PSA levels when the imaging variable was $SUV_{60,ave}$ ($r=0.7$, $p=0.04$), but not $SUV_{60,max}$ ($r=0.6$, $p=0.09$) after NAD. However, this association with $SUV_{60,ave}$ was lost after RT-CAD ($r=0.5$, $p=0.19$).

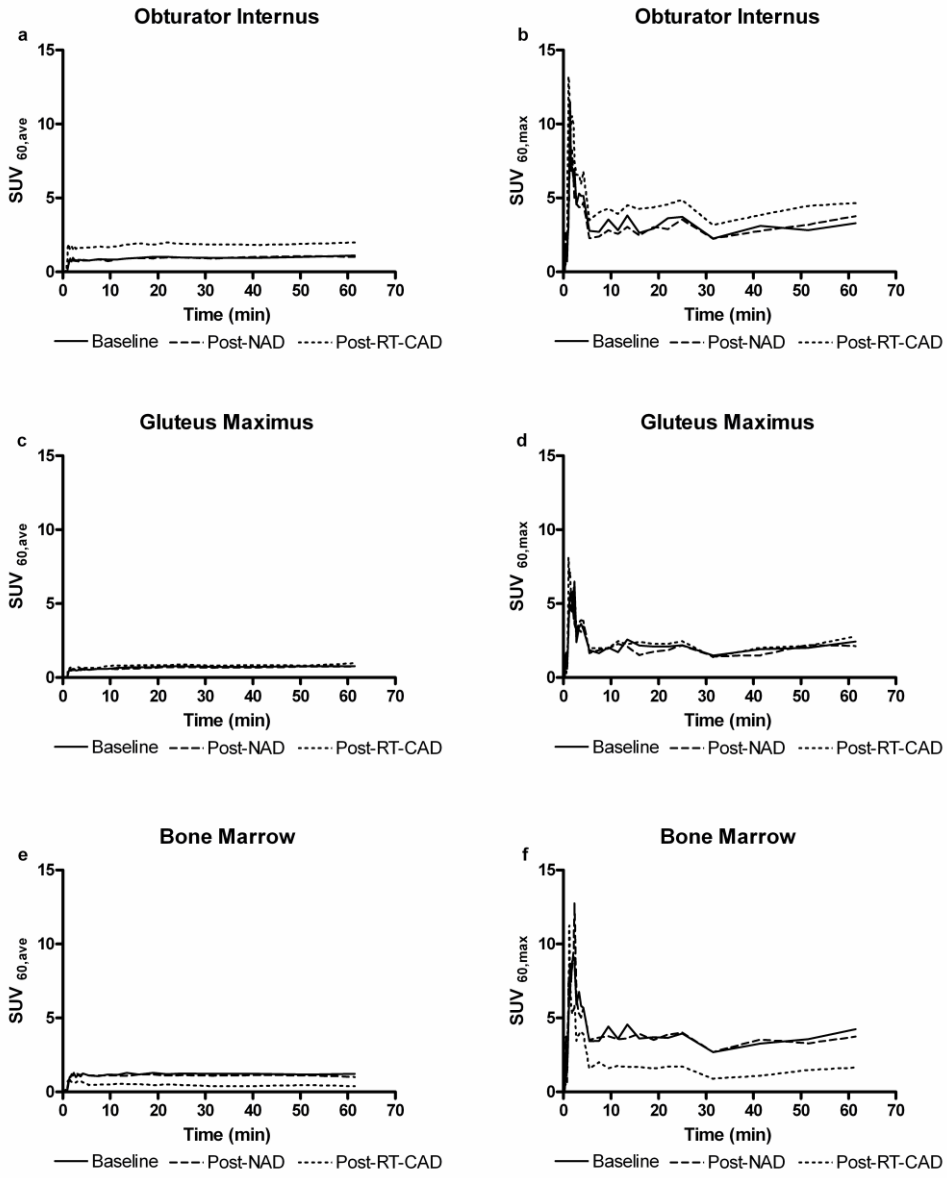

Figure 44: **Changes in the median $SUV_{60,ave}$- and $SUV_{60,max}$- derived TACs of normal tissues.**

TACs at baseline, after neo-adjuvant androgen deprivation (Post-NAD), and radiotherapy combined with concurrent androgen deprivation (Post-RT-CAD). The left panels represent $SUV_{60,ave}$ and the right panels represent plots of $SUV_{60,max}$. The plots were obtained from manual regions of interest placed on the obturator internus muscle (**a, b**); gluteus maximus muscle (**c, d**) and bone marrow (**e, f**).

Table 23: **Median [^{11}C]choline uptake variables in normal tissue and PSA at baseline and changes with neo-adjuvant androgen-deprivation (NAD) and changes with radiotherapy combined with concurrent androgen-deprivation (RT-CAD) in 8 patients.**

		$SUV_{60, ave}$	$SUV_{60, max}$	$Ki_{mod-pat}$ (mL/min/cm^3)			
OI	**Baseline**	1.12 (0.64-2.06)	3.30 (1.65-4.36)	0.013 (0.006-0.030)	**PSA (ng/mL)**	**Baseline**	14.75 (5.4-28.5)
	Post-NAD	1.02 (0.89-1.19)	3.77 (1.87-4.89)	0.017 (0.008-0.024)		**Post-NAD**	0.96 (0.41-6.16)
	Post RT-CAD	2.03 (1.15-2.33)	4.86 (1.82-7.20)	0.029 (0.015-0.040)		**Post RT-CAD**	0.16 (0.03-0.4)
	% Reduction NAD	9	-14	-33		**% Reduction NAD**	94***
	% Reduction NAD+RT-CAD	-81***	-47**	-123**		**% Reduction NAD+RT-CAD**	99***
GM	**Baseline**	0.74 (0.50-1.10)	2.45 (1.79-3.75)	0.010 (0.004-0.018)	**Prostate Volume (cm^3)**	**Baseline**	31.08 (17.29-73.87)
	Post-NAD	0.73 (0.61-0.86)	2.13 (1.30-3.29)	0.009 (0.005-0.020)		**Post-NAD**	30.66 (15.28-64.87)
	Post RT-CAD	0.93 (0.69-1.14)	2.49 (2.11-3.66)	0.012 (0.007-0.027)		**Post RT-CAD**	27.3 (14.58-56.03)
	% Reduction NAD	1	14	3		**% Reduction NAD**	1
	% Reduction NAD+RT-CAD	-26*	-2	-20		**% Reduction NAD+RT-CAD**	12
BM	**Baseline**	1.29 (0.98-2.16)	5.06 (2.47-6.71)	0.020 (0.007-0.034)			
	Post-NAD	1.01 (0.67-2.08)	3.74 (2.11-6.33)	0.016 (0.005-0.035)			
	Post RT-CAD	0.51 (0.26-0.90)	1.78 (0.76-3.19)	0.006 (0.002-0.021)			
	% Reduction NAD	22	26	22			
	% Reduction NAD+RT-CAD	60***	65***	70***			

-ve sign indicates an increase. OI-obturator internus, GM-gluteus maximus, BM-bone marrow, PSA-Prostate specific antigen, *, **, *** denotes significant changes ($p< 0.05$, $p<0.01$, $p<0.001$, respectively; Repeated measures ANOVA, Tukey's multiple comparison). Values in brackets represent the range.

Discussion

This proof of concept study shows that choline uptake in prostate tumours, determined by [^{11}C]choline PET/CT, is sensitive to NAD and RT-CAD and could be used as an objective quantitative tool for response assessment. NAD decreased tumour imaging variables by 26-60% for $SUV_{60,ave}$, $SUV_{60,max}$, TMR_{ave}, TMR_{max}, and $Ki_{mod-pat}$. RT-CAD also decreased [^{11}C]choline uptake within primary prostate tumours (though of lesser magnitude: 12-27%; $p>0.05$), compared to that seen with NAD, except for TMR_{max} where a significant reduction (40%; $p<0.05$) was seen. The kinetics of tumour [^{11}C]choline uptake was rapid, reaching a plateau within 15 min, suggesting that earlier time points, when levels of radiolabelled metabolites are low, could be explored to enhance patient comfort and improve PET count statistics.

To date, only anecdotal reports (DeGrado, Coleman et al. 2001; De Waele, Van Binnebeek et al. 2010) and two small clinical studies (Giovacchini, Picchio et al. 2008; Fuccio, Schiavina et al. 2011) have assessed the role of [^{11}C]choline PET as a method to monitor the therapeutic effects of androgen deprivation therapy (ADT). Fuccio et al (Fuccio, Schiavina et al. 2011) retrospectively evaluated the effect of 6 months of androgen deprivation (Zoladex in 12 and Bicalutamide in 2 patients) in 14 prostate cancer patients with recurrence after radical prostatectomy. They concluded that androgen deprivation significantly decreases [^{11}C]choline uptake in androgen sensitive patients. In another study Giovacchini et al (Giovacchini, Picchio et al. 2008), showed an average reduction of 45% in the [^{11}C]choline uptake (SUV_{max}) from 11.8 to 6.4 with a 78% decrease in PSA with a median of 4 months of bicalutamide therapy in 6 patients with primary prostate cancer. This is a similar magnitude of reduction in SUV_{ave} and SUV_{max} in the prostate tumours to our study, with a 94% reduction in PSA with NAD. The possible mechanisms of decrease in [^{11}C]choline uptake consequent to androgen deprivation include: a) thinning and

atrophy of glandular cells, b) down-regulation of the expression of genes involved in lipid metabolism, and c) possible decrease in choline kinase and choline transporter activity and d) cell cycle arrest and apoptosis (Giovacchini 2011).

Notably, the initial PSA showed good association with baseline $SUV_{60,max}$ (r=0.7, p=0.04) but not with $SUV_{60,ave}$ (r=0.6, p=0.11), a finding that may be attributed to potentially heterogeneous low-grade disease in four patients (**Table 17**). Although NAD induced significant reductions in PSA (94%), the magnitude of change in [^{11}C]choline uptake was lower than for PSA. Despite this, a good association was found between the changes in PSA and $SUV_{60,ave}$ (r=0.7, p=0.04), consistent with the effect of NAD on the prostate and systemic PSA expression. In support of this assertion, the net retention of radiotracer at steady-state ($Ki_{mod-pat}$; broadly indicative of the conversion of [^{11}C]choline to [^{11}C]phosphocholine) also decreased after treatment. Low-grade lesions probably precluded $SUV_{60,max}$ being a sensitive endpoint variable for evaluating efficacy of NAD (PSA correlation: r=0.6, p=0.09).

Interestingly, a wide range of reduction in $SUV_{60,ave}$ (38 – 83.7%) and $SUV_{60,max}$ (22.2 – 85.3%) was seen with combined NAD and RT-CAD despite patients universally achieving PSA suppression (99% reduction: narrow range of 93.5 – 99.7%). This suggests that in spite of a global reduction in PSA following NAD and RT-CAD there is a differential reduction in [^{11}C]choline uptake which could perhaps provide prognostic information in a larger study with long term outcome data. Furthermore the wide range of reduction (2-71% reduction) in the TMR post-RT-CAD highlights the fact that PSA may be a suboptimal surrogate for predicting overall biological response. While PSA is a useful marker of treatment response, it takes years for trials using PSA to mature. PSA also has other notable limitations: fluctuations in PSA (Hanlon, Pinover et al. 2001), long time to reach nadir

(Buyyounouski 2010), and lack of correlation with treatment outcomes (Collette, Burzykowski et al. 2006); also indicating that early PSA changes could have poor specificity. A promising alternative method, [^{11}C]choline PET/CT offers the potential for spatial visualisation of choline-metabolism at multiple disease sites (local and distant) in a single scan (Jadvar 2012).

There is paucity of data on use of [^{11}C]choline PET to monitor response to radiotherapy and the optimal time-point for this assessment is unknown. Casamassima and colleagues inferred that high dose radiotherapy is effective in eradication of limited nodal recurrences as detected by choline PET/CT 2 months post-RT (Casamassima, Masi et al. 2011). More recently, in a study of 11 patients with intermediate-risk PCa, Amani and co-workers evaluated sequential [^{11}C]choline PET/CT scans before and up to 12 months after completion of RT (74Gy/ 37 fractions). None of the patients received hormonal therapy. They concluded that RT significantly decreased intra-prostatic [^{11}C]choline uptake (as measured by SUV_{max} and TMR) (Amanie, Jans et al. 2013). Selection of the four month RT-CAD interval was based on a ^{18}F-fluorodeoxyglucose PET study, which reported false positive findings when imaging was conducted at 1 month (Greven, Williams et al. 1994). However, the optimum time point requires further study.

Radiotherapy (RT-CAD) resulted in minor overall reductions in tumour [^{11}C]choline uptake. It was postulated that this could signify sterilisation of the prostate. While direct investigation of this biology will entail histopathological assessment, the higher $SUV_{60,max}$ (above background) seen in the prostate could be due, in part to post-radiotherapy inflammation (all patients achieved excellent biochemical control (**Table 17**)). This probably resulted in the loss of association between PSA and $SUV_{60,max}$ after RT-CAD compared to NAD alone. Interestingly RT-CAD increased OI muscle activity. This and the decrease in bone-marrow

uptake could be attributed to radiotherapy, as there was no significant change in uptake in these normal tissues after NAD alone.

Radiotherapy causes inflammation through release of pro-inflammatory cytokines (Rodemann and Blaese 2007). Potential mechanisms linking increased [^{11}C]choline uptake with inflammation include up-regulation of CHKα in macrophages, and hyper perfusion associated with regional inflammation (Roivainen, Parkkola et al. 2003). $TMR_{60,max}$ was implemented in an attempt to overcome the systematic bias on SUV variables induced by radiotherapy. The magnitude of reduction in $TMR_{60,max}$ after RT-CAD (40%; $p<0.05$) was higher than that of SUV supporting the notion that tumour/tissues in the radiotherapy field-of-view may have an increase in uptake due to radiotherapy related inflammation.

The non-malignant normal prostate gland also showed [^{11}C]choline uptake, albeit significantly lower than that in tumour foci. This heterogeneity of [^{11}C]choline uptake was also reported in one other study (Piert, Park et al. 2009). A reduction in uptake (lower magnitude than in tumours) with NAD and RT-CAD was also seen in the normal gland suggesting a global metabolic change with therapy.

A high radiotracer uptake over and above background levels in the iliac nodes of 5 patients was observed, which were less than a centimetre in size and, hence, reported as node negative on the staging MRI. It has been previously shown that [^{11}C]choline PET/CT has higher sensitivity and specificity for detecting nodal disease, including sub-centimetre disease (Contractor, Challapalli et al. 2011). This could indicate the presence of microscopic metastatic disease in these nodes. Apart from the internal iliac node in patient 8, there was no change in the $Ki_{mod\text{-}pat}$ of the distal external iliac nodes with therapy. This suggests that the uptake in the distal external iliac nodes (next echelon of nodes from inguinal), represents non-

metastatic inflammatory uptake as in the inguinal nodes (Contractor, Challapalli et al. 2011).

While this study focussed on detailed assessment of sequential imaging variables, a key limitation was the small sample size masking true associations. However, this study is a useful precursor to a larger study associated with long term outcome data, using imaging variables defined here. In addition, further studies should include patients with extra prostatic foci. The use of two different scanners was an additional limitation. Delineation of the tumour foci, normal prostate and subcentimeter lymphnodes could give rise to uncertainties in measuring choline uptake due to partial-volume effect. This has not been corrected, as the partial-volume correction algorithms assume homogeneous tracer uptake (Aston, Cunningham et al. 2002). Ideally I would have liked to co-localise the foci of [^{11}C]choline uptake with template-based pathology, however, this was not feasible as TRUS-guided biopsies are routinely used for diagnosis (2010). In an attempt to overcome this limitation, fusion of the MRI to the PET was performed to facilitate tumour localisation.

In conclusion, the consistent decrease in the [^{11}C]choline uptake variables with treatment, particularly $SUV_{,ave}$ and $TMR_{,max}$, supports the choice of analysis. SUV and TMR_{max} (at early and/or late time-points) warrant further evaluation as objective measures of response to NAD and RT-CAD, alongside functional MRI parameters and PSA as early response biomarker endpoints in PCa during radical treatment. Long-term follow-up in a larger cohort of patients, including those with pelvic nodal disease will be required to conclusively determine whether [^{11}C]choline PET/CT would predict true long-term biochemical control or relapse and to permit exploitation of this technology as a vehicle for response evaluation in radiotherapy dose-escalation trials, as well as novel hormonal therapies.

CHAPTER 5: Deuterium substituted [^{18}F]fluoromethyl-[1,2-$^{2}H_4$]choline PET/CT: Biodistribution, radiation dosimetry and imaging in Non-Small Cell Lung Carcinoma.

5.1: [^{18}F]D4-FCH: Biodistribution and radiation dosimetry in healthy volunteers

5.1.1: Rationale

The short physical half-life of [^{11}C] in [^{11}C]choline (20.4 min) is, disadvantageous for routine clinical use. As a result [^{18}F]-labelled choline analogs were developed to overcome this limitation (**Figure 45**). The longer half-life of ^{18}F (109.8 min) is potentially advantageous in permitting late imaging of tumours when sufficient clearance of parent tracer in systemic circulation had occurred. Since [^{18}F]fluoromethylcholine ([^{18}F]FCH) was first developed by DeGrado et al in 2001 (DeGrado, Coleman et al. 2001), it has been extensively used in patients with no reported adverse effects.

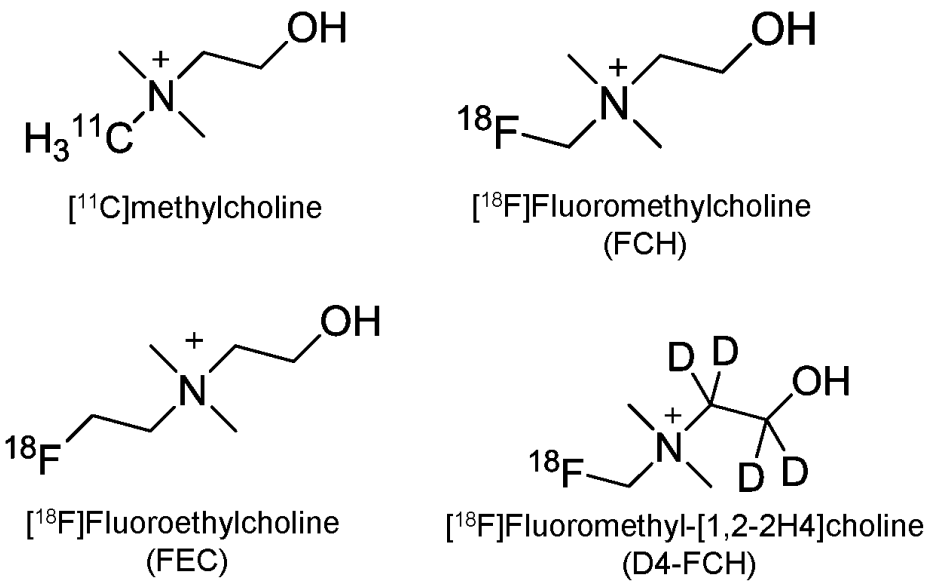

Figure 45: Major choline-based tracers in current use and in development.

[^{11}C]Choline (and fluoro-analogue) is, however, readily oxidised to [^{11}C]betaine by choline oxidase mainly in kidney and liver tissues, with metabolites detectable in plasma soon after injection of the radiotracer (Roivainen, Forsback et al. 2000; Bansal, Shuyan et al. 2008; Smith, Zhao et al. 2011). This makes discrimination of the relative contributions of parent radiotracer from catabolites difficult when a late imaging protocol is used. A more metabolically stable FCH analogue, [^{18}F]fluoromethyl-[1,2-$^{2}H_4$]choline ([^{18}F]D4-FCH), based on the deuterium isotope effect (Gadda 2003) has been developed (**Figure 45**). The simple substitution of Deuterium [^{2}D] for Hydrogen [^{1}H] and the presence of [^{18}F] improves the stability of the compound and reduces degradation of the parent tracer (Leyton, Smith et al. 2009; Smith, Zhao et al. 2011; Witney, Alam et al. 2012). This modification is hypothesised to increase the net availability of the parent tracer for phosphorylation and trapping within cells leading to a better signal-to-background contrast, thus improving tumour detection sensitivity of PET.

[^{18}F]D4-FCH has been validated for imaging tumours pre-clinically and was found to be a very promising, metabolically stable radiotracer for imaging choline metabolism in tumours (Leyton, Smith et al. 2009; Witney, Alam et al. 2012).

In order to translate the pre-clinical findings into humans, this study in healthy volunteers was designed with the following aim:

- To evaluate the biodistribution, dosimetry and safety of [^{18}F]D4-FCH in healthy volunteers.

5.1.2: Materials and Methods

5.1.2.1: Radiopharmaceutical Preparation

[^{18}F]D4-FCH was synthesised from the precursor as previously described (Smith, Zhao et al. 2011). The radiochemical purity of [^{18}F]D4-FCH was 100% with a mean (±SD; range) specific activity of 48.4 GBq/μmol (±22.8; 27.3-99.4 GBq/μmol) and a pH of 5.5 (±0.39; 4.84-5.88). The average level of the precursor D4-N, N-dimethylaminoethanol (D4-DMAE) used was 2.4 μg/ mL (±1.52; 0.8 – 4 μg/ mL).

5.1.2.2: Subjects

Eight healthy volunteers (4 men, 4 women), with a mean (±SD; range) age of 62.6 years (±6.12; range: 55-71 years), and mean weight of 65.4 kg (±16.6; range: 46.2-96.7 kgs) were enrolled. The main inclusion and exclusion criteria for this study were:

Inclusion Criteria:

Subjects were included in the study if they meet all of the following criteria:

1) Male or female aged 50 years or above.
2) If female, the subject is either post-menopausal (at least 1 year), or surgically sterilised (has had a documented bilateral oophorectomy and/or documented hysterectomy for at least 2 years). All female subjects of child bearing potential must have a negative urine beta human chorionic gonadotropin (β-hCG) pregnancy test (urine dipstick) done at initial screening (up to 21 days before administration) and on the day of tracer administration. The result of the pregnancy test must be known before administration of [^{18}F]D4-FCH Injection.

3) The subject was able and willing to comply with study procedures, and provide a signed and dated informed consent.
4) The subject had a normal medical history with no significant co morbidities, physical examination findings, and vital signs during the screening period (from 21 days before administration).
5) The subject's ECG and clinical laboratory tests were within normal limits and/or considered clinically insignificant.
6) Drug and Alcohol screening tests were negative.

Exclusion Criteria:

Subjects were excluded from participating in this study if they met any of the following criteria:

1) The subject was lactating.
2) The subject had been previously included in this study.
3) The subject had received, or is scheduled to receive, another investigative medicinal product/radioactive tracer 1 month before administration of [^{18}F]D4-FCH Injection.
4) The subject had received any chemotherapy, immunotherapy, biologic therapy or investigational therapy within 14 days or five half-lives of a drug (whichever is longer) prior to the first dose of [^{18}F]D4-FCH Injection.
5) The subject had received ionising radiation exposure from their occupation or from participation in clinical trials within the 3 months prior to their enrolment.

Subjects were asked to fast for 4-6 hours prior to tracer injection. Ethical approval for the study was granted by the West-London Research Ethics Committee. All volunteers gave written informed consent to participate in the study, according to

the Declaration of Helsinki guidelines. The administration of radioactivity for the PET/CT scans was approved by the Administration of Radioactive Substances Advisory Committee, United Kingdom. Medicines and Healthcare products Regulatory Agency (MHRA) has approved this study as a non-investigational medicinal product (IMP) study.

5.1.2.3: Safety

Safety data collected up to 72 h after injection included adverse events (AEs), graded according to common toxicity criteria (CTC v. 4.03); vital signs (blood pressure, respiratory rate, heart rate, and body temperature); physical examination (cardiovascular, lung, abdomen, and neurologic examinations); electrocardiogram; and laboratory parameters (serum biochemistry, haematology, coagulation, and urinalysis). Blood samples were collected through an in-dwelling cannula, and to avoid occlusion, heparinised saline was used to maintain line patency.

5.1.2.4: Image Acquisition and In Vivo Activity Measurement

Images were acquired on a Siemens Biograph 6 True Point PET/CT scanner (with TrueV; extended field of view) with 21.6cm axial and 60.5cm transaxial fields of view. **Table 24** describes the image acquisition protocol. The mean (±SD; range) injected [^{18}F]D4-FCH activity and D4-FCH cold dose in the subjects were 161 MBq (±2.17; 156-163 MBq) and 4.5 µg (±1.07; 2–5 µg), respectively.

Table 24: **Image acquisition protocol**

Scan	Field of view (FOV)	Number of bed positions	Minutes per bed position
Attenuation CT1*	Vertex to Mid-thigh	6-7	
[^{18}F]D4-FCH Injection			
Emission scan 1†	Vertex to Mid-thigh‡	6-7	1
Emission scan 2	Vertex to Mid-thigh	6-7	2
Emission scan 3	Vertex to Mid-thigh	6-7	5
Emission scan 4	Vertex to Mid-thigh	6-7	5
Voiding			
Attenuation CT2*	Vertex to Mid-thigh	6-7	
Emission scan 5	Vertex to Mid-thigh	6-7	7
Emission scan 6	Vertex to Mid-thigh	6-7	7

***** CT settings; 130 kV, 15 effective mAs, pitch 1.5, slice thickness 5 mm, rotation time 0.6 sec, and effective dose 2.5 mSv.
†Emission data were reconstructed using the ordered-subsets expectation maximisation (OSEM) algorithm (3 iterations and 21 subsets).
‡Imaging performed caudo-cranially.

Volumes of interest (VOIs) were delineated manually on the attenuation CT scan, using a circle of a fixed diameter, depending on the size of the organ. In order to avoid tissue inhomogeneity, particularly near organ boundaries, the VOIs were defined within the boundaries of the normal tissue organs, as visualised on the CT images. The VOIs were mapped to the corresponding emission scans by means of shape-based interpolation to extract the [^{18}F] activities using the Analyze analysis software (version 11; Biomedical Imaging Resource, Mayo Clinic). For urinary bladder where the volume changes over time, the organ was outlined manually on the emission scans. All the volumes were outlined by a single investigator to avoid any inter-observer variation. VOIs included brain, thyroid, thymus, breast, lungs, heart wall, aortic lumen, liver, gall bladder, spleen, stomach wall, pancreas, adrenals, kidneys, small intestine wall and contents, large intestine wall and

contents, urinary bladder contents, uterus, testes/ovaries, gluteus maximus muscle, and red marrow (iliac crest).

5.1.2.5: Measurement of blood & urine radioactivity

Venous blood samples were taken at nominal times of 5, 10, 15, 30, 60, 90, 150, and 240 min after injection. Single aliquots, each of whole blood and plasma were obtained from each sample, and ^{18}F activity concentration was measured in a well counter previously cross-calibrated to the PET scanner. Urine was collected as voided up to 240 min after injection, and the volume and time of each micturition recorded. Dual aliquots of urine were sampled from each void, and the mean [^{18}F] activity was measured. The resulting [^{18}F] activity concentration was multiplied by the volume of voided urine to provide the [^{18}F] activity excreted.

5.1.2.6: Metabolite analysis

Discrete venous blood samples drawn at the above mentioned time points were centrifuged at ~8000 *g* for 3 min at 4º C to obtain plasma. Plasma metabolite analysis was performed and samples were clarified by protein precipitation (Smith, Zhao et al. 2011). All samples were instantly processed for analysis by high-performance liquid chromatography (HPLC; Agilent 1200 series system). A guard column (Waters-Bondapak-C18: 10µm, 125A) and an analytical column (Phenomenex-luna-SCX: 240*4.6mm, 10µm) were used. Briefly, ice-cold acetonitrile (3.75-12ml) was added to plasma samples (0.5-2.0ml). The resulting suspension was centrifuged (15,490 *g*, 4^{o} C, 3 min). The supernatant was then decanted and evaporated to dryness on an evaporator under vacuum (at 40^{o} C), then re-suspended in HPLC mobile phase (1.1ml) and filtered through a syringe filter (0.2 µm) to remove particulates. The mobile phase comprised of 0.25 M

Sodium dihydrogen phosphate (pH 4.8) and acetonitrile (9:1 v/v) delivered at a flow rate of 2 ml/min and a total run time of 10 min. A total of 30 fractions were collected over the course of the analysis and radioactivity was measured using a Perkin Elmer (Cambridge, UK) Wizard 1470 automated gamma counter.

5.1.2.7: Biodistribution and Dosimetry

For each subject and for each source region, the non-decay-corrected ^{18}F activity concentration over the 6 time points (time-activity curve: TAC) was generated. The cumulative activity concentrations (area-under-curve: AUC) were calculated for all organ VOIs by applying a trapezoidal integration to the non-decay-corrected TACs over the duration of the scan. The total number of disintegrations in each organ normalised to injected activity (subsequently referred to as the Residence Time (RT; τ): kBq.hour/kBq) were calculated as follows (Eq. 10):

$$\tau = (AUC \times V_{organ}) / Injectedactivity \qquad \textbf{Equation 10}$$

where *AUC* is the time integral of the non-decay corrected TAC and V_{organ} is the tabulated organ volume as used in OLINDA/EXM version 1.1 (Stabin, Sparks et al. 2005). For most organs, the AUC included a contribution beyond the scan duration assuming no further activity redistribution. As the volume of the urinary bladder changed over time, the image derived organ volume at each scan time point was used to estimate RT, rather than the tabulated organ volume. Lung activity was corrected for tissue density using a density value of 0.33 g/ml (Rhodes, Wollmer et al. 1981). The tissue density in the other organs was assumed to be 1.0 g/ml. With the exception of the urinary bladder, extrapolation of the integration past the last image data point (4 hours) only assumed physical decay of the [^{18}F] label without biologic clearance, i.e. an additional contribution to the AUC of TAC_l/λ where TAC_l is

the last TAC value measured and λ the decay constant for ^{18}F. For bladder, the measured voided activities were included to form an extended 8 time point TAC (**Figure 46**). The bladder TAC was modelled according to (Eq. 11)

$$A(1-e^{-Bt})e^{-\lambda t}-\sum_{i} A_i e^{-\lambda(t-t_i)} \qquad \textbf{Equation 11}$$

where *A, B* are fitted parameters, *t* the tracer administration time, A_i the urine activity voided at time t_i (Graham, Peterson et al. 1997; Thomas, Stabin et al. 1999). Residual bladder activity was not included in the model since it was not known if complete voiding had occurred for these subjects, although any residual activities must have been small compared to the voided activities. The sum of the squared differences between the function and the extended TAC was minimised for each subject using the solver function in Excel 2010 (Microsoft, Inc., Redmond, WA). Across all 8 subjects the fitted AUCs matched the measured AUCs calculated above with a fractional mean difference of 3% and standard deviation of 7%. The fitted functions were extrapolated to estimate the bladder RT for each subject for the following voiding scenarios: complete bladder voids every hour, every 2 hours, and every 4 hours post tracer administration. Finally the RT of the remainder term (assumed to be homogeneously distributed in the body) was obtained by subtracting the sum of all defined organ RTs from the inverse of the decay constant for [^{18}F].

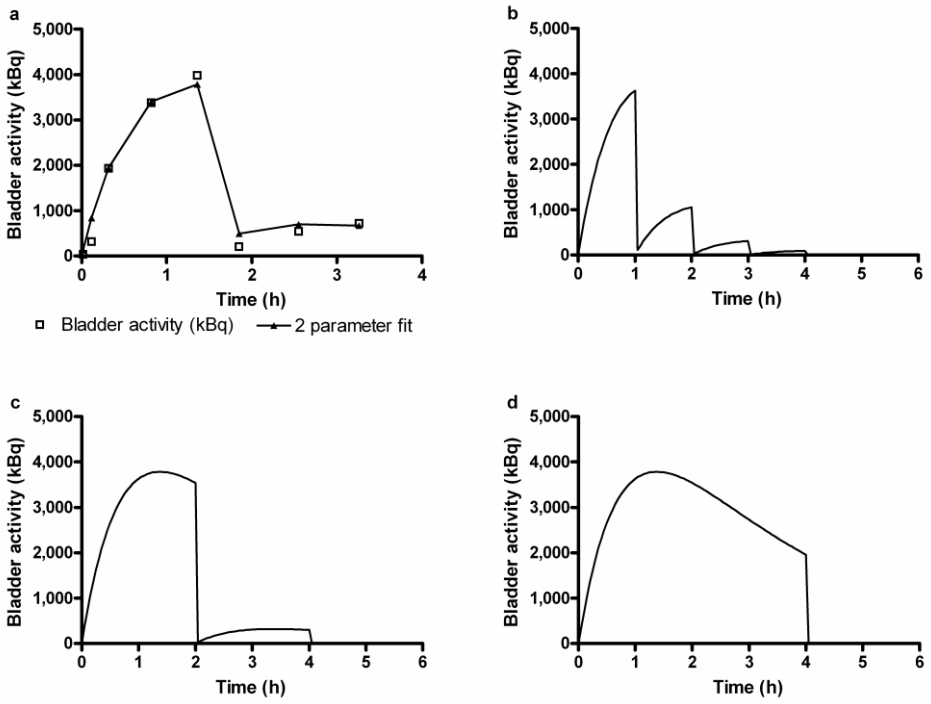

Figure 46: **Representative bladder fits for a subject.**
(**a**) The measured image and urine sample-derived time activity curves (TACs) for one subject and the fitted function, Eq. 11 (both shown uncorrected for radioactive decay). The fitted functions extrapolated to the following voiding scenarios: complete bladder voids (**b**) every hour, (**c**) every 2 hours, and **(d)** every 4 hours post tracer administration.

The internal radiation dosimetry was estimated from the RTs for the organs in each subject, which was provided as input to the OLINDA/EXM version 1.1 (Stabin, Sparks et al. 2005). The organ absorbed doses, and effective dose (ED) for each individual subject were subsequently averaged. Since ICRP 103 (2007) tissue-weighting factors (W_T) are not implemented in OLINDA/EXM 1.1, the male and female EDs are based on W_T from ICRP-60 (1991).

An additional correction to the dose estimates arises because OLINDA/EXM 1.1 assumes that the stomach activity is all in the contents rather than the organ wall. The former was considered unlikely in this case. This only affects the beta

(positron) contribution to the dose and is corrected by noting that the energy deposited in the wall from the contents is assumed within OLINDA/EXM to be half that calculated for the contents.

5.1.2.8: Statistical Considerations

There was no formal sample size calculation performed for this study. Based on the biodistribution studies published in the literature, a total of 8 evaluable healthy volunteers (with a minimum of 3 females) were recruited. Descriptive statistics were used for biodistribution data and absorbed doses to the target organs.

5.1.3: Results

5.1.3.1: Safety

[^{18}F]D4-FCH was found to be safe and well tolerated in all subjects. No tracer related serious AEs or AEs were observed in relation to [^{18}F]D4-FCH injection. No significant changes in vital signs, clinical laboratory blood tests or electrocardiograms were observed.

5.1.3.2: Biodistribution

Following the administration of [^{18}F]D4-FCH, radioactivity was initially detected in the vascular compartment and then rapidly distributed to the liver, kidneys, pancreas and spleen. About 7% of the injected activity (decay-corrected to injection time) was eliminated within the first 4 hours through the kidneys (6% after 2h). Radioactivity was already detectable in the urinary bladder at about 7 min after tracer administration. The initial radioactivity uptake in the liver gradually increased

with time after tracer injection. Increased uptake was also noted in the pituitary, salivary glands and bone marrow. Typical images illustrating tracer uptake at various time points from a representative female and male subject are shown in **Figure 47**. There were no differences in biodistribution profiles between men and women. TACs were generated for various organs (**Figure 48**). The mean RTs for male and female subjects are summarised in **Table 25**. The RT contribution from the extrapolated part of AUC beyond the last time point for imaging accounted for 38% of the total RT, contributing to 61% of the total ED.

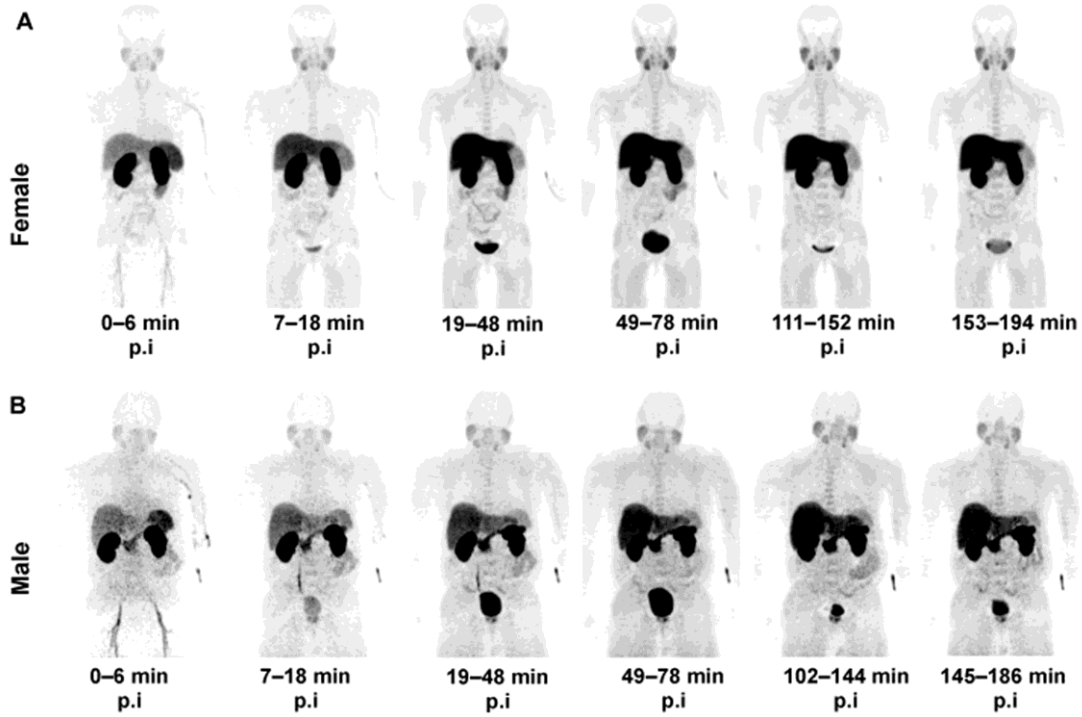

Figure 47: A series of whole body maximum intensity projection (MIP) images.
MIP images of representative female **(a)** and male **(b)** subjects showing biodistribution of [^{18}F] activity following tracer injection up to 194 min post injection of [^{18}F]D4-FCH. The incidental increased uptake of the radiotracer noted in the prostate of the male subject was secondary to benign prostatic hyperplasia. The apparent delayed uptake in the liver of the male subject was not present in other male subjects.

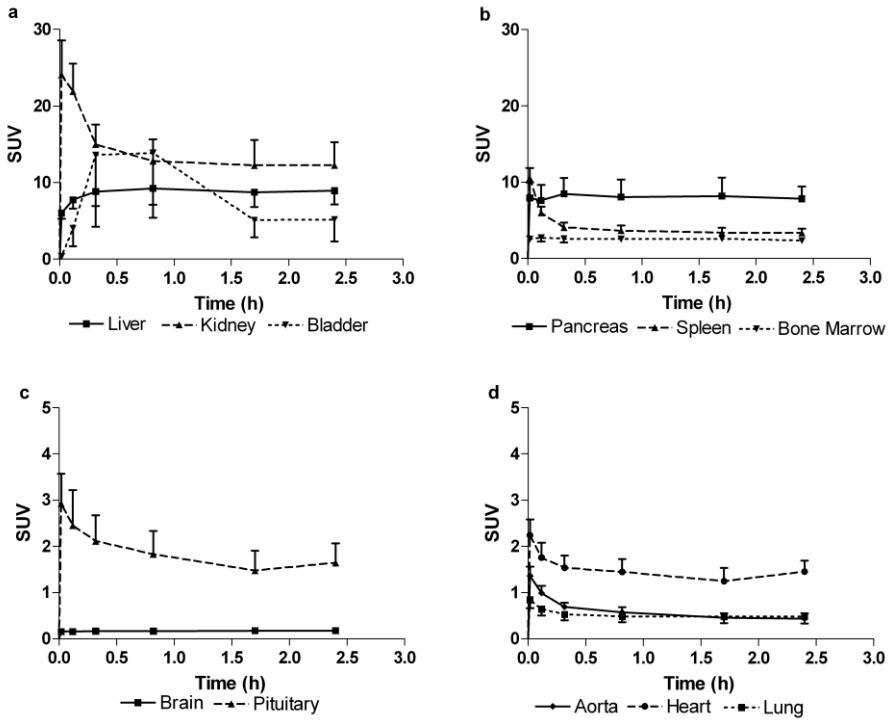

Figure 48: Mean decay corrected time-activity curves (TACs).

TACs normalised to injected activity (kBq) and body weight (grams), for [^{18}F]D4-FCH. TACs were generated for several organs at various time points up to 4 hours after tracer administration in (**a**) the elimination organs (liver, kidney and urinary bladder), (**b**) pancreas, spleen and bone marrow, (**c**) cranium, and (**d**) thorax. Error bars represent one standard deviation from the mean and are shown one-sided for clarity.

Table 25: **Mean Residence Times (τ) of [^{18}F]D4-FCH for different organs in Male (n=4) and Female (n=4) Volunteers.**

	τ (kBq.h/ kBq) - Males		τ (kBq.h/ kBq) - Females	
Organ	**Mean**	**SD**	**Mean**	**SD**
Adrenal	0.003	0.001	0.003	0.001
Brain	0.009	0.001	0.012	0.003
Breast			0.005	0.001
Gall Bladder	0.005	0.001	0.006	0.006
Heart contents	0.009	0.003	0.009	0.001
Heart wall	0.017	0.004	0.017	0.001
Kidney	0.126	0.043	0.170	0.046
Liver	0.534	0.138	0.681	0.097
LLI	0.008	0.003	0.007	0.003
Lung*	0.061	0.009	0.042	0.006
Muscle	1.036	0.381	0.873	0.191
Ovaries†			0.00004	0.00008
Pancreas	0.027	0.002	0.025	0.006
Red marrow	0.102	0.018	0.125	0.013
Small Intestine	0.071	0.015	0.108	0.033
Spleen	0.022	0.002	0.026	0.002
Stomach wall	0.027	0.008	0.022	0.012
Testis	0.001	0.000		
Thymus	0.00047	0.00015	0.00164	0.00038
Thyroid	0.001	0.000	0.001	0.000
ULI	0.010	0.001	0.013	0.001
Urinary Bladder‡	0.059	0.027	0.075	0.025
Uterus			0.004	0.003
Remainder	0.511	0.450	0.414	0.076

LLI-lower large intestine, ULI-upper large intestine, SD-standard deviation

* Lung activity was corrected for tissue density value of 0.33 g/ml and other organs with a density value of 1 g/ml.

† In three subjects ovaries were not visible due to post-menopausal atrophy.

‡ Urinary Bladder residence time is for a 2-hour voiding scenario.

5.1.3.3: Dosimetry

Table 26 summarises the mean organ absorbed dose estimates for [^{18}F]D4-FCH injection. The mean effective dose averaged over both males and females (±SD) was estimated to be 0.025±0.004 mSv/MBq (male 0.022±0.002; female 0.027±0.002). The 5 organs receiving the highest absorbed dose (mGy/MBq), averaged over both males and females (±SD), were the kidneys (0.106±0.03), liver (0.094±0.03), pancreas (0.066±0.01), urinary bladder wall (0.047±0.02), and adrenals (0.046±0.01). The values quoted are based on the 2-hour bladder voiding scenario. This is likely to be conservative in routine imaging scenarios where subjects would be encouraged to consume moderate quantities of fluids and empty their bladders regularly as is done for [^{18}F]FDG studies. If the 4-hour voiding scenario were used, this would increase the bladder wall absorbed dose by 59% (increase of 0.027 mGy/MBq: averaged for male and female).

Table 26: **Mean organ absorbed dose estimates expressed in mGy/MBq for [^{18}F]D4-FCH (n=8) with bladder voiding scenarios.**

	Mean Absorbed Dose estimates (mGy/MBq)		Mean Absorbed Dose estimates (mGy/MBq)	
Bladder Voiding	**2-hr voiding scenario**		**4-hr voiding scenario**	
Organ	**Mean**	**SD**	**Mean**	**SD**
Adrenals	0.046	0.011	0.046	0.011
Brain	0.004	0.001	0.004	0.001
Breasts	0.007	0.001	0.007	0.001
Gall Bladder wall	0.034	0.009	0.033	0.009
LLI wall	0.015	0.002	0.015	0.002
Small Intestine	0.031	0.009	0.031	0.009
Stomach wall	0.040	0.010	0.040	0.010
ULI wall	0.019	0.003	0.019	0.003
Heart wall	0.023	0.004	0.023	0.004
Kidneys	0.106	0.034	0.106	0.033
Liver	0.093	0.028	0.093	0.029
Lungs	0.019	0.002	0.019	0.002
Muscle	0.014	0.003	0.014	0.003
Ovaries	0.013	0.002	0.013	0.002
Pancreas	0.066	0.009	0.066	0.008
Red marrow	0.017	0.001	0.017	0.001
Osteogenic cells	0.015	0.002	0.014	0.002
Skin	0.005	0.001	0.005	0.001
Spleen	0.038	0.007	0.038	0.007
Testes	0.010	0.002	0.010	0.002
Thymus	0.015	0.006	0.015	0.006
Thyroid	0.017	0.003	0.017	0.003
Urinary Bladder wall	0.046	0.018	0.074	0.030
Uterus	0.017	0.006	0.018	0.006
Total body	0.014	0.002	0.014	0.002
Mean ED (mSv/MBq)	**0.025**	**0.004**	**0.027**	**0.004**

LLI-lower large intestine, ULI-upper large intestine, ED-effective dose

5.1.3.4: Metabolism of [^{18}F]D4-FCH

The metabolism of [^{18}F]D4-FCH in plasma at discrete time points after tracer injection was evaluated using HPLC. Typical HPLC chromatograms of [^{18}F]D4-FCH and its metabolite in the plasma at various time points after tracer injection are shown in **Figure 49a-h**. [^{18}F]D4-FCH eluted at approximately 6 min and [^{18}F]D4-betaine at 3min. [^{18}F]D4-betaine was detected as early as 10 min after injection. The chromatogram of [^{18}F]D4-FCH and its metabolite in urine (**Figure 50**) shows elimination of [^{18}F]D4-betaine predominantly. The [^{18}F]D4-FCH parent fraction (fraction of radioactivity in blood remaining as [^{18}F]D4-FCH) and the whole blood to plasma ratio of radioactivity are shown in **Figure 51a-b**. At about 3.5 h post tracer injection, 31% of radioactivity remained as parent ^{18}F-D4-FCH in circulation. The ratio of radioactivity in blood to that in plasma approximated unity, over the time course of the study.

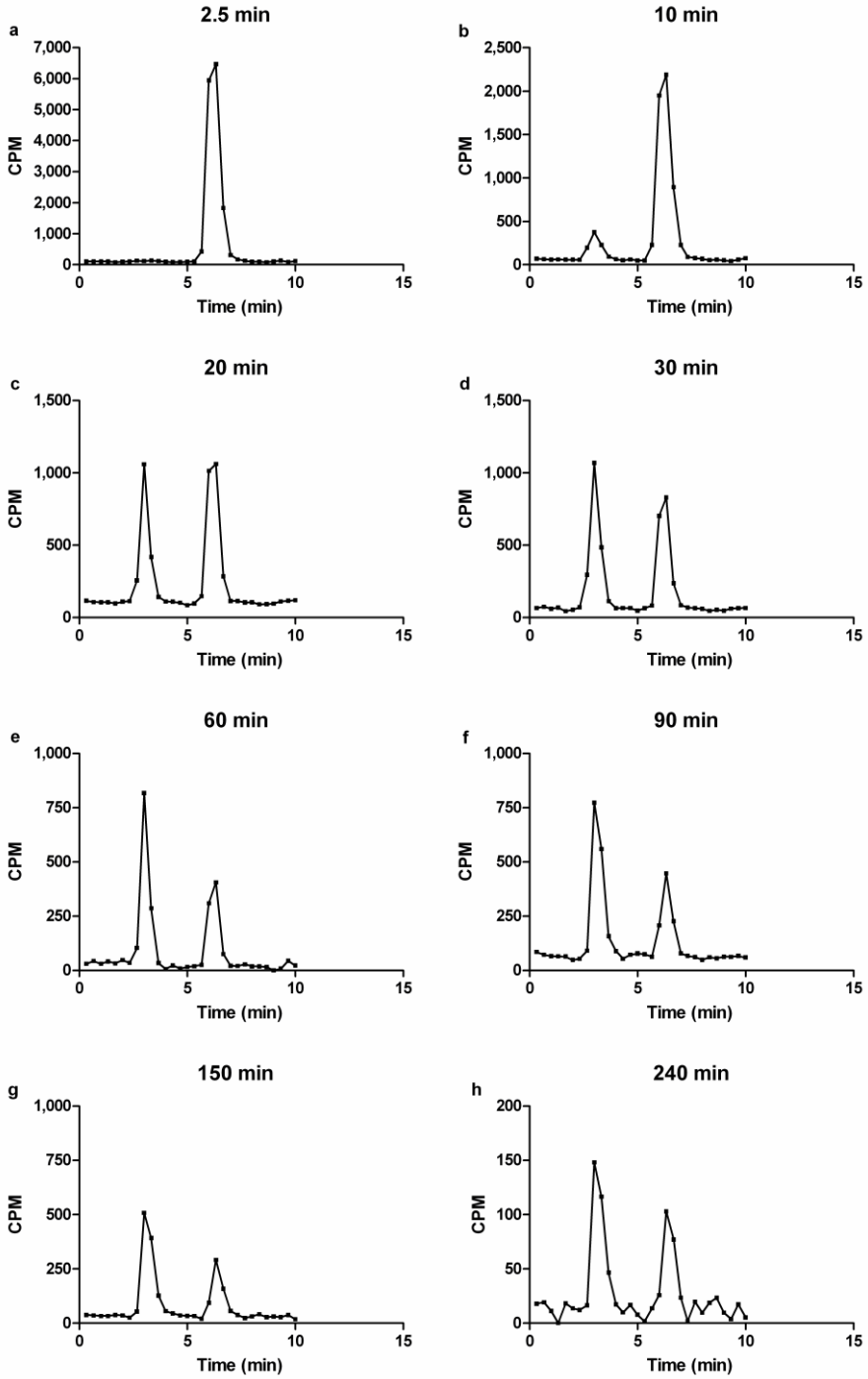

Figure 49: **Typical high-performance liquid chromatography (HPLC) chromatogram of [^{18}F]D4-FCH and its metabolite [^{18}F]D4-betaine in plasma.**

Analysis of the metabolism of [^{18}F]D4-FCH at **(a)** 2.5 min, **(b)** 10 min, **(c)** 20 min, **(d)** 30 min, **(e)** 60 min, **(f)** 90 min, **(g)** 150 and **(h)** 240 min post tracer injection, shows detection of [^{18}F]D4-betaine as early as 10 min, the proportion of which increases with time. Note that the Y-axis scale is different due to decrease in counts per minute (CPM).

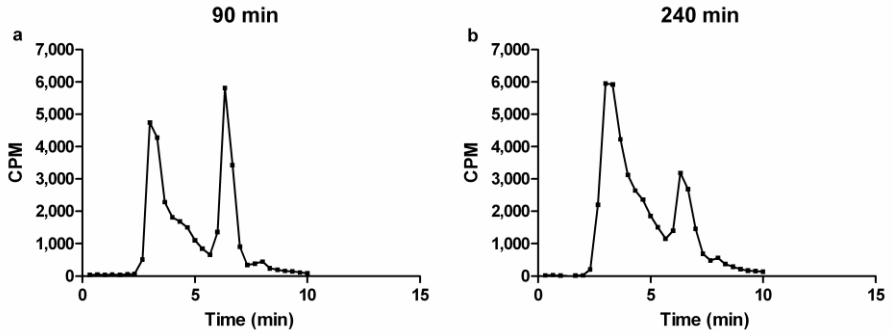

Figure 50: **Typical high-performance liquid chromatography (HPLC) chromatogram of [^{18}F]D4-FCH and its metabolite [^{18}F]D4-betaine in urine.**

Analysis of the metabolism of [^{18}F]D4-FCH at **(a)** 90 min, **(b)** 240 min post tracer injection, shows predominant excretion of [^{18}F]D4-betaine.

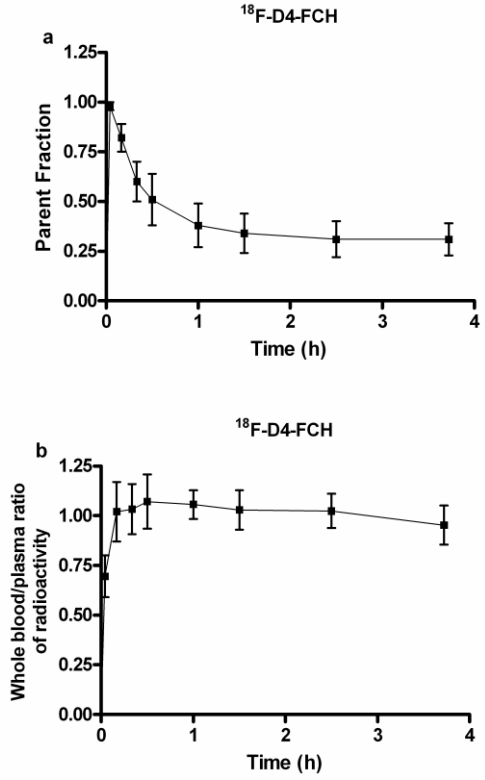

Figure 51: **Time course of *in vivo* oxidation of [^{18}F]D4-FCH and the ratio of whole blood to plasma radioactivity.**

Thirty-one percent of radioactivity remains as parent [^{18}F]D4-FCH in circulation at about 3.5 h post tracer injection **(a)**. The ratio of radioactivity in blood to that in plasma was close to unity **(b)**.

5.1.4: Discussion

This first in human study has shown that the deuterium substituted FCH analogue, [^{18}F]D4-FCH, is safe and well tolerated. To date, [^{11}C]choline and [^{18}F]FCH have been extensively used for the clinical imaging of prostate, brain, breast and oesophageal carcinomas (Treglia, Giovannini et al. 2012; Umbehr, Muntener et al. 2013). Due to the metabolic instability of choline radiotracers and the desire to use late imaging protocols (~60 min, to permit elimination of non-specific metabolites), a more stable choline radiotracer, [^{18}F]D4-FCH was developed (Smith, Zhao et al. 2011). A series of pre-clinical studies showed that the new tracer has improved protection against oxidation by choline oxidase, the key choline catabolic enzyme, via a ^{1}H/^{2}D isotope effect, together with fluorine substitution (Leyton, Smith et al. 2009; Smith, Zhao et al. 2011; Witney, Alam et al. 2012). The objective of this study was to investigate the biodistribution and dosimetry in human subjects, and extend pharmacokinetic aspects of the pre-clinical findings into human application.

The early tissue distribution of [^{18}F]D4-FCH was not dissimilar from that of [^{18}F]FCH reported by DeGrado and colleagues (DeGrado, Reiman et al. 2002), though their study evaluated the distribution and dosimetry over a period of up to 1 h only. Injection of [^{18}F]D4-FCH led to rapid washout of the ^{18}F activity from the vascular compartment, and elimination was primarily via the renal and hepatic routes. Renal excretion (7% in 4 h) was relatively lower than for routinely used radiotracers such as [^{18}F]FDG (21% in 2 h) (Jones, Alavi et al. 1982; 1998) and similar to that of the other choline analogs (**Table 27**). The mean ED of [^{18}F]D4-FCH was determined as 0.025 mSv/MBq, which is comparable with the ED of [^{18}F]FDG (0.019 mSv/MBq) (1998). The dose limits specified in the Code of Federal Regulations (USA) per single administration of a radioactive drug for research

purposes, are 30 mSv to the whole-body, blood-forming organs, lens of the eye, and gonads, with a maximum annual dose of 50 mSv. The maximum allowable single and annual dose to all other organs are 50 and 150 mSv, respectively (2012). If a 370 MBq administered radioactivity for [^{18}F]D4-FCH (typical of many PET tracers) was assumed, the ED would be 9.3 mSv. For this administered radioactivity level, the equivalent dose received by the gonads would be estimated as 1.1 mSv. These are well within the dose limits specified above.

Table 27: **Comparison between [^{18}F]D4-FCH, [^{11}C]choline and [^{18}F]FCH**

	[^{11}C]Choline * (Hara 2002)	**[^{11}C]Choline† (Tolvanen, Yli-Kerttula et al. 2010)**	**[^{18}F]FCH* *(DeGrado, Reiman et al. 2002)***	**[^{18}F]D4-FCH† (*this study*)**
Absorbed dose (mGy/ MBq)				
Kidney	0.018	0.021	0.16	0.106
Liver	0.017	0.02	0.061	0.094
Pancreas	0.013	0.029		0.066
Urinary Bladder		0.003	0.065	0.047
Adrenals		0.004		0.046
Stomach wall		0.006		0.04
Spleen	0.008	0.009	0.055	0.038
ED (mSv/ MBq)				
	0.0028	0.0044‡	0.020‡	0.025‡
Urinary Excretion (% of injected activity)				
		2% in 1.5 h	3.4% in 1 h	4% in 1h, 6% in 2h, 7% in 4h

*Estimated using MIRDOSE
†Estimated using OLINDA/EXM
‡The higher radiation dose of [^{18}F]FCH compared to that of [^{11}C]choline is due to the longer half life of [^{18}F]

As indicated above, both transport and phosphorylation by CHKα, are putative mechanisms for radiotracer localisation. Examination of [^{18}F]D4-FCH localisation in brain tissue was very low, with the pituitary being the only organ of the brain showing a high uptake (**Figure 48c**). This is in keeping with previous

reports of radiolabelled choline (Hara, Kosaka et al. 1997; Mertens, Ham et al. 2012). The brain has a limited capacity to synthesise choline *de novo*. Thus, the majority of choline enters the brain from the circulation through saturable transport at the blood-brain barrier (Allen and Smith 2001) or through the high affinity choline transporters (CHTs), which are highly expressed in the neural tissues (Michel, Yuan et al. 2006). The lack of significant radiotracer localisation in healthy brain in some ways leads us to speculate that the rate limiting step for [^{18}F]D4-FCH tissue localisation in humans is phosphorylation by CHKα rather than transport. The higher uptake in the pituitary gland noted in this study and in the report of Mertens and colleagues (Mertens, Ham et al. 2012), could be due to this gland being situated outside the blood-brain barrier. This is in contrast to that reported by Schillaci and colleagues, who documented physiological uptake in the pituitary in only 1 of the 80 subjects evaluated (Schillaci, Calabria et al. 2010). Physiological accumulation of [^{18}F]D4-FCH was also seen in the salivary glands and pancreas as reported previously (Hara, Kosaka et al. 1998; Mertens, Ham et al. 2012). However, the mechanism of uptake is unclear. It has been suggested that uptake in the pancreas could be due to the incorporation of radiolabelled choline into phosphatidylcholine and lysophosphatidylcholine, which are in abundance in the pancreatic exocrine secretions (Hara, Kosaka et al. 1998).

There is paucity of plasma metabolism information on [^{18}F]choline analogs in humans. In translating the findings from pre-clinical validation to patients, it was hypothesised that the slower metabolism of choline tracers in humans compared to rodents (Roivainen, Forsback et al. 2000; Bansal, Shuyan et al. 2008) will result in relatively slow metabolism of [^{18}F]D4-FCH to [^{18}F]D4-betaine compared to published studies for [^{11}C]choline (Contractor, Kenny et al. 2009; Contractor, Challapalli et al. 2011; Contractor, Kenny et al. 2011). In support of this hypothesis, there was 38% of parent [^{18}F]D4-FCH in plasma at 60 min, decreasing to 31% at 4h. This

represents an improvement in metabolic stability for choline tracers in use clinically; for example a 2-fold higher metabolic stability is observed for [^{18}F]D4-FCH relative to published data for [^{11}C]choline by the Aboagye group (**Figure 52a**). The metabolic stability of [^{18}F]D4-FCH observed, was not due to a high total cold compound(s) in the radiopharmaceutical which may negatively impact on clearance. In contrast, the dose solution had higher specific activity (48.4 GBq/μmol) and pseudo-specific activity (relative to the precursor, D4-DMAE) than previously reported for [^{11}C]choline (Pascali 2000); the upper quality control release limit with respect to precursor being set at 10 μg (at least 10-20-fold lower). The lower levels of the precursor D4-DMAE along with the high specific activity is an added theoretical advantage, as DMAE is known to modulate the transport and phosphorylation of radiolabelled choline (Hara 2001). The lower concentration of DMAE is also known to enhance the visualisation of the tumours (Slaets, De Bruyne et al. 2010). The role of specific activity on [^{18}F]D4-FCH tumour uptake requires further evaluation.

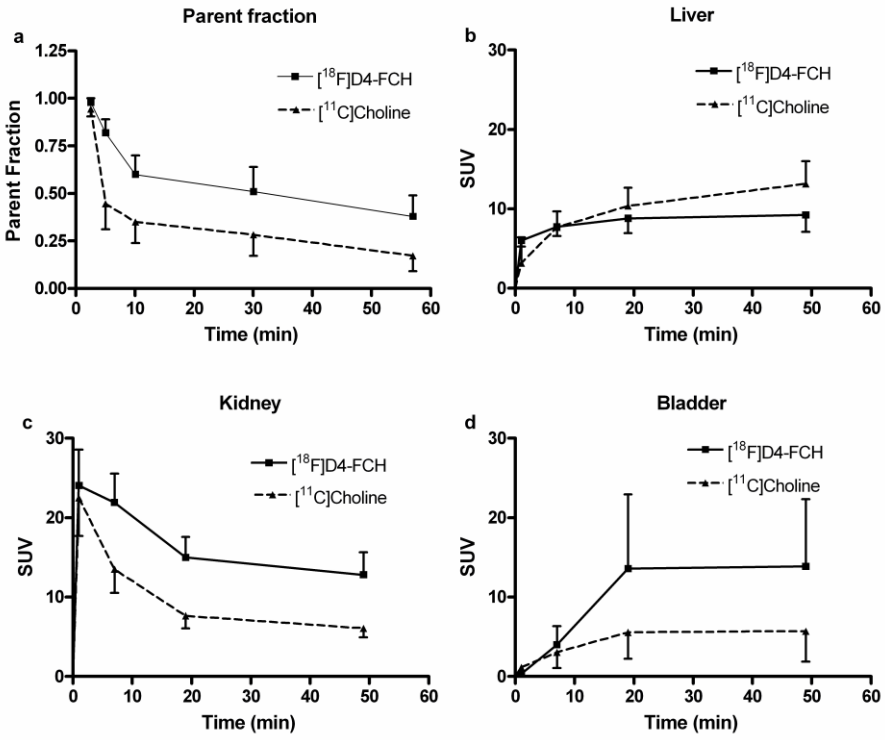

Figure 52: **TACs of [^{18}F]D4-FCH liver, kidney and bladder and comparison with [^{11}C]choline in breast and prostate cancer patients**

(primary data excluding the metabolites and normal tissue uptake were published in (Contractor, Kenny et al. 2011) and (Contractor, Challapalli et al. 2011). **(a)** Comparison of parent radiotracer fraction over 1 h post tracer injection. Thirty-eight percent of parent [^{18}F]D4-FCH remains in circulation compared with 17% of parent [^{11}C]choline in the breast (mean injected activity: 320 MBq) patient cohort. The mean decay-corrected and normalised radioactivity levels for [^{18}F]D4-FCH and [^{11}C]choline in: **(B)** liver **(C)** kidney and **(D)** bladder. The key difference between the two [^{11}C]choline studies relates to the approximately ten fold higher levels of unlabelled choline and dimethylaminoethanol precursor ([^{11}C]choline synthesised as per Pascali et al (Pascali 2000)). The [^{18}F]D4-FCH dose solution has extremely low levels of both precursor and unlabelled cold material, i.e., high specific radioactivity. [^{11}C]choline metabolite analysis was performed as described in (Contractor, Kenny et al. 2009).

In keeping with the pre-clinical studies (Leyton, Smith et al. 2009; Smith, Zhao et al. 2011; Witney, Alam et al. 2012), localisation of the [^{18}F]D4-FCH was most pronounced in kidneys and liver. Radiotracer uptake in kidneys and liver is likely to represent phosphorylation by CHKα with minor oxidation of [^{18}F]D4-FCH to [^{18}F]D4-betaine (Leyton, Smith et al. 2009; Witney, Alam et al. 2012). Comparison of the early phase (0-60 min) biodistribution profiles of [^{18}F]D4-FCH and [^{11}C]choline showed lower liver radioactivity and higher kidney and bladder radioactivity's for [^{18}F]D4-FCH (**Figure 52b-d)**. The differences in radiotracer distribution kinetics are likely due to the preponderance of phosphorylation over oxidation (Witney, Alam et al. 2012). The higher activity of [^{18}F]D4-FCH in the bladder (enhanced urinary clearance; **Figure 52d**) and the predominance of [^{18}F]D4-betaine in the excreted urine chromatograms (**Figure 50**) suggests incomplete tubular reabsorption of the parent tracer, similar to that seen with [^{18}F]FCH (DeGrado, Coleman et al. 2001). This is in contrast to the efficient tubular reabsorption of the nature-identical [^{11}C]betaine (Pummer, Dantzler et al. 2000).

Given the low background uptake of [^{18}F]D4-FCH in thorax and brain it is envisaged that this radiotracer will find utility in the following clinical scenarios: a) as a prognostic marker in lung cancer, supported by the observation that overexpression of CHKα predicts for patient survival in lung cancer (Ramirez de Molina, Sarmentero-Estrada et al. 2007) and b) detection of primary and recurrent brain tumours, supported by MRS imaging studies (Horska and Barker 2010). The use of [^{18}F]D4-FCH in prostate cancer including localised and advanced disease remains to be determined. In this regard, the urinary excretion of [^{18}F]D4-FCH while lower than [^{18}F]FDG, for example, may still obscure detection. Furthermore, it should be noted that patients were fasted in this study, thus, the impact of post-prandial bowel uptake needs further clarification.

In summary, [^{18}F]D4-FCH injection is safe and well tolerated with a favourable dosimetry profile in healthy volunteers. Organ dose estimates are similar to that seen with other routine [^{18}F]-labelled tracers. The potential risks due to radiation are within accepted limits. The radiotracer was relatively stable *in vivo*. Further clinical studies are now warranted to evaluate the utility of [^{18}F]D4-FCH in cancer patients.

5.2: [^{18}F]D4-FCH PET/CT in Non-Small Cell Lung Carcinoma: Proof of concept study.

5.2.1: Rationale

After establishing the safety, biodistribution and radiation dosimetry in human volunteers, [^{18}F] D4-FCH, was used to image patients with newly diagnosed non-small cell lung cancer (NSCLC) to establish an initial proof of concept. The choice of lung cancer was predicated in part by important emerging data linking choline kinase activity to patient survival in lung cancer patients (Ramirez de Molina, Sarmentero-Estrada et al. 2007). The aim of this proof of concept study was

- To examine the kinetics and magnitude of uptake of [^{18}F]D4-FCH and its association with CHK expression in lung cancer patients.

This will test the hypothesis that untreated malignant lung lesions will have enhanced radiolabelled choline accumulation due to their high expression and activity of CHKα.

5.2.2: Materials and Methods

5.2.2.1: Patients

Patients with newly diagnosed, biopsy confirmed NSCLC, suitable for radical surgery, radiotherapy or systemic therapy (i.e. localised or locally advanced or metastatic NSCLC), ECOG performance status ≤2 and with at least one (primary or metastatic) lesion ≥20 mm as assessed by the most recent CT were included.

Thus the main inclusion and exclusion criteria were:

Inclusion Criteria:

1. Histologically confirmed, newly diagnosed NSCLC fit for radical surgery, radiotherapy or systemic therapy (localised or locally advanced or metastatic)
2. At least one measurable lesion of ≥ 2cm (primary tumour or lymph node)
3. WHO performance status ≤ 2
4. Written informed consent
5. Clinically acceptable full blood count, renal and liver function (as judged by the investigator)

Exclusion Criteria:

1) Concurrent treatment with other experimental drugs. Participation in another clinical trial with any investigational drug within 30 days prior to study entry.
2) Pregnant or lactating women.
3) Previous invasive malignancy within the last five years other than basal cell carcinoma.

Ethical approval for the study was granted by the West London REC 1 Committee. All patients gave fully informed consent to participate in the study, which was done according to the Declaration of Helsinki guidelines. The administration of radioactivity for the PET scans was approved by the Administration of Radioactive Substances Advisory Committee, United Kingdom.

5.2.2.2: Imaging Protocol

The patients were scanned on a Siemens Biograph 6 TruePoint PET/CT scanner (specifications given in previous section), after being positioned such that the field of view (FOV) included the primary tumour (thorax). This was followed by a helical CT scan (settings: 30 mAs, 0.6 sec rotation. 1.5 pitch) over the region of the thorax which was used for attenuation correction and accurate anatomical localisation. [^{18}F]D4-FCH was administered by a bolus intravenous injection (up to 370 MBq) over 10 to 30 seconds. Dynamic PET scanning (3-dimensional acquisition) was commenced over a single bed position covering the thorax for 65 minutes. This was followed by a static whole body sweep (vertex to mid thigh) attenuation CT and PET scan (around 25 min, depending on the height of the patient; 3 min per bed position).

5.2.2.3: Image Analysis

Raw PET data were corrected for scatter and attenuation, and reconstructed with an iterative OSEM (ordered subset expectation maximum) algorithm comprising 8 iterations and 21 subsets. Decay corrected dynamic images were then viewed using Analyze® software (Analyze Version 11; Biomedical Imaging Resource, Rochester, MN, USA). From summed images, VOIs were drawn manually around the primary tumours in the lung, any visible metastatic lesions and

normal lung. The [^{18}F]D4-FCH radioactivity concentration within the VOIs was then determined and normalised for injected radioactivity and body weight to obtain SUV. The average and maximum SUV at 60 minutes ($SUV_{60,\ ave}$, and $SUV_{60,\ max}$) were then determined. The static whole body images of [^{18}F]D4-FCH and [^{18}F]FDG were analysed using Hermes diagnostic software (Sweden). The primary tumours and distant metastatic lesions were outlined using an automated isocontour adjusted to 41% of the maximum pixel intensity in the region (Kobe, Scheffler et al. 2012). The nodal lesions were outlined manually.

5.2.2.4: Statistical Considerations

As this is an exploratory study, there will be no power calculations involved for an estimate of the sample size. Based on previous studies with similar fluorinated radiotracers, it was estimated that 25 patients will be sufficient to provide initial estimates of the magnitude of tracer uptake. Hence it was intended to use a sample size of 25. Up to 30 patients may be enrolled to account for dropouts.

The mean (± SD) was used as the primary descriptive measure. The significance of differential uptake in tumour and normal lung was assessed by Mann-Whitney test. $P \leq 0.05$ was considered significant. Statistical analyses were performed using Graph-Pad™ Prism (USA).

5.2.3: Results

5.2.3.1: Patients

Five patients were recruited so far, out of whom 3 had [^{18}F]FDG scans as part of their routine staging. The patient characteristics are given in **Table 28**. All patients tolerated the [^{18}F]D4-FCH PET/CT scans without any complications. The

mean (±SD) injected activity of [^{18}F]D4-FCH was 260.9 (±100.5) MBq with a radiochemical purity of >95%.

5.2.3.2: Imaging characteristics of [^{18}F]D4-FCH uptake

On visual analysis all the lung tumours were visible above the background (**Figure 53a**). The liver metastases, in one patient were photopenic (adenocarcinoma) and in the other it showed a higher uptake (squamous cell carcinoma) relative to normal liver background (**Figure 54**). Physiological activity was seen in the salivary glands, liver, kidneys, pancreas and the bladder.

Table 28: **Patient Characteristics**

Pt. No	Sex	TNM Stage	Histology	Lesion	[^{18}F]D4-FCH Dynamic Scan		[^{18}F]D4-FCH Static Scan		[^{18}F]FDG Static Scan	
					$SUV_{60,ave}$	$SUV_{60,max}$	$SUV_{60,ave}$	$SUV_{60,max}$	$SUV_{60,ave}$	$SUV_{60,max}$
1	F	$T_{3b}N_2M_{1b}$	Adeno carcinoma	Pri Tumour	4.78	8.46	4.73	8.64		
				Satellite nodule	7.65	11.14	7.18	13.72		
				Normal Lung	0.19	0.67	0.19	0.67		
				Scapular Met	7.78	10.62	7.17	10.64		
				Scalp Met			6.73	10.56		
				Liver Met			6.36	8.36		
				Liver			12.31	17.84		
2	F	$T_4N_1M_0$	SqCC	Pri Tumour	5.69	8.96	6.06	10.13		
				Hilar node	6.37	9.51	7.17	9.75		
				Normal Lung	0.17	0.58	0.17	0.58		
				Liver Met			8.83	12.7		
				Liver			5.52	8.15		
3	M	$T_{2a}N_0M_0$	SqCC	Pri Tumour	2.95	5.72	2.95	6.14	7.46	11.95
				Paratracheal node*	2.7	4.25	3.42	5.11	2.38	2.82
				Hilar node*	2.18	3.28	3.01	4.32	2.04	2.19
				Normal Lung	0.6	0.99	0.6	0.99		
4	F	$T_{1b}N_1M_0$	SqCC	Pri Tumour	2.9	4.53	3.46	5.41	7.1	10.77
				Hilar node†	2.35	2.92	2.41	3.13	4.48	6.12
				Normal Lung	0.71	1.02	0.71	1.02		
5	M	$T_4N_1M_0$	SqCC	Pri Tumour	5.06	7.79	5.47	9.15	8.02	14.1
				Normal Lung	1.13	1.86	1.13	1.86		

M-Male, F-Female, SqCC- Squamous cell carcinoma, Pri - Primary, Met – Metastasis. * No nodal metastatic deposits on histology after surgery. † Nodal metastases present on histology after surgery.

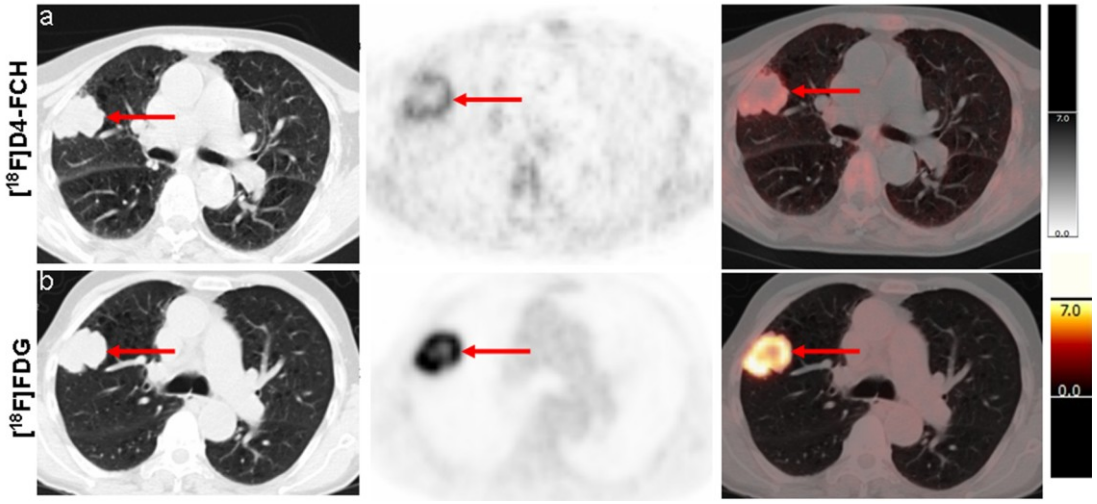

Figure 53: **Axial slices of the CT, PET and fused PET/CT showing uptake of [^{18}F]D4-FCH and [^{18}F]FDG in a right upper lobe primary lung tumour in the same patient.**
Visually, the uptake of [^{18}F]D4-FCH **(a)** in the primary tumour (red arrow) appears lower than that of [^{18}F]FDG uptake **(b)**.

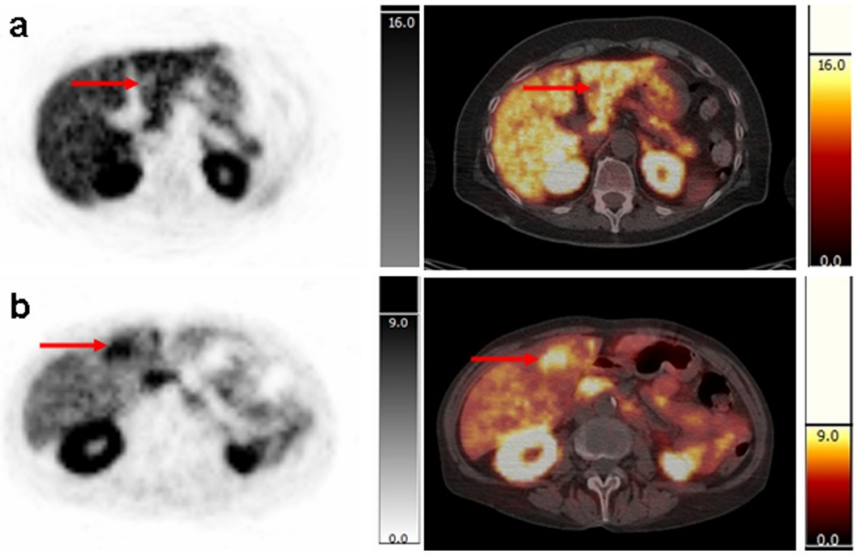

Figure 54: **Axial slices of the PET and fused PET/CT showing uptake of [^{18}F]D4-FCH in the liver metastases of two patients.**
In one patient the metastasis (red arrow) is photopenic **(a)** and in the other it shows a higher uptake relative to normal liver background **(b)**. The images are windowed to 50% of the maximum intensity.

5.2.3.3: Kinetics of [^{18}F]D4-FCH uptake

The mean $SUV_{60,max}$ (±SD) for the primary tumours was significantly higher than that of the normal lung; 7.89 (±2.02), and 0.99 (±0.55), respectively. The distant metastatic lesions had a higher uptake than the primary tumours, with a mean $SUV_{60,max}$ (±SD) of 11.2 (±2.09). Dynamic time activity curves (TAC's) for [^{18}F]D4-FCH in primary lung tumours (**Figure 55**) and the nodal metastases demonstrated a good retention of activity after plateauing at ~30 min until 60 min with SUV_{ave} and $SUV_{max.}$

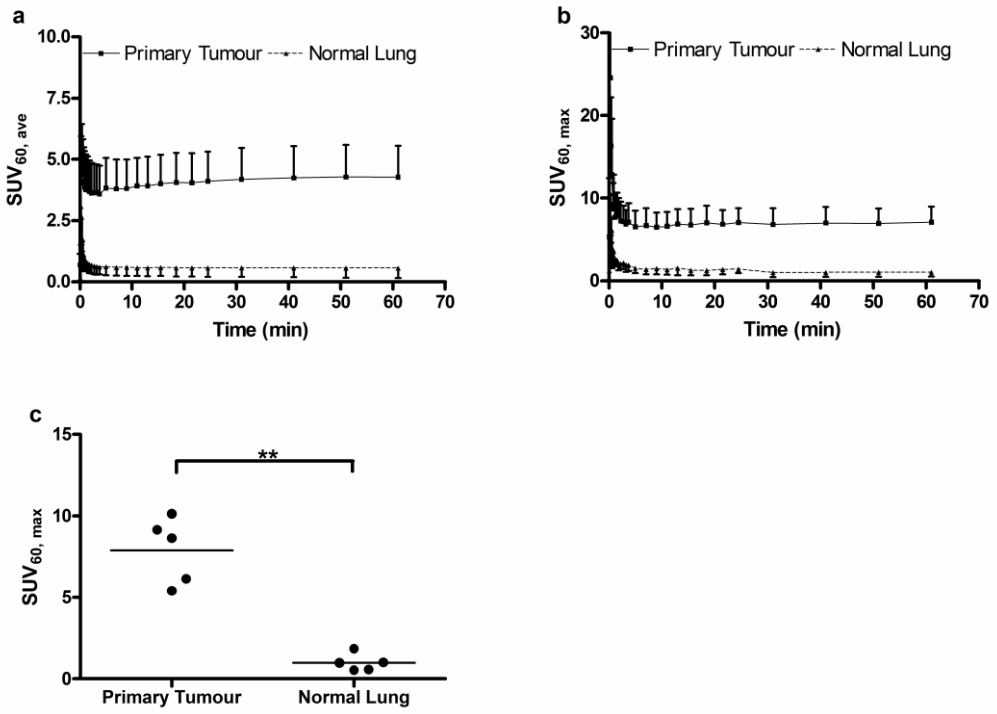

Figure 55: **Kinetics of [^{18}F]D4-FCH uptake in tumours and normal lung.**
The time activity curves show good retention and plateauing of uptake after 30 min of tracer injection (a, b). There is a significant difference between uptake of [^{18}F]D4-FCH in the tumour and normal lung (c). The bar represents the mean SUV.

5.2.3.4: Comparison with [^{18}F]FDG

In the three patients who routinely had [^{18}F]FDG PET/CT as part of their staging, the [^{18}F]FDG uptake ($SUV_{60,max}$) was higher than that of [^{18}F]D4-FCH uptake. Interestingly, the reactive paratracheal and hilar nodes (mediastinoscopy proven) in patient 3 showed a higher uptake with [^{18}F]D4-FCH (**Table 28**).

5.2.4: Discussion

The early preliminary results of [^{18}F]D4-FCH PET/CT have shown that imaging primary lung tumours is feasible. The kinetics of tumour [^{18}F]D4-FCH uptake were rapid, reaching a plateau within 30 min, suggesting that earlier time points could be explored to enhance patient comfort and improve PET count statistics. The higher uptake seen in the distant metastatic lesions suggests that more aggressive disease may have higher CHK expression. This hypothesis however, needs further evaluation and correlation with CHK expression. The different appearance of the liver metastases in patients with adenocarcinoma and squamous cell carcinoma also requires further evaluation.

The discordance in the uptake of [^{18}F]FDG compared to that of [^{18}F]D4-FCH could be the reflection of the mechanism of tracer accumulation; [^{18}F]FDG uptake relating to rate of glycolysis and the [^{18}F]D4-FCH uptake relating to rate of cell membrane synthesis (Khan, Oriuchi et al. 2003).

PET imaging with [^{18}F]FDG, has allowed more accurate detection of both nodal and distant metastatic disease (Pieterman, van Putten et al. 2000; Vansteenkiste and Dooms 2007). Staging [^{18}F]FDG PET/CT has been shown to reduce futile thoracotomies compared to conventional work up (van Tinteren, Hoekstra et al. 2002) and to be cost effective (Verboom, van Tinteren et al. 2003). However the performance of [^{18}F]FDG PET/CT in the evaluation of nodal disease is

limited by false positives in reactive nodes such that patients with equivocal N_2 nodal disease on PET/CT require mediastinal nodal sampling confirmation (2011). Therefore, there is a clinical need for more specific PET tracers.

An early study by Hara et al, comparing [^{11}C]choline and [^{18}F]FDG PET for the detection of mediastinal lymph node metastases in 29 patients prior to surgical thoracotomy and ipsilateral nodal dissection, reported excellent results with 100% sensitivity of choline PET (Hara, Inagaki et al. 2000). However this sensitivity may be overestimated by the low SUV criteria used for detection of disease. Two similar small studies have shown discrepant results reporting [^{11}C]choline to be less sensitive than FDG PET for nodal disease but superior for the detection of metastatic disease (Pieterman, Que et al. 2002; Khan, Oriuchi et al. 2003). Notably these studies were all on PET only cameras. However, more recently when the diagnostic performance of [^{11}C]choline PET/CT was evaluated against the standard CECT, a higher accuracy of [^{11}C]choline PET/CT for nodal staging was reported but not for primary lesion characterisation (Peng, Liu et al. 2012; Li, Peng et al. 2013). Given the uptake of [^{18}F]D4-FCH in reactive nodes, the diagnostic performance of [^{18}F]D4-FCH in nodal staging remains to be assessed.

CHK has been linked to proliferation index and survival outcome in lung cancer (Ramirez de Molina, Sarmentero-Estrada et al. 2007). A moderate correlation between [^{11}C]choline uptake and CHK expression has been shown in a study of 53 patients with NSCLC, thus establishing the biological basis of choline uptake in lung cancer (Li, Peng et al. 2013). Therefore, [^{18}F]D4-FCH PET/CT could be used as a noninvasive surrogate for CHK expression and thus potentially used as a prognostic marker and for predicting patient outcome. It is also envisaged that [^{18}F]D4-FCH PET/CT could play a further role in selection and/ or evaluation of lung cancer patients for targeted therapy.

Additional Work

CHAPTER 6: [^{18}F]ICMT-11, a caspase-3 specific PET tracer for apoptosis: Biodistribution and radiation dosimetry

Rationale

Apoptosis is an essential process for eliminating unwanted cells during embryonic development, growth, differentiation, and maintenance of tissue homeostasis. Apoptosis is regulated by both intrinsic (via mitochondria) and extrinsic (activation of death receptors) signaling networks that control a family of enzymes known as caspases (cysteine aspartate specific proteases) (Nicholson and Thornberry 1997; Degterev, Boyce et al. 2003). The pathways activate "initiator" caspases 8 (extrinsic) or 9 (intrinsic), which in turn cleave the inactive pro-caspases 3, 6, and 7 into the active "executioner" caspases-3, -6, and -7 (Okada and Mak 2004). Deregulation of apoptosis signaling pathways is therefore associated with various pathologies including autoimmunity, neuro-degeneration, cardiac ischemia, and transplant rejection (Reed 2002), and the capacity to evade apoptosis has been defined as one of the hallmarks of cancer (Hanahan and Weinberg 2000).

In cancer, apoptosis is induced by a large variety of stimuli including cytotoxic and mechanism-based therapeutics, and radiotherapy. Although those stimuli trigger different apoptotic signaling pathways, the molecular events in the execution phase of apoptosis are largely shared and involve caspases. Within the caspase family, the effector caspases (caspases-3, -6, and -7) orchestrate the demolition phase of apoptosis that results in the controlled dismantling of a range of key structures within the cell and its subsequent disposal (Taylor, Cullen et al. 2008). Moreover, one of the most noticeable and specific features of apoptosis is the degradation of the DNA into numerous fragments, often down to multiples of

200 base pairs, driven by the activation of caspase-3 (Porter and Janicke 1999), the central effector caspase, which makes it an attractive biomarker of apoptosis.

Effective anticancer therapy often requires induction of tumour cell death through apoptosis. Monitoring of this process could provide important predictive outcome information in the context of routine patient management and early clinical trials (Dubray, Breton et al. 1998; Chang, Ormerod et al. 2000). Apoptotic index has been shown to correlate with chemotherapy efficacy and has been shown to be of prognostic significance (Faried, Sohda et al. 2004; Jia, Dong et al. 2012). A noninvasive apoptosis imaging technology such as PET could permit the detection of biological changes in the tumour that evolve over hours of initiating treatment. This is in contrast to changes in tumour size that evolve over months, which forms the basis for Response Evaluation Criteria in Solid Tumours (RECIST 1.1) guidelines (Eisenhauer, Therasse et al. 2009).

Based on various biochemical events that characterize apoptosis, a number of positron emitting radiotracers have been developed to noninvasively detect this process, both in preclinical studies and in humans (Nguyen, Challapalli et al. 2012). [^{18}F](S)-1-((1-(2-fluoroethyl)-1H-[1,2,3]-triazol-4-yl)methyl)-5-(2(2,4 difluorophenoxymethyl)-pyrrolidine-1-sulfonyl) isatin ([^{18}F]ICMT-11) was designed as a small molecule radiotracer with potential advantages such as facile radiolabelling and improved biodistribution and clearance profiles. It has been characterised as a novel reagent designed to noninvasively image caspase-3 activation and, hence, drug-induced apoptosis. [^{18}F]ICMT-11 was validated as a caspase-3 specific PET imaging radiotracer for the assessment of tumour apoptosis preclinically in murine lymphoma xenografts treated with cyclophosphamide (Nguyen, Smith et al. 2009).

The promising mechanistic and biological profile of [^{18}F]ICMT-11 supports its transition into clinical development (Nguyen, Challapalli et al. 2012).

In order to translate the pre-clinical findings into humans, this study in healthy volunteers was designed with the following aim:

- To evaluate the biodistribution, dosimetry and safety of [^{18}F]ICMT-11 in healthy volunteers.

Materials and Methods

Radiopharmaceutical Preparation

[^{18}F]ICMT-11 was synthesised from the precursor as previously described (Fortt, Smith et al. 2012). The radiochemical purity of [^{18}F]ICMT-11 was 100% with a mean (±SD; range) specific activity of 1951.5 GBq/μmol (±4084; 110-12032 GBq/μmol: the high specific activity in one subject was due to a lower cold concentration of [^{18}F]ICMT-11, below the limit of quantification) and a pH of 5.41 (±0.16; 5.16-5.71).

Subjects

Eight healthy volunteers (4 men, 4 women), with a mean (±SD; range) age of 63.1 yrs (±2.58; range: 59-68 yrs), and weighing an average of 74 kg (±15.4; range: 52.1-98.7 kgs) were enrolled. The main inclusion and exclusion criteria for this study were the same as that used for the study discussed in chapter 5, section 5.1. No specific subject fasting/ food protocol was implemented. Ethical approval for the study was granted by the West-London Research Ethics Committee. All volunteers gave written informed consent to participate in the study, according to the Declaration of Helsinki guidelines. The administration of radioactivity for the PET/CT scans was approved by the Administration of Radioactive Substances

Advisory Committee, United Kingdom. MHRA has approved this study as a non-IMP study.

Safety, Image acquisition, analysis and dosimetry

Collection of safety data, image acquisition protocol, image analysis, measurement of blood and urine radioactivity and the dosimetry calculations were performed as previously described in Chapter 5. The mean (±SD; range) injected [^{18}F]ICMT-11 activity and ICMT-11 cold dose in the subjects were 159 MBq (±3; 154-161 MBq) and 2.18 μg (±1.39; 0.1–4.44 μg) respectively.

For each subject and for each source region, the non-decay-corrected ^{18}F activity concentration over the 6 time points (time-activity curve: TAC) was generated. The total number of disintegrations in each organ normalised to injected activity (subsequently referred to as the Residence Time (RT; τ): kBq.hour/kBq) were calculated as follows (Eq. 12):

$$\tau = (AUC \times V_{organ}) / Injected\ activity \qquad \textbf{Equation 12}$$

where *AUC* is the time integral of the non-decay corrected TAC, V_{organ} the tabulated organ volume as used in OLINDA/EXM version 1.1 (Stabin, Sparks et al. 2005). For most organs, the AUC included a contribution beyond the scan duration assuming no further activity redistribution. For bladder, the measured voided activities were also included to form an extended 8 time point TAC (**Figure 56**). The bladder TAC was modelled according to (Eq. 13)

$$A(1-e^{-Bt})e^{-Ct} - \sum_i A_i e^{-\lambda(t-t_i)} \qquad \textbf{Equation 13}$$

where *A, B, C* are the estimated parameters, *t* the time since administration of the tracer, A_i the urine radioactivity voided at time t_i (Graham, Peterson et al. 1997; Thomas, Stabin et al. 1999). Residual bladder activity was not included in the model since it was not known if complete voiding had occurred for these subjects, although any residual activities must have been small compared to the voided activities. The sum of the squared differences between the function and the extended TAC was minimised for each subject using the solver function in Excel 2010 (Microsoft, Inc., Redmond, WA). Across all 8 subjects the AUCs derived from the fitted function matched the measured AUCs calculated above with a fractional mean difference of -3% and standard deviation of 6%. The decay constant *C* is usually assumed to be the same as λ on physical grounds but in this case a larger value was observed. This may be attributed to activity becoming trapped in other tissues of the body, most notably the gall bladder. As a result, for *t* greater than 5 hours, Eq 13. predicts a faster decline in bladder activity than is physically possible. This is however, beyond the observation time in the present study for which the bladder activity accumulation rate was always positive and was predicted to be very small after 4 hours. The fitted functions were extrapolated to estimate the bladder RT for each subject for the following voiding scenarios: complete bladder voids every hour, every 2 hours, and every 4 hours post tracer administration. Finally the RT of the remainder term (assumed to be homogeneously distributed in the body) was obtained by subtracting the sum of all defined organ RTs from the inverse of the decay constant for ^{18}F. The internal radiation dosimetry was calculated from the τ for the organs in each subject, whihc was provided as input to the OLINDA/EXM version 1.1 (Stabin, Sparks et al. 2005).

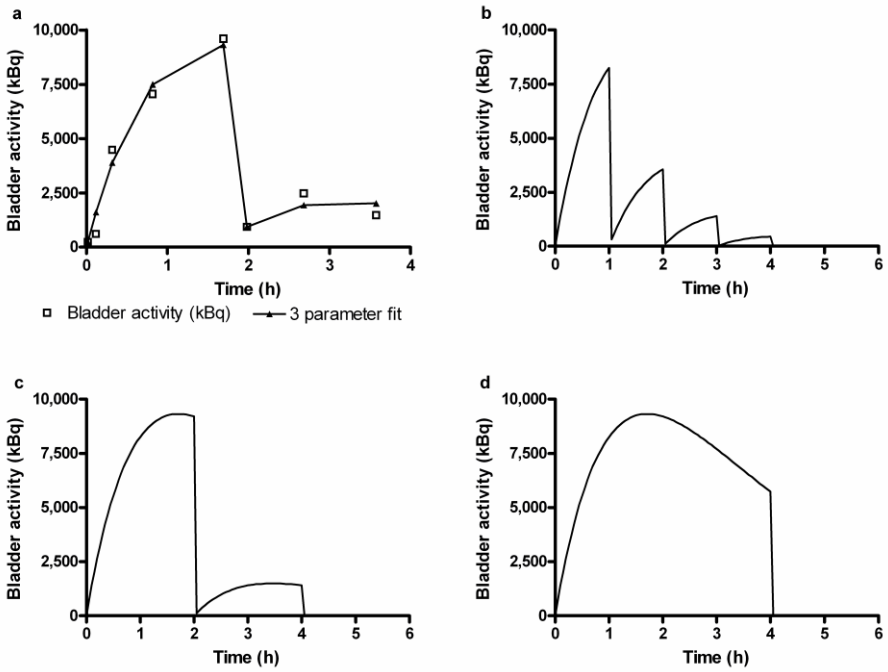

Figure 56: **Representative bladder fits for a subject.**

(**a**) The measured image and urine sample derived time activity curves (TACs) for one subject and the fitted function Eq. 2 (both shown uncorrected for radioactive decay). The fitted functions extrapolated to the following voiding scenarios: complete bladder voids (**b**) every hour, (**c**) every 2 hours, and (**d**) every 4 hours post tracer administration.

Statistical Considerations

There was no formal sample size calculation performed for this study. Based on the biodistribution studies published in the literature, a total of 8 evaluable healthy volunteers (with a minimum of 3 females) were recruited. Descriptive statistics were used for biodistribution data and absorbed doses to the target organs.

Results

Safety

[^{18}F]ICMT-11 was found to be safe and well tolerated in all subjects. No tracer related serious AEs or AEs were observed in relation to [^{18}F]ICMT-11 injection. Three of the eight subjects had a total of 4 non-tracer related AEs (grade 1), including headache, transient blurring of vision, transient fluctuations in blood pressure, and neutropenia (associated with a concurrent eye infection) which resolved spontaneously within 24-48 hours. No significant changes in vital signs, clinical laboratory blood tests or electrocardiograms were observed. The safety results were reviewed by an independent data monitoring committee.

Biodistribution

Following the administration of [^{18}F]ICMT-11, radioactivity was initially detected in the vascular compartment and then rapidly distributed to the liver and kidneys, followed by rapid elimination through the kidneys and the hepatobiliary system. About 18% of the injected activity (decay corrected back to injection time) was eliminated within the first 4 hours through the kidneys (9% in the first hour, 14% after 2 hours). Radioactivity was already detectable in the urinary bladder at 8 min after tracer administration. The initial radioactivity uptake in the liver was gradually cleared approximately 3 h after injection. At about 30 minutes after the [^{18}F]ICMT-11 injection, there was a gradual increase in accumulation of radioactivity in the gall bladder and bowel. Typical images illustrating tracer uptake at various time points from two representative subjects are shown in **Figure 57 a, b**. TACs were generated for various organs (**Figure 58**). There were no differences in the biodistribution profiles between men and women. The mean RTs for male and

female subjects are summarised in **Table 29**. The residence time contribution from the extrapolated part of AUC beyond the last time point for imaging accounted for 40% of the total residence time, contributing to 65% of the total ED and 57% of total EDE.

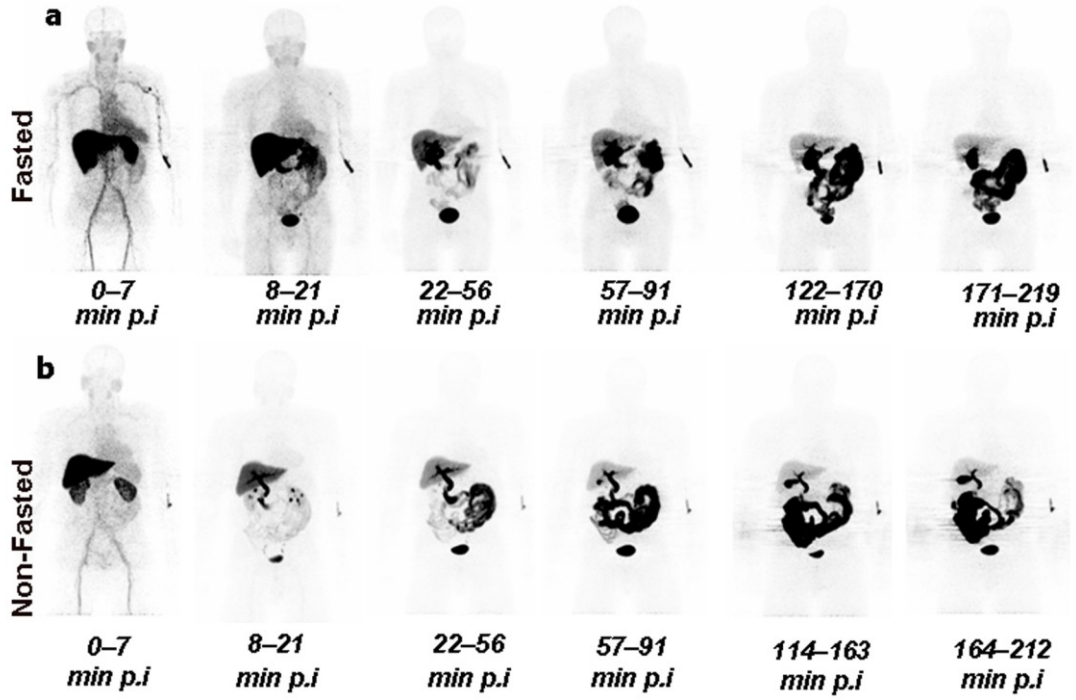

Figure 57: A series of whole body maximum intensity projection (MIP) images of representative subjects

MIPs show biodistribution of ^{18}F activity following tracer injection up to 219 min post injection of [^{18}F]ICMT-11. **(a)** Biodistribution of ^{18}F activity in a subject who had a meal 2-3 hours prior to tracer injection; Note, the rapid clearance of radioactivity in the cranium and thorax approximately 20 min after tracer injection. There is accumulation of radioactivity in the gall bladder and bowel from about 30 min after tracer injection. **(b)** Biodistribution of ^{18}F activity in a subject who had a meal just before tracer injection (due to delays in tracer production); The notable difference, compared to (a), is the reduced physiological activity in the liver at earlier time points and increased activity in the bowel at later time points.

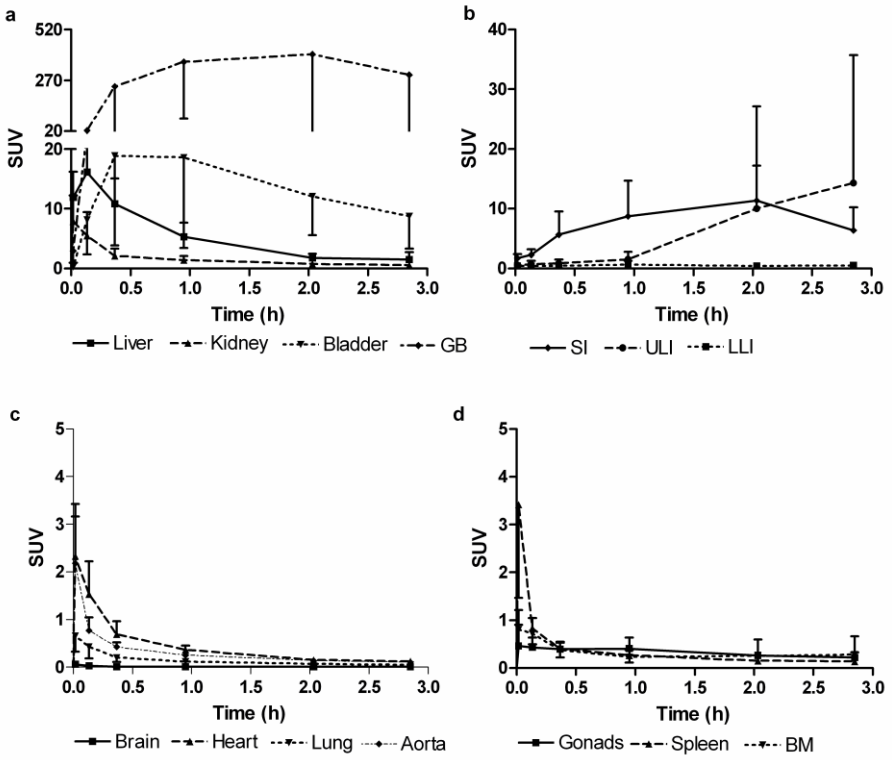

Figure 58: Mean non-decay corrected time-activity curves (TACs) normalised to injected activity (kBq) and body weight (grams), for [^{18}F]ICMT-11.

TACs were generated for several organs at various time points up to 4 hours after tracer administration in (**a**) the elimination organs (renal and hepatobiliary system), (**b**) the bowel (small intestine, upper and lower large intestine), (**c**) cranium and thorax, and (**d**) organs with potential physiological apoptosis (gonads, spleen and bone marrow). Error bars represent one standard deviation from the mean and are shown one-sided for clarity.

Table 29: **Mean Residence Times (τ) of [^{18}F]ICMT-11 for different organs in Male (n=4) and Female (n=4) Volunteers.**

	τ (kBq.h/ kBq) - Males		τ (kBq.h/ kBq) - Females	
Organ	**Mean**	**SD**	**Mean**	**SD**
Adrenal	0.001	0.0001	0.001	0.001
Bladder*	0.127	0.020	0.120	0.033
Brain	0.001	0.0004	0.001	0.0003
Breast			0.004	0.002
Gall Bladder	0.369	0.407	0.321	0.143
Heart contents	0.006	0.001	0.005	0.0004
Heart wall	0.006	0.002	0.004	0.001
Kidney	0.021	0.004	0.019	0.011
Liver	0.381	0.062	0.351	0.130
LLI	0.004	0.001	0.005	0.004
Lung†	0.018	0.007	0.012	0.007
Muscle	0.255	0.025	0.170	0.043
Ovaries‡			0.0003	0.00002
Pancreas	0.007	0.006	0.005	0.005
Red marrow	0.026	0.022	0.013	0.003
Small Intestine	0.449	0.202	0.514	0.306
Spleen	0.003	0.0004	0.002	0.001
Stomach	0.005	0.002	0.003	0.001
Testis	0.001	0.0001		
Thyroid	0.000	0.00004	0.0001	0.00003
ULI	0.214	0.242	0.039	0.064
Uterus			0.005	0.001
Thymus	0.0001	0.00003	0.0003	0.0001
Remainder	0.745	0.321	1.059	0.200

LLI-lower large intestine, ULI-upper large intestine, SD-standard deviation
*Bladder residence time is for a 2-hour voiding scenario.
†Lung activity was corrected for tissue density value of 0.33 g/ml and other organs with a density value of 1 g/ml.
‡In two subjects ovaries were not visible due to post-menopausal atrophy.

Dosimetry

Table 30 summarises the mean organ absorbed dose estimates for [^{18}F]ICMT-11 injection. The mean effective dose averaged over both males and females (±SD) was estimated to be 0.025±0.004 mSv/MBq (male 0.022±0.004; female 0.027±0.004). The 5 organs receiving the highest absorbed dose (mGy/MBq), averaged over both males and females (±SD) were the gall bladder wall (0.59±0.44), small intestine (0.12±0.05), upper large intestinal wall (0.08±0.07), urinary bladder wall (0.08±0.02), and liver (0.07±0.01). The values quoted are based on the 2-hour bladder voiding scenario. This is likely to be conservative in routine imaging scenarios where subjects would be encouraged to consume moderate quantities of fluids and empty their bladders regularly as done for [^{18}F]FDG studies. If the 4-hour voiding scenario were used, this would increase the bladder wall absorbed dose by 64% (increase of 0.05 mGy/MBq: averaged for male and female).

Table 30: **Mean organ absorbed dose estimates expressed in mGy/MBq for [^{18}F]ICMT-11 (n=8) with bladder voiding scenarios.**

	Mean Absorbed Dose estimates (mGy/MBq)		Mean Absorbed Dose estimates (mGy/MBq)	
Bladder Voiding	**2-hr voiding scenario**		**4-hr voiding scenario**	
Organ	**Mean**	**SD**	**Mean**	**SD**
Adrenals	0.022	0.005	0.022	0.005
Brain	0.003	0.001	0.002	0.001
Breasts	0.006	0.001	0.006	0.001
Gall Bladder wall	0.594	0.446	0.593	0.446
LLI wall	0.021	0.006	0.022	0.006
Small Intestine	0.122	0.056	0.122	0.056
Stomach wall	0.016	0.002	0.016	0.002
ULI wall	0.084	0.071	0.084	0.071
Heart wall	0.012	0.001	0.012	0.001
Kidneys	0.027	0.005	0.027	0.005
Liver	0.065	0.016	0.065	0.016
Lungs	0.010	0.002	0.010	0.002
Muscle	0.010	0.001	0.010	0.001
Ovaries	0.025	0.007	0.026	0.007
Pancreas	0.029	0.008	0.029	0.008
Red marrow	0.012	0.001	0.012	0.001
Osteogenic cells	0.012	0.003	0.012	0.003
Skin	0.006	0.001	0.006	0.001
Spleen	0.011	0.001	0.011	0.001
Testes	0.007	0.000	0.008	0.000
Thymus	0.007	0.001	0.007	0.001
Thyroid	0.005	0.001	0.005	0.001
Urinary Bladder wall	0.080	0.019	0.131	0.031
Uterus	0.028	0.009	0.030	0.009
Total body	0.013	0.002	0.013	0.002
Mean ED (mSv/MBq)	**0.025**	**0.004**	**0.026**	**0.004**

LLI-lower large intestine, ULI-upper large intestine, ED-effective dose

Effect of Food

Three of the 8 subjects had a meal just before the tracer injection due to delays in tracer production and scan scheduling on the day. Interestingly, in those 3 subjects, the distribution of radioactivity in the abdomen was notably different when compared to the other subjects (**Figure 57b**). The intake of food has reduced physiological activity in the liver at earlier time points and increased activity in the bowel (changed the absorbed dose as follows: Stomach (5% decrease), SI (79% increase), ULI (197% increase) and LLI (25% increase) at later time points. This is consistent with normal postprandial physiology, with emptying of gall bladder content (bile juice) to aid digestion. This is also demonstrated in the TAC profiles of the elimination organs (**Figure 59**). However, there was no difference in the other organs and in the plasma ^{18}F activity concentrations.

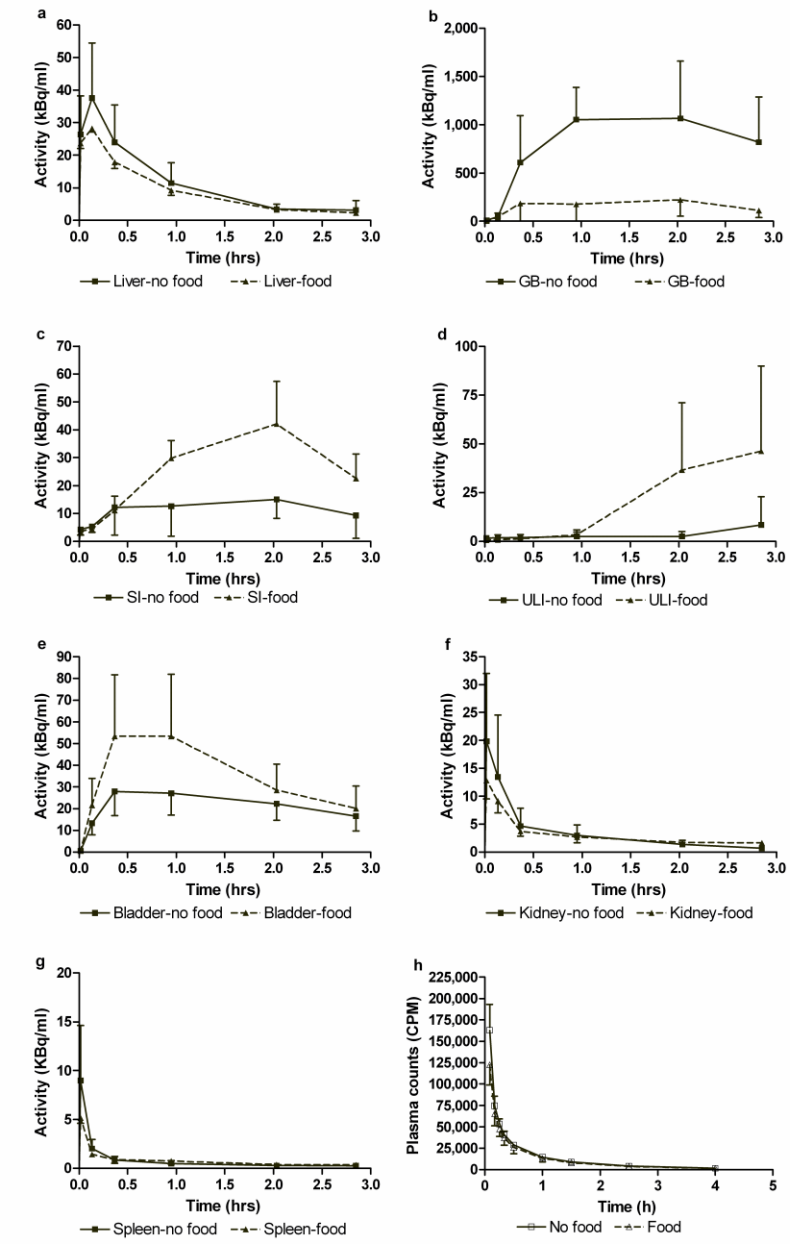

Figure 59: Mean time-activity curves (TACs; normalised to injected activity (kBq), body weight (grams) and uncorrected for radioactive decay) and plasma ^{18}F radioactivity concentrations for [^{18}F]ICMT-11 in subjects who had a meal and in subjects who did not have a meal prior to tracer injection.

There was a difference in the TAC profiles of (**a**) Liver, (**b**) Gall Bladder, (**c**) Small intestine, (**d**) Upper large intestine and (**e**) Urinary bladder, but no difference in the (**f**) Kidneys, (**g**) Spleen or the (**h**) plasma ^{18}F radioactivity concentrations. Error bars represent one standard deviation from the mean and are shown one-sided for clarity.

Discussion

This first in human study has shown that the caspase-3 specific apoptosis imaging agent [^{18}F]ICMT-11 is safe and well tolerated. Injection of [^{18}F]ICMT-11 led to rapid washout of the ^{18}F activity from the vascular compartment and elimination primarily via the renal and hepatobiliary routes. Renal excretion (18% in 4 hours) was comparably lower than for routinely used radiotracers such as [^{18}F]FDG (30%) (Jones, Alavi et al. 1982; 1998) and [^{18}F]Fluorodihydroxyphenylalanine ([^{18}F]FDOPA) (31%) (Brown, Oakes et al. 1998). In contrast, tracer localisation within the gall bladder was relatively high, with slow washout into the gastrointestinal tract.

The mean ED of [^{18}F]ICMT-11 was 0.025 mSv/MBq, which is comparable with the ED of [^{18}F]FDG (0.019 mSv/MBq) (1998). The dose limits specified in the Code of Federal Regulations (USA) per single administration of a radioactive drug for research purposes, are 30 mSv to the whole-body, blood-forming organs, lens of the eye, and gonads, with a maximum annual dose of 50 mSv. The maximum allowable single and annual dose to all other organs are 50 and 150 mSv, respectively (2012). If a 370 MBq administered radioactivity for [^{18}F]ICMT-11 (typical of many PET tracers) was assumed, the ED would be 9.3 mSv. For this administered radioactivity level, the equivalent dose received by the gonads would be estimated as 1.9 mSv. These are well within the dose limits specified above.

Regarding radiotracer uptake in normal adult tissues with potentially high intrinsic apoptosis, increased [^{18}F]ICMT-11 uptake was not seen in testes. Apoptosis plays a significant role in normal testicular physiology and up to 75% of the spermatogonia die by apoptosis before reaching maturity thus regulating sperm production, a phenomenon that is accentuated in patients with infertility (Martincic,

Virant Klun et al. 2001). The biodistribution study of [^{18}F]ML-10, a small molecule apoptotic tracer, demonstrated a distinct pattern of uptake in the testes (Hoglund, Shirvan et al. 2011). However, the biodistribution studies of annexin-V based radiotracers, (^{99m}Tc-annexin-V, ^{99m}Tc-hydrazino nicotinate (HYNIC)-annexin-V and ^{99m}Tc-4,5-bis thioacetoamide pentanoyl (BTAP)-annexin-V) did not show increased uptake in the testes, with the absorbed dose in the testes ranging from 0.005 – 0.015 mGy/MBq (Kemerink, Boersma et al. 2001; Kemerink, Liem et al. 2001; Kemerink, Liu et al. 2003). This is comparable to the absorbed testes dose observed with [^{18}F]ICMT-11 (0.007 mGy/MBq). The significantly increased uptake of [^{18}F]ML-10 in testes could be attributed to the young age of the male volunteers enrolled in the study (mean; 23 years, range 21-44 yrs). The average age of the male volunteers in the ^{99m}Tc-annexin-V, and ^{99m}Tc-BTAP-annexin-V biodistribution studies was 53 years, which is comparable to the age range in our study (63.1 yrs (±2.58; range: 59-68 yrs)). There is a strong relationship between testicular apoptotic index and age (Ng, Donat et al. 2004; Schmelz, Meiswinkel et al. 2005), with a reduction in semen volume by nearly 50% and reduced sperm production (Johnson 1986) with increasing age. This suggests a decrease in the physiological apoptosis with increasing age, which could explain the lack of significant uptake seen in the testes with [^{18}F]ICMT-11.

There was uptake of [^{18}F]ICMT-11 in the bone marrow, with a mean absorbed dose of 0.012 mGy/MBq. This is comparable to that of ^{99m}Tc-HYNIC-annexin-V (0.004 – 0.008 mGy/MBq) (Ohtsuki, Akashi et al. 1999; Kemerink, Liu et al. 2003), suggesting that the marrow uptake was physiologic, since apoptotic cell death is a physiologic component of normal hematopoiesis (Domen 2000).

While no specific instructions were given to the subjects to fast prior to the scan, in three of the subjects who had a meal before the scan, there was notably

reduced physiological activity in the liver at earlier time points and increased activity in the bowel at later time points. The impact of food appeared to be restricted to the hepatobiliary and intestinal elimination organs as no differences in the TACs from other organs or the plasma ^{18}F radioactivity were observed. This interesting observation suggests that abdominal imaging could be facilitated by incorporating a standard pre-scan meal and/or a pro-motility agent to help clear out the bowel activity and improve the signal to background ratio.

In summary, [^{18}F]ICMT-11 injection is safe and well tolerated with a favourable dosimetry profile in healthy volunteers. Organ dose estimates are similar to that seen with other routine [^{18}F]labelled tracers. The potential risks due to radiation are within accepted limits. Further clinical studies are now warranted to evaluate the utility of [^{18}F]ICMT-11 in measuring the effects of treatment on tumour apoptosis.

Summary and Future Directions

This thesis has demonstrated the ability of the newer PET radiotracers, [^{18}F]FLT and [^{11}C]choline to image cell proliferation, characterise various tumour phenotypes and to be used as imaging biomarkers for early response evaluation. Furthermore, a more stable novel choline analogue [^{18}F]D4-FCH, was successfully translated for clinical imaging. The elucidation of the biological basis of tracer uptake provides important information about the tumour biology. The improved diagnostic performance of these tracers would aid in decision making of the delivery of appropriate treatment. The early metabolic changes with therapy could potentially enable the treating oncologist to help stratify and tailor the patients' treatment and/ or consider alternative treatment options, if required. This would prevent exposure of patients to unnecessary treatment related morbidity and thus, improve their quality of life. These novel noninvasive imaging biomarkers could be used in conjunction with the existing generic tumour biomarkers as an aid to the existing diagnostic and decision making process.

The main outcomes of studies done as part of this thesis are as follows:

Chapter 2

The use of the novel kinetic filtering method (KSF) enabled visual distinction between tumours and normal pancreas, liver. All the primary pancreatic tumours were visualised and of the 11 liver metastases, 8 were visible after kinetic filtering. As seen previously (Contractor, Challapalli et al. 2012) the KSF has a detection rate of ~73% for liver metastases. Similarly, the larger liver metastases showed a central core of almost no FLT uptake surrounded by a rim of uptake at the periphery. This suggests that the rim of proliferation phenotype of the liver metastases is independent of the site of origin of the primary tumours. FLT uptake was quantified

by semi-quantitative measures and it was seen that $SUV_{60,max}$ significantly increased in the non-responders (p=0.04). The voxel analysis to explore the detailed changes of FLT uptake in tumours revealed that high intensity voxel occurrences decreased with chemotherapy. This supported the mechanism of action of chemotherapeutic agents which act on rapidly proliferating cells to cause their anti-tumour and anti-proliferative effects. The persistence of the low intensity voxels (lack of change in activity with therapy), on the other hand, may explain why these tumours progress. To summarise, FLT PET/CT and FLT PET/CT_{KSF} detected changes in proliferation, with early changes in $SUV_{60,max}$ being a negative predictor for response. Therefore, FLT PET/CT could be used as a response biomarker for gemcitabine based chemotherapy and to evaluate efficacy of novel therapeutic agents in advanced pancreatic cancer.

Since the tumours, not within the predefined range of the defined tumour class in the filtering algorithm were completely filtered out, future studies should involve pooling together of the missing patients' datasets to refine the limits set by the filter in tumours. This would improve the detection rate. In view of the encouraging results and the proliferation phenotype of the liver metastases being independent of the site of origin of the tumours, the KSF application could be extended to characterise other tumours. To this effect, a study is underway to image cell proliferation in HCC using FLT PET/CT_{KSF}.

Chapter 3

Dynamic PET/CT imaging of prostate tumours with [^{11}C]choline demonstrated a good retention of activity after plateauing (achieving a steady state) at ~15 min until 60 min with SUV_{ave}. However, with SUV_{max} there was a suggestion of increasing activity at 60 min which could be due to the contribution of

[^{11}C]betaine. Out of the 406 lymph nodes assessed, in 26 patients, 27 (6.7%) involved pelvic nodes at eLPL were detected in 9 patients. 17 out of these 27 nodes were sub-centimetre. The sensitivity and specificity on a per nodal basis were 18.5 % and 98.7%, 40.7% and 98.4 %, and 51.9% and 98.4% for MRI, [^{11}C]choline PET and [^{11}C]choline PET/CT, respectively. Sensitivity was higher for [^{11}C]choline PET/CT compared with MRI (p=0.007). This study established the feasibility of using [^{11}C]choline PET/CT as a noninvasive means of staging pelvic lymph nodes in high risk prostate cancer, being highly specific and more sensitive than PET alone or MRI including the detection of sub-centimetre disease. The high specificity could potentially be helpful clinically in terms of selecting out patients who may not require pelvic radiotherapy. The use of [^{11}C]choline PET/CT in patients with node positive disease could help in the integration with radiotherapy planning to allow the potential for dose escalation to nodal disease using Intensity Modulated Radiotherapy while avoiding unnecessary inclusion of normal healthy tissues.

Quantitative analyses of the [^{11}C]choline breast data using arterial IF showed that irreversible kinetics account for [^{11}C]choline uptake in breast tumours. The use of a validated population-based total plasma IF from the breast data, predicted that irreversible kinetics also account for [^{11}C]choline uptake in prostate cancer, thus further validating the limited venous sampling approach (Contractor, Kenny et al. 2012).

In order to establish the biological basis of [^{11}C]choline uptake in prostate cancer, IHC of the 29 malignant prostate cores and 7 nodal sections was performed with CHKα and Ki-67 antibodies. A spectrum of cytoplasmic CHKα expression was seen in the pre-malignant and malignant lesions. This study showed for the first time that tumour radiolabelled choline uptake is closely related to CHKα expression in prostate cancer, suggesting that [^{11}C]choline PET/CT could be used as a noninvasive surrogate for CHK expression. Both semi-quantitative parameters of

choline uptake in tumours correlated well with CHKα scores (best with $SUV_{60,ave}$ r=0.7, p<0.0001). Interestingly, the CHKα expression was found to be a proliferation independent phenotype in prostate cancer, unlike that seen in breast cancer (Contractor, Kenny et al. 2011).

Based on the interesting observations seen in the malignant prostate cores of patients who had [^{11}C]choline PET/CT, further cores of prostate tissue from 75 patients diagnosed with prostate cancer (malignant) and 25 patients with no prostate cancer (normal) were subsequently analysed. There was increased expression of CHK (mild staining intensity) in up to 28% of the normal prostate cores and the benign cores in a malignant prostate. This was supported by the increased CHKα gene expression in the normal prostate cores, seen on qRT-PCR. This could form the basis for the differential [^{11}C]choline uptake seen in the normal and tumour prostate (as shown in chapter 4). CHKα staining in areas of PIN, different intensities of positive staining and the low Ki67 labelling index in the malignant prostate cores were consistently seen. This pattern of CHKα expression and the availability of [^{11}C]choline PET/CT as a noninvasive surrogate could be exploited to develop and test new drug targets against CHKα in prostate cancer.

Chapter 4

[^{11}C]choline PET/CT was explored as imaging biomarker to assess the effects of neoadjuvant-androgen deprivation (NAD) alone and radical radiotherapy combined with concurrent-androgen deprivation (RT-CAD) to the prostate, in 10 patients with histologically confirmed prostate cancer. It was seen that the combination of NAD and RT-CAD significantly decreased tumour [^{11}C]choline uptake ($SUV_{60,ave}$, $SUV_{60,max}$, $TMR_{60,max}$ or $Ki_{mod\text{-}pat}$) and prostate-specific-antigen (PSA) levels (Analysis-of-Variance, p<0.001 for all variables). Although, the

magnitude of reduction in the variables was larger after NAD, there was a smaller additional reduction after RT-CAD. A wide range of reduction in tumour $SUV_{60,ave}$ (38 – 83.7%) and $SUV_{60,max}$ (22.2 – 85.3%) was seen with combined NAD and RT-CAD despite patients universally achieving PSA suppression (narrow range of 93.5 – 99.7%).

This feasibility study shows that [^{11}C]choline PET/CT detects metabolic changes within tumours following NAD and RT-CAD to the prostate. A differential reduction in [^{11}C]choline uptake in spite of a global reduction in PSA following NAD and RT-CAD could provide prognostic information. SUV and TMR_{max} (at early and/or late time-points) warrant further evaluation as objective measures of response to NAD and RT-CAD, alongside functional MRI parameters and PSA as early response biomarker endpoints in PCa during radical treatment. This would enable the use of [^{11}C]choline PET/CT as a vehicle for response evaluation in radiotherapy dose-escalation trials, as well as novel hormonal therapies.

Chapter 5

The safety, biodistribution, and internal radiation dosimetry study of [^{18}F]D4-FCH in eight healthy human volunteers, showed it to be a safe and well tolerated tracer. There were no radiotracer-related serious adverse events reported. The mean effective dose averaged over both males and females was estimated to be 0.025 (male 0.022; female 0.027) mSv/MBq. The 5 organs receiving the highest absorbed dose (mGy/MBq) were the kidneys (0.106), liver (0.094), pancreas (0.066), urinary bladder wall (0.047), and adrenals (0.046). Elimination was through the renal and hepatic systems. [^{18}F]D4-FCH was found to be more stable with 38% of parent tracer in plasma at 60 min, decreasing to 31% at 4h. This represented an improvement in metabolic stability for choline tracers in use clinically; for example a

2-fold higher metabolic stability was observed for [^{18}F]D4-FCH relative to published data for [^{11}C]choline (17% at 60 min).

To summarise, [^{18}F]D4-FCH was safe, with a dosimetry profile comparable to other common [^{18}F] PET tracers. These data support the further development of [^{18}F]D4-FCH for clinical imaging of choline metabolism. Proof-of-concept study of [^{18}F]D4-FCH in non-small cell lung cancer patients is underway. The early preliminary results of [^{18}F]D4-FCH PET/CT in 5 patients with NSCLC have shown that imaging primary lung tumours is feasible. In future [^{18}F]D4-FCH PET/CT could be used as a noninvasive surrogate for CHK expression and thus potentially used as a prognostic marker and for predicting patient outcome. It is also envisaged that [^{18}F]D4-FCH PET/CT could play a further role in selection and/ or evaluation of lung cancer patients for targeted therapy.

Chapter 6

The safety, biodistribution, and internal radiation dosimetry study of [^{18}F]ICMT-11 in eight healthy human volunteers, showed it to be a safe and well tolerated tracer. There were no radiotracer-related serious adverse events reported. The mean effective dose averaged over both males and females was estimated to be 0.025 (male 0.022; female 0.027) mSv/MBq. The 5 organs receiving the highest absorbed dose (mGy/MBq), averaged over both males and females, were the gall bladder wall (0.59), small intestine (0.12), upper large intestinal wall (0.08), urinary bladder wall (0.08), and liver (0.07). Elimination was both renal and via the hepatobiliary system. [^{18}F]ICMT-11 is safe, with a dosimetry profile comparable to other common [^{18}F] PET tracers. These data support the further development of [^{18}F]ICMT-11 for clinical imaging of apoptosis, as there is a need for biomarkers, for imaging both cell proliferation and cell death. A study is underway to evaluate

chemotherapy induced activation of caspase 3/7 using [^{18}F]ICMT-11 in breast cancer patients.

In summary, this thesis has established the feasibility of using [^{18}F]FLT and [^{11}C]choline PET as imaging biomarkers. The application of the novel KSF has been extended and validated for application to pancreatic cancer. It was also shown that [^{11}C]choline PET could be used as a noninvasive surrogate for CHK expression and for response evaluation in radiotherapy dose-escalation trials and novel hormonal therapies. It also translated [^{18}F]D4-FCH for clinical imaging. Additional work included translation of a novel isatin sulphonamide ([^{18}F]ICMT-11), to detect activated caspase 3, into humans for biodistribution and radiation dosimetry. Therefore, exciting times await future imaging strategies using the novel PET tracers translated for clinical use in this thesis.

References

(1991). "1990 Recommendations of the International Commission on Radiological Protection. ICRP Publication 60." Ann ICRP **21**(1-3): 1-201.

(1998). "Radiation dose to patients from radiopharmaceuticals (addendum 2 to ICRP publication 53).ICRP Publication 80." Ann ICRP **28**(3): 1-126.

(2007). "The 2007 Recommendations of the International Commission on Radiological Protection. ICRP publication 103." Ann ICRP **37**(2-4): 1-332.

(2011). "NICE, http://publications.nice.org.uk/lung-cancer-cg121/guidance." Retrieved 25 September, 2013.

(2012). ""Radioactive drugs for certain research uses." Code of Federal Regulations Title 21, Part 361.1 . http://www.accessdata.fda.gov/scripts/cdrh/cfdocs/cfcfr/CFRSearch.cfm?fr=361.1 " Retrieved 16 November, 2012.

(2012). ""Radioactive drugs for certain research uses." Code of Federal Regulations Title 21, Part 361.1. http://www.accessdata.fda.gov/scripts/cdrh/cfdocs/cfcfr/CFRSearch.cfm?fr=361.1 " Retrieved 04 July, 2013.

Abella, M., J. J. Vaquero, et al. (2009). "Sinogram bow-tie filtering in FBP PET reconstruction." Med Phys **36**(5): 1663-1671.

Aboagye, E. O. and Z. M. Bhujwalla (1999). "Malignant transformation alters membrane choline phospholipid metabolism of human mammary epithelial cells." Cancer Res **59**(1): 80-84.

Ackerstaff, E., B. R. Pflug, et al. (2001). "Detection of increased choline compounds with proton nuclear magnetic resonance spectroscopy subsequent to malignant transformation of human prostatic epithelial cells." Cancer Res **61**(9): 3599-3603.

Al-Saeedi, F., A. E. Welch, et al. (2005). "[methyl-3H]Choline incorporation into MCF7 tumour cells: correlation with proliferation." Eur J Nucl Med Mol Imaging **32**(6): 660-667.

Al-Saffar, N. M., L. E. Jackson, et al. (2010). "The phosphoinositide 3-kinase inhibitor PI-103 downregulates choline kinase alpha leading to

phosphocholine and total choline decrease detected by magnetic resonance spectroscopy." Cancer Res **70**(13): 5507-5517.

Alberts, B., Johnson, A., Lewis, J., Raff, M., Roberts, K., Walter, P. (2008). Molecular biology of the cell. New York, Garland Science, Taylor and Francis group.

Allaf, M. E., A. W. Partin, et al. (2006). "The importance of pelvic lymph node dissection in men with clinically localized prostate cancer." Rev Urol **8**(3): 112-119.

Allen, D. D. and Q. R. Smith (2001). "Characterization of the blood-brain barrier choline transporter using the in situ rat brain perfusion technique." J Neurochem **76**(4): 1032-1041.

Amanie, J., H. S. Jans, et al. (2013). "Analysis of intraprostatic therapeutic effects in prostate cancer patients using [(11)C]-choline pet/ct after external-beam radiation therapy." Curr Oncol **20**(2): 104-110.

Arora, K. K., D. M. Parry, et al. (1992). "Hexokinase receptors: preferential enzyme binding in normal cells to nonmitochondrial sites and in transformed cells to mitochondrial sites." J Bioenerg Biomembr **24**(1): 47-53.

Aston, J. A., V. J. Cunningham, et al. (2002). "Positron emission tomography partial volume correction: estimation and algorithms." J Cereb Blood Flow Metab **22**(8): 1019-1034.

Bading, J. R. and A. F. Shields (2008). "Imaging of cell proliferation: status and prospects." J Nucl Med **49 Suppl 2**: 64S-80S.

Balogova, S., V. Huchet, et al. (2010). "Detection of bronchioloalveolar cancer by means of PET/CT and 18F-fluorocholine, and comparison with 18F-fluorodeoxyglucose." Nucl Med Commun **31**(5): 389-397.

Bang, S., H. W. Chung, et al. (2006). "The clinical usefulness of 18-fluorodeoxyglucose positron emission tomography in the differential diagnosis, staging, and response evaluation after concurrent chemoradiotherapy for pancreatic cancer." J Clin Gastroenterol **40**(10): 923-929.

Bansal, A., W. Shuyan, et al. (2008). "Biodisposition and metabolism of [(18)F]fluorocholine in 9L glioma cells and 9L glioma-bearing fisher rats." Eur J Nucl Med Mol Imaging **35**(6): 1192-1203.

Barnard, R. M. (2012). "Flow cytometry: a flexible tool for biomarker research." Bioanalysis **4**(20): 2471-2483.

Barrett, T., A. B. Gill, et al. (2012). "DCE and DW MRI in monitoring response to androgen deprivation therapy in patients with prostate cancer: a feasibility study." Magn Reson Med **67**(3): 778-785.

Barthel, H., M. C. Cleij, et al. (2003). "3'-deoxy-3'-[18F]fluorothymidine as a new marker for monitoring tumor response to antiproliferative therapy in vivo with positron emission tomography." Cancer Res **63**(13): 3791-3798.

Barthel, H., M. Perumal, et al. (2005). "The uptake of 3'-deoxy-3'-[18F]fluorothymidine into L5178Y tumours in vivo is dependent on thymidine kinase 1 protein levels." Eur J Nucl Med Mol Imaging **32**(3): 257-263.

Barwick, T., B. Bencherif, et al. (2009). "Molecular PET and PET/CT imaging of tumour cell proliferation using F-18 fluoro-L-thymidine: a comprehensive evaluation." Nucl Med Commun **30**(12): 908-917.

Bastiaannet, E., H. Groen, et al. (2004). "The value of FDG-PET in the detection, grading and response to therapy of soft tissue and bone sarcomas; a systematic review and meta-analysis." Cancer Treat Rev **30**(1): 83-101.

Basu, S., T. C. Kwee, et al. (2011). "Fundamentals of PET and PET/CT imaging." Ann N Y Acad Sci **1228**: 1-18.

Beauregard, J. M., S. G. Williams, et al. (2010). "Pilot comparison of F-fluorocholine and F-fluorodeoxyglucose PET/CT with conventional imaging in prostate cancer." J Med Imaging Radiat Oncol **54**(4): 325-332.

Beheshti, M., L. Imamovic, et al. (2010). "18F choline PET/CT in the preoperative staging of prostate cancer in patients with intermediate or high risk of extracapsular disease: a prospective study of 130 patients." Radiology **254**(3): 925-933.

Bernd, H., E. De Kerviler, et al. (2009). "Safety and tolerability of ultrasmall superparamagnetic iron oxide contrast agent: comprehensive analysis of a clinical development program." Invest Radiol **44**(6): 336-342.

Bertoli, C., J. M. Skotheim, et al. (2013). "Control of cell cycle transcription during G1 and S phases." Nat Rev Mol Cell Biol **14**(8): 518-528.

Boellaard, R. (2009). "Standards for PET image acquisition and quantitative data analysis." J Nucl Med **50 Suppl 1**: 11S-20S.

Bouchelouche, K. and P. Oehr (2008). "Recent developments in urologic oncology: positron emission tomography molecular imaging." Curr Opin Oncol **20**(3): 321-326.

Bourguet, P. (2003). "[Standards, Options and Recommendations for the use of PET-FDG in cancerology. Results in sarcomas]." Bull Cancer **90 Spec No**: S96-102.

Breeuwsma, A. J., J. Pruim, et al. (2005). "In vivo uptake of [11C]choline does not correlate with cell proliferation in human prostate cancer." Eur J Nucl Med Mol Imaging **32**(6): 668-673.

Brockenbrough, J. S., T. Souquet, et al. (2011). "Tumor 3'-deoxy-3'-(18)F-fluorothymidine ((18)F-FLT) uptake by PET correlates with thymidine kinase 1 expression: static and kinetic analysis of (18)F-FLT PET studies in lung tumors." J Nucl Med **52**(8): 1181-1188.

Brown, W. D., T. R. Oakes, et al. (1998). "Fluorine-18-fluoro-L-DOPA dosimetry with carbidopa pretreatment." J Nucl Med **39**(11): 1884-1891.

Buck, A. C., H. H. Schirrmeister, et al. (2001). "Ki-67 immunostaining in pancreatic cancer and chronic active pancreatitis: does in vivo FDG uptake correlate with proliferative activity?" J Nucl Med **42**(5): 721-725.

Buck, A. K., G. Halter, et al. (2003). "Imaging proliferation in lung tumors with PET: 18F-FLT versus 18F-FDG." J Nucl Med **44**(9): 1426-1431.

Buck, A. K., M. Hetzel, et al. (2005). "Clinical relevance of imaging proliferative activity in lung nodules." Eur J Nucl Med Mol Imaging **32**(5): 525-533.

Budiharto, T., S. Joniau, et al. (2011). "Prospective evaluation of 11C-choline positron emission tomography/computed tomography and diffusion-weighted magnetic resonance imaging for the nodal staging of prostate cancer with a high risk of lymph node metastases." Eur Urol **60**(1): 125-130.

Buyse, M., P. Thirion, et al. (2000). "Relation between tumour response to first-line chemotherapy and survival in advanced colorectal cancer: a meta-analysis. Meta-Analysis Group in Cancer." Lancet **356**(9227): 373-378.

Buyyounouski, M. K. (2010). "Radiotherapy: PSA nadir predicts long-term mortality." Nat Rev Clin Oncol **7**(4): 188-190.

Cartwright, T., D. A. Richards, et al. (2008). "Cancer of the pancreas: are we making progress? A review of studies in the US Oncology Research Network." Cancer Control **15**(4): 308-313.

Casamassima, F., L. Masi, et al. (2011). "Efficacy of eradicative radiotherapy for limited nodal metastases detected with choline PET scan in prostate cancer patients." Tumori **97**(1): 49-55.

Cavanagh, B. L., T. Walker, et al. (2011). "Thymidine analogues for tracking DNA synthesis." Molecules **16**(9): 7980-7993.

Chalkidou, A., D. B. Landau, et al. (2012). "Correlation between Ki-67 immunohistochemistry and 18F-fluorothymidine uptake in patients with cancer: A systematic review and meta-analysis." Eur J Cancer **48**(18): 3499-3513.

Chang, J., M. Ormerod, et al. (2000). "Apoptosis and proliferation as predictors of chemotherapy response in patients with breast carcinoma." Cancer **89**(11): 2145-2152.

Cheebsumon, P., L. M. Velasquez, et al. (2011). "Measuring response to therapy using FDG PET: semi-quantitative and full kinetic analysis." Eur J Nucl Med Mol Imaging **38**(5): 832-842.

Chen, W. (2007). "Clinical applications of PET in brain tumors." J Nucl Med **48**(9): 1468-1481.

Chilosi, M., M. Lestani, et al. (1994). "A rapid immunostaining method for frozen sections." Biotech Histochem **69**(4): 235-239.

Choi, M., L. K. Heilbrun, et al. (2010). "Using 18F-fluorodeoxyglucose positron emission tomography to monitor clinical outcomes in patients treated with neoadjuvant chemo-radiotherapy for locally advanced pancreatic cancer." Am J Clin Oncol **33**(3): 257-261.

Chung, J. K., Y. J. Lee, et al. (1999). "Mechanisms related to [18F]fluorodeoxyglucose uptake of human colon cancers transplanted in nude mice." J Nucl Med **40**(2): 339-346.

Chung, T., K. S. Crilly, et al. (1997). "ATP-dependent choline phosphate-induced mitogenesis in fibroblasts involves activation of pp70 S6 kinase and phosphatidylinositol 3'-kinase through an extracellular site. Synergistic mitogenic effects of choline phosphate and sphingosine 1-phosphate." J Biol Chem **272**(5): 3064-3072.

Ciampi, R., A. Vivaldi, et al. (2008). "Expression analysis of facilitative glucose transporters (GLUTs) in human thyroid carcinoma cell lines and primary tumors." Mol Cell Endocrinol **291**(1-2): 57-62.

Ciliberto, D., C. Botta, et al. (2013). "Role of gemcitabine-based combination therapy in the management of advanced pancreatic cancer: a meta-analysis of randomised trials." Eur J Cancer **49**(3): 593-603.

Cimitan, M., R. Bortolus, et al. (2006). "[18F]fluorocholine PET/CT imaging for the detection of recurrent prostate cancer at PSA relapse: experience in 100 consecutive patients." Eur J Nucl Med Mol Imaging **33**(12): 1387-1398.

Claudio Pascali, A. B., Ren Itawa, Mara Cambiè, Emilio Bombardieri (2000). "[11C]Methylation on a C18 Sep-Pak cartridge: a convenient way to produce [N-methyl-11C]choline " J. Labelled Compds. Radiopharm **43**(2): 195-203.

Cleij, M. C., Steel, C.J., Brady, F., Ell, P.J., Pike, V.W., Luthra, S.K. (2001). "An improved synthesis of 3′-deoxy-3′-[18F]fluorothymidine ([18F]FLT) and the fate of the precursor 2,3′-anhydro-5′-O-(4,4′-dimethoxytrityl)-thymidine." J Labelled Compounds Radiopharm **44**: 871-873.

Clements, R. (2010). "Imaging in prostate cancer." from http://emedicine.medscape.com/article/379996-overview.

Collette, L., T. Burzykowski, et al. (2006). "Prostate-specific antigen (PSA) alone is not an appropriate surrogate marker of long-term therapeutic benefit in prostate cancer trials." Eur J Cancer **42**(10): 1344-1350.

Colozza, M., E. Azambuja, et al. (2005). "Proliferative markers as prognostic and predictive tools in early breast cancer: where are we now?" Ann Oncol **16**(11): 1723-1739.

Conti, M. (2009). "State of the art and challenges of time-of-flight PET." Phys Med **25**(1): 1-11.

Contractor, K., A. Challapalli, et al. (2011). "Use of [11C]choline PET-CT as a noninvasive method for detecting pelvic lymph node status from prostate cancer and relationship with choline kinase expression." Clin Cancer Res **17**(24): 7673-7683.

Contractor, K., A. Challapalli, et al. (2012). "Imaging of cellular proliferation in liver metastasis by [18F]fluorothymidine positron emission tomography: effect of therapy." Phys Med Biol **57**(11): 3419-3433.

Contractor, K. B., L. M. Kenny, et al. (2012). "Evaluation of limited blood sampling population input approaches for kinetic quantification of [18F]fluorothymidine PET data." EJNMMI Res **2**: 11.

Contractor, K. B., L. M. Kenny, et al. (2009). "[11C]choline positron emission tomography in estrogen receptor-positive breast cancer." Clin Cancer Res **15**(17): 5503-5510.

Contractor, K. B., L. M. Kenny, et al. (2011). "Biological basis of [11C]choline-positron emission tomography in patients with breast cancer: comparison with [18F]fluorothymidine positron emission tomography." Nucl Med Commun.

Contractor, K. B., L. M. Kenny, et al. (2011). "[18F]-3'Deoxy-3'-fluorothymidine positron emission tomography and breast cancer response to docetaxel." Clin Cancer Res **17**(24): 7664-7672.

Costello, E., W. Greenhalf, et al. (2012). "New biomarkers and targets in pancreatic cancer and their application to treatment." Nat Rev Gastroenterol Hepatol **9**(8): 435-444.

Cunningham, V. J. and T. Jones (1993). "Spectral analysis of dynamic PET studies." J Cereb Blood Flow Metab **13**(1): 15-23.

Daly, P. F., R. C. Lyon, et al. (1987). "Phospholipid metabolism in cancer cells monitored by 31P NMR spectroscopy." J Biol Chem **262**(31): 14875-14878.

Danella, J. F., J. B. deKernion, et al. (1993). "The contemporary incidence of lymph node metastases in prostate cancer: implications for laparoscopic lymph node dissection." J Urol **149**(6): 1488-1491.

Davies, M. A. and Y. Samuels (2010). "Analysis of the genome to personalize therapy for melanoma." Oncogene **29**(41): 5545-5555.

De Giorgi, U., M. Mego, et al. (2010). "18F-FDG PET/CT findings and circulating tumor cell counts in the monitoring of systemic therapies for bone metastases from breast cancer." J Nucl Med **51**(8): 1213-1218.

de Jong, I. J., J. Pruim, et al. (2003). "Preoperative staging of pelvic lymph nodes in prostate cancer by 11C-choline PET." J Nucl Med **44**(3): 331-335.

de Langen, A. J., B. Klabbers, et al. (2009). "Reproducibility of quantitative 18F-3'-deoxy-3'-fluorothymidine measurements using positron emission tomography." Eur J Nucl Med Mol Imaging **36**(3): 389-395.

De Waele, A., S. Van Binnebeek, et al. (2010). "Response assessment of hormonal therapy in prostate cancer by [11C] choline PET/CT." Clin Nucl Med **35**(9): 701-703.

DeGrado, T. R., R. E. Coleman, et al. (2001). "Synthesis and evaluation of 18F-labeled choline as an oncologic tracer for positron emission tomography: initial findings in prostate cancer." Cancer Res **61**(1): 110-117.

DeGrado, T. R., R. E. Reiman, et al. (2002). "Pharmacokinetics and radiation dosimetry of 18F-fluorocholine." J Nucl Med **43**(1): 92-96.

Degterev, A., M. Boyce, et al. (2003). "A decade of caspases." Oncogene **22**(53): 8543-8567.

Dehdashti, F., P. W. Grigsby, et al. (2013). "Positron emission tomography with [(18)F]-3'-deoxy-3'fluorothymidine (FLT) as a predictor of outcome in patients with locally advanced resectable rectal cancer: a pilot study." Mol Imaging Biol **15**(1): 106-113.

Dittmann, H., B. M. Dohmen, et al. (2002). "Early changes in [18F]FLT uptake after chemotherapy: an experimental study." Eur J Nucl Med Mol Imaging **29**(11): 1462-1469.

Domen, J. (2000). "The role of apoptosis in regulating hematopoiesis and hematopoietic stem cells." Immunol Res **22**(2-3): 83-94.

Dose Schwarz, J., M. Bader, et al. (2005). "Early prediction of response to chemotherapy in metastatic breast cancer using sequential 18F-FDG PET." J Nucl Med **46**(7): 1144-1150.

Dubray, B., C. Breton, et al. (1998). "In vitro radiation-induced apoptosis and early response to low-dose radiotherapy in non-Hodgkin's lymphomas." Radiother Oncol **46**(2): 185-191.

Eckel, F., K. Herrmann, et al. (2009). "Imaging of proliferation in hepatocellular carcinoma with the in vivo marker 18F-fluorothymidine." J Nucl Med **50**(9): 1441-1447.

Effert, P. J., R. Bares, et al. (1996). "Metabolic imaging of untreated prostate cancer by positron emission tomography with 18fluorine-labeled deoxyglucose." J Urol **155**(3): 994-998.

Eisenhauer, E. A., P. Therasse, et al. (2009). "New response evaluation criteria in solid tumours: revised RECIST guideline (version 1.1)." Eur J Cancer **45**(2): 228-247.

Esteves, F. P., D. M. Schuster, et al. (2006). "Gastrointestinal tract malignancies and positron emission tomography: an overview." Semin Nucl Med **36**(2): 169-181.

Evangelista, L., A. Guttilla, et al. (2013). "Utility of choline positron emission tomography/computed tomography for lymph node involvement identification in intermediate- to high-risk prostate cancer: a systematic literature review and meta-analysis." Eur Urol **63**(6): 1040-1048.

Facey, K., I. Bradbury, et al. (2007). "Overview of the clinical effectiveness of positron emission tomography imaging in selected cancers." Health Technol Assess **11**(44): iii-iv, xi-267.

Faried, A., M. Sohda, et al. (2004). "Expression of heat-shock protein Hsp60 correlated with the apoptotic index and patient prognosis in human oesophageal squamous cell carcinoma." Eur J Cancer **40**(18): 2804-2811.

Farrell, J. J., H. Elsaleh, et al. (2009). "Human equilibrative nucleoside transporter 1 levels predict response to gemcitabine in patients with pancreatic cancer." Gastroenterology **136**(1): 187-195.

Farsad, M., R. Schiavina, et al. (2005). "Detection and localization of prostate cancer: correlation of (11)C-choline PET/CT with histopathologic step-section analysis." J Nucl Med **46**(10): 1642-1649.

Fischer, B. M. and J. Mortensen (2006). "The future in diagnosis and staging of lung cancer: positron emission tomography." Respiration **73**(3): 267-276.

Fischer, B. M., J. Mortensen, et al. (2001). "Positron emission tomography in the diagnosis and staging of lung cancer: a systematic, quantitative review." Lancet Oncol **2**(11): 659-666.

Fleming, I. N., F. J. Gilbert, et al. (2010). "Opportunities for PET to deliver clinical benefit in cancer: breast cancer as a paradigm." Cancer Imaging **10**: 144-152.

Fletcher, J. W., B. Djulbegovic, et al. (2008). "Recommendations on the use of 18F-FDG PET in oncology." J Nucl Med **49**(3): 480-508.

Fletcher, J. W., S. M. Kymes, et al. (2008). "A comparison of the diagnostic accuracy of 18F-FDG PET and CT in the characterization of solitary pulmonary nodules." J Nucl Med **49**(2): 179-185.

Floor, S. L., J. E. Dumont, et al. (2012). "Hallmarks of cancer: of all cancer cells, all the time?" Trends Mol Med **18**(9): 509-515.

Foley, E. A. and T. M. Kapoor (2013). "Microtubule attachment and spindle assembly checkpoint signalling at the kinetochore." Nat Rev Mol Cell Biol **14**(1): 25-37.

Fonteyne, P., V. Casneuf, et al. (2009). "Expression of hexokinases and glucose transporters in treated and untreated oesophageal adenocarcinoma." Histol Histopathol **24**(8): 971-977.

Fortt, R., G. Smith, et al. (2012). "Automated GMP synthesis of [(18)F]ICMT-11 for in vivo imaging of caspase-3 activity." Nucl Med Biol **39**(7): 1000-1005.

Francis, D. L., A. Freeman, et al. (2003). "In vivo imaging of cellular proliferation in colorectal cancer using positron emission tomography." Gut **52**(11): 1602-1606.

Friedman, K. P. and R. L. Wahl (2004). "Clinical use of positron emission tomography in the management of cutaneous melanoma." Semin Nucl Med **34**(4): 242-253.

Fuccio, C., R. Schiavina, et al. (2011). "Androgen deprivation therapy influences the uptake of 11C-choline in patients with recurrent prostate cancer: the preliminary results of a sequential PET/CT study." Eur J Nucl Med Mol Imaging **38**(11): 1985-1989.

Gadda, G. (2003). "pH and deuterium kinetic isotope effects studies on the oxidation of choline to betaine-aldehyde catalyzed by choline oxidase." Biochim Biophys Acta **1650**(1-2): 4-9.

Gallego-Ortega, D., A. Ramirez De Molina, et al. (2006). "Generation and characterization of monoclonal antibodies against choline kinase alpha and their potential use as diagnostic tools in cancer." Int J Oncol **29**(2): 335-340.

Gallego-Ortega, D., A. Ramirez de Molina, et al. (2009). "Differential role of human choline kinase alpha and beta enzymes in lipid metabolism: implications in cancer onset and treatment." PLoS One **4**(11): e7819.

Gambhir, S. S., J. Czernin, et al. (2001). "A tabulated summary of the FDG PET literature." J Nucl Med **42**(5 Suppl): 1S-93S.

Garcia-Segura, J. M., M. Sanchez-Chapado, et al. (1999). "In vivo proton magnetic resonance spectroscopy of diseased prostate: spectroscopic features of malignant versus benign pathology." Magn Reson Imaging **17**(5): 755-765.

Gibellini, F. and T. K. Smith (2010). "The Kennedy pathway--De novo synthesis of phosphatidylethanolamine and phosphatidylcholine." IUBMB Life **62**(6): 414-428.

Giovacchini, G. (2011). "Do we have to withdraw antiandrogenic therapy in prostate cancer patients before PET/CT with [11C]choline?" Eur J Nucl Med Mol Imaging **38**(11): 1964-1966.

Giovacchini, G., M. Picchio, et al. (2008). "[(11)C]choline uptake with PET/CT for the initial diagnosis of prostate cancer: relation to PSA levels, tumour stage and anti-androgenic therapy." Eur J Nucl Med Mol Imaging **35**(6): 1065-1073.

Glunde, K. and Z. M. Bhujwalla (2007). "Choline kinase alpha in cancer prognosis and treatment." Lancet Oncol **8**(10): 855-857.

Glunde, K., Z. M. Bhujwalla, et al. (2011). "Choline metabolism in malignant transformation." Nat Rev Cancer **11**(12): 835-848.

Graham, M. M., L. M. Peterson, et al. (1997). "Fluorine-18-fluoromisonidazole radiation dosimetry in imaging studies." J Nucl Med **38**(10): 1631-1636.

Gray, K. R., K. B. Contractor, et al. (2010). "Kinetic filtering of [(18)F]Fluorothymidine in positron emission tomography studies." Phys Med Biol **55**(3): 695-709.

Greven, K. M., D. W. Williams, 3rd, et al. (1994). "Positron emission tomography of patients with head and neck carcinoma before and after high dose irradiation." Cancer **74**(4): 1355-1359.

Grierson, J. R., J. L. Schwartz, et al. (2004). "Metabolism of 3'-deoxy-3'-[F-18]fluorothymidine in proliferating A549 cells: validations for positron emission tomography." Nucl Med Biol **31**(7): 829-837.

Grierson, J. R. and A. F. Shields (2000). "Radiosynthesis of 3'-deoxy-3'-[(18)F]fluorothymidine: [(18)F]FLT for imaging of cellular proliferation in vivo." Nucl Med Biol **27**(2): 143-156.

Gunn, R. N., S. R. Gunn, et al. (2001). "Positron emission tomography compartmental models." J Cereb Blood Flow Metab **21**(6): 635-652.

Gunn, R. N., S. R. Gunn, et al. (2002). "Positron emission tomography compartmental models: a basis pursuit strategy for kinetic modeling." J Cereb Blood Flow Metab **22**(12): 1425-1439.

Gunn, R. N., J. T. Yap, et al. (2000). "A general method to correct PET data for tissue metabolites using a dual-scan approach." J Nucl Med **41**(4): 706-711.

Hacker, A., S. Jeschke, et al. (2006). "Detection of pelvic lymph node metastases in patients with clinically localized prostate cancer: comparison of [18F]fluorocholine positron emission tomography-computerized tomography and laparoscopic radioisotope guided sentinel lymph node dissection." J Urol **176**(5): 2014-2018; discussion 2018-2019.

Hain, S. F. (2005). "Positron emission tomography in uro-oncology." Cancer Imaging **5**(1): 1-7.

Hanahan, D. and R. A. Weinberg (2000). "The hallmarks of cancer." Cell **100**(1): 57-70.

Hanahan, D. and R. A. Weinberg (2011). "Hallmarks of cancer: the next generation." Cell **144**(5): 646-674.

Hanlon, A. L., W. H. Pinover, et al. (2001). "Patterns and fate of PSA bouncing following 3D-CRT." Int J Radiat Oncol Biol Phys **50**(4): 845-849.

Hansel, D. E., A. K. Meeker, et al. (2006). "Telomere length variation in biliary tract metaplasia, dysplasia, and carcinoma." Mod Pathol **19**(6): 772-779.

Hara, T. (2001). "18F-fluorocholine: a new oncologic PET tracer." J Nucl Med **42**(12): 1815-1817.

Hara, T. (2002). "11C-choline and 2-deoxy-2-[18F]fluoro-D-glucose in tumor imaging with positron emission tomography." Mol Imaging Biol **4**(4): 267-273.

Hara, T., K. Inagaki, et al. (2000). "Sensitive detection of mediastinal lymph node metastasis of lung cancer with 11C-choline PET." J Nucl Med **41**(9): 1507-1513.

Hara, T., N. Kosaka, et al. (1998). "PET imaging of prostate cancer using carbon-11-choline." J Nucl Med **39**(6): 990-995.

Hara, T., N. Kosaka, et al. (1997). "PET imaging of brain tumor with [methyl-11C]choline." J Nucl Med **38**(6): 842-847.

Harisinghani, M. G., J. Barentsz, et al. (2003). "Noninvasive detection of clinically occult lymph-node metastases in prostate cancer." N Engl J Med **348**(25): 2491-2499.

Harris, A. L. (2002). "Hypoxia--a key regulatory factor in tumour growth." Nat Rev Cancer **2**(1): 38-47.

Harris, R. J., T. F. Cloughesy, et al. (2012). "18F-FDOPA and 18F-FLT positron emission tomography parametric response maps predict response in recurrent malignant gliomas treated with bevacizumab." Neuro Oncol **14**(8): 1079-1089.

Hawass, N. E. (1997). "Comparing the sensitivities and specificities of two diagnostic procedures performed on the same group of patients." Br J Radiol **70**(832): 360-366.

Heidenreich, A., J. Bellmunt, et al. (2011). "EAU guidelines on prostate cancer. Part I: screening, diagnosis, and treatment of clinically localised disease." Actas Urol Esp **35**(9): 501-514.

Hellwig, D., D. Ukena, et al. (2001). "[Meta-analysis of the efficacy of positron emission tomography with F-18-fluorodeoxyglucose in lung tumors. Basis for discussion of the German Consensus Conference on PET in Oncology 2000]." Pneumologie **55**(8): 367-377.

Herholz, K., D. Coope, et al. (2007). "Metabolic and molecular imaging in neuro-oncology." Lancet Neurol **6**(8): 711-724.

Herrmann, K., A. K. Buck, et al. (2011). "A pilot study to evaluate 3'-deoxy-3'-18F-fluorothymidine pet for initial and early response imaging in mantle cell lymphoma." J Nucl Med **52**(12): 1898-1902.

Herrmann, K., F. Eckel, et al. (2008). "In vivo characterization of proliferation for discriminating cancer from pancreatic pseudotumors." J Nucl Med **49**(9): 1437-1444.

Herrmann, K., M. Erkan, et al. (2012). "Comparison of 3'-deoxy-3'-[(1)(8)F]fluorothymidine positron emission tomography (FLT PET) and FDG

PET/CT for the detection and characterization of pancreatic tumours." Eur J Nucl Med Mol Imaging **39**(5): 846-851.

Herrmann, K., K. Ott, et al. (2007). "Imaging gastric cancer with PET and the radiotracers 18F-FLT and 18F-FDG: a comparative analysis." J Nucl Med **48**(12): 1945-1950.

Herrmann, K., H. A. Wieder, et al. (2007). "Early response assessment using 3'-deoxy-3'-[18F]fluorothymidine-positron emission tomography in high-grade non-Hodgkin's lymphoma." Clin Cancer Res **13**(12): 3552-3558.

Higashi, K., Y. Ueda, et al. (1998). "Fluorine-18-FDG PET imaging is negative in bronchioloalveolar lung carcinoma." J Nucl Med **39**(6): 1016-1020.

Higashi, T., T. Saga, et al. (2003). "Diagnosis of pancreatic cancer using fluorine-18 fluorodeoxyglucose positron emission tomography (FDG PET) --usefulness and limitations in "clinical reality"." Ann Nucl Med **17**(4): 261-279.

Higashi, T., H. Sakahara, et al. (1999). "Evaluation of intraoperative radiation therapy for unresectable pancreatic cancer with FDG PET." J Nucl Med **40**(9): 1424-1433.

Hoglund, J., A. Shirvan, et al. (2011). "18F-ML-10, a PET tracer for apoptosis: first human study." J Nucl Med **52**(5): 720-725.

Hoh, C. K., M. A. Seltzer, et al. (1998). "Positron emission tomography in urological oncology." J Urol **159**(2): 347-356.

Horska, A. and P. B. Barker (2010). "Imaging of brain tumors: MR spectroscopy and metabolic imaging." Neuroimaging Clin N Am **20**(3): 293-310.

Hoshikawa, H., T. Kishino, et al. (2012). "Comparison of (18) F-FLT PET and (18) F-FDG PET for detection of cervical lymph node metastases in head and neck cancers." Acta Otolaryngol **132**(12): 1347-1354.

Hovels, A. M., R. A. Heesakkers, et al. (2008). "The diagnostic accuracy of CT and MRI in the staging of pelvic lymph nodes in patients with prostate cancer: a meta-analysis." Clin Radiol **63**(4): 387-395.

Hricak, H., G. C. Dooms, et al. (1987). "Prostatic carcinoma: staging by clinical assessment, CT, and MR imaging." Radiology **162**(2): 331-336.

Hudson, H. M. and R. S. Larkin (1994). "Accelerated image reconstruction using ordered subsets of projection data." IEEE Trans Med Imaging **13**(4): 601-609.

Huebner, R. H., K. C. Park, et al. (2000). "A meta-analysis of the literature for whole-body FDG PET detection of recurrent colorectal cancer." J Nucl Med **41**(7): 1177-1189.

Husarik, D. B., R. Miralbell, et al. (2008). "Evaluation of [(18)F]-choline PET/CT for staging and restaging of prostate cancer." Eur J Nucl Med Mol Imaging **35**(2): 253-263.

Hutton, B. F. (2011). "Recent advances in iterative reconstruction for clinical SPECT/PET and CT." Acta Oncol **50**(6): 851-858.

Iorio, E., A. Ricci, et al. "Activation of phosphatidylcholine cycle enzymes in human epithelial ovarian cancer cells." Cancer Res **70**(5): 2126-2135.

Isasi, C. R., P. Lu, et al. (2005). "A metaanalysis of 18F-2-deoxy-2-fluoro-D-glucose positron emission tomography in the staging and restaging of patients with lymphoma." Cancer **104**(5): 1066-1074.

Isasi, C. R., R. M. Moadel, et al. (2005). "A meta-analysis of FDG-PET for the evaluation of breast cancer recurrence and metastases." Breast Cancer Res Treat **90**(2): 105-112.

Isles, M. G., C. McConkey, et al. (2008). "A systematic review and meta-analysis of the role of positron emission tomography in the follow up of head and neck squamous cell carcinoma following radiotherapy or chemoradiotherapy." Clin Otolaryngol **33**(3): 210-222.

Jadvar, H. (2012). "Can Choline PET Tackle the Challenge of Imaging Prostate Cancer?" Theranostics **2**(3): 331-332.

Jadvar, H. and P. S. Conti (2004). "The reproductive tract." Semin Nucl Med **34**(4): 262-273.

Jager, G. J., J. O. Barentsz, et al. (1996). "Pelvic adenopathy in prostatic and urinary bladder carcinoma: MR imaging with a three-dimensional TI-weighted magnetization-prepared-rapid gradient-echo sequence." AJR Am J Roentgenol **167**(6): 1503-1507.

Jager, P. L., T. H. Que, et al. (2001). "Carbon-11 choline or FDG-PET for staging of oesophageal cancer?" Eur J Nucl Med **28**(12): 1845-1849.

Jia, Y., B. Dong, et al. (2012). "Apoptosis index correlates with chemotherapy efficacy and predicts the survival of patients with gastric cancer." Tumour Biol **33**(4): 1151-1158.

Jiang, B. H. and L. Z. Liu (2009). "PI3K/PTEN signaling in angiogenesis and tumorigenesis." Adv Cancer Res **102**: 19-65.

Jimenez, B., L. del Peso, et al. (1995). "Generation of phosphorylcholine as an essential event in the activation of Raf-1 and MAP-kinases in growth factors-induced mitogenic stimulation." J Cell Biochem **57**(1): 141-149.

Johnson, L. (1986). "Spermatogenesis and aging in the human." J Androl **7**(6): 331-354.

Jones, S., X. Zhang, et al. (2008). "Core signaling pathways in human pancreatic cancers revealed by global genomic analyses." Science **321**(5897): 1801-1806.

Jones, S. C., A. Alavi, et al. (1982). "The radiation dosimetry of 2 [F-18]fluoro-2-deoxy-D-glucose in man." J Nucl Med **23**(7): 613-617.

Judenhofer, M. S., H. F. Wehrl, et al. (2008). "Simultaneous PET-MRI: a new approach for functional and morphological imaging." Nat Med **14**(4): 459-465.

Juweid, M. E. and B. D. Cheson (2006). "Positron-emission tomography and assessment of cancer therapy." N Engl J Med **354**(5): 496-507.

Kahraman, D., A. Holstein, et al. (2012). "Tumor lesion glycolysis and tumor lesion proliferation for response prediction and prognostic differentiation in patients with advanced non-small cell lung cancer treated with erlotinib." Clin Nucl Med **37**(11): 1058-1064.

Kameyama, R., Y. Yamamoto, et al. (2011). "Correlation of 18F-FLT uptake with equilibrative nucleoside transporter-1 and thymidine kinase-1 expressions in gastrointestinal cancer." Nucl Med Commun **32**(6): 460-465.

Kameyama, R., Y. Yamamoto, et al. (2009). "Detection of gastric cancer using 18F-FLT PET: comparison with 18F-FDG PET." Eur J Nucl Med Mol Imaging **36**(3): 382-388.

Karp, J. S., S. Surti, et al. (2008). "Benefit of time-of-flight in PET: experimental and clinical results." J Nucl Med **49**(3): 462-470.

Katz-Brull, R., D. Seger, et al. (2002). "Metabolic markers of breast cancer: enhanced choline metabolism and reduced choline-ether-phospholipid synthesis." Cancer Res **62**(7): 1966-1970.

Kaufmann, S. H. and W. C. Earnshaw (2000). "Induction of apoptosis by cancer chemotherapy." Exp Cell Res **256**(1): 42-49.

Kawai, T., S. Hiroi, et al. (2007). "Telomere length and telomerase expression in atypical adenomatous hyperplasia and small bronchioloalveolar carcinoma of the lung." Am J Clin Pathol **127**(2): 254-262.

Kelloff, G. J., J. M. Hoffman, et al. (2005). "Progress and promise of FDG-PET imaging for cancer patient management and oncologic drug development." Clin Cancer Res **11**(8): 2785-2808.

Kemerink, G. J., H. H. Boersma, et al. (2001). "Biodistribution and dosimetry of 99mTc-BTAP-annexin-V in humans." Eur J Nucl Med **28**(9): 1373-1378.

Kemerink, G. J., I. H. Liem, et al. (2001). "Patient dosimetry of intravenously administered 99mTc-annexin V." J Nucl Med **42**(2): 382-387.

Kemerink, G. J., X. Liu, et al. (2003). "Safety, biodistribution, and dosimetry of 99mTc-HYNIC-annexin V, a novel human recombinant annexin V for human application." J Nucl Med **44**(6): 947-952.

Kenny, L., R. C. Coombes, et al. (2007). "Imaging early changes in proliferation at 1 week post chemotherapy: a pilot study in breast cancer patients with 3'-deoxy-3'-[18F]fluorothymidine positron emission tomography." Eur J Nucl Med Mol Imaging **34**(9): 1339-1347.

Kenny, L. M., K. B. Contractor, et al. (2010). "Reproducibility of [11C]choline-positron emission tomography and effect of trastuzumab." Clin Cancer Res **16**(16): 4236-4245.

Kenny, L. M., D. M. Vigushin, et al. (2005). "Quantification of cellular proliferation in tumor and normal tissues of patients with breast cancer by [18F]fluorothymidine-positron emission tomography imaging: evaluation of analytical methods." Cancer Res **65**(21): 10104-10112.

Khan, N., N. Oriuchi, et al. (2003). "A comparative study of 11C-choline PET and [18F]fluorodeoxyglucose PET in the evaluation of lung cancer." Nucl Med Commun **24**(4): 359-366.

Kishino, T., H. Hoshikawa, et al. (2012). "Usefulness of 3'-deoxy-3'-18F-fluorothymidine PET for predicting early response to chemoradiotherapy in head and neck cancer." J Nucl Med **53**(10): 1521-1527.

Klein, W. M., R. H. Hruban, et al. (2002). "Direct correlation between proliferative activity and dysplasia in pancreatic intraepithelial neoplasia (PanIN): additional evidence for a recently proposed model of progression." Mod Pathol **15**(4): 441-447.

Kobe, C., M. Scheffler, et al. (2012). "Predictive value of early and late residual 18F-fluorodeoxyglucose and 18F-fluorothymidine uptake using different SUV measurements in patients with non-small-cell lung cancer treated with erlotinib." Eur J Nucl Med Mol Imaging **39**(7): 1117-1127.

Kobori, O., Y. Kirihara, et al. (1999). "Positron emission tomography of esophageal carcinoma using (11)C-choline and (18)F-fluorodeoxyglucose: a novel method of preoperative lymph node staging." Cancer **86**(9): 1638-1648.

Kotzerke, J., J. Prang, et al. (2000). "Experience with carbon-11 choline positron emission tomography in prostate carcinoma." Eur J Nucl Med **27**(9): 1415-1419.

Krause, B. J., M. Souvatzoglou, et al. (2011). "Imaging of prostate cancer with PET/CT and radioactively labeled choline derivates." Urol Oncol.

Kroemer, G., L. Galluzzi, et al. (2009). "Classification of cell death: recommendations of the Nomenclature Committee on Cell Death 2009." Cell Death Differ **16**(1): 3-11.

Kuang, Y., N. Salem, et al. (2010). "Transport and metabolism of radiolabeled choline in hepatocellular carcinoma." Mol Pharm **7**(6): 2077-2092.

Kumar, S., M. Shelley, et al. (2006). "Neo-adjuvant and adjuvant hormone therapy for localised and locally advanced prostate cancer." Cochrane Database Syst Rev(4): CD006019.

Kuwatani, M., H. Kawakami, et al. (2009). "Modalities for evaluating chemotherapeutic efficacy and survival time in patients with advanced pancreatic cancer: comparison between FDG-PET, CT, and serum tumor markers." Intern Med **48**(11): 867-875.

Kwee, S. A., M. N. Coel, et al. (2004). "Combined use of F-18 fluorocholine positron emission tomography and magnetic resonance spectroscopy for brain tumor evaluation." J Neuroimaging **14**(3): 285-289.

Kwee, S. A., M. N. Coel, et al. (2005). "Prostate cancer localization with 18fluorine fluorocholine positron emission tomography." J Urol **173**(1): 252-255.

Kwee, S. A., J. P. Ko, et al. (2007). "Solitary brain lesions enhancing at MR imaging: evaluation with fluorine 18 fluorocholine PET." Radiology **244**(2): 557-565.

Kwee, S. A., H. Wei, et al. (2006). "Localization of primary prostate cancer with dual-phase 18F-fluorocholine PET." J Nucl Med **47**(2): 262-269.

Lam, W. W., D. C. Ng, et al. (2010). "Promising role of [18F] fluorocholine PET/CT vs [18F] fluorodeoxyglucose PET/CT in primary brain tumors-Early experience." Clin Neurol Neurosurg.

Langsteger, W., M. Heinisch, et al. (2006). "The role of fluorodeoxyglucose, 18F-dihydroxyphenylalanine, 18F-choline, and 18F-fluoride in bone imaging with emphasis on prostate and breast." Semin Nucl Med **36**(1): 73-92.

Laudanski, P., M. Koda, et al. (2004). "Expression of glucose transporter GLUT-1 and estrogen receptors ER-alpha and ER-beta in human breast cancer." Neoplasma **51**(3): 164-168.

Lehr, H. A., C. Rochat, et al. (2013). "Mitotic figure counts are significantly overestimated in resection specimens of invasive breast carcinomas." Mod Pathol **26**(3): 336-342.

Leibel, S. A., Z. Fuks, et al. (1994). "The effects of local and regional treatment on the metastatic outcome in prostatic carcinoma with pelvic lymph node involvement." Int J Radiat Oncol Biol Phys **28**(1): 7-16.

Leyton, J., J. P. Alao, et al. (2006). "In vivo biological activity of the histone deacetylase inhibitor LAQ824 is detectable with 3'-deoxy-3'-[18F]fluorothymidine positron emission tomography." Cancer Res **66**(15): 7621-7629.

Leyton, J., J. R. Latigo, et al. (2005). "Early detection of tumor response to chemotherapy by 3'-deoxy-3'-[18F]fluorothymidine positron emission tomography: the effect of cisplatin on a fibrosarcoma tumor model in vivo." Cancer Res **65**(10): 4202-4210.

Leyton, J., G. Smith, et al. (2009). "[18F]fluoromethyl-[1,2-2H4]-choline: a novel radiotracer for imaging choline metabolism in tumors by positron emission tomography." Cancer Res **69**(19): 7721-7728.

Li, M., Z. Peng, et al. (2013). "Value of 11C-choline PET/CT for lung cancer diagnosis and the relation between choline metabolism and proliferation of cancer cells." Oncol Rep **29**(1): 205-211.

Lim, D. S., S. T. Kim, et al. (2000). "ATM phosphorylates p95/nbs1 in an S-phase checkpoint pathway." Nature **404**(6778): 613-617.

Linecker, A., C. Kermer, et al. (2008). "Uptake of (18)F-FLT and (18)F-FDG in primary head and neck cancer correlates with survival." Nuklearmedizin **47**(2): 80-85; quiz N12.

Loo, D. T. (2011). "In situ detection of apoptosis by the TUNEL assay: an overview of techniques." Methods Mol Biol **682**: 3-13.

Lopes, J. M., E. Hannisdal, et al. (1998). "Synovial sarcoma. Evaluation of prognosis with emphasis on the study of DNA ploidy and proliferation (PCNA and Ki-67) markers." Anal Cell Pathol **16**(1): 45-62.

Mac Manus, M. P. and R. J. Hicks (2003). "PET scanning in lung cancer: current status and future directions." Semin Surg Oncol **21**(3): 149-155.

Maisey, N. R., A. Webb, et al. (2000). "FDG-PET in the prediction of survival of patients with cancer of the pancreas: a pilot study." Br J Cancer **83**(3): 287-293.

Malumbres, M. and M. Barbacid (2005). "Mammalian cyclin-dependent kinases." Trends Biochem Sci **30**(11): 630-641.

Mamede, M., T. Higashi, et al. (2005). "[18F]FDG uptake and PCNA, Glut-1, and Hexokinase-II expressions in cancers and inflammatory lesions of the lung." Neoplasia **7**(4): 369-379.

Mankoff, D. A., A. F. Shields, et al. (1996). "A graphical analysis method to estimate blood-to-tissue transfer constants for tracers with labeled metabolites." J Nucl Med **37**(12): 2049-2057.

Martincic, D. S., I. Virant Klun, et al. (2001). "Germ cell apoptosis in the human testis." Pflugers Arch **442**(6 Suppl 1): R159-160.

Martorana, G., R. Schiavina, et al. (2006). "11C-choline positron emission tomography/computerized tomography for tumor localization of primary prostate cancer in comparison with 12-core biopsy." J Urol **176**(3): 954-960; discussion 960.

McCarthy, M., T. Siew, et al. (2010). "(18)F-Fluoromethylcholine (FCH) PET imaging in patients with castration-resistant prostate cancer: prospective comparison with standard imaging." Eur J Nucl Med Mol Imaging.

Meikle, S. R., J. C. Matthews, et al. (1998). "Pharmacokinetic assessment of novel anti-cancer drugs using spectral analysis and positron emission tomography: a feasibility study." Cancer Chemother Pharmacol **42**(3): 183-193.

Menda, Y. and M. M. Graham (2005). "Update on 18F-fluorodeoxyglucose/positron emission tomography and positron emission tomography/computed tomography imaging of squamous head and neck cancers." Semin Nucl Med **35**(4): 214-219.

Merrimen, J. L., A. J. Evans, et al. (2013). "Preneoplasia in the prostate gland with emphasis on high grade prostatic intraepithelial neoplasia." Pathology **45**(3): 251-263.

Mertens, K., H. Ham, et al. (2012). "Distribution patterns of 18F-labelled fluoromethylcholine in normal structures and tumors of the head: a PET/MRI evaluation." Clin Nucl Med **37**(8): e196-203.

Michel, V., Z. Yuan, et al. (2006). "Choline transport for phospholipid synthesis." Exp Biol Med (Maywood) **231**(5): 490-504.

Minn, H., K. R. Zasadny, et al. (1995). "Lung cancer: reproducibility of quantitative measurements for evaluating 2-[F-18]-fluoro-2-deoxy-D-glucose uptake at PET." Radiology **196**(1): 167-173.

Miyake, K., A. Shinomiya, et al. (2012). "Usefulness of FDG, MET and FLT-PET studies for the management of human gliomas." J Biomed Biotechnol **2012**: 205818.

Montironi, R., L. Diamanti, et al. (1992). "Computer-aided S-phase fraction determination in DNA static cytometry in breast cancer. A preliminary methodologic study on cytologic material." Anal Quant Cytol Histol **14**(5): 379-385.

Munch-Petersen, B., L. Cloos, et al. (1991). "Diverging substrate specificity of pure human thymidine kinases 1 and 2 against antiviral dideoxynucleosides." J Biol Chem **266**(14): 9032-9038.

Ng, K. K., R. Donat, et al. (2004). "Sperm output of older men." Hum Reprod **19**(8): 1811-1815.

Nguyen, Q. D., A. Challapalli, et al. (2012). "Imaging apoptosis with positron emission tomography: 'bench to bedside' development of the caspase-3/7 specific radiotracer [(18)F]ICMT-11." Eur J Cancer **48**(4): 432-440.

Nguyen, Q. D., G. Smith, et al. (2009). "Positron emission tomography imaging of drug-induced tumor apoptosis with a caspase-3/7 specific [18F]-labeled isatin sulfonamide." Proc Natl Acad Sci U S A **106**(38): 16375-16380.

Nguyen, X. C., W. W. Lee, et al. (2007). "FDG uptake, glucose transporter type 1, and Ki-67 expressions in non-small-cell lung cancer: correlations and prognostic values." Eur J Radiol **62**(2): 214-219.

Nicholson, D. W. and N. A. Thornberry (1997). "Caspases: killer proteases." Trends Biochem Sci **22**(8): 299-306.

O'Donoghue, N., T. Sweeney, et al. (2009). "Control of choline oxidation in rat kidney mitochondria." Biochim Biophys Acta **1787**(9): 1135-1139.

O'Leary, T. J. and M. W. Steffes (1996). "Can you count on the mitotic index?" Hum Pathol **27**(2): 147-151.

Ohba, S., H. Fujii, et al. "Overexpression of GLUT-1 in the invasion front is associated with depth of oral squamous cell carcinoma and prognosis." J Oral Pathol Med **39**(1): 74-78.

Ohtsuki, K., K. Akashi, et al. (1999). "Technetium-99m HYNIC-annexin V: a potential radiopharmaceutical for the in-vivo detection of apoptosis." Eur J Nucl Med **26**(10): 1251-1258.

Okada, H. and T. W. Mak (2004). "Pathways of apoptotic and non-apoptotic death in tumour cells." Nat Rev Cancer **4**(8): 592-603.

Ott, K., K. Herrmann, et al. (2011). "Molecular imaging of proliferation and glucose utilization: utility for monitoring response and prognosis after neoadjuvant therapy in locally advanced gastric cancer." Ann Surg Oncol **18**(12): 3316-3323.

Pakzad, F., A. M. Groves, et al. (2006). "The role of positron emission tomography in the management of pancreatic cancer." Semin Nucl Med **36**(3): 248-256.

Paproski, R. J., J. D. Young, et al. (2010). "Predicting gemcitabine transport and toxicity in human pancreatic cancer cell lines with the positron emission tomography tracer 3'-deoxy-3'-fluorothymidine." Biochem Pharmacol **79**(4): 587-595.

Parkin, J., F. X. Keeley, Jr., et al. (2002). "Laparoscopic lymph node sampling in locally advanced prostate cancer." BJU Int **89**(1): 14-17; discussion 17-18.

Pascali, C., Bogni, A., Itawa, R., Cambiè, M., Bombardieri, E. (2000). "[11C]Methylation on a C18 Sep-Pak cartridge: a convenient way to produce [N-methyl-11C]choline. ." Journal of Labelled Compounds and Radiopharmaceuticals **43**(2): 195-203.

Patlak, C. S., R. G. Blasberg, et al. (1983). "Graphical evaluation of blood-to-brain transfer constants from multiple-time uptake data." J Cereb Blood Flow Metab **3**(1): 1-7.

Peeters, S. T., W. D. Heemsbergen, et al. (2006). "Dose-response in radiotherapy for localized prostate cancer: results of the Dutch multicenter randomized phase III trial comparing 68 Gy of radiotherapy with 78 Gy." J Clin Oncol **24**(13): 1990-1996.

Pelosi, E., V. Arena, et al. (2008). "Role of whole-body 18F-choline PET/CT in disease detection in patients with biochemical relapse after radical treatment for prostate cancer." Radiol Med **113**(6): 895-904.

Peng, B. H. and C. S. Levin (2010). "Recent development in PET instrumentation." Curr Pharm Biotechnol **11**(6): 555-571.

Peng, Z., Q. Liu, et al. (2012). "Comparison of (11)C-choline PET/CT and enhanced CT in the evaluation of patients with pulmonary abnormalities and locoregional lymph node involvement in lung cancer." Clin Lung Cancer **13**(4): 312-320.

Perumal, M., R. G. Pillai, et al. (2006). "Redistribution of nucleoside transporters to the cell membrane provides a novel approach for imaging thymidylate synthase inhibition by positron emission tomography." Cancer Res **66**(17): 8558-8564.

Perumal, M., E. A. Stronach, et al. (2012). "Evaluation of 2-deoxy-2-[18F]fluoro-D-glucose- and 3'-deoxy-3'-[18F]fluorothymidine-positron emission tomography as biomarkers of therapy response in platinum-resistant ovarian cancer." Mol Imaging Biol **14**(6): 753-761.

Picchio, M. and P. Castellucci (2012). "Clinical Indications of C-Choline PET/CT in Prostate Cancer Patients with Biochemical Relapse." Theranostics **2**(3): 313-317.

Piert, M., H. Park, et al. (2009). "Detection of aggressive primary prostate cancer with 11C-choline PET/CT using multimodality fusion techniques." J Nucl Med **50**(10): 1585-1593.

Pieterman, R. M., T. H. Que, et al. (2002). "Comparison of (11)C-choline and (18)F-FDG PET in primary diagnosis and staging of patients with thoracic cancer." J Nucl Med **43**(2): 167-172.

Pieterman, R. M., J. W. van Putten, et al. (2000). "Preoperative staging of non-small-cell lung cancer with positron-emission tomography." N Engl J Med **343**(4): 254-261.

Plotnik, D. A., L. E. Emerick, et al. (2010). "Different modes of transport for 3H-thymidine, 3H-FLT, and 3H-FMAU in proliferating and nonproliferating human tumor cells." J Nucl Med **51**(9): 1464-1471.

Porter, A. G. and R. U. Janicke (1999). "Emerging roles of caspase-3 in apoptosis." Cell Death Differ **6**(2): 99-104.

Poulsen, M. H., K. Bouchelouche, et al. (2010). "[18F]-fluorocholine positron-emission/computed tomography for lymph node staging of patients with prostate cancer: preliminary results of a prospective study." BJU Int **106**(5): 639-643; discussion 644.

Poulsen, M. H., K. Bouchelouche, et al. (2012). "[18F]fluoromethylcholine (FCH) positron emission tomography/computed tomography (PET/CT) for lymph node staging of prostate cancer: a prospective study of 210 patients." BJU Int **110**(11): 1666-1671.

Pummer, S., W. H. Dantzler, et al. (2000). "Reabsorption of betaine in Henle's loops of rat kidney in vivo." Am J Physiol Renal Physiol **278**(3): F434-439.

Quon, A., S. T. Chang, et al. (2008). "Initial evaluation of 18F-fluorothymidine (FLT) PET/CT scanning for primary pancreatic cancer." Eur J Nucl Med Mol Imaging **35**(3): 527-531.

Rahmim, A., Rousset, O., Zaidi, H. (2007). "Strategies for motion tracking and correction in PET." PET Clin **2**(2): 251-266.

Ramirez de Molina, A., M. Banez-Coronel, et al. (2004). "Choline kinase activation is a critical requirement for the proliferation of primary human mammary epithelial cells and breast tumor progression." Cancer Res **64**(18): 6732-6739.

Ramirez de Molina, A., D. Gallego-Ortega, et al. (2008). "Choline kinase as a link connecting phospholipid metabolism and cell cycle regulation: implications in cancer therapy." Int J Biochem Cell Biol **40**(9): 1753-1763.

Ramirez de Molina, A., V. Penalva, et al. (2002). "Regulation of choline kinase activity by Ras proteins involves Ral-GDS and PI3K." Oncogene **21**(6): 937-946.

Ramirez de Molina, A., A. Rodriguez-Gonzalez, et al. (2002). "Overexpression of choline kinase is a frequent feature in human tumor-derived cell lines and in lung, prostate, and colorectal human cancers." Biochem Biophys Res Commun **296**(3): 580-583.

Ramirez de Molina, A., J. Sarmentero-Estrada, et al. (2007). "Expression of choline kinase alpha to predict outcome in patients with early-stage non-small-cell lung cancer: a retrospective study." Lancet Oncol **8**(10): 889-897.

Reed, J. C. (2002). "Apoptosis-based therapies." Nat Rev Drug Discov **1**(2): 111-121.

Reske, S. N., N. M. Blumstein, et al. (2006). "Imaging prostate cancer with 11C-choline PET/CT." J Nucl Med **47**(8): 1249-1254.

Reske, S. N. and S. Deisenhofer (2006). "Is 3'-deoxy-3'-(18)F-fluorothymidine a better marker for tumour response than (18)F-fluorodeoxyglucose?" Eur J Nucl Med Mol Imaging **33 Suppl 1**: 38-43.

Revel, M. P., A. Bissery, et al. (2004). "Are two-dimensional CT measurements of small noncalcified pulmonary nodules reliable?" Radiology **231**(2): 453-458.

Rhodes, C. G., P. Wollmer, et al. (1981). "Quantitative measurement of regional extravascular lung density using positron emission and transmission tomography." J Comput Assist Tomogr **5**(6): 783-791.

Roach, M., 3rd (1993). "Re: The use of prostate specific antigen, clinical stage and Gleason score to predict pathological stage in men with localized prostate cancer." J Urol **150**(6): 1923-1924.

Robnett, T. J., R. Whittington, et al. (2002). "Long-term use of combined radiation therapy and hormonal therapy in the management of stage D1 prostate cancer." Int J Radiat Oncol Biol Phys **53**(5): 1146-1151.

Rodemann, H. P. and M. A. Blaese (2007). "Responses of normal cells to ionizing radiation." Semin Radiat Oncol **17**(2): 81-88.

Roivainen, A., S. Forsback, et al. (2000). "Blood metabolism of [methyl-11C]choline; implications for in vivo imaging with positron emission tomography." Eur J Nucl Med **27**(1): 25-32.

Roivainen, A., R. Parkkola, et al. (2003). "Use of positron emission tomography with methyl-11C-choline and 2-18F-fluoro-2-deoxy-D-glucose in comparison with magnetic resonance imaging for the assessment of inflammatory proliferation of synovium." Arthritis Rheum **48**(11): 3077-3084.

Rorvik, J., O. J. Halvorsen, et al. (1998). "Lymphangiography combined with biopsy and computer tomography to detect lymph node metastases in localized prostate cancer." Scand J Urol Nephrol **32**(2): 116-119.

Rose, D. M., D. Delbeke, et al. (1999). "18Fluorodeoxyglucose-positron emission tomography in the management of patients with suspected pancreatic cancer." Ann Surg **229**(5): 729-737; discussion 737-728.

Roselli, F., N. M. Pisciotta, et al. (2010). "Brain F-18 Fluorocholine PET/CT for the assessment of optic pathway glioma in neurofibromatosis-1." Clin Nucl Med **35**(10): 838-839.

Roy, C., G. Bierry, et al. (2010). "Value of diffusion-weighted imaging to detect small malignant pelvic lymph nodes at 3 T." Eur Radiol **20**(8): 1803-1811.

Schafer, K. A. (1998). "The cell cycle: a review." Vet Pathol **35**(6): 461-478.

Scher, B., M. Seitz, et al. (2007). "Value of 11C-choline PET and PET/CT in patients with suspected prostate cancer." Eur J Nucl Med Mol Imaging **34**(1): 45-53.

Schiavina, R., V. Scattoni, et al. (2008). "11C-choline positron emission tomography/computerized tomography for preoperative lymph-node staging in intermediate-risk and high-risk prostate cancer: comparison with clinical staging nomograms." Eur Urol **54**(2): 392-401.

Schillaci, O., F. Calabria, et al. (2010). "18F-choline PET/CT physiological distribution and pitfalls in image interpretation: experience in 80 patients with prostate cancer." Nucl Med Commun **31**(1): 39-45.

Schmelz, H. U., J. Meiswinkel, et al. (2005). "Apoptosis in non-tumorous adult human testis tissue. Comparison of so-called 'normal' testis tissues." Urol Int **74**(4): 349-354.

Schmid, D. T., H. John, et al. (2005). "Fluorocholine PET/CT in patients with prostate cancer: initial experience." Radiology **235**(2): 623-628.

Schmittgen, T. D. and K. J. Livak (2008). "Analyzing real-time PCR data by the comparative C(T) method." Nat Protoc **3**(6): 1101-1108.

Schoder, H. and S. M. Larson (2004). "Positron emission tomography for prostate, bladder, and renal cancer." Semin Nucl Med **34**(4): 274-292.

Schwarzenberg, J., J. Czernin, et al. (2012). "3'-deoxy-3'-18F-fluorothymidine PET and MRI for early survival predictions in patients with recurrent malignant glioma treated with bevacizumab." J Nucl Med **53**(1): 29-36.

Sciarra, A., V. Panebianco, et al. (2010). "Magnetic resonance spectroscopic imaging (1H-MRSI) and dynamic contrast-enhanced magnetic resonance (DCE-MRI): pattern changes from inflammation to prostate cancer." Cancer Invest **28**(4): 424-432.

Semelka, R. C., S. M. Hussain, et al. (2000). "Perilesional enhancement of hepatic metastases: correlation between MR imaging and histopathologic findings-initial observations." Radiology **215**(1): 89-94.

Sherr, C. J. and J. M. Roberts (2004). "Living with or without cyclins and cyclin-dependent kinases." Genes Dev **18**(22): 2699-2711.

Shie, P., R. Cardarelli, et al. (2008). "Meta-analysis: comparison of F-18 Fluorodeoxyglucose-positron emission tomography and bone scintigraphy in the detection of bone metastases in patients with breast cancer." Clin Nucl Med **33**(2): 97-101.

Shields, A. F. (2003). "PET imaging with 18F-FLT and thymidine analogs: promise and pitfalls." J Nucl Med **44**(9): 1432-1434.

Shields, A. F., J. R. Grierson, et al. (2002). "Kinetics of 3'-deoxy-3'-[F-18]fluorothymidine uptake and retention in dogs." Mol Imaging Biol **4**(1): 83-89.

Shields, A. F., S. M. Larson, et al. (1984). "Short-term thymidine uptake in normal and neoplastic tissues: studies for PET." J Nucl Med **25**(7): 759-764.

Shields, A. F., J. M. Lawhorn-Crews, et al. (2008). "Analysis and reproducibility of 3'-Deoxy-3'-[18F]fluorothymidine positron emission tomography imaging in patients with non-small cell lung cancer." Clin Cancer Res **14**(14): 4463-4468.

Shields, A. F., D. Mankoff, et al. (1996). "Analysis of 2-carbon-11-thymidine blood metabolites in PET imaging." J Nucl Med **37**(2): 290-296.

Siegel, R., D. Naishadham, et al. (2012). "Cancer statistics, 2012." CA Cancer J Clin **62**(1): 10-29.

Slaets, D., S. De Bruyne, et al. (2010). "Reduced dimethylaminoethanol in [(18)F]fluoromethylcholine: an important step towards enhanced tumour visualization." Eur J Nucl Med Mol Imaging **37**(11): 2136-2145.

Smith, G., Y. Zhao, et al. (2011). "Radiosynthesis and pre-clinical evaluation of [(18)F]fluoro-[1,2-(2)H(4)]choline." Nucl Med Biol **38**(1): 39-51.

Smyczek-Gargya, B., N. Fersis, et al. (2004). "PET with [18F]fluorothymidine for imaging of primary breast cancer: a pilot study." Eur J Nucl Med Mol Imaging **31**(5): 720-724.

Sohn, H. J., Y. J. Yang, et al. (2008). "[18F]Fluorothymidine positron emission tomography before and 7 days after gefitinib treatment predicts response in patients with advanced adenocarcinoma of the lung." Clin Cancer Res **14**(22): 7423-7429.

Sokoloff, L., M. Reivich, et al. (1977). "The [14C]deoxyglucose method for the measurement of local cerebral glucose utilization: theory, procedure, and normal values in the conscious and anesthetized albino rat." J Neurochem **28**(5): 897-916.

Soret, M., S. L. Bacharach, et al. (2007). "Partial-volume effect in PET tumor imaging." J Nucl Med **48**(6): 932-945.

Souvatzoglou, M., G. Weirich, et al. (2011). "The sensitivity of [11C]choline PET/CT to localize prostate cancer depends on the tumor configuration." Clin Cancer Res **17**(11): 3751-3759.

Spence, A. M., M. Muzi, et al. (2008). "NCI-sponsored trial for the evaluation of safety and preliminary efficacy of FLT as a marker of proliferation in patients with recurrent gliomas: safety studies." Mol Imaging Biol **10**(5): 271-280.

Stabin, M. G., R. B. Sparks, et al. (2005). "OLINDA/EXM: the second-generation personal computer software for internal dose assessment in nuclear medicine." J Nucl Med **46**(6): 1023-1027.

Stone, N. N. and R. G. Stock (1999). "Laparoscopic pelvic lymph node dissection in the staging of prostate cancer." Mt Sinai J Med **66**(1): 26-30.

Storey, S. (2008). "Targeting apoptosis: selected anticancer strategies." Nat Rev Drug Discov **7**(12): 971-972.

Sugiyama, M., H. Sakahara, et al. (2004). "Evaluation of 3'-deoxy-3'-18F-fluorothymidine for monitoring tumor response to radiotherapy and photodynamic therapy in mice." J Nucl Med **45**(10): 1754-1758.

Sultana, A., C. T. Smith, et al. (2007). "Meta-analyses of chemotherapy for locally advanced and metastatic pancreatic cancer." J Clin Oncol **25**(18): 2607-2615.

Sutinen, E., M. Nurmi, et al. (2004). "Kinetics of [(11)C]choline uptake in prostate cancer: a PET study." Eur J Nucl Med Mol Imaging **31**(3): 317-324.

Talbot, J. N., L. Fartoux, et al. (2010). "Detection of hepatocellular carcinoma with PET/CT: a prospective comparison of 18F-fluorocholine and 18F-FDG in patients with cirrhosis or chronic liver disease." J Nucl Med **51**(11): 1699-1706.

Talbot, J. N., F. Gutman, et al. (2006). "PET/CT in patients with hepatocellular carcinoma using [(18)F]fluorocholine: preliminary comparison with [(18)F]FDG PET/CT." Eur J Nucl Med Mol Imaging **33**(11): 1285-1289.

Tamura, K., K. Yoshikawa, et al. (2002). "[Diagnosis of esophageal cancer using positron emission tomography]." Nippon Geka Gakkai Zasshi **103**(4): 325-330.

Taylor, R. C., S. P. Cullen, et al. (2008). "Apoptosis: controlled demolition at the cellular level." Nat Rev Mol Cell Biol **9**(3): 231-241.

Tehrani, O. S. and A. F. Shields (2013). "PET Imaging of Proliferation with Pyrimidines." J Nucl Med **54**(6): 903-912.

Tekola, P., J. P. Baak, et al. (1996). "Three-dimensional confocal laser scanning DNA ploidy cytometry in thick histological sections." J Pathol **180**(2): 214-222.

Therasse, P., S. G. Arbuck, et al. (2000). "New guidelines to evaluate the response to treatment in solid tumors. European Organization for Research and Treatment of Cancer, National Cancer Institute of the United States, National Cancer Institute of Canada." J Natl Cancer Inst **92**(3): 205-216.

Thomas, S. R., M. G. Stabin, et al. (1999). "MIRD Pamphlet No. 14 revised: A dynamic urinary bladder model for radiation dose calculations. Task Group of the MIRD Committee, Society of Nuclear Medicine." J Nucl Med **40**(4): 102S-123S.

Tian, M., H. Zhang, et al. (2004). "Oncological diagnosis using (11)C-choline-positron emission tomography in comparison with 2-deoxy-2-[(18)F] fluoro-D-glucose-positron emission tomography." Mol Imaging Biol **6**(3): 172-179.

Tolvanen, T., T. Yli-Kerttula, et al. (2010). "Biodistribution and radiation dosimetry of [(11)C]choline: a comparison between rat and human data." Eur J Nucl Med Mol Imaging **37**(5): 874-883.

Tomasi, G. and E. O. Aboagye (2013). "Introduction to the analysis of PET data in oncology." J Pharmacokinet Pharmacodyn **40**(4): 419-436.

Tomasi, G., S. Kimberley, et al. (2012). "Double-input compartmental modeling and spectral analysis for the quantification of positron emission tomography data in oncology." Phys Med Biol **57**(7): 1889-1906.

Tomasi, G., F. Turkheimer, et al. (2012). "Importance of quantification for the analysis of PET data in oncology: review of current methods and trends for the future." Mol Imaging Biol **14**(2): 131-146.

Tong, W. G., R. Chen, et al. (2010). "Phase I and pharmacologic study of SNS-032, a potent and selective Cdk2, 7, and 9 inhibitor, in patients with advanced chronic lymphocytic leukemia and multiple myeloma." J Clin Oncol **28**(18): 3015-3022.

Torigian, D. A., H. Zaidi, et al. (2013). "PET/MR imaging: technical aspects and potential clinical applications." Radiology **267**(1): 26-44.

Toyohara, J., A. Waki, et al. (2002). "Basis of FLT as a cell proliferation marker: comparative uptake studies with [3H]thymidine and [3H]arabinothymidine, and cell-analysis in 22 asynchronously growing tumor cell lines." Nucl Med Biol **29**(3): 281-287.

Treglia, G., E. Giovannini, et al. (2012). "The role of positron emission tomography using carbon-11 and fluorine-18 choline in tumors other than prostate cancer: a systematic review." Ann Nucl Med **26**(6): 451-461.

Troost, E. G., J. Bussink, et al. (2010). "18F-FLT PET/CT for early response monitoring and dose escalation in oropharyngeal tumors." J Nucl Med **51**(6): 866-874.

Ueland, P. M. (2011). "Choline and betaine in health and disease." J Inherit Metab Dis.

Umbehr, M. H., M. Muntener, et al. (2013). "The Role of 11C-Choline and 18F-Fluorocholine Positron Emission Tomography (PET) and PET/CT in Prostate Cancer: A Systematic Review and Meta-analysis." Eur Urol **64**(1): 106-117.

Valentini, A. L., B. Gui, et al. (2012). "Locally advanced prostate cancer: three-dimensional magnetic resonance spectroscopy to monitor prostate response to therapy." Int J Radiat Oncol Biol Phys **84**(3): 719-724.

Van den Bergh, L., M. Koole, et al. (2012). "Is there an additional value of (1)(1)C-choline PET-CT to T2-weighted MRI images in the localization of intraprostatic tumor nodules?" Int J Radiat Oncol Biol Phys **83**(5): 1486-1492.

van den Esschert, J. W., M. Bieze, et al. (2010). "Differentiation of hepatocellular adenoma and focal nodular hyperplasia using (18)F-fluorocholine PET/CT." Eur J Nucl Med Mol Imaging.

van Rossum, G. D. and C. A. Boyd (1998). "Sodium-dependent and -independent choline uptake by type II epithelial cells from rat lung." J Membr Biol **162**(2): 147-156.

van Tinteren, H., O. S. Hoekstra, et al. (2002). "Effectiveness of positron emission tomography in the preoperative assessment of patients with suspected non-small-cell lung cancer: the PLUS multicentre randomised trial." Lancet **359**(9315): 1388-1393.

van Waarde, A., D. C. Cobben, et al. (2004). "Selectivity of 18F-FLT and 18F-FDG for differentiating tumor from inflammation in a rodent model." J Nucl Med **45**(4): 695-700.

van Waarde, A. and P. H. Elsinga (2008). "Proliferation markers for the differential diagnosis of tumor and inflammation." Curr Pharm Des **14**(31): 3326-3339.

van Westreenen, H. L., D. C. Cobben, et al. (2005). "Comparison of 18F-FLT PET and 18F-FDG PET in esophageal cancer." J Nucl Med **46**(3): 400-404.

van Westreenen, H. L., M. Westerterp, et al. (2004). "Systematic review of the staging performance of 18F-fluorodeoxyglucose positron emission tomography in esophageal cancer." J Clin Oncol **22**(18): 3805-3812.

Vanderhoek, M., M. B. Juckett, et al. (2011). "Early assessment of treatment response in patients with AML using [(18)F]FLT PET imaging." Leuk Res **35**(3): 310-316.

Vansteenkiste, J. and C. Dooms (2007). "Positron emission tomography in nonsmall cell lung cancer." Curr Opin Oncol **19**(2): 78-83.

Vansteenkiste, J. F. and S. G. Stroobants (2004). "Positron emission tomography in the management of non-small cell lung cancer." Hematol Oncol Clin North Am **18**(1): 269-288.

Verboom, P., H. van Tinteren, et al. (2003). "Cost-effectiveness of FDG-PET in staging non-small cell lung cancer: the PLUS study." Eur J Nucl Med Mol Imaging **30**(11): 1444-1449.

Villa, A. M., E. Caporizzo, et al. (2005). "Choline and phosphatidylcholine fluorescent derivatives localization in carcinoma cells studied by laser scanning confocal fluorescence microscopy." Eur J Cancer **41**(10): 1453-1459.

von Schulthess, G. K., F. P. Kuhn, et al. (2013). "Clinical positron emission tomography/magnetic resonance imaging applications." Semin Nucl Med **43**(1): 3-10.

Wahl, R. L., H. Jacene, et al. (2009). "From RECIST to PERCIST: Evolving Considerations for PET response criteria in solid tumors." J Nucl Med **50 Suppl 1**: 122S-150S.

Waldherr, C., I. K. Mellinghoff, et al. (2005). "Monitoring antiproliferative responses to kinase inhibitor therapy in mice with 3'-deoxy-3'-18F-fluorothymidine PET." J Nucl Med **46**(1): 114-120.

Wang, R. M., H. Y. Zhu, et al. (2012). "[Value of (18)F-FLT positron emission tomography/computed tomography in diagnosis and staging of diffuse large B-cell lymphoma]." Zhongguo Shi Yan Xue Ye Xue Za Zhi **20**(3): 603-607.

Wang, T., J. Li, et al. (2007). "Choline transporters in human lung adenocarcinoma: expression and functional implications." Acta Biochim Biophys Sin (Shanghai) **39**(9): 668-674.

Warburg O, P. K., Negelein E. (1924). "Uber den stoffwechsel der carcinomzelle." Biochem Zeitschrift **152**: 309-325.

Webb, S. (1990). From the watching of shadows: the origins of radiological tomography. New York, NY, Oxford Medical.

Weber, W. A. (2010). "Monitoring tumor response to therapy with 18F-FLT PET." J Nucl Med **51**(6): 841-844.

Weber, W. A., S. I. Ziegler, et al. (1999). "Reproducibility of metabolic measurements in malignant tumors using FDG PET." J Nucl Med **40**(11): 1771-1777.

Wechalekar, K., B. Sharma, et al. (2005). "PET/CT in oncology--a major advance." Clin Radiol **60**(11): 1143-1155.

Wells, P., C. West, et al. (2004). "Measuring tumor pharmacodynamic response using PET proliferation probes: the case for 2-[(11)C]-thymidine." Biochim Biophys Acta **1705**(2): 91-102.

Westphalen, A. C., D. A. McKenna, et al. (2008). "Role of magnetic resonance imaging and magnetic resonance spectroscopic imaging before and after radiotherapy for prostate cancer." J Endourol **22**(4): 789-794.

Wiering, B., P. F. Krabbe, et al. (2007). "The role of FDG-PET in the selection of patients with colorectal liver metastases." Ann Surg Oncol **14**(2): 771-779.

Witney, T. H., I. S. Alam, et al. (2012). "Evaluation of deuterated 18F- and 11C-labeled choline analogs for cancer detection by positron emission tomography." Clin Cancer Res **18**(4): 1063-1072.

Wlodkowic, D., W. Telford, et al. (2011). "Apoptosis and beyond: cytometry in studies of programmed cell death." Methods Cell Biol **103**: 55-98.

Wyler, S. F., T. Sulser, et al. (2006). "Laparoscopic extended pelvic lymph node dissection for high-risk prostate cancer." Urology **68**(4): 883-887.

Wyllie, A. H., J. F. Kerr, et al. (1972). "Cellular events in the adrenal cortex following ACTH deprivation." J Pathol **106**(1): Pix.

Yamaguchi, T., J. Lee, et al. (2005). "Prostate cancer: a comparative study of 11C-choline PET and MR imaging combined with proton MR spectroscopy." Eur J Nucl Med Mol Imaging **32**(7): 742-748.

Yamamoto, Y., R. Kameyama, et al. (2009). "Detection of colorectal cancer using (1)(8)F-FLT PET: comparison with (1)(8)F-FDG PET." Nucl Med Commun **30**(11): 841-845.

Yamamoto, Y., Y. Nishiyama, et al. (2007). "Correlation of 18F-FLT and 18F-FDG uptake on PET with Ki-67 immunohistochemistry in non-small cell lung cancer." Eur J Nucl Med Mol Imaging **34**(10): 1610-1616.

Yamamoto, Y., Y. Nishiyama, et al. (2008). "Comparison of (18)F-FLT PET and (18)F-FDG PET for preoperative staging in non-small cell lung cancer." Eur J Nucl Med Mol Imaging **35**(2): 236-245.

Yang, W., Y. Zhang, et al. (2012). "Imaging proliferation of (1)(8)F-FLT PET/CT correlated with the expression of microvessel density of tumour tissue in non-small-cell lung cancer." Eur J Nucl Med Mol Imaging **39**(8): 1289-1296.

Yerushalmi, R., R. Woods, et al. (2010). "Ki67 in breast cancer: prognostic and predictive potential." Lancet Oncol **11**(2): 174-183.

Yoshimoto, M., A. Waki, et al. (2004). "Radiolabeled choline as a proliferation marker: comparison with radiolabeled acetate." Nucl Med Biol **31**(7): 859-865.

Yoshioka, M., T. Sato, et al. (2004). "Role of positron emission tomography with 2-deoxy-2-[18F]fluoro-D-glucose in evaluating the effects of arterial infusion chemotherapy and radiotherapy on pancreatic cancer." J Gastroenterol **39**(1): 50-55.

Young, H., R. Baum, et al. (1999). "Measurement of clinical and subclinical tumour response using [18F]-fluorodeoxyglucose and positron emission tomography: review and 1999 EORTC recommendations. European Organization for Research and Treatment of Cancer (EORTC) PET Study Group." Eur J Cancer **35**(13): 1773-1782.

Yuan, T. L. and L. C. Cantley (2008). "PI3K pathway alterations in cancer: variations on a theme." Oncogene **27**(41): 5497-5510.

Yue, J., L. Chen, et al. (2010). "Measuring tumor cell proliferation with 18F-FLT PET during radiotherapy of esophageal squamous cell carcinoma: a pilot clinical study." J Nucl Med **51**(4): 528-534.

Zander, T., M. Scheffler, et al. (2011). "Early prediction of nonprogression in advanced non-small-cell lung cancer treated with erlotinib by using [(18)F]fluorodeoxyglucose and [(18)F]fluorothymidine positron emission tomography." J Clin Oncol **29**(13): 1701-1708.

Zeisel, S. H. (1981). "Dietary choline: biochemistry, physiology, and pharmacology." Annu Rev Nutr **1**: 95-121.

Zeisel, S. H. (2000). "Choline: an essential nutrient for humans." Nutrition **16**(7-8): 669-671.

Zheng, X., L. Wen, et al. (2012). "A study of non-invasive Patlak quantification for whole-body dynamic FDG-PET studies of mice." Biomed Signal Process Control **7**(5): 438-446.

Zhu, A., D. Lee, et al. (2011). "Metabolic positron emission tomography imaging in cancer detection and therapy response." Semin Oncol **38**(1): 55-69.

Zijlstra, J. M., G. Lindauer-van der Werf, et al. (2006). "18F-fluoro-deoxyglucose positron emission tomography for post-treatment evaluation of malignant lymphoma: a systematic review." Haematologica **91**(4): 522-529.

Appendix 1

The Eastern Co-operative Cancer Group (ECOG) performance scoring

Grade	Performance scale
0	Able to carry out all normal activity without restriction
1	Restricted in physically strenuous activity but ambulatory and able to carry out light work.
2	Ambulatory and capable of all self-care but unable to carry out any work; up and about more than 50% of waking hours.
3	Capable of only limited self-care; confined to bed or chair more than 50% of waking hours
4	Completely disabled; cannot carry on any self-care; totally confined to bed or chair.
5	Death

Appendix 2

METHODS

Selection of target lesions

Target lesions in the pancreas and the liver were defined as lesions with the longest diameters (LD) as defined by RECIST 1.1 (Eisenhauer, Therasse et al. 2009) on CT. The lesions on the FLT PET/CT corresponding to those on the CT, showing an increased uptake and visualised on both the unfiltered and the filtered images were considered as target lesions. In patients with multiple lesions, the sum of the parameters (SUV) of all the lesions was calculated and the change with treatment documented. The data were analysed as described in Chapter 2.

RESULTS

Effect of Treatment on FLT PET variables

The waterfall plots of the changes in tumour variables are shown in **Figure (1a-c)**. The changes were similar to those seen with only the most metabolically active lesion taken for analysis. For $SUV_{60,ave}$ and $SUV_{60,max}$ nearly half of the tumours showed some degree of reduction in proliferation. Most of tumours also showed some degree of reduction in proliferation when the measure was HiVox. Interestingly, majority of the RECIST lesion P showed an increase in $SUV_{60,max}$; 6 out of the 7 progressors had a 12-132% increase in the $SUV_{60,max}$. The one progressed patient, who had a decrease in the $SUV_{60,max}$, was classed as a P by virtue of developing new liver metastases. The mean percentage reduction after treatment was 6%, -2%, and 21% for $SUV_{60,ave}$, $SUV_{60,max}$, and HiVox, respectively.

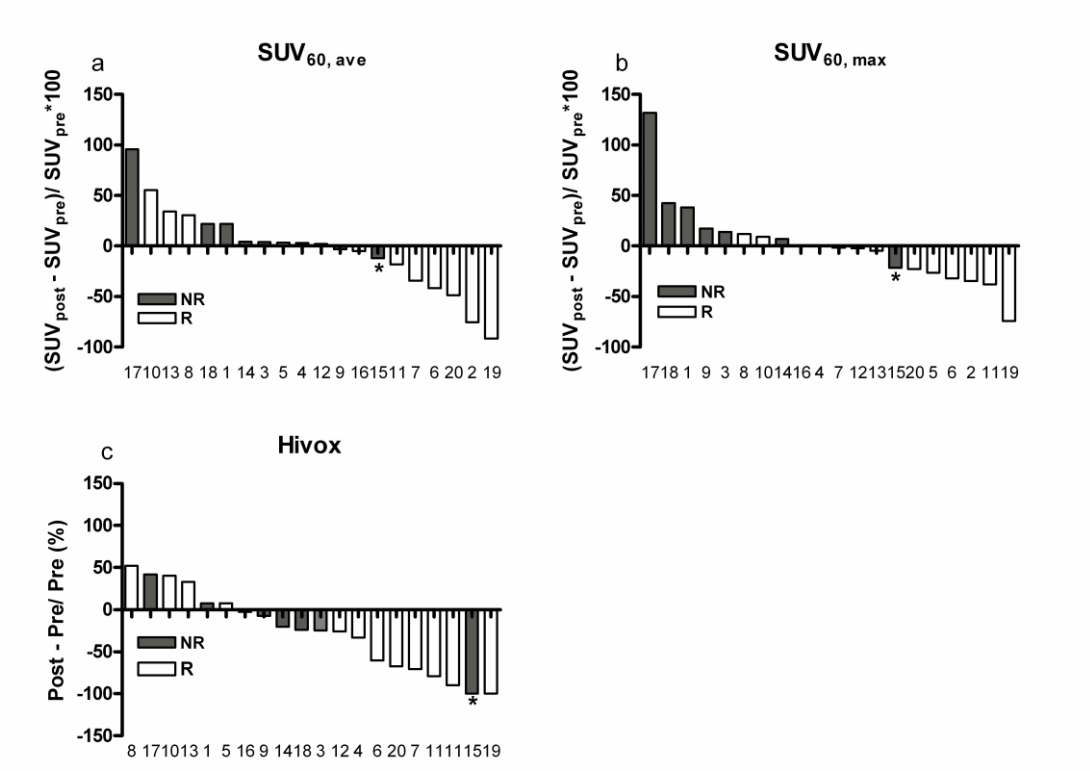

Figure 1: Waterfall plots of the sum of all the lesions.

Waterfall plots for the measures of **(a)** $SUV_{60,ave}$, **(b)** $SUV_{60,max}$, **(c)** HiVox. The RECIST lesion non-responders are shaded in grey. Majority of the RECIST lesion progressors showed an increase in FLT uptake when the measure was $SUV_{60,ave}$, $SUV_{60,max}$; 6 out of the 7 progressors had the biggest increase in $SUV_{60,max}$.

Group analyses of the imaging data were also performed. The difference between baseline and post-treatment FLT uptake showed a statistically significant decrease of $SUV_{60,max}$ in the non-progressors. In the P there was a significant increase in the $SUV_{60,max}$ but a significant decrease in the HiVox **(Figure 2 a-c)**.

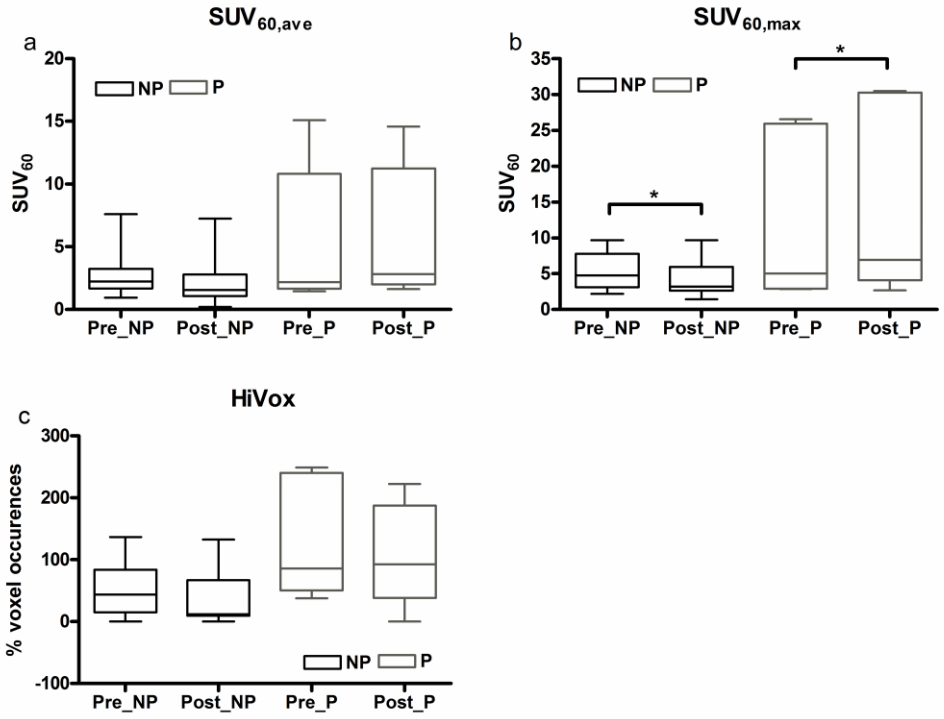

Figure 2: Group analysis of the imaging data

showing the difference between baseline and post-treatment FLT uptake in the most metabolically active lesions in non-progressors and progressors: box and whiskers plots for the measures of **(a)** $SUV_{60,ave}$, **(b)** $SUV_{60,max}$, and **(c)** HiVox.

Prediction of Survival

Of the 20 patients only 6 patients were alive after mean follow up of 10 months (range: 1.4 to 32.4 months). Based on the cut-off of 12% reduction in $SUV_{60,max}$ derived from the ROC curves, the median PFS of FLT non-progressors and progressors was 7.6 and 3.9 months (p=0.5, CI=0.24-2.01; Log rank test), respectively and the median OS was 11.5 and 8.7 months (p=0.15, CI=0.15-1.33; Log rank test), respectively in the non-progressors and progressors (**Figure 3**).

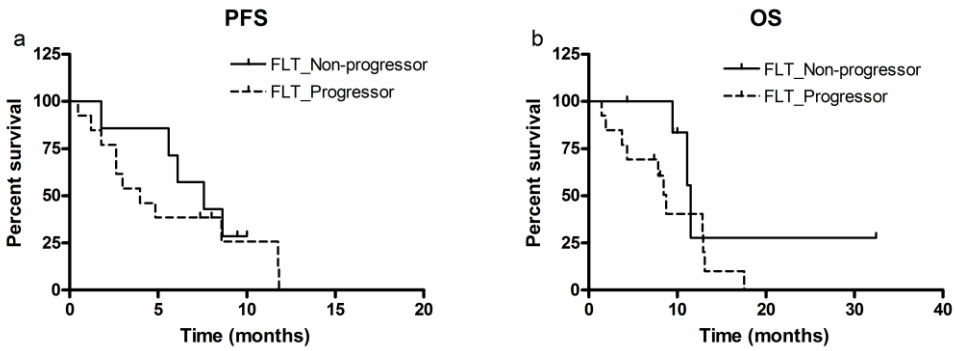

Figure 3: Kaplan-Meier Survival curves

for progression free survival (PFS; **a**) and overall survival (OS; **b**). The response classification was based on a cut-off of 12% reduction in $SUV_{60,\ max}$ for FLT.

Appendix 3

METHODS

Image analysis

The whole prostate was outlined assuming that the maximum activity is always in the tumour. This method of assessment avoided bias on repeat measurements. The data were analysed using the methodology described in Chapter 4.

RESULTS

[^{11}C]Choline uptake in malignant prostate

The baseline median (range) $SUV_{60,ave}$ and $SUV_{60,max}$ in the whole prostate (tumour) was 2.81 (1.78-4.22) and 12.04 (5.78-14.96), respectively. The median (range) $Ki_{mod\text{-}pat}$ was 0.041 mL/min/cm^3 (0.015-0.064).

Effect of NAD and RT-CAD on tissue [^{11}C]choline uptake

NAD and RT-CAD decreased tumour radiotracer uptake variables in all eight patients who completed both post-NAD and post-RT-CAD scans (**Figure 1; Table 1**). Repeated measures ANOVA demonstrated significant reductions for the following imaging variables: $SUV_{60,ave}$, $SUV_{60,max}$, $TMR_{60,max}$ and $Ki_{mod\text{-}pat}$ ($p<0.001$, <0.001, <0.001 and <0.05, respectively). There was a large reduction in radiotracer uptake in the interval between baseline and post-NAD scan. Within this period, NAD decreased whole prostate (tumour) imaging variables by 37-54% for the following imaging variables: $SUV_{60,ave}$, $SUV_{60,max}$, TMR_{ave}, TMR_{max}, and $Ki_{mod\text{-}pat}$. The reduced [^{11}C]choline uptake seen within whole prostate (tumour) with NAD was maintained after RT-CAD treatment. [^{11}C]Choline uptake was lower by 48-52% for the following imaging variables compared to baseline values: $SUV_{60,ave}$, $SUV_{60,max}$, $TMR_{60,max}$, and $Ki_{mod\text{-}pat}$ (**Figure 1; Table 1**). The magnitude of reduction in uptake was similar even at early time points ($SUV_{15,max}$ and $SUV_{30,max}$; **Table 2**). The reduction in whole

prostate (tumour) [^{11}C]choline uptake variables was also seen when the patients who did not have a post-NAD scan were included in the analysis (**Table 3**).

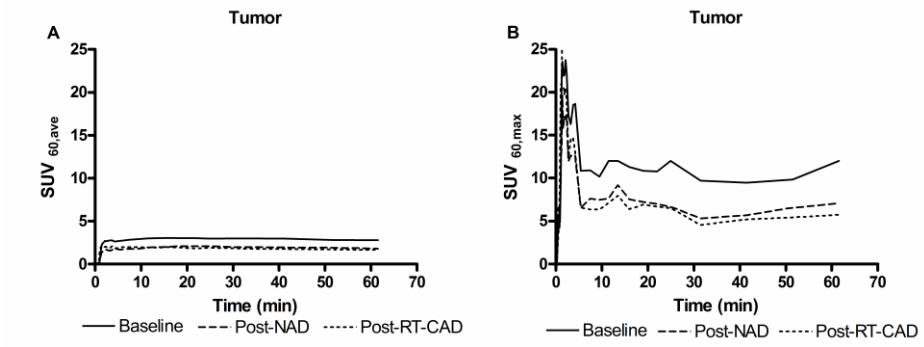

Figure 1: Time activity curves (TACs) in whole prostate (tumour) at baseline, following treatment with neo-adjuvant androgen deprivation (Post-NAD), and radiotherapy combined with concurrent androgen deprivation (Post-RT-CAD). Median TACs expressed as (**A**) $SUV_{60,ave}$ or (**B**) $SUV_{60,max}$ in the whole prostate.

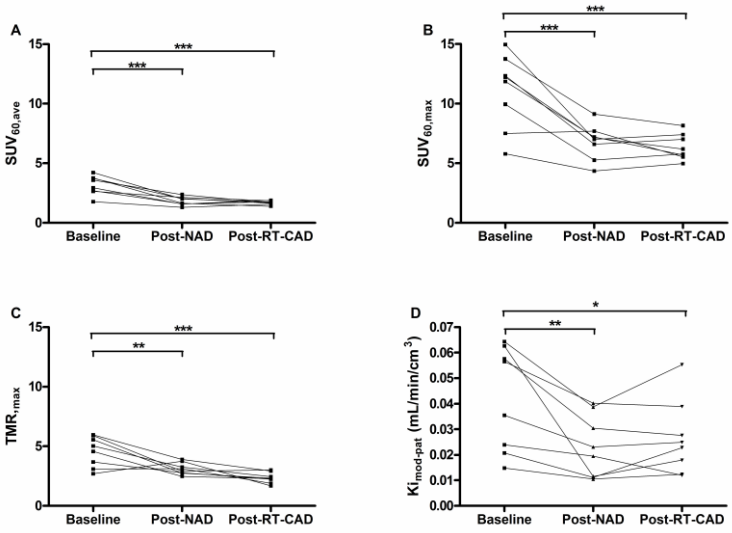

Figure 2: Semi-quantitative and quantitative measures of choline uptake in whole prostate (tumour). Trends in (**A**) $SUV_{60,ave}$, (**B**) $SUV_{60,max,}$ (**C**) maximum tumour-muscle ratio TMR_{max}, and, (**D**) Ki at baseline, following neo-adjuvant androgen deprivation (Post-NAD) and radiotherapy combined with concurrent androgen deprivation (Post-RT-CAD) in eight patients who completed all three scans. *, **, *** denotes significant changes $p< 0.05$, $p<0.01$ and $p<0.001$ respectively.

Table 1: Median [^{11}C]choline uptake variables in whole prostate (tumour) at baseline and reduction with neo-adjuvant androgen-deprivation (NAD) and radiotherapy combined with concurrent androgen-deprivation (RT-CAD) in 8 patients.

		$SUV_{60,ave}$	$SUV_{60,max}$	$Ki_{mod-pat}$ (mL/min/cm^3)	$TMR_{60,max}$
Tumour	**Baseline**	3.26	12.04	0.046	4.80
		(1.74-3.76)	(5.78-14.96)	(0.015-0.064)	(2.71-5.96)
	Post-NAD	1.83	7.08	0.021	3.02
		(1.3-2.37)	(4.07-9.13)	(0.011-0.040)	(2.48-3.90)
	Post RT-CAD	1.71 (1.38-1.89)	5.98 (4.97-8.16)	0.024 (0.012-0.055)	2.30 (1.68-3.0)
	% Reduction NAD	44***	41***	54**	37**
	% Reduction NAD+RT-CAD	48***	50***	48*	52***

TMR-Tumour-to-muscle ratio, *, **, *** denotes significant changes (p< 0.05, p<0.01, p<0.001 respectively; Repeated measures ANOVA, Tukey's multiple comparison), Values in brackets represent the range.

Table 2: SUV_{max} of whole prostate (tumour) at early and late imaging time points. Median [^{11}C]choline uptake variables in whole prostate (tumour) at baseline and reduction with neo-adjuvant androgen-deprivation (NAD) and radiotherapy combined with concurrent androgen-deprivation (RT-CAD) in 8 patients.

		$SUV_{15,max}$	$SUV_{30,max}$	$SUV_{60,max}$
Tumour	**Baseline**	12.27	10.48	12.04
		(5.79-15.18)	(6.42-12.15)	(5.78-14.96)
	Post-NAD	7.55	5.30	7.08
		(4.02-10.72)	(3.22-6.77)	(4.07-9.13)
	Post RT-CAD	6.63 (5.20-8.61)	5.08 (3.32-6.23)	5.98 (4.97-8.16)
	% Reduction NAD	39***	49***	41***
	% Reduction NAD+RT-CAD	46***	52***	50***

*** denotes significant changes (p<0.001; Repeated measures ANOVA, Tukey's multiple comparison), Values in brackets represent the range.

Table 3: Median [^{11}C]choline uptake variables in whole prostate (tumour) at baseline and changes with combined neo-adjuvant androgen-deprivation (NAD) and radiotherapy combined with concurrent androgen-deprivation and RT-CAD in 10 patients.

		$SUV_{60,ave}$	$SUV_{60,max}$	$TMR_{60,max}$	$Ki_{mod\text{-}pat}$ ($mL/min/cm^3$)
Tumour	**Baseline**	2.81	12.04	4.74	0.041
		(1.78-4.22)	(5.78-14.96)	(2.71-5.96)	(0.015-0.064)
	Post Tx	1.67	5.73	2.25	0.024
		(1.38-1.89)	(4.25-8.16)	(1.27-3.0)	(0.012-0.055)
	% Reduction	41***	52***	53***	41**

Publications and presentations to support this thesis

Publications

1. Exploring the potential of [^{11}C]Choline-PET/CT as a novel imaging biomarker for predicting early treatment response in Prostate Cancer.

   Challapalli A, Barwick T, Tomasi G, O' Doherty M, Contractor K, Stewart S, Al-Nahhas A, Behan K, Coombes C, Aboagye E, and Mangar S.

   Nuclear Medicine Communications. **In Press**

2. Biodistribution and Radiation Dosimetry of Deuterium substituted [^{18}F]fluoromethyl-[1, 2-$^{2}H_4$]choline in Healthy volunteers.

   Challapalli A, Sharma R, Hallett W, Kozlowski K, Carroll L, Brickute D, Twyman F, Al-Nahhas A and Aboagye E.

   Journal of Nuclear Medicine. **In Press**

3. [^{18}F]ICMT-11, a Caspase-3 specific PET tracer for Apoptosis: Biodistribution and Radiation dosimetry.

   Challapalli A, Kenny L, Hallett W, Kozlowski K, Tomasi G, Gudi M, Al-Nahhas A, Coombes C and Aboagye E.

   Journal of Nuclear Medicine. 2013; 54(9):1551-1556.

4. Imaging apoptosis with positron emission tomography: 'Bench to bedside' development of the caspase-3/7 specific radiotracer [^{18}F]ICMT-11.

   Nguyen QD, **Challapalli A**, Smith G, Fortt R, Aboagye EO.

   European Journal of Cancer. 2012; 48: 432-440.

5. Imaging of cellular proliferation in liver metastasis by [^{18}F]fluorothymidine positron emission tomography: effect of therapy

   Contractor K*, **Challapalli A***, Tomasi G, Rosso L, Wasan H, Stebbing J, Kenny L, Mangar S, Riddle P, Palmieri C, Al-Nahhas A, Sharma R, Turkheimer F, Coombes C and Aboagye E. * ***Joint first authors***

   Physics in Medicine and Biology. 2012; 57: 3419–3433.

6. Use of [^{11}C]choline PET/CT as a non invasive method for detecting pelvic lymph node status from prostate cancer and relationship with choline kinase expression.

Contractor K*, **Challapalli A***, Barwick T, Winkler M, Hellawell G, Hazell S, Tomasi G, Al-Nahhas A, Mapelli P, Kenny L, Tadrous P, Coombes C, Aboagye E, and Mangar S. * ***Joint first authors***

Clinical Cancer Research. 2011; 17(24):7673-7683.

Sections in chapter 3 were adapted from this publication

Presentations/ Abstracts

Chapter 2:

1. **E-abstract:** ^{18}F-Fluorothymidine (FLT) PET/CT for early response assessment in advanced pancreatic cancer.

   Challapalli A, Wasan H, Al-Nahhas A, Aboagye E, Coombes C, Sharma R.

   The ASCO Annual Meeting, Chicago, USA, June 2012.

   J Clin Oncol. 2012; 30: (suppl; abstr e21093).

2. **Oral Presentation:** [^{18}F]Fluorothymidine (FLT) PET/CT for early response assessment in advanced pancreatic cancer: initial evaluation.

   Challapalli A, Barwick T, Merchant S, Wasan H, Al-Nahhas A, Aboagye E, Coombes C, Sharma R.

   Imperial College Academic Trainees Annual Event, London, May 2013.

3. **Poster Presentation:** [^{18}F]Fluorothymidine (FLT) PET/CT for early response assessment in advanced pancreatic cancer: initial evaluation.

   Challapalli A, Barwick T, Merchant S, Wasan H, Al-Nahhas A, Aboagye E, Coombes C, Sharma R.

   Accepted for 2013 NCRI Cancer Conference, London, Nov 2013.

Chapter 3:

4. **Poster Presentation:** Immunohistochemistry of human prostate samples using choline kinase alpha antibody.

   Challapalli A, Contractor K, Pinato D, Sharma R, Hazell S, Mangar S, Coombes C, Aboagye EO.

   Imperial College Comprehensive Cancer Imaging Cancer away day, London Zoo, Regents Park, London, Nov 22nd 2010.

5. **E-abstract:** Determination of pelvic node status in patients with high-risk localised or locally advanced prostate cancer by [^{11}C]choline PET/CT.

Contractor K, **Challapalli A**, Sharma R, Kenny L M, Maher L, Winkler M, Hellawell G, Al-Nahhas A, Aboagye E, Mangar S.

The ASCO Annual Meeting, Orlando, USA, June 2010.

J Clin Oncol 28, 2010 (suppl; abstr e13546)

6. **Poster Presentation:** Initial Experience with Extended Laparoscopic Extra-peritoneal Pelvic Lymphadenectomy to Stratify Patients with Prostate Cancer for Whole Pelvic Radiotherapy.

   Contractor K B, Hellawell G, Winkler M, **Challapalli A**, Agrawal S, Dunn P, Mangar S.

   The 29 ESTRO meeting, Barcelona, Spain, 12-15th Sep, 2010.

   Radiotherapy Oncology. 2010; 96: Suppl 1, Page S359.

Chapter 4:

7. **Poster Presentation:** Evaluation of effects of Neoadjuvant Androgen Deprivation (NAD) and Radical Radiotherapy (RT) in Prostate cancer patients using [^{11}C]choline PET/CT.

   Challapalli A, Barwick T, Tomasi G, O' Doherty M, Contractor K, Stewart S, Al-Nahhas A, Behan K, Coombes C, Aboagye E, and Mangar S.

   Annual CRUK Imaging Centre Conference, London 2012.

8. **Poster Discussion:** Establishing the Use of [^{11}C]Choline PET/CT as an Image-based Biomarker in Prostate Cancer: Evaluation of [^{11}C]Choline Parameters Following Neoadjuvant Androgen Deprivation and Radical Radiation Therapy.

   Challapalli A, Barwick T, Tomasi G, O' Doherty M, Contractor K, Stewart S, Al-Nahhas A, Behan K, Coombes C, Aboagye E, and Mangar S.

   The 54th Annual Meeting of the American-Society-for-Radiation-Oncology (ASTRO), Boston, MA, 28 Oct 2012 - 31 Oct 2012.

   Int J Radiat Oncol Biol Phys. 2012; 84:pp. S184.

Chapter 6:

9. **Poster Presentation:** Imaging apoptosis with positron emission tomography: bench-to-bedside development of the caspase-3/7-specific radiotracer [^{18}F]ICMT-11.

   Nguyen, Q, **Challapalli, A**, Smith, G, Fortt R, Glaser M, Årstad E, Gudi M, Carroll L, Perumal M, Witney T, Graham M, Aboagye E.

The AACR/SNMMI Conference on State-of-the-Art Molecular Imaging in Cancer Biology and Therapy, San Diego, CA, 27 Feb 2013 - 02 Mar 2013.

J Nucl Med 2013; 54: No.2 (Suppl 1): abstract 57, Pg 19.

10. **Oral Presentation:** Biodistribution and radiation dosimetry of [^{18}F]ICMT-11: A caspase-3 specific PET tracer for apoptosis.

    Challapalli A, Kenny L, Hallett W, Kozlowski K, Tomasi G, Gudi M, Al-Nahhas A, Coombes C and Aboagye E.

    The SNMMI 2013 Annual Meeting, Vancouver, BC, Canada, June 2013.

    J Nucl Med. 2013; 54 (Supplement 2):161.

Ethics applications and ARSAC licenses for the studies in this thesis

1. **[^{18}F]Fluoro-L-Thymidine PET for assessment of treatment response in Exocrine Carcinoma of the Pancreas**

   REC: West London REC 1, 10/H0707/50, JRO: CRO1564,
   ARSAC: RPC 262/2892/26205, CSP: 53026, NCRN ID: 9298

2. **Immunohistochemistry of human prostate tumour samples using choline kinase antibody**

   Tissue bank: R12051

3. **Establishing the use of [^{11}C]Choline PET/CT in the detection of nodal disease to improve target delineation for delivery of conformal radiotherapy**

   REC: Hammersmith and Queen Charlotte's & Chelsea REC, 07/H0707/151, JRO: RD9/ 042, ARSAC: RPC 262-2892-22626

4. **The use of [^{11}C]Choline PET/CT in evaluating the early response of neo-adjuvant androgen deprivation and radical external beam radiotherapy treatment for prostate cancer.**

   REC: North London REC3, 10/H0709/55, JRO: JROHH0045,
   ARSAC: RPC 262/2892/26256, CSP: 57704, NCRN ID: 9250

5. **Biodistribution and radiation dosimetry study of deuterium substituted [^{18}F]fluorocholine ([^{18}F]D4-FCH) injection in healthy volunteers.**

   REC: West London REC 2, 11/H0711/3, JRO: JROHH0195,
   ARSAC: RPC 630/2892/29007, CSP: 67347, NCRN ID: 9695

6. **Investigation of the heterogeneity of choline kinase expression in Non-Small Cell Lung Carcinoma using [^{18}F]D4-FCH PET/CT.**

   REC: NRES London-West London REC, 12/LO/2046, JRO: CRO2071,
   ARSAC: RPC 630/2892/29588, CSP: 121598, NCRN ID: 13925

7. **A phase 1, open label PET imaging study to assess bio-distribution, radiation dosimetry, and safety of [^{18}F]Isatin Sulfonamide (ICMT-11) Injection in healthy volunteers.**

   REC: North London REC 1, 11/H0717/7, JRO: JROHH0128,
   ARSAC: RPC 630/2892/28175, CSP: 62892, NCRN ID: 9439